Universidad de Alcalá

UNIVERSIDADE LUSÓFONA

EHEA Doctorate in Health Sciences

LIGAND-FUNCTIONALIZED NANOPARTICLES FOR TARGETED THERAPY OF MELANOMA *IN SITU*

Doctoral Thesis presented by

CATARINA MENDES ALVES DE OLIVEIRA SILVA

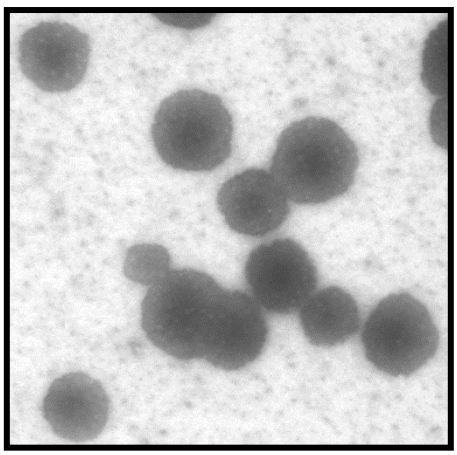

2016

Universidad de Alcalá

UNIVERSIDADE LUSÓFONA

EHEA Doctorate in Health Sciences

LIGAND-FUNCTIONALIZED NANOPARTICLES FOR TARGETED THERAPY OF MELANOMA *IN SITU*

Doctoral Thesis presented by

CATARINA MENDES ALVES DE OLIVEIRA SILVA

Directors:

Prof. Dr. Catarina Pinto Reis

Prof. Dr. Jesús Molpeceres

Co-Director:

Prof. Dr. Patrícia Mendonça Rijo

Alcalá de Henares, 2016

Universidad de Alcalá

DEPARTAMENTO DE CIENCIAS BIOMÉDICAS
Campus Universitario
Ctra. de Barcelona Km. 33,600
E-28871 Alcalá de Henares (Madrid)
Teléfono: 91 885 46 57

D. FRANCISCO ZARAGOZÁ GARCÍA CATEDRÁTICO DE FARMACOLOGÍA Y DIRECTOR DEL DEPARTAMENTO DE CIENCIAS BIOMÉDICAS DE LA UNIVERSIDAD DE ALCALÁ

CERTIFICA:

Que la memoria para optar al Grado de Doctor, elaborada por Catarina Mendes Alves de Oliveira Silva, ha sido realizada en este Departamento bajo la dirección conjunta de Doña Catarina Pinto Reis y Doña Patricia Mendonça Rijo, profesores de la Escola de Ciências e Tecnologias da Saúde da Universidade Lusófona de Humanidades e Tecnologias de Lisboa y Don Jesús Molpeceres García del Pozo, Profesor Titular del Departamento de Ciencias Biomédicas de la Universidad de Alcalá, y se encuentra ya concluida, por lo que autorizo su presentación a fin de que pueda ser juzgada por el tribunal correspondiente.

Y para que así conste, firmo el presente certificado en Alcalá de Henares a veinte y dos de julio de dos mil dieciséis.

DEPARTAMENTO DE CIENCIAS BIOMÉDICAS
Campus Universitario
Ctra. de Barcelona Km. 33,600
E-28871 Alcalá de Henares (Madrid)
Teléfono: 91 885 46 57

CATARINA PINTO REIS PROFESORA DE TECNOLOGIA FARMACEUTICA Y PATRICIA MENDONÇA RIJO PROFESORA DE QUIMICA FARMACEUTICA DE LA ESCOLA DE CIÊNCIAS E TECNOLOGIAS DA SAÚDE DE LA UNIVERSIDADE LUSÓFONA DE HUMANIDADES E TECNOLOGIAS DE LISBOA, RESPECTIVAMENTE Y JESÚS MOLPECERES GARCÍA DEL POZO, PROFESOR TITULAR DE UNIVERSIDAD DE LA UNIDAD DE FARMACIA Y TECNOLOGIA FARMACEUTICA DEL DEPARTAMENTO DE CIENCIAS BIOMÉDICAS DE LA FACULTAD DE FARMACIA DE LA UNIVERSIDAD DE ALCALÁ

CERTIFICAN:

Que la memoria para optar al Grado de Doctor, elaborada por Catarina Mendes Alves de Oliveira Silva, cuyo título es:

"Ligand-Functionalized Nanoparticles For Targeted Therapy of Melanoma In Situ"

ha sido realizada bajo su dirección y que reúne todos los requisitos necesarios para su juicio y calificación.

Y para que así conste, firman el presente certificado en Alcalá de Henares a veinte y dos de julio de dos mil dieciséis.

Catarina Pinto Reis	Patrícia Rijo	Jesús Molpeceres

ILMO. Sr. Director del Departamento de Ciencias Biomédicas

In loving memory of my grandparents, Beatriz and Antino.

To my parents, family and friends.

“A scientist in his laboratory is not a mere technician:
he is also a child confronting natural phenomena
that impress him as though they were fairy tales.”
-- Marie Curie

ACKNOWLEDGMENTS

First of all, I would like to thank to Fundação para a Ciência e Tecnologia (FCT) for financially supporting the project PTDC/BBB-BMC/0611/2012 and ULHT/ CBIOS, which were crucial for the development and conduction of this work. Secondly and not less importantly, none of this would have been possible without my amazing directors and colleagues, especially Professor Catarina Pinto Reis, who has constantly inspired me and given me the strength to go beyond my needs, to try each day my very best in the laboratory and to never, never give up. Also, I would like to thank to Professor Jesús Molpeceres and his team in the Faculty of Pharmacy at University of Alcalá, for receiving me in his laboratory with warmth and was undoubtedly an inspiration and an influence to pursue this work. My thanks go also to Professor Patrícia Rijo, who has given me an enormous support on the analytical chemistry and phytomedicine subjects involved in this work, and who has always been patiently there for clarifying my doubts and concerns. Last, but not least, I must thank Professor Teresa Neves-Petersen and Professor Steffen B. Petersen, who have kindly received me in the Laboratory of Medical Photonics at Aalborg University, and showed me the beauty in exploring other paths in science and opening our minds by thinking “outside the box”. Finally, I would like to thank all the professors and researchers that have give their knowledge and expertise with me in a wide range of themes, such as Professor María del Rosário Aberturas, Professor Guillermo Torrado, Professor María Ángeles, Professor Belén Batanero, Professor Isabel Trabado and Martín from University of Alcalá; Professor Isabel Vitória and her students from University of Coimbra; Professor Andreia Gomes and Odete Gonçalves from University of Minho; Professor Isabel Correia from IST-University of Lisbon; Professor Pedro Vieira and Ana Gabriel from Nova University and Professor Lia Ascensão, Professor João Pinto Coelho and Ricardo Gomes from Faculty of Sciences of University of Lisbon.

I would like to thank to my incredibly supportive colleagues and friends from the CBiOS-ULHT in Lisbon: Diogo, Luís and Filipe for our long and cheerful talks, João and Sara for their support and joyfulness, and Ana and Catarina for accepting with open warms the challenge of continuing this work and allowing it to go further. From the Biomedical Department in Spain, I would like to thank to Concha for her friendship and company when I was away from home, and to Javier for his support and patience in the laboratory. I would also like to thank the kind help and patience provided by Professor Luís Monteiro Rodrigues, Professor Amílcar Roberto, Professor Ana Sofia Fernandes, Professor Pedro

Faísca, Professor Marisa Nicolai, Professor Nuno Saraiva, Professor Catarina Rosado and João Costa from CBiOS-ULHT. To all of you, my eternal and sincere gratitude.

Finally, and most of all, I would like to thank my family, my parents, Palmira and Álvaro, and my closest friends, Joana Figueiredo, Vânia, Stephanie, Vasco and Joana Vilas Boas for the unmeasurable and tender care, during every moment of this journey. Also my everlasting friends, from CSCM, FCUL and ULHT, who have never let me down. Your love was essential to keep me on the right track.

I dedicate this work to all of you that stayed with me during this long and sometimes difficult passage, to those in my family that passed away and I don't forget, and that made this the most incredible journey of my life so far.

Catarina

INDEX

RESUMEN

El melanoma cutáneo es un tipo de cáncer con origen en los melanocitos que se vuelven malignos. El tratamiento del melanoma cutáneo ha evolucionado mucho en los últimos treinta años, sin embargo, no ha conseguido incrementar significativamente la supervivencia de los pacientes con cáncer avanzado. Además, el tratamiento presenta muchas limitaciones, como una reducida especificidad, efectos secundarios graves y multi-resistencia a los fármacos.

De hecho, un paso importante para el éxito del tratamiento del melanoma es su detección precoz. En el caso de que no haya metástasis, el cáncer puede ser extirpado por cirugía, pero hay casos en que el riesgo de la intervención, así como el elevado riesgo de recurrencia, obligan a un tratamiento adyuvante. Actualmente, sólo está aprobado un tratamiento adyuvante, con interferón alfa, para estos casos.

De este modo, el principal objetivo de esta tesis es el estudio de alternativas para tratamientos adyuvantes, más eficientes y menos agresivos, del melanoma cutáneo. En este contexto, se han estudiado dos estrategias para aplicación de sistemas de nanopartículas. La primera estrategia consiste en el desarrollo de nanopartículas de oro, cubiertas con polímeros naturales y péptidos, con absorción en la región del infrarojo próximo, para terapia fototérmica. La segunda estrategia incluye el desarrollo de nanopartículas hibridas, para encapsulación de compuestos antitumorales, cubiertas con polímeros naturales y péptidos, capaces de una acción química local en el tumor. Conjuntamente, hemos investigado el comportamiento físico-químico y la estabilidad de las nanopartículas para cada aplicación. Reconociendo la importancia de un tratamiento eficaz y específico, ambas las estrategias se basan en un direccionamiento específico hacia las células de melanoma, que sobre-expresan múltiples receptores en su superficie. Por fin, se utilizaron modelos animales de melanoma humano para evaluación de la eficacia de las dos formulaciones propuestas.

En conclusión, es posible desarrollar nanosistemas que comprenden diferentes estrategias terapéuticas, basadas en núcleos con estructuras distintas y funcionalización de superficies con múltiples ligandos, para una aplicación amplia y exitosa en los cánceres heterogéneos, tales como el melanoma cutáneo.

ABSTRACT

Cutaneous melanoma occurs on the skin and is the most common type of melanoma. Treatment of cutaneous melanoma has improved over the last thirty years; however, without demonstrating a significant increase on survival of patients with advanced disease. Indeed, conventional treatment generally shows several limitations, such as reduced target specificity, severe adverse effects and multiple drug resistance.

In fact, an important step for the success of melanoma treatment is its early detection. In cases where there are no metastases, this cancer can be removed by surgery, but in some cases the risk of intervention has to be measured, as well as the high risk of recurrence, which impose the use of an adjuvant treatment. Currently, there is only one adjuvant treatment approved, with interferon alpha, in these cases.

Therefore, the main objective of this thesis was the study of alternatives as adjuvant treatments, more efficient and less aggressive, for cutaneous melanoma. In this context, two strategies have been studied for application of nanoparticles systems. The first strategy is focused on the development of gold nanoparticles, coated with natural polymers and peptides, with absorption at the near infrared range, for photothermal therapy. The second strategy includes the development of hybrid nanoparticles, for encapsulation of anti-tumor compounds, coated with natural polymers and peptides, capable of a local chemotherapy at the tumor site. Overall, the physico-chemical behavior and stability of both nanoparticles for each application were investigated. Recognizing the importance of an efficient and specific treatment, both strategies were based on a specific targeting to melanoma cells, which overexpressed multiple receptors at their surface. At last, animal models for human melanoma were used for evaluation of the efficiency of both proposed strategies.

In conclusion**,** it is possible to develop nanosystems comprising different therapeutic strategies, based on distinct core structures and surface functionalization with multiple targeting ligands, for a broad and potential application in heterogeneous cancers, such as cutaneous melanoma.

INTRODUCTION

INTRODUCTION

Biocompatible and biodegradable materials, explored since the mid- 1960's for drug delivery systems [1], were refined over the years to improve drug absorption and bioavailability. The main challenge in this field is still to increase targeted cellular uptake without reducing cell viability and permanent membranes' disruption of surrounding tissues. Drug delivery systems based on biomaterials – natural, synthetically or semi-synthetically produced – are gradually increasing. In general, biomaterials include both biomacromolecules (e.g., lipids, proteins and polysaccharides) and inorganic materials (e.g., gold, silica and magnetite). Generally Recognized as Safe (GRAS) materials, biomacromolecules are used as polymers that combine safety and biodegradability with ideal characteristics to promote drug stability and target delivery [2]. They are also cheaper to produce than synthetic polymers and can be modified, physically or chemically, to obtain the desirable characteristics, such as: controlled drug release, stimuli-responsive activation (e.g., pH, temperature and ionic strength) and "stealth" for opsonization or enzymes, by penetrating naturally into cells [3]. Biomacromolecules also increase drugs' molecular weight and target absorption to prolong their half-life circulation [4].

Beside biocompatibility and biodegradability improvement, these biomacromolecules can form stable and efficient drug carriers via electrostatic or hydrophobic interactions, innovating the actual pharmaceutical procedures into cleaner and organic solvent-free ones. Proteins, peptides, polysaccharides and lipids can be used as isolated polymers for formulation of drug delivery systems. Moreover, unlimited possible conjugations between these molecules open other possibilities and outcomes to pharmaceutical formulations, through the creation of "smart materials". Therefore, innovative nano-sized technologies can push more drugs (e.g., poor-soluble molecules) further in research pipelines and, eventually, be used in clinical medicine. Mimicking the natural processes that happen in the human body may be one way to create safer and more biocompatible drug carriers, improving our health and the efficacy of our medicines.

Hybrid nanoparticles for cancer treatment

Polyester-based nanoparticles

Polyester-based particles are commonly formed as the core structure of polymeric-coated nanosystems, by simple adsorption or chemical reactions, with other molecules

that promote a sustained or prolonged drug release, compared to uncoated systems [5]. These polyester-based particles are made of hydrophobic polymers, such as poly(lactic acid) (PLA), poly(lactide-co-glycolide) (PLGA) and poly(Ɛ-caprolactone) (PCL), and act as a stable drug reservoir [6,7]. In cancer therapy, polyester-based nanoparticles are used for encapsulating chemotherapy agents, typically water-insoluble compounds, increasing their bioavailability, stability and anti-tumor effect [8]. Polyesters are biocompatible and biodegradable materials, which undergo *in vivo* enzyme-catalyzed hydrolysis, and nanoparticles are generally uptaken by cells via endocytosis [8,9].

Lipid-based nanoparticles

Currently, a wide variety of lipid-based systems is currently described in literature: emulsions (e.g. micro- and nanoemulsions, self-micro- and nano-emulsifying drug delivery systems (S(M)EDDS)), lipid vesicles (e.g., transfersomes, ethosomes and phytosomes) and other systems (e.g., liposomes, solid lipid nanoparticles (SLNs), nanostructured lipid carriers (NLCs) and lipid nanocapsules (LNCs)) [10–13]. These carriers were first explored for transdermal and topical delivery [14], but rapidly were applied for oral, pulmonary and parenteral routes [15]. Due to biocompatibility and similarity with cells membranes' components, lipid-based nanoparticles improve drugs' permeation and cell uptake. Lipid-made systems can be obtained from complex glycerides or long-chain fatty acids (e.g. oleic or linoleic acids), which are also advantageous to increase drug solubility and absorption, drug loading and ease of upgradability to production scale [12,14,16].

Protein and Peptide-based nanoparticles

Coatings and new targeting moieties such as peptides and proteins are selected to promote a target therapy, especially in cancer treatment. Proteins and peptides can be attached to the surface of nanoparticles, as targeting ligands, in order to bind selectively to specific cell receptors, increasing the efficiency of drug delivery [17]. Therefore, they will improve cell uptake, mostly by receptor-mediated endocytosis, and significantly decrease the viability of the tumor cells [18,19]. Protein-based corona also improves biocompatibility and biodegradability of synthetic polymers as they stimulate the clearance of the polymers by enzymatic processes [20].

Polysaccharide-based nanoparticles

Polysaccharides are studied as biomacromolecules for drug delivery systems due to their high availability in nature, stability, safety and low cost production. As bio-responsive polymers, like hyaluronic acid, they respond naturally to physiological variations and are fully biocompatible and biodegradable, which make them desirable for drug delivery approaches [9,21]. Selection of these materials is related with the capacity of the polymeric carrier to show optimal dimensions and chemical properties adaptable to biological and pharmaceuticals compounds, through intermolecular associations. As an example, hyaluronan-coated nanoparticles were able to interact with epithelial cells via CD44 receptor-dependent endocytosis [22,23].

Metallic-based nanoparticles

Metallic-based and inorganic nanosystems, such as gold nanoparticles, silver nanoparticles, silica-based nanoparticles and iron oxide nanoparticles show a great flexibility for obtaining systems that comprise different capabilities, as a result of the interaction of conduction band electrons associated with formation of nanoparticles [24]. In particular, gold nanoparticles appear to be attractive platforms for biomedical applications, due to their unique optical properties, chemical stability, easy surface functionalization and potentially low cytotoxicity [24,25]. As in cancer therapy, functionalized gold nanoparticles show promising results for laser-based treatments, such as photothermal and photodynamic therapies, towards cancer cells, preventing damage to healthy tissue [26].

References

1. Langer RS, Peppas NA. Present and future applications of biomaterials in controlled drug delivery systems. *Biomaterials*. 2(4), 201–214 (1981).
2. Zhang Y, Chan HF, Leong KW. Advanced materials and processing for drug delivery: The past and the future. *Adv. Drug Deliv. Rev.* 65(1), 104-120 (2012).
3. Borgogna M, Bellich B, Cesàro A. Marine polysaccharides in microencapsulation and application to aquaculture: “from sea to sea”. *Mar Drugs*. 9(12), 2572–2604 (2011).
4. McDaniel JR, Callahan DJ, Chilkoti A. Drug delivery to solid tumors by elastin-like

polypeptides. *Adv. Drug Deliv. Rev.* 62(15), 1456–1467 (2010).

5. Natarajan V, Saravanakumar P, Madhan B. Collagen adsorption on quercetin loaded polycaprolactone microspheres: Approach for “stealth” implant. *Int. J. Biol. Macromol.* 50(4), 1091–1094 (2012).
6. Wolinsky JB, Liu R, Walpole J, Chirieac LR, Colson YL, Grinstaff MW. Prevention of *in vivo* lung tumor growth by prolonged local delivery of hydroxycamptothecin using poly(ester-carbonate)-collagen composites. *J. Control. Release*. 144(3), 280–7 (2010).
7. Lu Y, Park K. Polymeric micelles and alternative nanonized delivery vehicles for poorly soluble drugs. *Int. J. Pharm.* 453(1), 198-214 (2012).
8. Zhang Y, Huang Y, Li S. Polymeric micelles: Nanocarriers for cancer-targeted drug delivery. *AAPS PharmSciTech*. 15(4), 862–871 (2014).
9. Wurm FR, Weiss CK. Nanoparticles from renewable polymers. *Front. Chem.* 2, 49 (2014).
10. Baroli B. Penetration of nanoparticles and nanomaterials in the skin: Fiction or reality? *J. Pharm. Sci.* 99(1), 21–50 (2010).
11. Benson HAE, Namjoshi S. Proteins and peptides: Strategies for delivery to and across the skin. *J. Pharm. Sci.* 97(9), 3591–3610 (2008).
12. Elsayed MMA, Abdallah OY, Naggar VF, Khalafallah NM. Lipid vesicles for skin delivery of drugs: Reviewing three decades of research. *Int. J. Pharm.* 332(1-2), 1–16 (2007).
13. Gibaud S, Attivi D. Microemulsions for oral administration and their therapeutic applications. *Expert Opin. Drug Deliv.* 9(8), 937–951 (2012).
14. Abdel-Mottaleb MMA, Neumann D, Lamprecht A. Lipid nanocapsules for dermal application: A comparative study of lipid-based *versus* polymer-based nanocarriers. *Eur. J. Pharm. Biopharm.* 79(1), 36–42 (2010).
15. Elgart A, Cherniakov I, Aldouby Y, Domb AJ, Hoffman A. Lipospheres and pro-nano lipospheres for delivery of poorly water soluble compounds. *Chem. Phys. Lipids*. 165(4), 438–453 (2012).
16. Hackett MJ, Zaro JL, Shen W-C, Guley PC, Cho MJ. Fatty acids as therapeutic auxiliaries for oral and parenteral formulations. *Adv. Drug Deliv. Rev.* 65(10), 1331-1339 (2012).
17. Akbarzadeh A, Mikaeili H, Zarghami N, Mohammad R, Barkhordari A, Davaran S. Preparation and *in vitro* evaluation of doxorubicin-loaded Fe_3O_4 magnetic nanoparticles modified with biocompatible copolymers. *Int. J. Nanomedicine*. 7, 511–526 (2012).

18. Alam S, Panda JJ, Chauhan VS. Novel dipeptide nanoparticles for effective curcumin delivery. *Int. J. Nanomedicine*. 7(0), 4207–4221 (2012).
19. Saptarshi SR, Duschl A, Lopata AL. Interaction of nanoparticles with proteins: relation to bio-reactivity of the nanoparticle. *J. Nanobiotechnology*. 11(0), 26 (2013).
20. El-Faham A, Hassan H, Khattab S. Synthesis and characterization of new polyamides derived from alanine and valine derivatives. *Chem. Cent. J.* 6(1), 128 (2012).
21. Choi KY, Saravanakumar G, Park JH, Park K. Hyaluronic acid-based nanocarriers for intracellular targeting: interfacial interactions with proteins in cancer. *Colloids Surf. B. Biointerfaces*. 99(0), 82–94 (2012).
22. de la Fuente M, Seijo B, Alonso MJ. Novel hyaluronic acid-chitosan nanoparticles for ocular gene therapy. *Invest. Ophthalmol. Vis. Sci.* 49(5), 2016–2024 (2008).
23. de la Fuente M, Seijo B, Alonso MJ. Novel hyaluronan-based nanocarriers for transmucosal delivery of macromolecules. *Macromol. Biosci.* 8(5), 441–450 (2008).
24. Alkilany AM, Murphy CJ. Toxicity and cellular uptake of gold nanoparticles: What we have learned so far? *J. Nanoparticle Res.* 12(7), 2313–2333 (2010).
25. Murphy CJ, Gole AM, Stone JW, *et al.* Gold nanoparticles in biology: Beyond toxicity to cellular imaging. *Acc. Chem. Res.* 41(12), 1721–1730 (2008).
26. Kennedy LC, Bickford LR, Lewinski NA, *et al.* A New Era for cancer treatment: Gold-nanoparticle-mediated thermal therapies. *Small*. 7(2), 169–183 (2011).

Article I

Challenges and progresses in nanotechnology for melanoma prevention and treatment

Catarina Oliveira Silva[1, 2], Nuno Martinho[3], Natália Aniceto[3], Catarina Pinto Reis[1, 4, #]

[1]CBiOS, Research Center for Biosciences & Health Technologies, Universidade Lusófona, Campo Grande 376, 1749-024 Lisboa, Portugal.
[2]Department of Biomedical Sciences, Faculty of Pharmacy, University of Alcalá, Ctra. A2, km 33.600. Campus Universitario, 28871 Alcalá de Henares, Spain.
[3]iMed.ULisboa, Instituto de Investigação do Medicamento, Faculdade de Farmácia, Universidade de Lisboa, 1649-003, Lisboa, Portugal.
[4]Instituto de Biofísica e Engenharia Biomédica, Faculdade de Ciências, Universidade de Lisboa, Campo Grande, 1749-016, Lisboa, Portugal.

*Corresponding author: Prof. Dr. Catarina Pinto Reis

Adapted from: CRC Concise Encyclopedia of Nanotechnology. (2015).
Ed. Dr. B. I. Kharisov, Oxana Vasilievna Kharissova, and Ubaldo Ortiz-Mendez
CRC Press, Taylor & Francis Group, Pages 453-470
Print ISBN: 978-1-4665-8034-3; eBook ISBN: 978-1-4665-8089-3.

Abstract

Melanoma is one of the most prevalent and severe type of skin cancer and according to the World Health Organization (WHO) data, 132,000 melanoma cases occur every year, worldwide. Incidence of malignant melanoma has increased progressively in the last decades especially in Australia, North America and Northern Europe. Although earlier detection of melanoma increases the recovery prognostic to 80%, this value decreases a lot with the occurrence of metastases. Malignant melanoma rapidly spreads to other organs and sites of the body, increasing mortality and when ulcerated primary tumors develop, the 5-year survival rate greatly drops. Currently, melanoma treatment has several limitations, such as a reduced target specificity, severe adverse effects and multiple drug resistance. For the past decades, nanotechnology associated with sophisticated drug delivery systems allowed higher drug bioavailability, controlled drug release, targeting and local drug action, as well as reduced toxicity to healthy tissues. Nanosystems made of polymers, metals or natural substances like lipids, polysaccharides and proteins can overcome biological barriers and widen the possibilities associated with tumor cell targeting or administration route (e.g., topical and transdermal routes). Therefore, there is still plenty room for new therapies and approaches that can be devised for skin cancer treatment.

Keywords: Nanomedicine; Melanoma; Drug delivery; Diagnostic; Treatment.

1. Introduction

First described by Hippocrates, malignant melanoma is the seventh most common type of cancer in young adults [1]. Melanoma is one of the most prevalent and severe type of skin cancer [2], and according to the World Health Organization (WHO) data, 132,000 melanoma cases occur every year worldwide. Even though recent data is not available yet, incidence in 2008 for malignant melanoma increased progressively in the last decades, especially in Australia, North America and Northern Europe [3], with an estimated 46,000 deaths [4]. Although earlier detection of melanoma increases the recovery prognostic to 80%, this value greatly decreases upon development of metastases [3], rapidly spreading to other organs and sites of the body, especially to the lungs [5,6]. At this stage, resistance to almost every radio- and chemotherapies is high [7].

From the main types of skin cancer (i.e., basal cell carcinoma, squamous cell carcinoma, Kaposi's sarcoma, melanoma and Merkel cell carcinoma, by order of prevalence), melanoma is originated from the melanocytes of the skin [8]. Melanoma passes through a multi-stage process: (I) benign nevi with increased number of nested melanocytes; (II) dysplastic nevi with irregular borders, multiple colors, increased diameter and random and discontinuous cytological atypia; (III) radial growth phase melanoma with malignant cells proliferating within the epidermis; (IV) vertical growth phase melanoma with transgression of *lamina propria*; and finally, (V) metastatic melanoma with spread cells to other areas of the skin or organs [3]. Nowadays, it is widely accepted that development of dysplastic nevi is associated with an increased melanoma risk [3,9].

The field of Nanotechnology has contributed extensively towards drug delivery, through development of multifunctional drug carriers that allow the increase of drug bioavailability, controlled drug release, targeted delivery, as well as a more efficient and safer therapy. These systems have grown through a progressive generation of new structures, allowing the convergence of new materials, biomolecules, physical and chemical techniques, for better outcomes. Under the aim of improving patients' health and compliance for safer and more efficient diagnosis and therapy, these technologies broaden the possibilities within the medical field and, in the case of melanoma, may overcome issues related with tumor size, vascular structure or the identification of specific genomic signatures. One example is how researchers have undoubtedly tried to

develop strategies for transdermal drug delivery as a safer solution for skin cancer through the application of nanosystems [10–14]. Nanoparticles showed promising perspectives, for example, in efficiently penetrating the skin and delivering the drug at effective therapeutic concentrations [15]. Hence, development of a local treatment to be applied ideally in early melanoma (stage 0/ I), in dysplastic nevi (stage II) or even in melanoma stage III, associated to high risk recurrence and need of adjuvant therapy [16], could prevent it from reaching melanoma metastatic stage [17]. For other skin cancers (non-melanoma), topical and local immunomodulatory therapy is already available (e.g., Imiquimod®), which is effective against superficial primary skin tumors and cutaneous metastasis [18]. Recently, biphasic vesicles were efficiently used as a topical delivery system for alpha-interferon for human papillomavirus infections (e.g., Yallaferon®), which has already successfully completed Phase I and II of clinical trials [19,20]. In conclusion, there is still much room for new, improved therapies within established chemotherapy and radiotherapy, invasive methods (surgery), as well as, unavoidable systemic approaches in skin cancer treatment.

2. Challenges associated with melanoma issues

Melanoma is a complex cancer that contrasts with other types of cancers in terms of evolution and recovery. Mostly melanoma is detected at an early stage and removed by surgery; however, before metastases appearance, ulcerated primary tumors grow, dropping the 5-year median survival rate from 97% to 39% [3]; by then, patients have a life expectancy of 6 to 10 months and the overall survival rate for stage IV melanoma (with metastasis) is only 2.3% [21]. Besides, this cancer is associated with multiple factors, as demonstrated in Table 1, which aggravate its complexity.

Table 1. Internal and external factors related with appearance of melanoma. Adapted from [3,16,22].

Internal Factors	External Factors
Ethnicity Family history Fair skin and hair (blonde or red hair) Age of onset (< 40 years) Dysplastic nevi Immunossuppresion	Exposure to UV radiation (e.g., sun, tanning-bed) Occupational chemicals' exposure (e.g., arsenic) History of blistering sunburns at young age

Melanoma treatment shows limitations related to non-specific targeting, low survival rate after ulceration development and high multiple drug resistance (MRD) [2]. Melanoma is one of the most complex tumors in terms of tumorigenic stability and molecular standardization, which can be both regarded as a great source of difficulty but, at the same time, as an opportunity to develop new, specific and targeted treatments. Targeted therapies will be explored later in this chapter. Early diagnostic of melanoma based on the 1980s "ABCDE rule" (i.e., Asymmetry; Border irregularity; Color variation; Diameter < 5 mm; Evolution of the lesion) is used for diagnosis when suspicious lesions appear [23,24]. This has improved detection by physicians, based on experience, and, in parallel, the study of histological samples by dermoscopy or microscopy has helped diagnosis; still, this cannot cover many specific and inner characteristics of the tumor in terms of its histological complexity, lack of pattern or molecular identification. Consequently, 5-10% of melanoma cases are reported to be difficult to diagnose [23]. Also in 88-89% of the cases, no additional metastases are discovered within the analysis [21].

Melanoma risk increases with the number and size of atypical nevi in skin [3,9]. Monitoring atypical nevi, especially in people prone to develop melanoma is, therefore, crucial; however, it is difficult to establish said association by only conducting histological examination. Molecular phenotyping shows a big role in distinguishing common nevi and

dysplatic nevi that can be related to melanoma appearance. Atypical nevi show higher proliferation than common nevi, as well as the presence of reactive oxidative species, although molecular markers are still unknown or too similar to differentiate.

One of melanoma's complex characteristics is the enormous quantity of receptors involved in the development of this cancer. There is still a lot left to know about the presence of receptors, molecules and factors involved in melanocytes' growth, differentiation and migration in the skin [5]. The behavior of melanoma treatment resistance is also not clear yet [7]. Refractory response and MDR of cancer are associated with genetic and molecular heterogeneity that results in complex biological mechanisms for multiple and different subpopulations of cell pools within the same tumor. For example, ATP-binding cassette B5 (ABCB5)-overexpressing cells increase along with tumor aggressiveness, after the first treatment attempt (e.g., dacarbazine, vemurafenib and doxorubicin). In addirion, these cells are accompanied by drug efflux properties in several melanoma cell lines, which increase resistance to chemotherapy in advanced stages of the disease. Until now, it was thought that melanoma cells showed enhanced tumorigenecity with stem cell-like properties, meaning that some of these cells had the ability to renew themselves and alter their aggressiveness as a whole identity. However, it seems that melanoma does not follow a cancer stem cell model, showing a high degree of plasticity, which results in switching between different stages of proliferation and malignancy (interconversion). Thus, metastatic melanoma may contain a high proportion of cells with intrinsic tumorigenic potential that may not be detected in follow-up assays [25].

Finally, another issue in melanoma's progression is the chronic inflammation already demonstrated for colorectal carcinoma, esophageal adenocarcinoma and Marjolins's ulcers [18]. Inflammatory processes play a role in all of the main stages of cancer, namely initiation, proliferation and invasion, as tumor cells produce cytokines and chemokines to attract immune cells that infiltrate into the tumor tissue [26]. Chemokine receptors regulate migration of leukocytes and play a role in infection and inflammation. It is also important to find the inflammatory gene expression profile in melanoma since it can work as a useful biomarker for response to vaccines and other immunotherapies [21]. Besides, melanoma cells show high expression of glucocorticoid receptors [27,28] and, therefore, targeted glucocorticoid-based therapy could also be selected to treat this immune-related cancer by inhibiting tumor growth [29], reducing the negative effects and controversy associated to this therapy. New molecules are currently being explored and

specifically plants with known anti-inflammatory and anti-tumor actions (e.g. polyphenols) [26], and seem to be a good source for new therapeutics. However, most of these molecules may exhibit difficulty in targeting melanoma, prompting the use of nanoparticles for these advanced therapies. This has been driven by key events of scientific evidence on their ability to overcome the ineffectiveness of many cancer treatments, prevent side effects and be able to detect early cancer that would not be identified by other means (Figure 1). For example, camptothecin, an alkaloid with anti-tumor action extracted from *Camptotheca acuminate*, with poor solubility and limited bioavailability, was incorporated into polymeric polyethylene glycol - poly(lactic acid) (PEG-PLA) nanocapsules, with high encapsulation efficiency (> 80%) for treatment of melanoma lung metastasis, demonstrating better results as *in vivo* compared to free drug, plain PLA nanocapsules and untreated tumor [30].

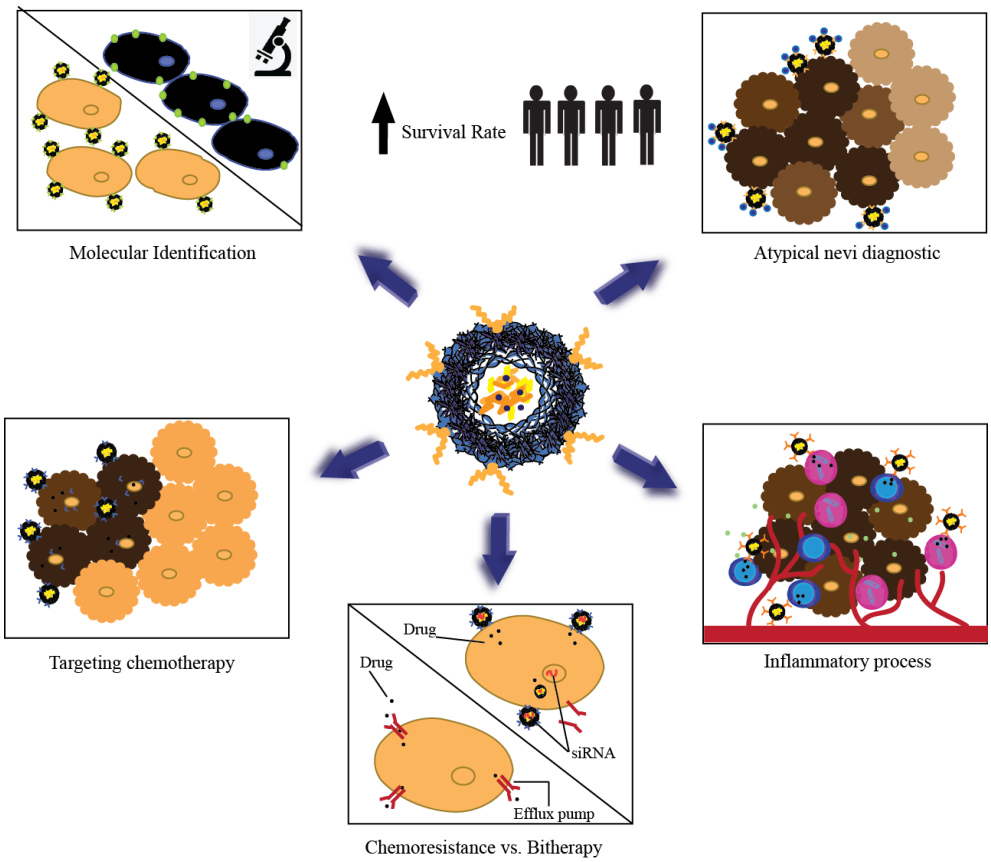

Figure 1. Multiple actions of nanoparticles in melanoma improve survival rate.

Targeting melanoma cells

Advances in molecular cancer biology have led to an increasing the knowledge of tumor receptors and ligands. As regarded before, melanoma is a heterogeneous cancer with different genetic patterns for each melanoma subtype [31], which have been reviewed extensively [5,32,33]. In order to effectively treat melanoma, a targeted inhibition of key points in molecular and biological mechanisms of tumor cells may be the most effective solution ahead. There are several pathways that can be targeted for disruption: cell proliferation (growth) and differentiation, angiogenesis, invasion (metastasis) and apoptosis [5,33]. By understanding the molecular basis behind these pathways, we may go further in unraveling the mechanisms by which chemo- and radiotherapy resistance occur and how can we beat this type of cancer [5,33]. We may find interesting to try a combined approach – simultaneously targeting multiple signaling cascades – or by first doing a molecular trial to identify the main targets characteristic to a given tumor. Herein, we will focus only on the most important receptors and those that are well described, understanding that there are many others involved in melanoma development.

Melanocytes' proliferation occurs coupled with that of keratinocytes, which regulate their growth and receptor expression profile at their surface, via cell adhesion and growth factors (e.g., cadherins, growth factors and endothelins). One of the most important receptor is melanocortin receptor 1 (MC1R), regulated by melanocortins, such as α-melanocyte-stimulating hormone (α-MSH), adrenocorticotropic hormone (ACTH) and β-endorphin [34]. MC1R is expressed in high levels in the majority of melanoma cell lines and at low levels in normal cells (i.e., keratinocytes, melanocytes, fibroblasts and immunologic cells) [34,35]; besides, MC1R may play an important role in immune and inflammatory processes: although expressed in lower levels than in both cutaneous and uveal melanomas (α-MSH binds up to 5 times more to melanoma), this receptor appears significantly in activated monocytes [36]. The ligand α-MSH confers attachment and internalization to MC1R overexpressed on the surface of melanoma cells, simultaneously reducing the metastasis growth, but also diminishing the immune response against melanoma [37,38]. MC1R is also responsible for stimulating eumelanin synthesis in melanocytes, which protects the skin from UV radiation and the damage it can cause in DNA [39,40]. Studies made with gold nanospheres covered with PEG and displaying an agonist targeting moiety against MC1R achieved a successful targeting with high doses at the tumor site, which after laser treatment, induced high levels of necrotic tissue therefore having efficient photothermal ablation ability. Gold nanoparticles

were selectively taken up by the cell even reaching the cytoplasm [41]. In addition, an agonist moiety targeting (α-MSH analog) also shows superior internalization by tumor capillaries, suggesting a receptor-mediated endocytosis, while antagonist targeting stays at the cell surface, since it cannot mediate endocytosis [42]. In another study, Polyethylene glycol-coated (PEGylated) protein nanoparticles formulation based on human ferritin were developed and functionalized with α-MSH through a link created by genetic modification with increased specific binding to melanoma cells. *In vivo* administration of these nanoparticles in mice also demonstrated higher accumulation into cutaneous tumor as compared with other organs (e.g. liver) [43].

Mutations in MC1R receptor are related to melanoma proliferation: this highly polymorphic receptor affects the response to UV light by melanocytes increasing the DNA damage effects. A recent study found that α-MSH is useless in absence of MC1R expression, increasing the risk of melanoma; also, activation of the p53 pathway by α-MSH can work as a preventive strategy against DNA damage [39]. Desai *et al.* (2013) showed successful tumor regression in mice that received a melanoma xenograft, upon intraperitoneal administration of complexes of danaciclib- 2-hydroxypropyl-β-cyclodextrin (HPβCD). *In vitro* 2D adherent and 3D organotypic melanoma models revealed a positive response to the administration of the complexed drug, with inhibition of cell growth, depending on p53 signaling [44]. In fibroblasts, for example, cellular growth seems to be compromised after α-MSH stimulation, but in presence of polymorphisms, proliferation occurs [35]. Recently, as fibroblasts present this metabolic support to melanocytes, including when melanoma cells are formed, new targets based on overexpression or knock-down of key metabolic genes have been validated, for promoting tumor growth and /or metastasis in mice models [45]. Melanoma cells also activate fibroblasts and, in return, these cells provide them both structural (i.e., extracellular matrix proteins that increase tumor cells survival) and chemical support (i.e., growth factors) [34]. Interactions between melanoma and stromal cells through the microenvironment promote the tumor growth, malignancy and also drug resistance. Melatonin receptors are also important since they regulate the phenotypic actions of cells growth and differentiation [5]. Lipid-polymeric nanoparticles for melatonin transdermal delivery were applied to treat early stage melanoma [46,47]. Melatonin is a suitable molecule for transdermal and topical transport and could benefit from the advantages of a nanoparticulate system, such as controlled release, targeted action and deposition on specific cell pools in the skin.

Also present in the signaling pathway, protein WNT5A expression increases with melanoma progression; present also in common nevi, it is related to melanoma aggressiveness, motility and invasion of cutaneous melanoma [48]. Extracellular-signal-regulated kinase (ERK) is the only known activated protein by Mitogen-activated protein kinase kinase (MEK 1/ 2), which influence on melanoma is still unknown. Still, higher levels of ERK are identified in subcutaneous metastases compared with lymph node metastases or common nevi, indicating that protein activation occurs at advanced melanoma stages. Insurgence of medicines to inhibit MEK 1/2 is, therefore, promising for these kinds of tumors [33], since it is overexpressed in the majority of melanomas [21]. Other markers help in clinical diagnosis by accurately distinguishing melanoma cases from dysplastic nevi ones, showing some progress, in spite of the cancer complexity [49]. The majority of melanomas (50-60%) also show an active mutation (V600E) for B-Raf proto-oncogene (BRAF), inducing tumor cells growth and angiogenesis. Thus, therapy with BRAF inhibitors is also promising [31,33]. Vemurafenib (*per os*) shows a 30-fold selectivity for the pV600E mutated form compared with wtBRAF. But, this drug causes keratoacanthomas and invasive cell carcinoma, treatment resistance and melanoma relapse [31]. MEK and phosphoinositide 3-kinase (PI3K) pathways also interfere in BRAF mutations and, as targets for melanoma, can reinforce the idea of conjugated bitherapy in this type of cancer [26]. Uveal melanoma causes metastases mainly (95%) in the liver and lack mutations of the BRAF gene, which indicates that it acts by different signaling cascades than cutaneous melanoma (e.g., MEK/ MAPK), mainly mutually exclusive GNAQ or GNA11 mutations. However, BRAF (V600E) mutation could be identified in small populations of cells within the uveal tumor. Other ocular tumors that not arise from uvea are biologically similar to cutaneous melanoma [50].

Finally, vitamin D3 receptors may also be an interesting alternative to explore for a possible role in anti-melanoma mechanism [5]; tyrosine is also an interesting target, since melanoma needs higher concentrations of this amino acid residue to proliferate. Specific targeting is highly valuable and can affect the biodistribution. PEG-PLA nanocapsules delivering a modified form of tyrosinase enzyme improved its stability for more time at body temperature, in order to lower the systemic tyrosine available for melanoma [51]. This approach can also benefit from the different scale sizes since smaller particles (< 100 nm) can enter melanoma cells and inhibit proliferation and invasion, but larger particles (> 200 nm) can also convert tyrosine, lowering the levels in

the extracellular environment and acting by following the same path as the metastases [52].

3. Nanotechnology and progress of drug delivery systems

As the nanotechnology field grows, with almost 40 years of study, employment of new mechanisms to reach specific targets is now on its way. In terms of cancer (with the same years of study), we can see that a lot has been done to overcome the drawbacks of this disease, as more complex and unpredictable cancers are occurring [53]. Melanoma is considered one of the most challenging cancers, in terms of diagnosis and treatment efficacy. Enhanced knowledge of biomolecules and polymers, as suitable structures for drug transport, improve the performance of those drug delivery systems. Throughout the studies over the last years, physical and chemical characteristics of commonly used biomaterials have been described and the *pros* and *cons* demonstrated [54–57]. By working with different materials it is possible to tune their interaction with biological environment. Interactions between materials are also being studied, and they may occur by simple electrostatic interactions or by reactive promoted links, such as covalent ligations. Interactions with drugs can also be used, as both slow or fast release, obtained directly by adsorption at the particle surface, might also be required [58]. All these facts are currently background knowledge for the seeking of hybrid nanocarriers. Also, there is a main importance in the use of biomolecules and natural ligands that can mimic natural cell responses and mechanisms, facilitating the active compounds entrance and avoiding their rapid clearance [59]. It is also accepted that binding ligands at the surface of the nanoparticles facilitate their penetration through the biological barriers to reach the specific targets (e.g., BIND-014) [60]. Especially for hydrophobic substances with anti-tumor and anti-inflammatory activities, these systems work as a promising solution for poor drug bioavailability and also offer other ways to enter the body, such as pulmonary, ocular or transdermal routes [61]. Solid tumors, like melanoma, have a pore cut-off between 380 and 780 nm [59], so particle size is an important factor, as nanoparticles with 200 nm cannot escape the normal vasculature, but accumulate in cancer vicinity, due to extravasation and diffusional barriers [59]. As will be further explained in this chapter, with the help of nanotechnology we may be closer to the desirable personalized cancer therapy.

4. Nanomedicine applied to melanoma prevention

One of the main problems associated to poor survivability of patients with melanoma is the difficulty of early diagnosis. Clinical and self-examination for high risk patients is the first way for prevention. In spite of physicians' experience, we may be facing a remarkable development with the advent of molecular identification and genetic typing, for improved diagnostic of cancer. Another important advance is the use of imaging techniques that permit a clear visualization of the skin distinguishing different morphologies and depths of dysplastic nevi. In conjugation with fluorescent markers, incorporated within small sub-micron particles, we may be able to target specific receptors and proteins on the tumors' surface, facilitating its identification. There is already some work in this field, especially with metallic-based nanoparticles as multifunctional systems. For example, the use of ultrasound imaging to follow the progression of tumors can work for diagnostic and therapy associated with drug delivery systems [62]. Gold nanoparticles can be used as contrast agents in photoacustic imaging (PAI), which is based on the delivery of non-ionizing optical pulses at near-infrared (NIR, 650-900 nm) for an accurate and early diagnosis of melanoma. These techniques will be further explained.

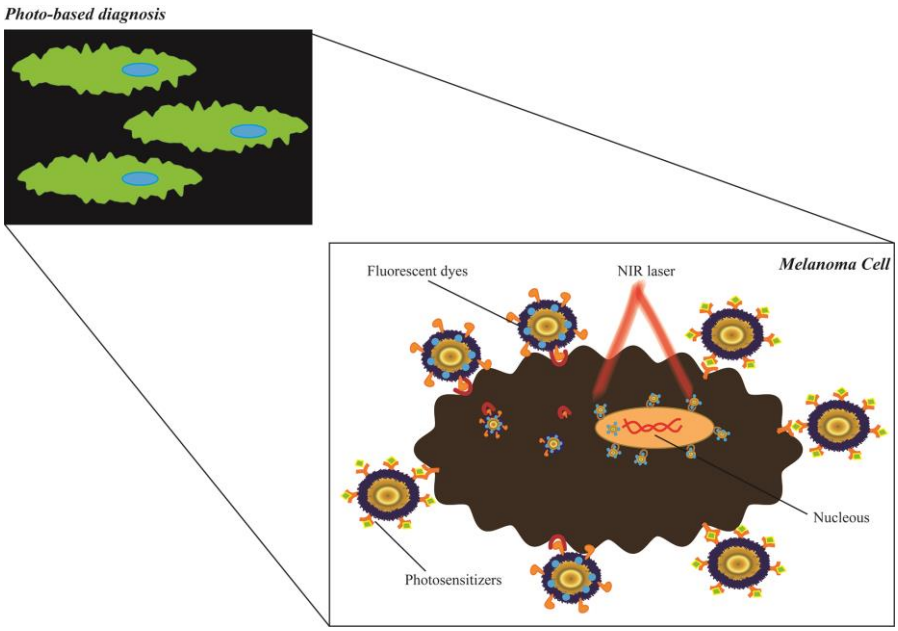

Figure 2. Gold nanoparticles' mechanisms in melanoma prevention. Diagnosis by near infrared (NIR) light activation and targeting penetration into melanoma cells, by photosensitizers and fluorescent dyes, for further molecular plotting.

Chemoprevention of melanoma, described elsewhere, suggests the use of targets for effective delivery of anti-tumor agents (e.g., statins, curcumins, selenium, non-steroid anti-inflammatory drugs (NSAIDs) and vitamin D) [63]. Most of them act hypothetically by inhibition of proliferation and invasion of melanoma. One example is the use of selenium supplementation as its antioxidant properties are described to prevent melanoma appearance, when used topically (twice a week) at an early stage; however, this activity is still controversial as it may aggravate the tumor growth in an advanced stage [64]. Another study conducted with a derivative of selenium with nitric oxide synthase *(*iNOS) inhibitor demonstrated that topical application was not aggressive to keratinocytes or dermal fibroblasts and decreased the tumor growth *in vitro* (70-80%) and *in vivo* (approx. 50%), by promotion of the tumor cell apoptosis [65]. In fact, as described in other papers, the use of selenium nanoparticles can promote a targeted activity and higher concentration at the tumor site, reducing possible adverse effects behind the controversial results. Selenium nanoparticles have also been tested as carriers for anti-tumor drug 5-Fluorouracil (5-FU), physically adsorbed at the surface, in order to obtain a synergistic effect and reduce the chemotherapy adverse effects. The authors also proposed the use of this system as a topical formulation in order to avoid the *in vivo* degradation of 5-FU- selenium nanoparticles and to reduce the non-target toxicity [66]. Finally, hyaluronic acid (HA) is described in the literature as both drug carrier and target ligand due to its affinity to CD44 receptors in cancer cells [67]. Spherical nanoparticles with a size less than 200 nm and a high negative surface charge demonstrated a receptor-mediated endocytosis for melanoma cell lines and reduced significantly the tumor growth in mouse models after intra-tumor (i.t.) and intravenous (i.v.) injections [67].

Photoprotection

Exposure to sunlight, the main environmental factor behind melanoma, and skin cancer in general, is still not completely described in terms of the exact influence of the wavelength and UV-B/ UV-A light on melanoma [68]. Although for many years this could not explain the appearance of melanoma in different body regions (e.g., brain, lung or vagina), or even the appearance of cancer in non-Caucasian people, it is clear that there is a relation between the disease and this risk factor. Recent studies have gone further in this investigation and found a relationship between the formation of cyclobutane pyrimidine dimmers – damaging the cells' DNA – and leading to tumor initial

development, as well as other unidentified bulky lesions mainly associated with UV-B light [69]. Nanoparticles also have an important impact in this field, as they serve as effective photo-protective carriers applied to cosmetic formulations, especially zinc oxide (ZnO) and titanium oxide (TiO_2) nanoparticles [53], reaching effectively the skin surface cells with sunscreen and protecting them from the damage action of UV light.

Tumor imaging and detection

Long goes the time where surgical management occurred according the Handley's principle of removal of 5 cm of the subcutaneous tissue for metastatic melanoma. Even narrower margins (1 cm for melanoma ≤ 1mm and 2 cm for thicker melanoma) are now supported by imaging techniques. Based on their colorimetric and fluorescence properties, nanoparticles may facilitate the localization of the tumor cells, minimizing the extent of skin removed from surgery. Nanoparticles can also identify other tumors dispersed within the body, if ulceration or metastases occur. For example, paramagnetic nanoparticles containing a targeting moiety to $\alpha v\beta 3$ integrin were used to detect early angiogenesis formation of early melanoma tumors [70]. This technology is valuable to avoid invasive approaches, as the majority of the relapses are also local (50-85%) during the first two years [71]. Confocal laser scanning microscopy (CLSM) is a useful imaging tool in distinguishing common nevi, dysplastic nevi and melanoma, through differences in cell morphology and loss of keratinocyte cell borders [72], as well as optical coherence tomography (OCT) similar to B-mode ultrasound pulse-echo imaging. Melanoma often appears with deformed borders of the dermis and spike morphology when compared with common benign nevi [68]. OCT also estimates the superficial thickness of the skin cancer, but cannot yet differentiate states of inflammatory processes or cancer [68]. High-frequency ultrasound (20 MHz) is also used in diagnosis of lesions close to the skin surface (epidermis and dermis) and other techniques including Terahertz Pulsed Imaging (TPI), Magnetic Resonance Imaging (MRI) and Raman Spectroscocpy (NIR, 650-900 nm) can also evaluate skin structure in relatively safe conditions [68]. Since biological tissues and fluids do not absorb the red wavelength range [73], light can penetrate deeper into the skin layers [74]. Most anatomical imaging techniques do not require contrast agents, but molecular ones do. Photon Emission Tomography (PET) and Single-Photon Emission Computed Tomography (SPECT) are, nowadays, widely used for the diagnosis of cellular and molecular specificities. Several targeting peptide probes using radio-isotopes that do not block the receptor binding are being developed to improve these imaging techniques. Development of radio-labeled α-MSH can improve

the diagnostic of melanoma, especially as cyclic analogs with higher stability in physiological conditions, improved pharmacokinetics and superior *in vivo* tumor targeting [75]. Cyclized α-MSH peptide derivatives can also be used for melanoma imaging and radiotherapy, since they can get higher binding activity, tumor cells' uptake and good imaging properties [76]. In terms of nanotechnology application, the most used systems are magnetic iron oxide nanoparticles (IONPs), quantum dots (QDs), polymeric nanoparticles and carbon nanotubes [75]. Nanoparticles, besides their small size and capacity to penetrate the cells, can be linked to multiple probes and targeting ligands by surface functionalization, improving the imaging of cellular and molecular subjects. For example, arginylglycylaspartic acid (RGD) was linked to partially thiolated polyamidoamine (PAMAM) G4 dendrimers coating cadmium selenide (CdSe) QDs to reach melanoma cells that overexpress $\alpha v\beta 3$ integrin in their vessels. With a final size of 13.5 nm, QDs were useful for detection, while dendrimers were used to confer the desirable surface properties and link the intended residues. Both *in vivo* and *in vitro* uptake was associated to the binding of RGD to the integrin receptor while no passive targeting was observed after three hours [77]. Cases of inflammatory regions could be counteracted by nanotechnology application and targeted delivery of fluorescent drugs, avoiding other invasive methods [74,75].

Theranostics

In terms of diagnostic and detection, nanoparticles can function as both tumor markers and as carriers for photodynamic substances. Metallic particles made of gadolinium, nickel, iron and gold can be used as contrast agents and as standards for these approaches, which are regarded as safe and can work together with other techniques such as ultrasounds, laser or thermal therapies to destroy tumors. Commonly, liposomes and polymersomes are selected [78], mainly because these vesicles can easily penetrate the cell interstices and reach the tumor site. They can also incorporate highly hydrophobic drugs for therapy and hydrophilic molecules/ probes normally selected for imaging [78], as mono- or bitherapy. Nanoparticles are the most used systems for theranostics purposes, especially after increased stability by coating the particles' surface with ligands or molecules (e.g., peptides, carbohydrates, oligonucleotides), which also serve a therapeutic action [73]. This fact broadens our possibilities in terms of the applications, as these particles are suitable for visualization of living cells and all dynamic processes occurring in them, combining different probes to stain different locations on the cell surface and within the cell. Still, very small gold nanoparticles (1-2

nm) show high toxicity due to the possible irreversible binding to DNA molecules [73]. Silica has gradually gained its space in the field, as this polymer is highly stable, biocompatible, with a strong potential in terms of particle functionalization and drug release [79]. New ligands or modification of existing ones can be used to improve the binding affinity and activity. One example is the development of peptides with single, double and triple bonds harboring lysine residues and other moieties, for cells overexpressing MC1R. It was found that trivalent ligands can reach higher selectivity and better affinity in presence of high density receptors [80]. This approach could offer promising tools for both diagnosis and therapy in melanoma. Finally, a different approach of theranostics is the use of imaging nanoparticles for drug follow-up during treatment. A study focused on the distribution of paclitaxel in solid tumors, such as melanoma, by the use of TiO_2 nanoparticles coupled with imaging techniques (mass spectrometry imaging, 2D) that show some drawbacks, like high background noise and presence of endogenous molecules that mask the signal; nanoparticles improved the resolution due to their physical behavior for localized uniform deposition of energy, being used as a matrix for imaging. Therefore, it was possible to visualize the drug presence in the central portions of the tumors, after different treatment schedules [81].

5. Nanomedicine applied to melanoma treatment

Most melanoma-related advances have been made at the level of treatment development [82]. Nanomedicine appears as an alternative to traditional therapeutics that combine an ineffective action and systemic side effects, associated with the destruction of both tumor and healthy cells. There is also a possibility to combine different approaches and new molecules (e.g., monoclonal antibodies (mAb)) at the particle surface, since melanoma is essentially an immunogenic tumor, and encapsulate an anti-tumor drug to effectively destroy the cancer. To this matter, PAMAM G2 linked with octavalent N-acetyl-glucosamine showed *ex-vivo* enhanced T-cell and natural killer cell activity, which may explain the resulting in reduced tumor growth and enhanced mean survival time in a dose-dependent manner *in vivo* [83]. The complexity of the disease shows that higher selectivity and specificity have to be fulfilled with the selected treatment. Therapeutic agents have to be determined for each person or each type of cancer. Until now, few drugs have been approved by the Food and Drug Administration (FDA) and the European Medicines Agency (EMA) for melanoma treatment (Table 2).

Table 2. Approved drugs by U.S.A. and European Agencies for melanoma treatment (Food and Drug Administration (FDA), 2016, at http://www.fda.gov; European Medicines Agency (EMA), 2016, at http://www.ema.europa.eu).

Therapy	Type of agent	FDA approval	EMA approval
Chemotherapy	Akylating agents	Dacarbazine (1970)	Dacarbazine (2002)
Immunotherapy	Oncolytic herpes virus	Talimogene Laherparepvec "T-Vec" (2015)	Talimogene Laherparepvec "T-Vec" (2015)
	Monoclonal antibody anti-PD-1	Pembrolizumab (2015)	Pembrolizumab (2015)
	Monoclonal antibody anti-PD-1	Nivolumab (2014)	Nivolumab (2015)
	Antiviral	PEGinterferon alfa-2b (2011)	-
	Monoclonal antibody anti-CTLA4	Ipilimumab (2011)	Ipilimumab (2011)
	Interleukins	Aldesleukin, IL-2 (1998)	-
	Antiviral	Interferon alfa-2b (1986)	Interferon alfa-2b (2000)
Targeted therapy	BRAF V600 mutation / MEK inhibitors	Cobimetinib (2015) *used in combination with vemurafenib	Cobimetinib (2015)
		Trametinib (2013)	Trametinib (2014)
		Dabrafenib (2013)	Dabrafenib (2013)
		Vemurafenib (2011)	Vemurafenib (2012)

Nanomedicine can also help to accomplish this approach and reach the complexity of each cancer, such as combining different therapeutic agents. One suggestion is the association of anti-CTLA4 ipilimumab and BRAF-inhibitor vemurafenib to improve intra-tumor infiltration by acting synergistically to avoid the immunosusceptibility of the tumor, since ipilimumab increases the overall survival of melanoma patients [21]. Ipilimumab

was actually the first agent to reach this positive reaction in cases of advanced melanoma and conjugation approaches are already in phase II for clinical trials (Table 3). This drug is proposed for patients with refractory and advanced melanoma stage and has demonstrated overall improvement of patients' survival, but cause immune related reactions that are counteracted by administration of glucocorticoids and other immunosuppressants [6,84]. Another important strategy includes mAb and anti-angiogenetic drugs (e.g., paclitaxel and docetaxel) [21]. This approach can also be improved by nanotechnology as demonstrated for docetaxel incorporated into lipid-based nanomicelles (20-25 nm) [85] and into solid lipid nanoparticles (SLN) (140-180 nm), including a variety of lipids for better hydrophobic drug incorporation, tolerability and cell transport [86].

Dendrimers are another class of polymeric nanoparticles with a promising application in cancer diagnostics and therapeutic [87,88]. By virtue of their small size and large number of functional terminal groups, dendrimers are highly favorable to interact with biological systems at molecular level. Since their surface chemistry is one of the key critical elements between therapeutic value *versus* toxicity, specialized moieties can be precisely attached to increase molecular targeting (e.g., attachment of antibodies, folate or RGD), to avoid unspecific interaction with cellular components (e.g*.,* by cationic charges) or with reticuloendothelial system (RES), as well as to increase the residence time by attachment of PEG. The architecture, composition and size of the polymer may also influence the cell uptake and, therefore, the therapeutic effect [89,90]. Dendrimers show a protein-like structure, so they can also have therapeutic activity of their own. For example, Poly(L-lysine) G6 dendrimers were shown to have anti-angiogenic activity both *in vitro* and *in vivo* in B16F10 model after i.v. administration at a dose of 50 mg/kg/day, being able to delay tumor growth while increasing apoptosis [91].

Table 3. Current clinical trials studies associated with nanosystems (U.S. National Institutes of Health, 2013-2016, at http://clinicaltrials.gov).

Systems	Subject	Melanoma stage – Clinical stage	Reference
Inorganic Nanoparticles	Targeted Silica Nanoparticles for Image-Guided Intraoperative Sentinel Lymph Node Mapping Head and Neck Melanoma	Head and Neck Melanoma - Phase 0	NCT02106598
Protein-based Nanoparticles	Paclitaxel Albumin-Stabilized Nanoparticle Formulation (and Bevacizumab or Ipilimumab) as First-Line Therapy	Stage IV inoperable - Phase II (completed)	NCT01879306
	Bevacizumab and Temozolomide or Bevacizumab and Paclitaxel Albumin-Stabilized Nanoparticle Formulation and Carboplatin	Stage IV inoperable - Phase II (completed)	NCT00626405
	Paclitaxel Albumin-Stabilized Nanoparticle Formulation (nab-paclitaxel, Abraxane®)	Intraocular melanoma inoperable - Phase II (completed)	NCT00738361
	Paclitaxel Albumin-Stabilized Nanoparticle Formulation (ABI-007)	Inoperable locally recurrent or metastatic melanoma - Phase II (completed)	NCT00081042
	Carboplatin and ABI-007 (Abraxane®)	Stage IV melanoma inoperable - Phase II (completed)	NCT00404235
	Abraxane and Avastin	Metastatic malignant melanoma - Phase II (completed)	NCT00462423
	BIND-014	Advanced or metastatic cancer - Phase I	NCT01300533
Liposomes	Liposomal Cytarabine in combination with Radiotherapy and Lomustine for treatment of Leptomeningeal Metastasis from Malignant Melanoma	Advanced or metastatic melanoma - Phase I	NCT01563614
	Vincristine Sulfate Liposomes Injection (Marqibo®)	Malignant melanoma – Phase I (completed)	NCT00145041
	Vincristine sulfate liposomes injection (Marqibo®)	Metastatic malignant uveal Melanoma – Phase II (completed)	NCT00506142
	Liposomal Vaccine (Lipovaxin-MM®)	Melanoma – Phase I (completed)	NCT01052142
	Vaccine Therapy Plus Interleukin-2 With or Without Interferon Alfa-2b	Metastatic (stage III) cutaneous Melanoma – Phase II (completed)	NCT00004104

Radiotherapy

Radiotherapy is based on radiation use for cancer cells destruction. However, this treatment is very complicated and dreadful for patients, who suffer from several side effects, and is rarely used only as monotherapy. Based on this fact, we can bring together the two approaches (radio- and chemotherapy) and, for example, administer anti-tumor drugs encapsulated inside nanocarriers that respond to the action of lasers or radiation. Metallic-based nanoparticles release anti-tumor drugs only after reaching the tumor site, by means of a radiation beam, or after thermal ablation, acting as a synergistic multifunctional therapy for cancer [74].

High-frequency ultrasound (HFUS) imaging creates a B-scan image of the tissue evolution after tumor implementation in melanoma orthotopic models [92]. Electrochemotherapy (ECT) is a new technology that combines electric pulses (non-thermal) and anti-tumor agents (e.g., bleomicin). External electrical stimulations increase the cells permeability and facilitate drug penetration into the tissue. However, it shows side effects such as erythema, erosion or ulceration (scaring) and oedema and pain [21]. Still, in a long-term response (5 years) study, made on patients having malignant melanoma (refractory or relapsed cutaneous melanoma), and treated with ECT, it showed that approximately 50% of the patients displayed a complete response and were free of the disease after two years [1].

Photodynamic therapy (PDT) is a non-invasive procedure including a photosensitizing drug (e.g., prodrug 5-aminolevulinic acid named as 5-ALA) that can be activated by light to produce oxidative reactions locally and destroy the tumor cells [74,93]. Light is obtained through a laser that can emit pulses; metallic nanoparticles improve PDT by focusing the beam to a localized area, minimizing eventual damage to adjacent normal cells and by triggering drug release only on the tumor site. This technique may be used in all areas of research, diagnosis, prevention and treatment. Laser-based therapies already approved as topical treatment by FDA and EMA for non-melanoma cancers and previous lesions like actinic keratosis, can also allow combination of treatments, through the use of targeting agents (photosensitizer plus immunomodulator) or, more recently, coupled with nanoparticles to increase the penetration of the photosensitizers deeper into the skin. Actually, PDT allied to nanomedicine could revolutionize dermal melanoma treatment by applying non-invasive local therapies, with minimal side effects [74], and also reduce the thermal dose required for cytotoxicity that affect both cancer and healthy

tissue, since the two techniques work synergistically together [94]. For example, by assessing the effectiveness of two model sensitizers used in PDT (meso-tetrakis[4-sulphonatophenyl]porphine,TPPS4 and its zinc metallocomplex, ZnTPPS4), in the presence and absence of Hydroxypropyl-β (HPβ)-CD, both compounds revealed >1.2 fold decrease in IC_{50} when complexed with CDs [95]. And, in a follow-up work [96], the same authors showed that binding the same sensitizer to HPβCD improves its cellular uptake and induces DNA damage on melanoma cells, at a relatively low radiation dose. Multifunctional particles for melanoma-target drug delivery become evident for a role in this part, meaning above that all different approaches and, with them, different materials, such as complex organization of organic, inorganic molecules, biological agents and polymers, are stably conjugated for specific goal. Poly(lactic-co-glycolic acid) (PLGA) coated magnetite nanoparticles, further incorporated into a thermosensitive polymer revealed a slowly release of curcumin (anti-tumor model drug) for more than 25 days, depending on temperature and polymer degradation. These particles also showed a targeted accumulation in the tumor cells, after application of a magnetic field on the tumor site. Polymeric coating seems to reduce the toxicity of these systems, while preserving their magnetic properties [2].

Modular nanotransporters (MNTs) are developed based on natural cell mechanisms (e.g., polypeptide that mimics cell transportation and attachment) and can be improved by surface modification with α-MSH for a targeted delivery of the photosensitizers to the melanoma cells. This method accomplished 93% inhibition of melanoma proliferation and increased mice lifespan, comparing with the ones treated with the free photosensitizer [97]. The same system tested with Epidermal Growth Factor (EGF) for other tumors demonstrated a broad variety and flexibility of these transport systems [98]. Targeting moieties also improve the treatment results due to reduction of effectiveness caused by melanin light absorption and increased in two-fold the median survival of the mice, significantly inhibiting tumor growth. Selecting the most appropriate targeting moieties is, therefore, important to conjugate with the microenvironment and molecular mechanisms associated with the tumor before and after thermal damage [94]. Smaller particles (20-200 nm) with longer half-lives (e.g., surface modification with PEG) seem to have the desirable characteristics for an efficient tumor targeting. As for possible targeting moieties, anti-CTLA4 antibodies and tumor necrosis factor alpha (TNF-α) appear to be good candidates, as well as compounds that reduce the hyperpermeability threshold of cell membranes (e.g., antioxidants or anti-inflammatory agents) and that facilitate the anti-tumor drug entrance into the cancer cells [94].

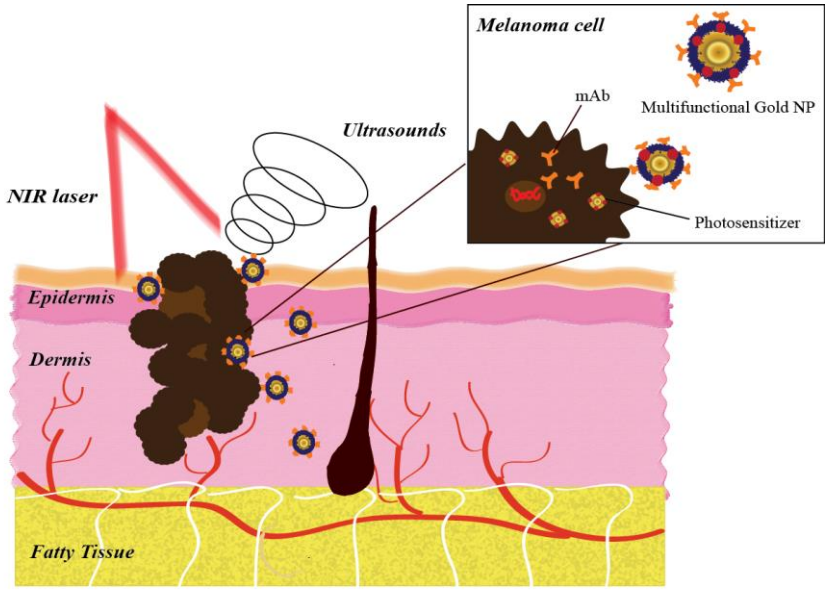

Figure 3. Different approaches applied to photodynamic therapy. Nanoparticles can enter the cells and reach the cytoplasm through targeting moieties at the surface and promote PDT by focusing thermal ablation and laser action to the tumor site.

Chemotherapy

In chemotherapy, nanotechnology has played a significant and distinctive role over the last 20 years. Along with many studies, there is a consensus that small nanocarriers between 10 and 100 nm can penetrate into the tumor vasculature, reaching the tumor cells by a target- effect. Also, nanocarriers are an interesting mean for new molecules and compounds with anti-tumor activity. Normally, these substances show a poor solubility and then bioavailability, as they have a lipophilic character and high molecular weight. Transport via nanocarriers facilitates the substances' penetration by endocytosis, aiming a more effective action. Another advantage is the possibility of bitherapy: one active agent encapsulated inside the core and another adsorbed at the surface of the carrier, for a synergistic treatment approach. Finally, nanoparticles can facilitate the administration of chemotherapy agents that is, through i.v. injections sometimes seen, as a disadvantage for the patient. Controlled drug release and the broad possibilities for incorporation into other pharmaceutical formulations, for administration through other routes, can ease this great difficulty for both clinicians and patients, aiming an independent and secure chemotherapy [99].

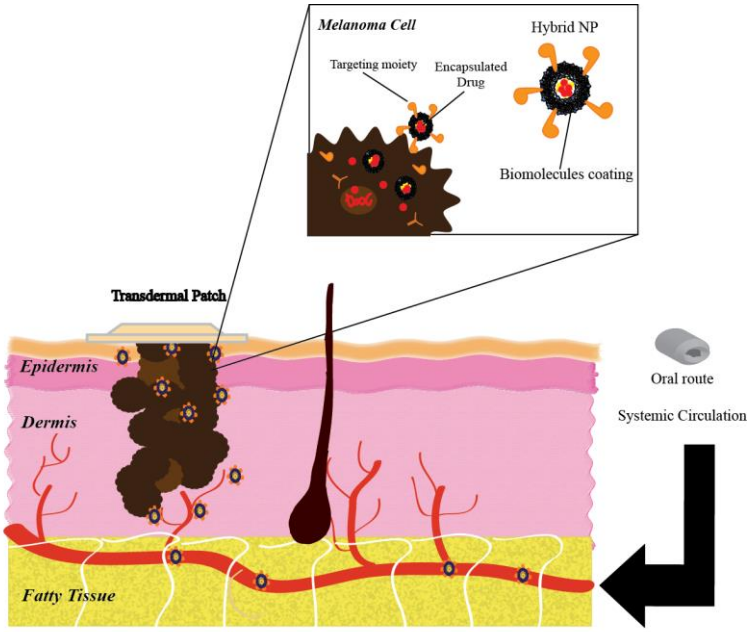

Figure 4. Nanomedicine applications in melanoma treatment for improvement of local efficiency and, ultimately, patient compliance.

An example of how nanotechnology can implement several approaches in one system is the use of polymeric PLA particles to carry the anti-tumor drug, dacarbazine, and immunotherapeutic agent for TRAIL-receptor, DR5, related with the tumor necrosis factor family, inducing apoptosis in melanoma cells overexpressing this receptor. The mAb was dispersed onto the nanoparticles surface, which was confirmed by fluorescence techniques. Binding and specificity of nanoparticles were very important for the tumor cytotoxicity increase, since it promoted the entrance of dacarbazine by receptor-mediated endocytosis. Particles showed a size smaller than 200 nm and a zeta potential of -30 mV [100].

In another study, PAMAM dendrimer of different sizes (G2, G3 and G4) were conjugated with oregon green and compared to linear and branched polymer polyethylenimine (PEI) for their uptake on B16F10 melanoma cells. The mechanism of absorption for the PAMAM G4 was found to be cholesterol-dependent since a reduction of 44% of uptake was observed when Methyl-β (Mβ)-CD was used while no efflux activity was observed. This may be particularly important when devising systems that can avoid efflux resistance mechanisms [90]. Together with size and architecture, the charge also determines preferential interactions within biological media, especially with cell

membranes. Although both positive and neutral dendrimers were distributed to all major organs with rapid clearance within 24 hours, deposition was slightly higher for the positively charged dendrimers at the tumor site [101]. Docosahexenoic acid-PAMAM dendrimers linked to doxorubicin by a hydrazone link were compared to free drug [102]. Since doxorubicin is linked to the dendrimer backbone, it cannot interact with its receptor due to steric hindrance. Therefore, as tumors are slightly more acidic than normal cells, release of doxorubicin was achieved by a pH-triggered mechanism by the hydrazone linker, resulting in 2-fold higher drug release in acidic conditions. Consequently, a higher area under the curve (AUC) was observed for the dendrimer (452 µg/mL *versus* 65 µg/mL) that resulted in a higher growth inhibition and apoptotic induction in comparison to the free drug [102].

Paclitaxel, although not approved yet for melanoma therapy, has been extensively studied for this purpose. Paclitaxel promotes the polymerization of tubulin proteins, essential for microtubules stabilization during cell mytosis, inhibiting tumor growth [103]. Abraxane® is a nanoparticulate system with 130 nm in which paclitaxel is bounded to albumin protein (nab - nanoparticle albumin bound) and was first introduced and approved for breast cancer in 2005. The use of albumin, a natural human protein, prevents some additional toxicity and has shown to have reduced adverse effects compared to the traditional formulation (Cremophor®), which is commonly associated with hypersensitivity reactions and neuropathy [104]. There are various mechanisms by which nanoparticles can accumulate in the tumor but they can be divided into two major groups: (I) passive (i.e., enhanced permeation and retention (EPR), which is a series of phenomena related with enhanced blood circulation and leaky tumors) and (II) active targeting (e.g., folate, RGD or antibodies). Nab-paclitaxel achieves high concentrations within the tumor site both by EPR effect and receptor mediated targeting. Secreted protein acidic and rich in cysteine (SPARC) is highly secreted in malignant melanocytes and has been shown to be important in Abraxane® mechanism. The value of nab-paclitaxel has recently been tested for its potential value in clinical trials for melanoma [105–107]. Nevertheless, there is always space for improvement in nanomedicine, where new opportunities constantly rise to explore other strategies. Nanoemulsions for dermal delivery of paclitaxel can work as localized therapy in deep skin layers for melanoma treatment in rats [108]. Another study compared liposomal paclitaxel carriers, showing that it increased the drug encapsulation up to 90%, overcoming a common problem in conventional lipid formulations, suppressed the tumor growth and the appearance of

metastasis in a dose-dependent rate, reducing the toxicity to normal tissues in mice [109].

Liposomes are extensively used for melanoma treatment, since they are low-toxicity systems and suitable for dermal application, decreasing adverse effects and increasing the local accumulation and action of the anti-tumor drug; also they allow prolonged systemic circulation when modified by PEGylation, for an effective treatment of metastastic melanoma [110]. Liposomes have been studied for encapsulation of common anti-tumor drugs in mono- or bi-therapy for synergistic effects, nucleic acids (gene therapy), improvement by addition of targeting moieties (e.g., folic acid, transferrin and monoclonal antibodies) [110]. Although liposomes are good platforms for topical drug delivery, most of the studies performed with them use invasive administration, such as i.v. injections, except when associated with other techniques like PDT [93].

Cyclodextrins are cyclic oligomers of α-D-glucopyranose (or α-D-glucose) units linked by 1,4-glicosidic bonds, produced by bacteria that degrade starch by an enzymatic process [111,112]. CD's structure allows them to have a hydrophobic cavity and a hydrophilic outer surface, and the cavity's dimension enables them to bind to several different compounds, generically called guest molecules, forming inclusion complexes [112,113]. Few studies were conducted with CDs for melanoma treatment. However, they revealed some interesting results that show CDs as promising carriers for this application. For example, betulinic acid, a pentacyclic lupane-type triterpene, widely found in a variety of plants and synthesized from betulin. As this compound is poorly soluble in aqueous medium, octakis-[6-deoxy-6-(2-sulfanyl ethanesulfonate)]-γCD was chosen as carrier and revealed that the complexation of this compound is potentially interesting for the treatment of melanoma, since it displays similar activity to free betulin (in cell lines) while allowing solubilization, and thus, making it possible for the compound to be administered in an aqueous (non-toxic) vehicle [114]. Another study reported a significant antitumor potential of mistletoe-derived triterpenes (which major component is oleanolic acid) with highest necrosis rates when animals received aqueous extract with CD-complexed triterpenes [115]. In fact, natural compounds and derivatives have been selected to be conjugated with CDs, as either carriers or active participants on the therapeutic effect for melanoma, promoting the cytotoxicity's selectivity [116–120]. CDs can be administered by oral route [121], or topical administration, with successful results. A CD-surfactant carrier for topical application and delivery of two curcumin analogs showed remarkable cellular selectivity, within primary keratinocyte cells and human fibroblasts and high

apoptotic activity (five to nine-fold higher than untreated cells) [122]. Also, oleanolic acid and ursolic acid complexed with both HPβCD and HPγCD were applied topically in induced skin melanoma murine model [123]. By using the lipid layer-disrupting property of cyclodextrins, it appears that CDs can decrease the cell membrane constituent, syndecan-2, translocation to the lipid rafts, causing their disruption, which leads to melanoma cell migration inhibition [124].

Another recent and promising approach is the use of hyaluronidase coated plain silica nanoparticles. Recent experiments have found that subcutaneous (s.c.) injected nanoparticles in concomitance with a therapeutic agent (i.e., carboplatin) would stay longer and more attached to the skin tumor after administration. This facilitated attachment is due to the high molecular weight of the enzyme and the multiple interactions between nanoparticles and the hyaluronan present in cancer cells. The enzyme maintained its biological activity after immobilization into the particles. These systems were tested in human, non-metastatic melanoma cancer cell lines A375 (overexpressing CD44 receptors for hyaluronic acid) and showed a higher decrease of the tumor size [125]. The use of bioactive compounds associated with nanocarriers is also increasing, such as tripterine (*Tripterygium wilfordii*) encapsulation in NLCs for topical treatment of skin cancer. Anionic NLCs allow a more controlled release over time, show better encapsulation efficiency, cumulative skin permeation, less cell inhibition and high cell uptake [12,17]. A recently synthesized derivative of the natural compound Royleanone (7α-acetoxyroyleanone) demonstrated cytotoxicity against melanoma cells; and also SK-MEL-1 human melanoma cells showed a special sensitivity to other derivatives of this compound, which is very promising for counteracting melanoma's MDR [126]. Curcumin was proven to be used for melanoma since it can have an immunotherapy action in melanoma treatment. It shows an immune responsive action by promoting the release of tumor pro-apoptotic cytokines that destroys human melanoma cell lines after 48 hours treatment [127]. However, curcumin also appears to inhibit the immune-mediated recognition of tumors by affecting the responsiveness to other anti-tumor factors (STAT1 and STAT5), so its use should be further studied [127]. It seems that curcumin acts by inhibiting cyclic nucleotide phosphodiesterases 1 (PDE1) in order to decrease melanoma cell proliferation and also may act by a preventive mechanism, via gene encoding the cell life cycle. Another study developed chitin nanogels for selective toxicity towards melanoma cells, with a safer behavior compared to the anti-tumor free drug (i.e., curcumin). This nanogel was applied via transdermal route mainly through both intercellular and transcellular pathways [13]. Curcumin has

also been encapsulated into nanoniosomes for dermal application as skin cancer prevention strategy [128]. Zhao *et al.* (2010) reported a high efficacy against melanoma *in vivo* through transdermal route by incorporation of realgar into nanosystems, with lower systemic toxicity levels [17]. Finally, corticosteroids, such as prednisolone phosphate, used in cancer treatment can be incorporated into liposomes for oral administration against melanoma. These liposomes, called long-circulating liposomes (LCLs), target tumor-associated macrophages (TAMs), which seem to control the tumor growth and angiogenesis, in immunogenic cancers [29].

6. Other therapies: Gene and viral therapies

Gene therapy involves a more complex approach in cancer treatment. It may be more promising for diagnosis than for treatment due to the genetic flexibility of tumor cells and the different molecular identities, including during metastasis. In this last case, we should develop a unique system that could reorient its structure, like a virus, according to the tumor adjustments. Some virus (e.g., vesicular stomatitis virus) demonstrated to selectively enter malignant melanoma cells working as a targeting machinery and vector for oncologic therapeutics, due to a defective barrier of the cancer cells for the virus. Besides the issues associated with unexpected viral reactions or consequences, the great variability of melanoma cancer cells can make them resistant to virus infection [129]. Yao *et al.* (2011) produced a carrier composed of PEI linked to βCD and conjugated with folate [130]. This carrier was studied mainly because of its ability to deliver interleukin IL-2 plasmid, after s.c. administration. The resulting polycomplex system had around 100 nm and was able to suppress tumor growth and extend animal survival. In addition, this polycomplex was able to stimulate a positive immune response, namely through CD4+ and 8+ LyT, and natural killer cells increase activation, proliferation and infiltration into the tumor, showing a constantly high level of IL-2 [130].

In alternative, the potential of small interfering RNA (siRNA) has also been studied. This approach reduced associated-therapy adverse effects, compared to classic agents and it is tumor specific. However, due to the lack of stability of the nucleic acids in the blood stream, nanoparticles work as a carrier to protect the molecule until it reaches the tumor site. Nanoparticulate systems may also interact synergistically with the agent to activate tumor cell death, avoiding all the biosafety issues related to the use of viral vectors [131]. When applied to the “suicide gene” approach, nanocarriers involve a therapy where a

gene is delivered to the tumor cells and transformed into an enzyme/protein by the cells' machinery, which will convert a prodrug (e.g., ganciclovir) into a cytotoxic metabolite, reducing the cancer growth [132,133]. In fact, DNA molecules can be completely compacted into nanoparticles, to perform virus-like properties such as cell-targeted internalization and interaction with proteins. These multifunctional carriers – with less than 100 nm – can incorporate α-MSH at the surface in order to facilitate a receptor-mediated endocytosis and increased DNA transfection more than three-fold over plain nanocarriers [134]. To finish, delivery of genetic materials through the skin has also been evaluated. Immunotherapy by transdermal administration of synthetic oligodeoxynucleotides with iontophoresis, preventing tumor growth and reaching deeper skin layers, like epidermis and dermis. However, in this case the nucleotides did not penetrate the tumor tissue, which results may be explained by non-specific antitumor immune response [135]. Topical delivery of siRNA using nanoliposomes targeted for BRAF (V600E) mutation and the signaling-related Akt3 protein (overexpressed in melanoma), combining low-frequency ultrasound – to increase cell permeability – has the potential to selectively decrease the expression of the mutant protein by 25-60%, inhibiting tumor growth [110]. Actually, it was possible to deliver siRNA specifically to melanoma cells, reducing the area injured; the authors also proposed this system as a potential way to decrease the melanoma development and invasion, like a nonsurgical approach, when applied to early melanocytic lesions.

7. Future perspectives

Development of effective medicines for introduction as final products in the market is a complex, expensive and slow process, hindered not straightforward application of the knowledge created mostly by the academia research to an industry scale [136]. The use of increasingly high number of materials, mostly natural biomolecules, improve the safety profile of medicines, but there is still an unknown response when conjugated with nanocarriers. In addition, there is a great controversy about how nanoparticles interact and move through the biological barriers, especially in the skin. Is this relationship dependent on size and system composition? The nanoparticles may interact with some mitochondrial and cell membranes and promote apoptosis events, and may play a role in internalization processes and affect the cells toxicity [137-138]. Are there also physicochemical factors determinants do nanoparticles entail? What kind of genotoxicity and molecular determinants? How does the exposure and biodistribution occur? And

finally, how can we regulate all these issues to guarantee its safety? In fact, *in vitro* results based on classical methods are difficult to evaluate [139–141]. Alternatives such as cell damage and microscopy tools are being explored. Answers and solutions should come into sight, as well as a way to deal with the high value in cost of this emerging adaptation, for both entrepreneurs and patients [142].

8. Conclusion

Melanoma is a complex cancer, with multiple stages and high genetic flexibility that compromise its diagnostic and treatment. More guidelines and cohort studies are needed to follow different populations and access relevant biomarkers, develop serious recommendations based on proven evidence and avoid lack of evidence, which promotes the variability. By reviewing several available guidelines [22, 143], it seems there are some particular differences especially in diagnose and disease follow-up and treatment. For example, Australian guidelines are stricter in terms of diagnostic and follow-up but for treatment there are more non-specific recommendations. This could help both assessment and innovation in melanoma diagnostics and therapies.

References

1. Caraco C, Mozzillo N, Marone U, *et al.* Long-lasting response to electrochemotherapy in melanoma patients with cutaneous metastasis. *BMC Cancer*. 13(1), 564 (2013).
2. Wadajkar AS, Bhavsar Z, Ko C-Y, *et al.* Multifunctional particles for melanoma-targeted drug delivery. *Acta Biomater.* 8(8), 2996–3004 (2012).
3. Pacheco I, Buzea C, Tron V. Towards new therapeutic approaches for malignant melanoma. *Expert Rev. Mol. Med.* 13(1), 13e33 (2012).
4. Erdmann F, Lortet-Tieulent J, Schüz J, *et al.* International trends in the incidence of malignant melanoma 1953–2008—are recent generations at higher or lower risk? *Int. J. Cancer*. 132(2), 385-400 (2012).
5. Carlson JA, Linette GP, Aplin A, Ng B, Slominski A. Melanocyte receptors: clinical implications and therapeutic relevance. *Dermatol. Clin.* 25(4), 541–557 (2007).
6. Weber J. Review: Anti-CTLA-4 antibody ipilimumab: Case studies of clinical

response and immune-related adverse events. *Oncologist*. 12(7), 864–872 (2007).

7. Chartrain M, Riond J, Stennevin A, *et al.* Melanoma chemotherapy leads to the selection of ABCB5-expressing cells. *PLoS One*. 7(5), e36762 (2012).
8. Lanssens S, Ongenae K. Dermatologic lesions and risk for cancer. *Acta Clin. Belg.* 66(3), 177–185 (2011).
9. Duffy K, Grossman D. The dysplastic nevus: From historical perspective to management in the modern era: Part II. Molecular aspects and clinical management. *J. Am. Acad. Dermatol.* 67(1), 19.e1–19.e12 (2012).
10. Zhao X, Zu Y, Zu S, Wang D, Zhang Y, Zu B. Insulin nanoparticles for transdermal delivery: preparation and physicochemical characterization and *in vitro* evaluation. *Drug Dev. Ind. Pharm.* 36(10), 1177–1185 (2010).
11. Shibagaki N, Okamoto T, Mitsui H, Inozume T, Kanzaki M, Shimada S. Novel immunotherapeutic approaches to skin cancer treatments using protein transduction technology. *J. Dermatol. Sci.* 61(3), 153–161 (2011).
12. Chen Y, Zhou L, Yuan L, Zhang ZH, Liu X, Wu Q. Formulation, characterization, and evaluation of *in vitro* skin permeation and *in vivo* pharmacodynamics of surface-charged tripterine-loaded nanostructured lipid carriers. *Int. J. Nanomedicine*. 7(0), 3023–3032 (2012).
13. Mangalathillam S, Rejinold NS, Nair A, Lakshmanan V-K, Nair S V, Jayakumar R. Curcumin loaded chitin nanogels for skin cancer treatment via the transdermal route. *Nanoscale*. 4(1), 239–250 (2012).
14. Paolino D, Celia C, Trapasso E, Cilurzo F, Fresta M. Paclitaxel-loaded ethosomes®: Potential treatment of squamous cell carcinoma, a malignant transformation of actinic keratoses. *Eur. J. Pharm. Biopharm.* 81(1), 102–112 (2012).
15. Li L, Xu X, Fang L, *et al.* The transdermal patches for site-specific delivery of letrozole: A new option for breast cancer therapy. *AAPS PharmSciTech*. 11(3), 1054–1057 (2010).
16. Savage LM, Boehmer L, McBride A. Melanoma: Review of pathogenesis and treatment options. *US Pharm*. 35(9), (Oncology suppl), 8–16 (2010).
17. Zhao Q-H, Zhang Y, Liu Y, *et al.* Anticancer effect of realgar nanoparticles on mouse melanoma skin cancer *in vivo* via transdermal drug delivery. *Med. Oncol.* 27(2), 203–212 (2010).
18. Rangwala S, Tsai KY. Roles of the immune system in skin cancer. *Br. J. Dermatol.* 165(5), 953–965 (2011).

19. Foldvari M, Badea I, Kumar P, *et al.* Biphasic vesicles for topical delivery of interferon alpha in human volunteers and treatment of patients with human papillomavirus infections. *Curr. Drug Deliv.* 8(3), 307–319 (2011).
20. Foldvari M. Biphasic vesicles: A novel topical drug delivery system. *J. Biomed. Nanotechnol*. 6(5), 543–557 (2010).
21. Ascierto PA, Marincola FM, Ribas A. Anti-CTLA4 monoclonal antibodies: The past and the future in clinical application. *J. Transl. Med.* 9, 196 (2011).
22. Fong ZV, Tanabe KK. Comparison of melanoma guidelines in the United States, Canada, Europe, Australia and New Zealand. A critical appraisal and comprehensive review. *Br. J. Dermatol.* 170(1), 20-30 (2013).
23. Neila J, Soyer HP. Key points in dermoscopy for diagnosis of melanomas, including difficult to diagnose melanomas, on the trunk and extremities. *J. Dermatol.* 38(1), 3–9 (2011).
24. Dummer R, Hauschild A, Guggenheim M, Keilholz U, Pentheroudakis G, Group on behalf of the EGW. Cutaneous melanoma: ESMO clinical practice guidelines for diagnosis, treatment and follow-up. *Ann. Oncol.* 23 (suppl 7), vii86–vii91 (2012).
25. Shackleton M, Quintana E. Progress in understanding melanoma propagation. *Mol. Oncol.* 4(5), 451–457 (2010).
26. Nair HB, Sung B, Yadav VR, Kannappan R, Chaturvedi MM, Aggarwal BB. Delivery of anti-inflammatory nutraceuticals by nanoparticles for the prevention and treatment of cancer. *Biochem. Pharmacol.* 80(12), 1833–1843 (2010).
27. Ristic-Fira A, Vujcic M, Krstic-Demonacos M, D. K. Identification and characterization of glucocorticoid receptors in B16 mouse melanoma cells. *Endocr Regul*. 33(3), 109–115 (1999).
28. Dobos J, Kenessey I, Tímár J, Ladányi A. Glucocorticoid receptor expression and antiproliferative effect of dexamethasone on human melanoma cells. *Pathol. Oncol. Res.* 17(3), 729–734 (2011).
29. Banciu M, Metselaar JM, Schiffelers RM, Storm G. Antitumor activity of liposomal prednisolone phosphate depends on the presence of functional tumor-associated macrophages in tumor tissue. *Neoplasia*. 10(2), 108–117 (2008).
30. Loch-Neckel G, Nemen D, Puhl AC, *et al.* Stealth and non-stealth nanocapsules containing camptothecin: *in-vitro* and *in-vivo* activity on B16-F10 melanoma. *J. Pharm. Pharmacol.* 59(10), 1359–1364 (2007).
31. Nikolaou VA, Stratigos AJ, Flaherty KT, Tsao H. Melanoma: New insights and new therapies. *J. Invest. Dermatol*. 132(3), 854–863 (2012).

32. Vidwans SJ, Flaherty KT, Fisher DE, Tenenbaum JM, Travers MD, Shrager J. A Melanoma Molecular Disease Model. *PLoS One*. 6(3), e18257 (2011).
33. Evans MS, Madhunapantula S V, Robertson GP, Drabick JJ. Current and future trials of targeted therapies in cutaneous melanoma. In: *Impact of Genetic Targets on Cancer Therapy*. El-Deiry WS (Ed.). Springer New York, 223–255 (2013).
34. Flach EH, Rebecca VW, Herlyn M, Smalley KSM, Anderson ARA. Fibroblasts contribute to melanoma tumor growth and drug resistance. *Mol. Pharm.* 8(6), 2039–2049 (2011).
35. Stanisz H, Seifert M, Tilgen W, Vogt T, Rass K. Reciprocal responses of fibroblasts and melanocytes to α-MSH depending on MC1R polymorphisms. *Dermatoendocrinol.* 3(4), 259–265 (2011).
36. Salazar-Onfray F, Lopez M, Lundqvist A, *et al.* Tissue distribution and differential expression of melanocortin 1 receptor, a malignant melanoma marker. *Br. J. Cancer*. 87(4), 414–422 (2002).
37. Solca F, Siegrist W, Drozdz R, Girard J, Eberle AN. The receptor for alpha-melanotropin of mouse and human melanoma cells. Application of a potent alpha-melanotropin photoaffinity label. *J. Biol. Chem.* 264(24), 14277–14281 (1989).
38. Miao Y, Whitener D, Feng W, Owen NK, Chen J, Quinn TP. Evaluation of the human melanoma targeting properties of radiolabeled-melanocyte stimulating hormone peptide analogues. *Bioconjug. Chem.* 14(6), 1177–1184 (2003).
39. Kadekaro AL, Chen J, Yang J, *et al.* Alpha-melanocyte–stimulating hormone suppresses oxidative stress through a p53-mediated signaling pathway in human melanocytes. *Mol. Cancer Res.* 10(6), 778–786 (2012).
40. Swope VB, Jameson JA, McFarland KL, *et al.* Defining MC1R regulation in human melanocytes by its agonist [alpha]-melanocortin and antagonists agouti signaling protein and [beta]-defensin 3. *J. Invest. Dermatol*. 132(9), 2255–2262 (2012).
41. Lu W, Xiong C, Zhang G, *et al.* Targeted photothermal ablation of murine melanomas with melanocyte-stimulating hormone analog-conjugated hollow gold nanospheres. *Clin. Cancer Res.* 15(3), 876–886 (2010).
42. Lu W, Xiong C, Zhang R, *et al.* Receptor-mediated transcytosis: A mechanism for active extravascular transport of nanoparticles in solid tumors. *J. Control. Rel*. 161(3), 959-966 (2012).
43. Vannucci L, Falvo E, Fornara M, *et al.* Selective targeting of melanoma by PEG-masked protein-based multifunctional nanoparticles. *Int. J. Nanomedicine*. 7(0), 1489–1509 (2012).
44. Desai BM, Villanueva J, Nguyen TT, *et al.* The anti-melanoma activity of dinaciclib,

a cyclin-dependent kinase inhibitor, is dependent on p53 signaling. *PLoS One*. 8, e59588 (2013).

45. Sotgia F, Martinez-Outschoorn UE, Lisanti MP. Cancer metabolism: New validated targets for drug discovery. *Oncotarget*. 4(8), 1309–1316 (2013).
46. Hafner A, Lovric J, Pepic I, Filipovic-Grcic J. Lecithin/chitosan nanoparticles for transdermal delivery of melatonin. *J. Microencapsul.* 28(8), 807–815 (2011).
47. Hafner A, Dürrigl M, Pepic I, Filipovic-Grcic J. Short- and long-term stability of lyophilised melatonin-loaded lecithin/chitosan nanoparticles. *Chem. Pharm. Bull.* 59(9), 1117–1123 (2011).
48. Da Forno PD, Pringle JH, Hutchinson P, *et al.* WNT5A expression increases during melanoma progression and correlates with outcome. *Clin. Cancer Res.* 14(18), 5825–5832 (2008).
49. Zhang G, Li G. Novel multiple markers to distinguish melanoma from dysplastic nevi. *PLoS One*. 7(9), e45037 (2012).
50. Griewank KG, Yu X, Khalili J, *et al.* Genetic and molecular characterization of uveal melanoma cell lines. *Pigment Cell Melanoma Res.* 25(2), 182–187 (2012).
51. Fustier C, Chang TMS. PEG-PLA nanocapsules containing a nanobiotechnological complex of polyhemoglobin-tyrosinase for the depletion of tyrosine in melanoma: Preparation and *in vitro* characterisation. *J. Nanomedicine Biother. Discov.* 2(1), 1–9 (2012).
52. Wang Y, Chang TMS. Nanobiotechnological nanocapsules containing polyhemoglobin-tyrosinase: Effects on murine B16F10 melanoma cell proliferation and attachment. *J. Skin Cancer*. 2012(0), Article ID 673291, 9 (2012).
53. Mansoori GA, Mohazzabi P, McCormack P, Jabbari S. Nanotechnology in cancer prevention, detection and treatment: Bright future lies ahead. *World Rev. Sci. Technol. Sustain. Dev.* 4(2/3), 226–257 (2007).
54. Reis CP, Ribeiro AJ, Veiga F, Neufeld RJ, Damgé C. Polyelectrolyte biomaterial interactions provide nanoparticulate carrier for oral insulin delivery. *Drug Deliv.* 15(2), 127–139 (2008).
55. Garcia-Fuentes M, Alonso MJ. Chitosan-based drug nanocarriers: Where do we stand? *J. Control. Rel*. 161(2), 496–504 (2012).
56. Reis CP, Damgé C. Chapter fourteen - Nanotechnology as a promising strategy for alternative routes of insulin delivery. In: *Methods in Enzymology*. Academic Press, 271–294 (2012).
57. Zhang L, Zhu W, Yang C, *et al.* A novel folate-modified self-microemulsifying drug delivery system of curcumin for colon targeting. *Int. J. Nanomedicine*. 7(0), 151–

162 (2012).

58. Kocbek P, Obermajer N, Cegnar M, Kos J, Kristl J. Targeting cancer cells using PLGA nanoparticles surface modified with monoclonal antibody. *J. Control. Rel*. 120(1–2), 18–26 (2007).
59. Gonçalves AS, Macedo AS, Souto EB. Therapeutic nanosystems for oncology nanomedicine. *Clin. Transl. Oncol.* 14(12), 883–890 (2012).
60. Sheridan C. Proof of concept for next-generation nanoparticle drugs in humans. *Nat. Biotech*. 30(6), 471–476 (2012).
61. Merisko-Liversidge EM, Liversidge GG. Drug nanoparticles: Formulating poorly water-soluble compounds. *Toxicol. Pathol.* 36(1), 43–48 (2008).
62. Cootney RW. Ultrasound imaging: Principles and applications in rodent research. *ILAR J.* 42(3), 233–247 (2001).
63. Madhunapantula S V, Robertson GP. Chapter twelve - Chemoprevention of melanoma. In: *Adv. Pharmacol*. Keiran SMS (Ed.). Academic Press, 361–398 (2012).
64. Cassidy P, Fain H, Cassidy J, *et al.* Selenium for the prevention of cutaneous melanoma. *Nutrients*. 5(3), 725–749 (2013).
65. Chung C-Y, Madhunapantula S V, Desai D, Amin S, Robertson GP. Melanoma prevention using topical PSIse. *Cancer Prev. Res.* 4(6), 935–948 (2011).
66. Liu W, Li X, Wong Y-S, *et al.* Selenium nanoparticles as a carrier of 5-fluorouracil to achieve anticancer synergism. *ACS Nano*. 6(8), 6578–6591 (2012).
67. Jin Y-J, Termsarasab U, Ko S-H, *et al.* Hyaluronic acid derivative-based self assembled nanoparticles for the treatment of melanoma. *Pharm. Res.* 29(12), 3443–3454 (2012).
68. Hong H, Sun J, Cai W. Anatomical and molecular imaging of skin cancer. *Clin. Cosmet. Investig. Dermatol.* 1(0), 1–17 (2008).
69. Pfeifer GP, Besaratinia A. UV wavelength-dependent DNA damage and human non-melanoma and melanoma skin cancer. *Photochem. Photobiol. Sci.* 11(1), 90–97 (2012).
70. Schmieder A, Winter PM, Caruthers SD, *et al.* Molecular MR imaging of melanoma angiogenesis with αvβ3-targeted paramagnetic nanoparticles. *Magn. Reson. Med.* 53(3), 621–627 (2005).
71. Bei D, Meng J, Youan B-BC. Engineering nanomedicines for improved melanoma therapy: progress and promises. *Nanomedicine*. 5(9), 1385–1399 (2010).
72. Rossetti FC, Depieri LV, Bentle MVLB. Confocal laser scanning microscopy as a tool for the investigation of skin drug delivery systems and diagnosis of skin

disorders. Dr. Neil Lagali (Ed.), In: *Confocal Laser Microscopy - Principles and Applications in Medicine, Biology, and the Food Sciences*. InTech (2013).

73. Khlebtsov N, Bogatyrev V, Dykman L, *et al.* Analytical and theranostic applications of gold nanoparticles and multifunctional nanocomposites. *Theranostics*. 3(3), 167–180 (2013).
74. Zhao B, He Y-Y. Recent advances in the prevention and treatment of skin cancer using photodynamic therapy. *Expert Rev. Anticancer Ther.* 10(11), 1797–1809 (2010).
75. Lee S, Xie J, Chen X. Peptides and peptide hormones for molecular imaging and disease diagnosis. *Chem. Rev.* 110(5), 3087–3111 (2010).
76. Raposinho PD, Correia JDG, Oliveira MC, Santos I. Melanocortin-1 receptor-targeting with radiolabeled cyclic α-melanocyte-stimulating hormone analogs for melanoma imaging. *Pept. Sci.* 94(6), 820–829 (2010).
77. Li Z, Huang P, Lin J, *et al.* Arginine-glycine-aspartic acid-conjugated dendrimer-modified quantum dots for targeting and imaging melanoma. *J. Nanosci. Nanotechnol.* 10(8), 1–9 (2010).
78. Chen J, Shao R, Zhang XD, Chen C. Applications of nanotechnology for melanoma treatment, diagnosis, and theranostics. *Int. J. Nanomedicine*. 8(1), 2677–2688 (2013).
79. Cao X, Fu M, Wang L, *et al.* Oral bioavailability of silymarin formulated as a novel 3-day delivery system based on porous silica nanoparticles. *Acta Biomater.* 8(6), 2104–2112 (2012).
80. Brabez N, Lynch RM, Xu L, *et al.* Design, synthesis, and biological studies of efficient multivalent melanotropin ligands: Tools toward melanoma diagnosis and treatment. *J. Med. Chem.* 54(20), 7375–7384 (2011).
81. Morosi L, Spinelli P, Zucchetti M, *et al.* Determination of paclitaxel distribution in solid tumors by nano-particle assisted laser desorption ionization mass spectrometry imaging. *PLoS One*. 8(8), e72532 (2013).
82. Yurgel V, Collares T, Seixas F. Developments in the use of nanocapsules in oncology. *Brazilian J. Med. Biol. Res.* 46(6), 486–501 (2013).
83. Vannucci L, Fiserová A, Sadalapure K, *et al.* Effects of N-acetyl-glucosamine-coated glycodendrimers as biological modulators in the B16F10 melanoma model *in vivo*. *Oncology*. 23(2), 285–296 (2003).
84. Revicki D, van den Eertwegh A, Lorigan P, *et al.* Health related quality of life outcomes for unresectable stage III or IV melanoma patients receiving ipilimumab treatment. *Health Qual. Life Outcomes*. 10(1), 66 (2012).

85. Ma M, Hao Y, Liu N, *et al.* A novel lipid-based nanomicelle of docetaxel: evaluation of antitumor activity and biodistribution. *Int. J. Nanomedicine*. 7(0), 3389–3398 (2012).
86. Mosallaei N, Jaafari MR, Hanafi-Bojd MY, Golmohammadzadeh S, Malaekeh-Nikouei B. Docetaxel-loaded solid lipid nanoparticles: Preparation, characterization, *in vitro*, and *in vivo* evaluations. *J. Pharm. Sci.* 102(6), 1994–2004 (2013).
87. Cheng Y, Zhao L, Li Y, Xu T. Design of biocompatible dendrimers for cancer diagnosis and therapy: Current status and future perspectives. *Chem. Soc. Rev.* 40(5), 2673–2703 (2011).
88. Mintzer M, Grinstaff M. Biomedical applications of dendrimers: a tutorial. *Chem. Soc. Rev.* 40(1), 173–190 (2011).
89. Gillies ER, Dy E, Fréchet JMJ, Szoka FC. Biological evaluation of polyester dendrimer: Poly(ethylene oxide) “Bow-Tie” hybrids with tunable molecular weight and architecture. *Mol. Pharm.* 2(2), 129–138 (2005).
90. Seib FP, Jones AT, Duncan R. Comparison of the endocytic properties of linear and branched PEIs, and cationic PAMAM dendrimers in B16F10 melanoma cells. *J. Control. Rel*. 117(3), 291–300 (2007).
91. Al-Jamal KT, Al-Jamal WT, Akerman S, *et al.* Systemic antiangiogenic activity of cationic poly-L-lysine dendrimer delays tumor growth. *PNAS*. 107(9), 3966–3971 (2010).
92. Braun RD, Vistisen KS. Measurement of human choroidal melanoma xenograft volume in rats using high-frequency ultrasound. *Investig. Ophthalmol. Vis. Sci.* 49(1), 16-22 (2008).
93. Taveira SF, Lopez RFV. Topical administration of anticancer drugs for skin cancer treatment. Prof. Caterina La Porta (Ed.). In: *Skin Cancers - Risk Factors, Prevention and Therapy*. InTech (2011).
94. Shenoi MM, Shah NB, Griffin RJ, Vercellotti GM, Bischof JC. Nanoparticle preconditioning for enhanced thermal therapies in cancer. *Nanomedicine*. 6(3), 545–563 (2011).
95. Kolárová H, Mosinger J, Lenobel R, Kejlova K, Jirova D, Strnad M. *In vitro* toxicity testing of supramolecular sensitizers for photodynamic therapy. *Toxicol. Vitro* 17(5-6), 775–778 (2003).
96. Kolárová H, Macecek J, Nevrelova P, *et al.* Photodynamic therapy with zinc-tetra(p-sulfophenyl)porphyrin bound to cyclodextrin induces single strand breaks of cellular DNA in G361 melanoma cells. *Toxicol. Vitro* 19(7), 971–974 (2005).

97. Slastnikova TA, Rosenkranz AA, Lupanova TN, Gulak P V, Gnuchev N V, Sobolev AS. Study of efficiency of the modular nanotransporter for targeted delivery of photosensitizers to melanoma cell nuclei *in vivo*. *Dokl. Biochem. Biophys.* 446(1), 235–237 (2012).
98. Slastnikova TA, Rosenkranz AA, Gulak PV, *et al.* Modular nanotransporters: a multipurpose in vivo working platform for targeted drug delivery. *Int. J. Nanomedicine*. 7(0), 467–482 (2012).
99. Egusquiaguirre S, Igartua M, Hernández R, Pedraz J. Nanoparticle delivery systems for cancer therapy: advances in clinical and preclinical research. *Clin. Transl. Oncol.* 14(2), 83–93 (2012).
100. Ding B, Wu X, Fan W, *et al.* Anti-DR5 monoclonal antibody-mediated DTIC-loaded nanoparticles combining chemotherapy and immunotherapy for malignant melanoma: target formulation development and *in vitro* anticancer activity. *Int. J. Nanomedicine*. 6(0), 1991–2005 (2011).
101. Nigavekar SS, Sung LY, Llanes M, *et al.* 3H Dendrimer nanoparticle organ/tumor distribution. *Pharm. Res.* 21(3), 476-483 (2004).
102. Peng F, Gao P, Hu X. Acid sensitive doxorubicin-PAMAM with tumor targeting profile. *J. Chinese Pharm. Sci.* 22(1), 81–88 (2013).
103. Schiff PB, Horwitz SB. Taxol stabilizes microtubules in mouse fibroblast cells. *Proc. Am. Soc. Clin. Oncol*. 77(3), 1561–1565 (1980).
104. Feng Z, Zhao G, Yu L, Gough D, Howell SB. Preclinical efficacy studies of a novel nanoparticle-based formulation of paclitaxel that out-performs Abraxane®. *Cancer Chemother Pharmacol*. 65(5), 923–930 (2010).
105. Hawkins MJ, Soon-Shiong P, Desai N. Protein nanoparticles as drug carriers in clinical medicine. *Adv. Drug Deliv. Rev.* 60(8), 876–885 (2008).
106. Hersh EM, Day SJO, Ribas A, *et al.* A phase 2 clinical trial of nab-paclitaxel in previously treated and chemotherapy-naïve patients with metastatic melanoma. *Cancer.* 116(1), 1704–1710 (2010).
107. Kottschade LA, Suman VJ, Amatruda T, *et al.* A phase II trial of nab-paclitaxel (ABI-007) and carboplatin in patients with unresectable stage IV melanoma: a North Central Cancer Treatment Group Study, N057E(1). *Cancer*. 117(8), 1704–1710 (2011).
108. Khandavilli S, Panchagnula R. Nanoemulsions as versatile formulations for paclitaxel delivery: peroral and dermal delivery studies in rats. *J. Invest. Dermatol.* 127(1), 154–162 (2006).
109. Koudelka Š, Turánek-Knötigová P, MaŠek J, *et al.* Liposomes with high

encapsulation capacity for paclitaxel: Preparation, characterisation and *in vivo* anticancer effect. *J. Pharm. Sci.* 99(5), 2309–2319 (2010).

110. Tran MA, Watts RJ, Robertson GP. Use of liposomes as drug delivery vehicles for treatment of melanoma. *Pigment Cell Melanoma Res.* 22(4), 388–399 (2009).
111. Li P, Zhao L, Yalkowsky SH. Combined effect of cosolvent and cyclodextrin on solubilization of nonpolar drugs. *J. Pharm. Sci.* 88(11), 1107–1111 (1999).
112. Liu L, Guo Q-X. The driving forces in the inclusion complexation of cyclodextrins. *J. Incl. Phenom. Macrocycl. Chem.* 42(1), 1–14 (2002).
113. Fu Y, Liu L, Guo Q-X. A theoretical study on the inclusion complexation of cyclodextrins with inorganic cations and anions. *J. Incl. Phenom. Macrocycl. Chem.* 43(3), 223–229 (2002).
114. Şoica C, Dehelean C, Danciu C, *et al.* Betulin complex in gamma-cyclodextrin derivatives: properties and antineoplasic activities in *in vitro* and *in vivo* tumor models. *Int. J. Mo.l Sci*. 13(11), 14992–15011 (2012).
115. Struh CM, Jager S, Kersten A, Schempp CM, Scheffler A, Martin SF. Triterpenoids amplify anti-tumoral effects of mistletoe extracts on murine B16F10 melanoma *in vivo*. *PLoS One*. 8, e62168 (2013).
116. Stecca B, Mas C, Clement V, *et al.* Melanomas require HEDGEHOG-GLI signaling regulated by interactions between GLI1 and the RAS-MEK/AKT pathways. *Proc. Natl. Acad. Sci.* 104(14), 5895–5900 (2007).
117. Pereira C, Diogo CT V, Burgeiro A, *et al.* Complex formation between heptakis(2,6-di-o-methyl)-î^2-cyclodextrin and cyclopentadienyl molybdenum(ii) dicarbonyl complexes: Structural studies and cytotoxicity evaluations. *Organometallics*. 27(19), 4948–4956 (2008).
118. Soman NR, Baldwin SL, Hu G, *et al.* Molecularly targeted nanocarriers deliver the cytolytic peptide melittin specifically to tumor cells in mice, reducing tumor growth. *J. Clin. Invest.* 119(9), 2830–2842 (2009).
119. Mazzaglia A, Bondi ML, Scala A, *et al.* Supramolecular assemblies based on complexes of nonionic amphiphilic cyclodextrins and a meso-tetra(4-sulfonatophenyl)porphine tributyltin(IV) derivative: potential nanotherapeutics against melanoma. *Biomacromolecules*. 14(11), 3820–3829 (2013).
120. Pizzimenti S, Ciamporcero E, Pettazzoni P, *et al.* The inclusion complex of 4-hydroxynonenal with a polymeric derivative of beta-cyclodextrin enhances the antitumoral efficacy of the aldehyde in several tumor cell lines and in a three-dimensional human melanoma model. *Free Radic. Biol. Med*. 65(0), 765–777 (2013).

121. Hatanaka H, Komada F, Shiono M, Mishima Y, Okumura K. Tissue distribution of para-boronophenylalanine administered orally as a cyclodextrin inclusion complex to melanoma-bearing hamsters. *Pigment Cell Res*. 5(1), 38–40 (1992).
122. Michel D, Chitanda JM, Balogh R, *et al.* Design and evaluation of cyclodextrin-based delivery systems to incorporate poorly soluble curcumin analogs for the treatment of melanoma. *Eur. J. Pharm. Biopharm.* 81(3), 548–556 (2012).
123. Cerga O, Borcan F, Bernad E, Popovici I. *In vivo* evaluation of cyclodextrin complexes with oleanolic and ursolic acids. *J. Agroaliment. Process. Technol.* 18(2), 130–135 (2012).
124. Baljinnyam E, Iwatsubo K, Kurotani R, *et al.* Epac increases melanoma cell migration by a heparan sulfate-related mechanism. *Am. J. Physiol. Cell Physiol*. 297(4), C802–C813 (2009).
125. Scodeller P, Catalano PN, Salguero N, Duran H, Wolosiuk A, Soler-Illia GJAA. Hyaluronan degrading silica nanoparticles for skin cancer therapy. *Nanoscale*. 5(20), 9690–9698 (2013).
126. Burmistrova O, Simões MF, Rijo P, Quintana J, Bermejo J, Estévez F. Antiproliferative activity of abietane diterpenoids against human tumor cells. *J. Nat. Prod.* 76(8), 1413–1423 (2013).
127. Bill MA, Bakan C, Benson Don M., Fuchs J, Young G, Lesinski GB. Curcumin induces proapoptotic effects against human melanoma cells and modulates the cellular response to immunotherapeutic cytokines. *Mol. Cancer Ther.* 8(9), 2726–2735 (2009).
128. Das MK, Kumar R., Development of Curcumin nanoniosomes for skin cancer chemoprevention. *Int. J. ChemTech. Res.* 7(2), 747-754 (2015).
129. Blackham AU, Northrup SA, Willingham M, D'Agostino Jr RB, Lyles DS, Stewart Iv JH. Variation in susceptibility of human malignant melanomas to oncolytic vesicular stomatitis virus. *Surgery*. 153(3), 333–343 (2013).
130. Yao H, Ng SS, Huo LF, *et al.* Effective melanoma immunotherapy with interleukin-2 delivered by a novel polymeric nanoparticle. *Mol. Cancer Ther*. 10(6), 1082–1092 (2011).
131. Chen Y, Bathula SR, Yang Q, Huang L. Targeted nanoparticles deliver siRNA to melanoma. *J. Invest. Dermatol*. 130(12), 2790–2798 (2010).
132. David S, Carmoy N, Resnier P, *et al. In vivo* imaging of DNA lipid nanocapsules after systemic administration in a melanoma mouse model. *Int. J. Pharm.* 423(1), 108–115 (2012).
133. David S, Montier T, Carmoy N, *et al.* Treatment efficacy of DNA lipid nanocapsules

and DNA multimodular systems after systemic administration in a human glioma model. *J. Gene Med.* 14(12), 769–775 (2012).

134. Glover DJ, Ng SM, Mechler A, Martin LL, Jans DA. Multifunctional protein nanocarriers for targeted nuclear gene delivery in nondividing cells. *FASEB J.* 23(9), 2996–3006 (2009).
135. Kigasawa K, Kajimoto K, Nakamura T, *et al.* Noninvasive and efficient transdermal delivery of CpG-oligodeoxynucleotide for cancer immunotherapy. *J. Control. Rel*. 150(3), 256–265 (2011).
136. Chang EH, Harford JB, Eaton MAW, *et al*. Nanomedicine: Past, present and future–A global perspective. *Biochem. Biophys. Res. Commun*. 468 (3), 511-517 (2015).
137. Grudzinski IP, Bystrzejewski M, Cywinska MA, *et al.* Cytotoxicity evaluation of carbon-encapsulated iron nanoparticles in melanoma cells and dermal fibroblasts. *J. Nanopart. Res*. 15(8), 1835 (2013).
138. Monteiro-Riviere NA, Safety of nanoparticle skin penetration. In: *Percutaneous penetration enhancers chemical methods in penetration enhancement*. Dragicevic N and Maibach HI (Eds.), Springer Berlin Heidelberg, 363-376 (2016).
139. Dhawan A, Sharma V. Toxicity assessment of nanomaterials: methods and challenges. *Anal. Bioanal. Chem.* 398(2), 589–605 (2010).
140. Arora S, Rajwade JM, Paknikar KM. Nanotoxicology and *in vitro* studies: The need of the hour. *Toxicol. Appl. Pharmacol.* 258(2), 151–165 (2012).
141. Kroll A, Pillukat M, Hahn D, Schnekenburger J. Interference of engineered nanoparticles with *in vitro* toxicity assays. *Arch. Toxicol.* 86(7), 1123–1136 (2012).
142. Hofmann-Amtenbrink M, Grainger DW, Hofmann H. Nanoparticles in medicine: Current challenges facing inorganic nanoparticle toxicity assessments and standardizations. *Nanomedicine: NBM.* 11(7): 1689-1694 (2015).
143. Dummer R, Hauschild A, Lindenblatt, *et al*. Cutaneous melanoma: ESMO Clinical Practice Guidelines for diagnosis, treatment and follow-up. *Ann. Oncol.* 26: suppl. 5, v126-v132 (2015).

BACKGROUND, HYPOTHESIS AND OBJECTIVES

BACKGROUND

1. As a natural biological barrier, the skin limits permeation to a few numbers of drugs with singular characteristics (e.g., low molecular weight, moderate lipophilicity and great potency) [1,2]. To improve skin permeation, combination of physical methods (i.e., iontophoresis, electroporation) and chemical enhancers (i.e., surfactants and organic solvents) are selected for development of conventional formulations; however, some of those strategies usually cause adverse side effects, such as: disruption of the *stratum corneum* (skin outer barrier), alteration of the skin's physiological pH, inflammatory and immunologic reactions and bacterial infections, which reduce the treatment efficacy [3].

2. Skin keratinocytes regulate growth and differentiation of melanocytes through interaction of multiple receptors and ligand-mediated activation [4]. One of these receptors is the melanocortin-1 receptor (MC1R), which mutation is related with skin carcinoma [4,5]. MC1R is activated by alpha-melanocyte stimulating hormone (α-MSH), which is up-regulated in melanoma tissues than in other cells, such as normal melanocytes, keratinocytes, activated macrophages and immature dendritic cells [6]. This natural ligand molecule is mainly expressed intracellularly, but it is also present on the cell surface, showing a protective and metastasis-retard action in melanoma cells [4,6,7].

3. Epidermal Growth Factor Receptor (EGFR), a cell-surface receptor belonging to ErbB family of tyrosine kinases, is overexpressed in several cancers, such as melanoma [8,9], being responsible for melanoma growth and metastasis [10]. Epidermal Growth Factor (EGF) is the natural ligand peptide, which appears to act directly on the endothelial cells, promoting angiogenesis, such as on development of melanoma lymph node metastases, where it is up-regulated [10].

4. Emerging therapies for melanoma are currently focused on targeted chemotherapy or phototherapy, achieved by functionalizing nanoparticles with specific tumor targeting molecules [11,12]. Hybrid nanoparticles are developed for mitigating limitations and obtain synergistic advantages by a broad range of chemically modified polymeric-based nanosystems [13]. Self-assembled hybrid nanoparticles may favor of improved physical and chemical drug stability, versatile drug loading and release profiles, as well as an increased and highly specific efficiency [14,15].

HYPOTHESIS

1. Considering multiple applications of targeted drug delivery systems, hybrid lipid-polymer nanoparticles were developed for application in melanoma chemotherapy. Moreover, those nanoparticles were conjugated with a specific ligand, such as α-melanocyte stimulating hormone (α-MSH), in order to efficiently deliver an anti-tumor drug to the cancer site, with minimal toxicity to healthy tissues. On the other hand, both new and model anti-tumor agents, derived from plants, were assessed.

2. As an alternative to chemotherapy, hybrid polymeric-gold nanoparticles were developed for application in melanoma photothermal therapy. Gold nanoparticles were produced by a “green” reduction method, using phytochemicals. In addition, those nanoparticles were conjugated with a specific ligand, such as Epidermal Growth Factor (EGF), in order to efficiently accumulate at the tumor site, for further laser irradiation, with minimal toxicity to healthy tissues. Both laser and gold nanoparticles showed light absorbing properties at near infrared (NIR) region, in order to minimize the damage of surrounding healthy tissue.

OBJECTIVES

Regarding what has been previously presented, we propose the investigation of the application of hybrid lipid-polymer nanoparticles and hybrid polymer-gold nanoparticles for targeted chemotherapy and phototherapy of melanoma, respectively. To achieve these objectives, we have pursuit the following steps:

1. **Development of hybrid lipid-polymer nanoparticles for targeted transdermal drug delivery**

In this part, we have designed hybrid nanoparticles, with a core structure made of polyester polymer and long-chain fatty acids (stearic acid), and coated with another fatty acid (oleic acid), described as a permeation enhancer. Betamethasone-21-acetate was firstly used as a hydrophobic model drug for studying the nanoparticles release profile and *in vitro* and *in vivo* skin permeation.

The main results regarding this milestone were reported in Article II:
Polymeric nanoparticles modified with fatty acids encapsulating betamethasone for anti-inflammatory treatment. International Journal of Pharmaceutics. (2015). 493(1-2):271-284. doi: 10.1016/j.ijpharm.2015.07.044.

2. **Development of hybrid polymer-gold nanoparticles for targeted photothermal therapy**

In this step, we have designed hybrid nanoparticles, made of a gold core and polymeric coating, composed by a polysaccharide (hyaluronic acid) and a fatty acid (oleic acid). Bio-production of gold nanoparticles with phytochemicals obtained from an aqueous extract of *Plectranthus* sp. were assessed. Moreover, lysozyme was associated to the nanoparticles surface as a model protein of targeting peptides, and its photostability before and after conjugation was evaluated.

The main results regarding this milestone were reported in Article III and IV and in Supplementary Information:

Lysozyme photochemistry as a function of temperature. The protective effect of nanoparticles on lysozyme photostability. PLoS One. (2015). 10(12):e0144454. doi: 10.1371/journal.pone.0144454.

Bio-production of gold nanoparticles for photothermal therapy. Therapeutic Delivery (2016). 7(5):287-304. doi: 10.4155/tde-2015-0011.

Request of national patent nº 20151000093093 (Portugal). Nanossistema de ouro com revestimento biopolimérico e gama de absorção no infravermelho próximo e método para a sua preparação. 2015.

3. Physico-chemical characterization and *in vitro* bio-characterization of targeted hybrid lipid-polymer nanoparticles for melanoma chemotherapy

In this chapter, we have improved hybrid nanoparticles for targeted drug delivery by combining hyaluronic and oleic acids, as the coating material, and α-melanocyte stimulating hormone (α-MSH), as the specific surface ligand. Parvifloron D and paclitaxel were selected as the anti-tumor drugs. Both drugs are isolated from plant extracts. Nanosystems were characterized in terms of physico-chemical features, release profile, *in vitro* permeation and cytotoxicity.

The main results regarding this milestone were reported in Article V:
Functionalized diterpene Parvifloron D loaded hybrid nanoparticles for target delivery in melanoma therapy. Therapeutic Delivery (2016). 7(8), 521–544. doi: 10.4155/tde-2016-0027

4. Physico-chemical characterization and *in vitro* bio-characterization of targeted hybrid polymer-gold nanoparticles for melanoma photothermal therapy

In this chapter, we have associated Epidermal Growth Factor (EGF) onto the surface of hybrid polymeric-gold nanoparticles for targeted photothermal therapy. EGF was assessed for its photostability, before and after conjugation with nanoparticles. Resultant nanosystems were characterized in terms of physico-chemical properties, *in vitro* cytotoxicity and receptor-mediated internalization.

The main results regarding this milestone were reported in Annex I:
EGF functionalized polymer-coated gold nanoparticles promote EGF photostability and EGFR internalization for photothermal therapy. (2016). PLoS One (submitted, under review).

5. *In vivo* efficacy studies

In this chapter, *in vivo* efficacy studies were conducted on SCID mice used as xenograft models for human melanoma (A375 cell line). Both targeted chemotherapy and phototherapy were evaluated independently on mice with cutaneous melanoma. Tumor volume after treatment and histological analysis were assessed.

The main results regarding this milestone were reported in Annex II:
In vivo efficiency and safety studies of photothermal therapy for human cutaneous melanoma (Publication pending).

References

1. El-Kattan AF, Asbill CS, Michniak BB. The effect of terpene enhancer lipophilicity on the percutaneous permeation of hydrocortisone formulated in HPMC gel systems. *Int. J. Pharm.* 198(2), 179–189 (2000).
2. Peter HM Hoet, Irene Brüske-Hohlfeld, Salata O V. Nanoparticles - known and unknown health risks. *J. Nanobiotechnology*. 2(12), 1–15 (2004).
3. Paudel KS, Milewski M, Swadley CL, Brogden NK, Ghosh P, Stinchcomb AL. Challenges and opportunities in dermal/transdermal delivery. *Ther. Deliv.* 1(1), 109–131 (2010).
4. Carlson JA, Linette GP, Aplin A, Ng B, Slominski A. Melanocyte receptors: Clinical implications and therapeutic relevance. *Dermatol. Clin.* 25(4), 541–557 (2007).
5. Lu W, Xiong C, Zhang R, *et al.* Receptor-mediated transcytosis: A mechanism for active extravascular transport of nanoparticles in solid tumors. *J. Control. Rel*. 161(3), 959–966 (2012).
6. Salazar-Onfray F, Lopez M, Lundqvist A, *et al.* Tissue distribution and differential expression of melanocortin 1 receptor, a malignant melanoma marker. *Br. J. Cancer*. 87(4), 414–422 (2002).
7. Slastnikova TA, Rosenkranz AA, Gulak PV, *et al.* Modular nanotransporters: A

multipurpose *in vivo* working platform for targeted drug delivery. *Int. J. Nanomedicine*. 7(0), 467–482 (2012).

8. Boone B, Jacobs K, Ferdinande L, *et al.* EGFR in melanoma: Clinical significance and potential therapeutic target. *J. Cut. Pathol.* 38(6), 492–502 (2011).
9. Yewale C, Baradia D, Vhora I, Patil S, Misra A. Epidermal growth factor receptor targeting in cancer: a review of trends and strategies. *Biomaterials*. 34(34), 8690–8707 (2013).
10. Bracher A, Cardona AS, Tauber S, *et al.* Epidermal growth factor facilitates melanoma lymph node metastasis by influencing tumor lymphangiogenesis. *J. Invest. Dermatol*. 133(1), 230–238 (2013).
11. Lloyd-Hughes H, Shiatis AE, Pabari A, Mosahebi A, Seifalian A. Current and future nanotechnology applications in the management of melanoma: A review. *J. Nanomed. Nanotechnol.* 6(0), 334 (2015).
12. Bombelli FB, Webster CA, Moncrieff M, Sherwood V. The scope of nanoparticle therapies for future metastatic melanoma treatment. *Lancet Oncol.* 15(1), e22–e32 (2014).
13. Prabhu RH, Patravale VB, Joshi MD. Polymeric nanoparticles for targeted treatment in oncology: Current insights. *Int. J. Nanomedicine*. 10(1), 1001 (2015).
14. Mandal B, Bhattacharjee H, Mittal N, *et al.* Core–shell-type lipid–polymer hybrid nanoparticles as a drug delivery platform. *Nanomed. Nanotech. Biol. Med.* 9(4), 474–491 (2013).
15. Rana S, Bajaj A, Mout R, Rotello VM. Monolayer coated gold nanoparticles for delivery applications. *Adv Drug Deliv. Rev.* 64(2), 200–216 (2012).

PUBLICATIONS

Article II

Polymeric nanoparticles modified with fatty acids encapsulating betamethasone for anti-inflammatory treatment.

Catarina Oliveira Silva[1, 2], Patrícia Rijo[1, 3], Jesús Molpeceres[2], Isabel Vitória Figueiredo[4, 5], Lia Ascensão[6], Ana Sofia Fernandes[1, 3], Amílcar Roberto[1] and Catarina Pinto Reis[1, 7*].

[1]CBiOS, Research Center for Biosciences & Health Technologies, Universidade Lusófona, Campo Grande 376, 1749-024 Lisboa, Portugal.
[2]Department of Biomedical Sciences, Faculty of Pharmacy, University of Alcalá, Ctra. Universidad Complutense, 28871 Alcalá de Henares, Spain.
[3]iMed.ULisboa, Instituto de Investigação do Medicamento, Faculdade de Farmácia, Universidade de Lisboa, Av. Prof. Gama Pinto, 1649-003 Lisboa, Portugal.
[4]Pharmacology and Pharmaceutical Care, Faculty of Pharmacy, Universidade de Coimbra, Azinhaga de Santa Comba, 3000-354 Coimbra, Portugal.
[5]IBILI, Institute for Biomedical Imaging and Life Sciences, Universidade de Coimbra, Azinhaga de Santa Comba, 3000-548 Coimbra, Portugal.
[6]CESAM, Universidade de Lisboa, Faculdade de Ciências de Lisboa, CBV, Campo Grande, 1949-016 Lisboa, Portugal.
[7]IBEB, Biophysics and Biomedical Engineering, Faculty of Sciences, Universidade de Lisboa, 1749-016, Lisboa, Portugal.

Corresponding Author: Prof. Dr. Catarina Pinto Reis.

International Journal of Pharmaceutics, 493(1-2):271-284 (2015)

doi: 10.1016/j.ijpharm.2015.07.044. Epub 2015 Jul 26.

International Journal of Pharmaceutics 493 (2015) 271–284

Contents lists available at ScienceDirect

International Journal of Pharmaceutics

journal homepage: www.elsevier.com/locate/ijpharm

Pharmaceutical nanotechnology

Polymeric nanoparticles modified with fatty acids encapsulating betamethasone for anti-inflammatory treatment

Catarina Oliveira Silva[a,b], Patrícia Rijo[a,c], Jesús Molpeceres[b], Isabel Vitória Figueiredo[d,e], Lia Ascensão[f], Ana Sofia Fernandes[a,c], Amílcar Roberto[a], Catarina Pinto Reis[a,g,*]

[a] CBiOS, Research Center for Biosciences & Health Technologies, Universidade Lusófona, Campo Grande 376, 1749-024 Lisboa, Portugal
[b] Department of Biomedical Sciences, Faculty of Pharmacy, University of Alcalá, Ctra. Universidad Complutense, 28871 Alcalá de Henares, Spain
[c] iMed.ULisboa, Instituto de Investigação do Medicamento, Faculdade de Farmácia, Universidade de Lisboa, Av. Prof. Gama Pinto, 1649-003 Lisboa, Portugal
[d] Pharmacology and Pharmaceutical Care, Faculty of Pharmacy, Universidade de Coimbra, Azinhaga de Santa Comba, 3000-354 Coimbra, Portugal
[e] IBILI, Institute for Biomedical Imaging and Life Sciences, Universidade de Coimbra, Azinhaga de Santa Comba, 3000-548 Coimbra, Portugal
[f] Centro de Estudos do Ambiente e do Mar (CESAM), Universidade de Lisboa, Faculdade de Ciências de Lisboa, CBV, Campo Grande, 1949-016 Lisboa, Portugal
[g] IBEB, Biophysics and Biomedical Engineering, Faculty of Sciences, Universidade de Lisboa, 1749-016, Lisboa, Portugal

ARTICLE INFO

Article history:
Received 13 July 2015
Accepted 15 July 2015
Available online 26 July 2015

Chemical compounds studied in this article:
Poly-ε-caprolactone (PubChem CID: 10.401)
Stearic acid (PubChem CID: 5281)
Oleic acid (PubChem CID: 445.639)
Pluronic® F127 (PubChem CID: 24.751)
Betamethasone-21-acetate (PubChem CID: 443.967)
Betamethasone (PubChem CID: 9782)

Keywords:
Betamethasone-21-acetate
Nanoparticles
Chronic inflammation
Transdermal drug delivery
Oleic acid
Poly-ε-caprolactone

ABSTRACT

Topical glucocorticosteroids were incorporated into nanocarrier-based formulations, to overcome side effects of conventional formulations and to achieve maximum skin deposition. Nanoparticulate carriers have the potential to prolong the anti-inflammatory effect and provide higher local concentration of drugs, offering a better solution for treating dermatological conditions and improving patient compliance.

Nanoparticles were formulated with poly-ε-caprolactone as the polymeric core along with stearic acid as the fatty acid, for incorporation of betamethasone-21-acetate. Oleic acid was applied as the coating fatty acid. Improvement of the drug efficacy, and reduction in drug degradation with time in the encapsulated form was examined, while administering it locally through controlled release. Nanoparticles were spherical with mean size of 300 nm and negatively charged surface. Encapsulation efficiency was 90%. Physicochemical stability in aqueous media of the empty and loaded nanoparticles was evaluated for six months. Drug degradation was reduced compared to free drug, after encapsulation into nanoparticles, avoiding the potency decline and promoting a controlled drug release over one month. Fourier transform infrared spectroscopy and thermal analysis confirmed drug entrapment, while cytotoxicity studies performed *in vitro* on human keratinocytes, *Saccharomyces cerevisiae* models and *Artemia salina*, showed a dose–response relationship for nanoparticles and free drug. In all models, drug loaded nanoparticles had a greater inhibitory effect. Nanoparticles increased drug permeation into lipid membranes *in vitro*. Preliminary safety and permeation studies conducted on rats, showed betamethasone-21-acetate in serum after 48 h application of a gel containing nanoparticles. No skin reactions were observed.

In conclusion, the developed nanoparticles may be applied as topical treatment, after encapsulation of betamethasone-21-acetate, as nanoparticles promote prolonged drug release, increase drug stability in aqueous media, reducing drug degradation, and increase drug permeability through lipid membranes.

Abbreviations: BTMA, Betamethasone-21-acetate; DMSO, Dimethyl sulfoxide; DMEM, Dulbecco's Modified Eagle's Medium; DSC, Differential scanning calorimetry; EE, Encapsulation efficiency; FTIR, Fourier transform infrared spectroscopy; GCs, Glucocorticosteroids; HaCaT, Human adult low-calcium high-temperature keratinocytes; HPLC, High performance liquid chromatography; MTT, 3-(4,5-Dimethylthiazol-2-yl)-2,5-diphenyltetrazolium bromide; NP, Nanoparticles; NSAID, Non steroid anti-inflammatory drugs; OA, Oleic acid; PCL, Poly-ε-caprolactone; RC, Refrigeration conditions; RH, Relative humidity; RT, Room temperature; ROS, Reactive oxygen species; SA, Stearic acid; TLC, Thin layer chromatography; YPD, Yeast–peptone–dextrose.

* Corresponding author at: CBiOS, Research Center for Biosciences & Health Technologies, Universidade Lusófona, Campo Grande 376, 1749-024 Lisboa, Portugal. Fax: +351 2175 155 98/79.
E-mail address: catarina.reis@ulusofona.pt (C.P. Reis).

http://dx.doi.org/10.1016/j.ijpharm.2015.07.044
0378-5173/

1. Introduction

Treatment of inflammatory diseases benefit from a localized therapy accomplished with polymeric-based nanoparticles (Zhang et al., 2013). Recently, we have developed innovative nanoparticles (NP) for treatment of skin diseases, through application of drugs including glucocorticosteroids (GC) (Rosado et al., 2012), non-steroid anti-inflammatory drugs (NSAID) (Pinto Reis et al., 2011), antimicrobial agents (Gomes et al., 2013; Pinto Reis et al., 2013; Rijo et al., 2014) and anticancer drugs for melanoma (unpublished).

Glucocorticosteroids (GC) cover a broad spectrum of therapeutic actions such as anti-inflammatory, immunosuppressive, anti-proliferative and vasoconstrictive, having also apoptotic and anti-angiogenic effects (Banciu et al., 2006; Lebwohl et al., 2013). The absence of natural GC produced by skin cells is mainly visible in inflammatory diseases, such as atopic dermatitis and psoriasis (Slominski et al., 2013).

However, when treating common skin diseases like atopic dermatitis or psoriasis, chronic application of topical corticosteroids generally leads to local adverse effects such as skin atrophy, rosacea, *striae* and skin infections. When highly absorbed, systemic side effects (e.g., hypothalamic-pituitary-adrenal suppression, glaucoma, hyperglycemia and hypertension) appear, compromising the therapeutic effectiveness and patient adherence (Ference and Last, 2009). For this study, we chose betamethasone-21-acetate (BTMA) with the structure illustrated in Fig. 1, since it is a high-potency synthetic derivative of betamethasone and agonist to the GC-receptors. Betamethasone offers a 10-fold higher potency than hydrocortisone (Arica and Lamprecht, 2005), and has been applied through nanosystems for topical and percutaneous permeation, reducing associated side effects (Abdel-Mottaleb et al., 2012; Zhang and Smith, 2010). Previously, Abdel-Mottaleb et al. (2012) demonstrated that non-coated polymeric NP work as drug reservoirs, penetrating to 25 μm of skin depth (Abdel-Mottaleb et al., 2012), due to limited interaction with skin lipids. In contrast, some reported lipid NP (Zhang and Smith, 2010) interact with skin lipids but show many stability problems (e.g., drug leakage and chemical modifications during storage).

In this study, we provide evidence that the association of both fatty acids and polymers for development of hybrid nanoparticles may counteract individual disadvantages of these materials. In addition, our nanoparticles may also improve local drug delivery to specific inflammatory sites in the skin, by reducing hydrolysis and degradation of BTMA and controlling its release from the nanoparticles over a prolonged period. The concept of hybrid lipid-polymeric structures was first described for formation of bi-layered membranes (Shen et al., 2000). In the present study, the goal was to develop a stable platform for drug delivery, based on the association of a biodegradable polymer, poly-ε-caprolactone (PCL) and stearic and oleic acids as long chain fatty acids. The potential of these carriers is to increase skin permeation. Poly-ε-caprolactone (PCL) was used to control drug release, reduce the drug percutaneous penetration and protect the drug from potential photochemical degradation (Pohlmann et al., 2013). In addition, PLC was selected as the core polymer as previous work showed promise as an ideal depot system for prolonged drug release, with appropriate NP size and spherical shape when used for skin applications (Rosado et al., 2012). However, to overcome previous problems, such as the low encapsulation efficiency (62%), stearic acid (SA) was added to the core, to improve drug entrapment within the NP structure, also reduce the possibility of burst release (Chen et al., 2001; Lee et al., 2003). Since the penetration of polymeric NP across the skin is hindered by the *stratum corneum* mechanical barrier properties (Abdel-Mottaleb et al., 2012), oleic acid (OA) was incorporated as the coating lipid, since it has been previously shown to be a skin permeation enhancer and membrane fluidizing agent (Al Abood et al., 2013). OA is also reported to reduce nanoparticle aggregation (Bennet et al., 2012). SA is a saturated fatty acid unlike OA, but both are C_{18} fatty acids, and are presently approved for skin and food applications (Inoue et al., 2004). In addition, OA and SA are also present in many essential oils, providing higher skin permeation allied with lower toxicity, and have been reported as accepted for cosmetic and alimentary applications and documented by several organizations, such as the International Flavor and Fragrance Association (Herman and Herman, 2015).

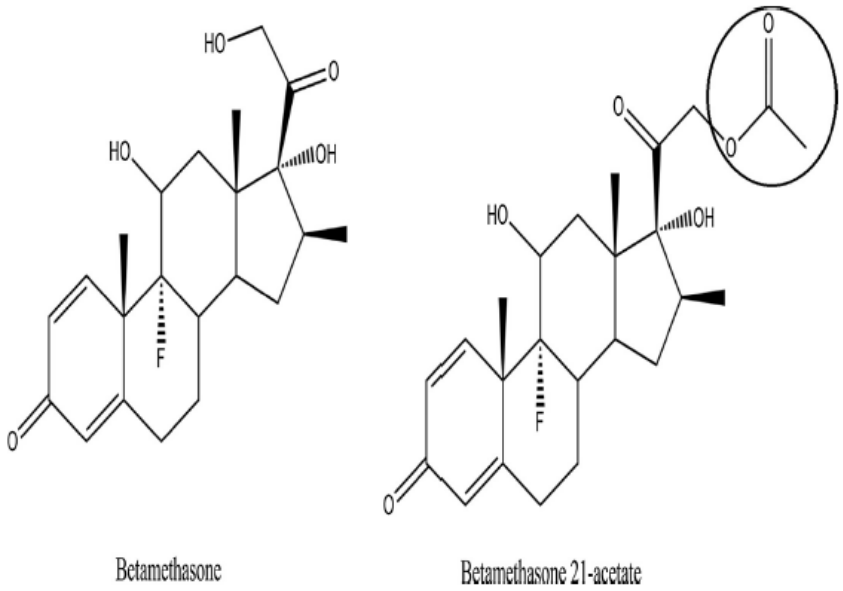

Fig. 1. Chemical structures of betamethasone and betamethasone-21-acetate.The modification of ester group in C_{21} of betamethasone-21-acetate, responsible for the molecule's high-potency action, is highlighted.

2. Materials and methods

2.1. Materials

Betamethasone (MW: 392.46 g mol^{-1}) and Betamethasone-21-acetate (MW: 434.50 g mol^{-1}) were kindly donated by Hovione S.A. Stearic acid, oleic acid, Pluronic® F127 (Poloxamer 147), PCL (MW: 14,000 g mol^{-1}), and 3-(4,5-dimethylthiazol-2-yl)-2,5-diphenyltetrazolium bromide (MTT) were supplied by Sigma–Aldrich (Steinheim, Germany). Lecithin soybean (>95% phosphatidylcholine) was supplied by MP Biomedicals (Madrid, Spain) and dodecane (99% purity) was supplied by Panreac (Madrid, Spain). All other compounds and reagents were also of analytical grade. The water used was purified to 18.2 MΩ cm at 25 °C through a Millipore system (Millipore, MA).

2.2. Preparation of hybrid nanoparticles

Empty oleic acid (OA) coated and non-coated NP (i.e., core NP) were prepared according to a previously described solvent displacement method, with some modifications (Calvo et al., 1997; Shah et al., 2012). Briefly, in a sealed glass beaker (32 × 46 mm, capacity: 25 mL, Simax, Czech Republic), an organic phase was prepared by mixing 100 mg of PCL and 4.975 mL of acetone, through 10 min ultrasound exposure (Bandelin Sonorex Super Rk 510H, frequency of 45 kHz). An aliquot of 25 μL stearic acid (SA) solution in ethanol (0.025%, w/v) was added to the organic phase and allowed to mix for 5–10 min with magnetic stirring. This solution was immediately poured on 10 mL aqueous solution of a Pluronic® F127 (0.25%, w/v), prepared in similar 25 mL glass beaker, under magnetic stirring (1200 rpm) for 10 min. For betamethasone-21-acetate (BTMA) loaded OA NP, the same procedure was conducted except that 5 mg of BTMA were dissolved in the organic phase. The suspension was stirred for 10 min and then concentrated under reduced pressure (Rotary evaporator from Heidolph type VV2000, Apeldoorn, Netherlands) to 10 mL (final volume). All NP were isolated by centrifugation at 18550 × *g* for 30 min (Hermle Labortechnik Gmbh type Z36HK, Wehingen, Germany) to remove unbound drug. Afterwards, empty and BTMA loaded NP were incubated with 80 μL of OA, for 2 h, under constant magnetic stirring. Formulations were made in triplicate to ensure the repeatability of the preparation method.

2.3. Physical characterization of the nanoparticles

Mean particle size, polydispersity index (PI) and zeta potential of the NP concentrated aqueous suspension were measured with a Coulter Nano-sizer Delsa™ Nano C (Fullerton, CA, USA). Experiments were conducted in triplicate for empty core NP, empty OA NP and BTMA-loaded OA NP ($n = 3$). A low value of PI factor (<0.25) indicates a less dispersed NP distribution in size. Results are expressed as mean of measurements on three different batches ±SD and the empty OA NP and BTMA-loaded OA NP distributions in terms of size as volume.

2.4. Morphology

Samples of fresh and one-month old empty OA NP and BTMA-loaded OA NP, as an aqueous suspension, were kept in glass vials (capacity: 10 mL), closed with lid and parafilm, at room temperature (25 ± 5 °C, RT) and at residual humidity (RH) of 60%. An aliquot (10 μL) of each sample was mounted on a glass coverslip and left to dry in a desiccator. Afterwards, the sample was coated with a thin layer of gold (500 nm thick) and observed on a JEOL 5200LV scanning electron microscope (JEOL Ltd., Tokyo, Japan) at an accelerating voltage of 20 kV. Images were recorded digitally.

2.5. Drug quantification

BTMA was determined by a previously validated reverse-phase HPLC chromatographic method (Petersen et al., 1980). Limit of detection (LOD) and limit of quantification (LOQ) were determined. LOD and LOQ were calculated to be 2.91 μg/mL and 9.71 μg/mL, respectively. An Agilent Technologies 1200 Infinity series was fitted with a dual wavelength UV spectrophotometer detector (Agilent Technologies, Waldbronn, Germany). The mobile phase consisted of methanol and Milli-Q water (60:40%, v/v) using a Zorbax Eclipse Plus C 18 column (4.6 × 100 mm, 3.5 μm, particle size) as the stationary phase. A flow rate of 1.0 mL/min and a detection wavelength of 240 nm were selected. The column conditions were maintained at 25 °C, with an injection volume of 20 μL and a run time of 15 min. Standards for BTMA between 5 and 60 μg/mL were evaluated in triplicate and a calibration curve was found to be $y = 29.33x + 144.82$, with $R^2 = 0.998$. The chromatographic data was processed using ChemStation software (Agilent Technologies, Waldbronn, Germany). Measurements were made in triplicate ($n = 3$).

2.6. Drug loading and encapsulation efficiency

Drug encapsulation efficiency (%) was determined by measuring the free drug present in the supernatant (Eq. (1)) and the encapsulated drug (Eq. (2)), after rupturing the NP in organic solvents, through exposure to temperature (60 °C) and ultrasonic bath (frequency of 45 kHz). Drug loading efficiency (wt%) was calculated based on the value for drug encapsulation (Eq. (3)). Measurements were made in triplicate with three independent NP batches ($n = 3$).

$$\left(\frac{\text{Total amount drug} - \text{Amount free drug}}{\text{Total amount drug}}\right) \times 100\% \quad (1)$$

$$\left(\frac{\text{Amount encapsulated drug}}{\text{Total amount drug}}\right) \times 100\% \quad (2)$$

$$\left(\frac{\text{weight of durg in nanoparticle}}{\text{weight of loaded nanoparticle}}\right) \times 100\% \quad (3)$$

2.7. Determination of nanoparticle recovery yield

Three independent batches for BTMA-loaded OA NP ($n = 3$) and OA empty NP ($n = 3$) were lyophilized at −50 ± 2 °C, for 24 h in FreeZone 2.5 L Benchtop Freeze Dry System (Labconco, Kansas City, Missouri, USA) and weighted for determination of the NP recovery yield, after production.

2.8. In vitro *release studies*

BTMA-loaded OA NP (400 mg, $n = 3$) were lyophilized for 24 h as described, placed in three stirred (200 rpm) amber glass bottles (capacity: 50 mL), containing 50 mL of phosphate buffer solution pH 5.5 (USP XXX) to simulate human skin pH (Knor et al., 2011). Sink conditions were considered during the whole assay, as the solubility of BTMA in aqueous solution is 30 μg/mL (Kabasakalian et al., 1966). At appropriate time intervals, aliquots of the release medium (300 μL) were collected and replaced immediately with fresh buffer. NP were recovered from the supernatant by centrifugation, at 18550 × *g* for 30 min (Hermle Labortechnik Gmbh type Z36HK, Wehingen, Germany), then returned to the release medium. BTMA concentration at each time point was

determined in triplicate using HPLC, according to the method described in Section 2.5. The assay was conducted for one month, until the total amount of drug was released. A standard calibration curve, performed with BTMA standards (5–60 μg/mL) in phosphate buffer pH 5.5, was found to be $y = 29.33x + 144.82$, with $R^2 = 0.998$. Volume corrections were applied to the drug release profile curve, as mean of three independent measurements of three different NP batches ±SD. During the release studies, BTMA-loaded OA NP and BTMA conversion to BTM was also monitored by HPLC and thin layer chromatography (TLC). TLC is described in the pharmacopeias as a semi-quantitative technique to detect impurities and degradation products and it is also used for steroid assays, in association with HPLC (Görög, 2011).

2.9. Stability studies of nanoparticles over time

Stability of aqueous suspensions (10 mL) of empty OA NP and BTMA-loaded OA NP was evaluated for 6 months in terms of physicochemical characteristics of the formulation, namely size, polydispersity index (PI), zeta potential and pH. Size, PI and zeta potential were measured with a Coulter Nano-sizer Delsa™ Nano C (Fullerton, CA, USA), while pH measurement was conducted with a pH electrode meter (827 pH Lab, Metrohm, Switzerland), calibrated daily with buffer solutions pH 4.00 ± 0.02 and 7.00 ± 0.02 (20 °C) ST (Panreac, Spain). Samples were divided into two groups with empty OA NP and BTMA-loaded OA NP: (1) empty OA NP ($n = 3$) and BTMA-loaded OA NP ($n = 3$) were kept under storage at 4 ± 2 °C and residual humidity (RH) of 70% (refrigeration conditions, RC); and (2) empty OA NP ($n = 3$) and BTMA-loaded OA NP ($n = 3$) were kept at room temperature (25 ± 5 °C, RT) and residual humidity (RH) of 60%. All samples were stored as aqueous suspensions of NP, in sealed vials protected from the light and without addition of stabilizers or other preservatives. Results are represented as mean of measurements of three independent batches ±SD.

2.10. Interactions between drug and nanoparticles

Empty OA NP and BTMA-loaded OA NP held in aqueous medium for 1 month at room temperature were selected for the study of interactions between drug and OA NP by FTIR spectroscopy and thin layer chromatography (TLC). Samples of fresh and one-month old NP were kept at room temperature, and then collected and lyophilized to obtain a powder for FTIR analysis. The KBr pellet method was used and spectra recorded in an IRAffinity-1 FT-IR Spectrophotometer (Shimadzu, Columbia, NY, USA). The pellet was prepared with a ratio of 1:10 (w/w) of KBr to NP and left to dry in a desiccator 24 h before analysis. The following samples were compared: fresh empty OA NP were compared with raw polymer (poly-ε-caprolactone) and fatty acids (stearic acid and oleic acid), and free BTMA was compared with fresh BTMA-loaded OA NP, as well as a physical mixture of raw components (i.e., poly-ε-caprolactone, stearic acid, oleic acid at 1:1:1, w/w) of the nanoparticle formulation (except the drug); in addition, free BTMA was compared with BTM and one-month old BTMA-loaded OA NP and the raw polymer (poly-ε-caprolactone) and fatty acids (stearic acid and oleic acid) were compared with one-month old empty OA NP.

2.11. Thermal stability of nanoparticles

Differential scanning calorimetry (DSC) is described as a technique meant to check the purity of drug and other components, characterization of solid phases and to confirm physicochemical interactions (Görög, 2011). Thermal transformations and phase transitions of the nanoparticles were studied by using a Mettler-Toledo DSC-30, TA 4000 Calorimeter (Columbus, Ohio, USA). Indium was used to calibrate the instrument. Samples were previously lyophilized, weighted (2.0 mg) and sealed in an aluminum pan. Free BTMA, empty OA NP, BTMA-loaded OA NP and a physical mixture (1:1, w/w) of BTMA and empty NP were studied. The results were demonstrated as curves of heat flux *versus* temperature (Celsius degrees, °C). A controlled heating rate of 10 °C/min under a continuous nitrogen purge (20–30 mL/ min) and over a temperature range from 25 to 375 °C was selected. The number of thermal transitions, the melting point (T_m, °C) and difference in Gibbs energy (ΔH, J g^{-1}) were also determined.

2.12. In vitro *permeation studies*

Parallel artificial membrane permeability assay (PAMPA) was conducted as a preliminary characterization of the role of NP on drug permeability using a 96-well filter plate Millipore Multi-Screen® IP 0.45 μm (Darmstadt, Germany). Previously lyophilized empty and BTMA-loaded OA NP (10 mg), as well as free BTMA (5 mg), were resuspended in Milli-Q water, in order to prepare the stock solutions for the assay. The initial concentration (C_0) in the starting solution was 50 μg/mL for the free BTMA, BTMA-loaded OA NP and free BTMA + empty OA NP (1:1, w/w), which was added (150 μL, 5% DMSO, v/v) to the donor compartment, to achieve a homogenous covering of the hydrophobic PVDF membrane. The acceptor compartment was filled with phosphate solution pH 5.5 (300 μL). The membrane solution was constituted of soybean lecithin at 2% (w/v) prepared in 5 μL dodecane. After 24 h incubation, the residual concentration in the donor compartment and the permeated drug concentration in the acceptor compartment were also measured. Retention factors (R) (Eq. (4)), permeation parameters ($C_A(t)/C_D(0)$) and permeability coefficients (log P_e) (Eq. (5)) of the three studied samples were calculated, according to the literature (Markovic et al., 2012):

$$R : 1 - \frac{CD(t = x)}{CD(t = 0)} - \frac{VA}{VD} \times \frac{CA(t = x)}{CA(t = 0)} \quad (4)$$

where V_A and V_D are, respectively, the volumes in the acceptor and donor wells.

$$\log P_e : \log\left(\frac{VD \times VA}{(VD + VA)A \times t}\right) - \ln\left(1 - \left(\frac{CA(t = x)}{CD(t = 0)}\right)\right) \quad (5)$$

where A is the filter surface (0.3 cm^2); t is the incubation time (s); and C_A and C_D are concentrations in the acceptor and donor wells, respectively (mg mL^{-1} cm^{-3}).

Two measurements were carried out, each comprising five replicate samples ($n = 5$), using the same HPLC method described previously in Section 2.5 (methanol: water 60:40%, v/v, as the mobile phase, with Scharlau Kromasil C 18 column (4.6 × 150 mm, 5 μm, particle size) as the stationary phase). BTMA standards in phosphate solution pH 5.5 were repeated and measured in triplicate. A calibration curve equation was found to be $y = 345.8x + 151.05$, with a $R^2 = 0.998$. Results are expressed as mean ± SD.

2.13. Toxicity studies

2.13.1. MTT assays on HaCaT cell model

Cell viability studies were conducted on human keratinocytes (HaCaT cells, CLS Cell Lines Service GmbH, Eppelheim, Germany) using the 3-(4,5-dimethylthiazol-2-yl)-2,5-diphenyltetrazolium bromide (MTT) assay (Rijo et al., 2014). Cells were cultured in Dulbecco's Modified Eagle's Medium (DMEM) supplemented with 10% fetal bovine serum and 1% penicillin/streptomycin solution. To assess the potential cytotoxicity of the NP, cells were seeded onto 96-well plate at a density of 5000 cells/ well to reach the desired

confluence. Stock solutions of free BTMA and NP were prepared by dilution in DMSO and DMEM medium respectively, to provide series of different BTMA concentrations (final well concentration): 5–250 μg/mL for free BTMA and 5–50 μg/mL for empty and BTMA-loaded OA NP. For empty OA NP, the equivalent weight of nanoparticles (without drug) was considered, according to the same concentrations used for BTMA-loaded OA NP. The final concentration of DMSO in the cultures did not exceed 0.5% (v/v). The cells were exposed to the treatments for 24 h, then washed twice with PBS and incubated with MTT solution (0.5 mg/mL in culture medium) for 2.5 h at 37 °C. Finally, the medium was removed and cells were washed with PBS. DMSO (200 μL/ well) was added to dissolve the formazan crystals and absorbance was read at 595 nm (Thermo Scientific Multiskan FC, Shanghai, China). The IC_{50} for BTMA was determined by extrapolating the concentration of BTMA which resulted in 50% inhibition of cell growth, using the software OriginPro 8 (OriginLab Corporation, Northampton, MA, USA). Three independent experiments were carried out, each comprising four replicate cultures ($n = 4$). Results are represented as mean ± SD.

2.13.2. *Toxicity on* Saccharomyces cerevisiae *model*

Cytotoxicity of BTMA and NP was determined against *Saccharomyces cerevisiae* (ATCC® 9763™) according to the method of Roberto and Caetano (2005). Approximately 0.5×10^6 cells/mL, in yeast–peptone–dextrose (YPD) medium, were exposed to different concentrations of empty OA NP (2 μg/mL), BTMA-loaded OA NP (2 and 4 μg/mL) and free BTMA (5–100 μg/mL), in cuvettes (final volume: 2 mL). Cell cultures grew for 5 h at 30 °C in Heidolph Incubator 1000 with shaker Heidolph Unimax 1010, Schwabach, Germany. The cuvettes were vortexed for 2 s and the absorbance measured at intervals of 30 min (Thermo Scientific model Evolution 300 BB, UK). The logarithmic phase from the growth curve was used to evaluate the toxicity, expressed as growth inhibition as percentage of the growth of control cells. Three series of measurements were performed each comprising four replicate cultures ($n = 4$). Results are expressed as mean ± SD.

2.13.3. *Toxicity on* Artemia salina *model*

The toxicity of empty NP (2 μg/mL), BTMA-loaded NP (2 and 4 μg/mL) and free BTMA (50 and 100 μg/mL) on *Artemia salina* was tested according the method described by Zhang et al. (2012), with some small adaptations on the hatching equipment, namely material for covering the compartments. Brine shrimp cysts (80 mg) obtained from JBL GmbH & Co., KG D-67141 (Neuhofen, Germany) were hatched in artificial sea water with the salinity concentration of 30 g/L. The cysts were incubated for 48 h at 30 °C. Ten nauplii were transferred into wells of 21-well cultures plates containing artificial sea water (final volume/well: 1 mL). The culture plates were incubated for 48 h at 30 °C; after every 24 h, the number of dead nauplii was counted microscopically. The mortality, expressed in percent, was calculated by using the following Eq. (6):

$$\%\text{Mortality} = \frac{(\text{dead nauplii in test} - \text{dead nauplii in control})}{(\text{dead nauplii in control})} \times 100 \quad (6)$$

Three series of measurements were performed in different days, each comprising four replicate groups of ten nauplii ($n = 4$). Results are expressed as mean ± SD.

2.14. *Preliminary* in vivo *studies*

Preliminary safety and permeation *in vivo* studies of topical administration of BTMA-loaded OA NP was conducted on male Wistar rats, according to Hayashi et al. (1974), with some modifications. The research was conducted in accordance to the internationally accepted principles for laboratory animal use and care as found in Directive 2010/63/EU and the project was approved by the Portuguese Veterinary General Division. Male Wistar rats weighing 350–400 g were obtained from Charles River (Barcelona, Spain). The animals were maintained with food and water *ad libitum* and kept at 22 ± 1 °C with controlled 12 h light/dark cycle at Faculty of Pharmacy, University of Coimbra. The animals were allowed to adapt to the laboratory for 7 days before testing. A selected group of animals ($n = 10$) were studied with topical formulation of Carbopol® 940 gel, prepared as described previously (Gomes et al., 2013), and incorporating 0.05% (w/w) BTMA-loaded NP, following the concentration of conventional topical formulations with free BTMA (dose equivalent). The topical formulation was characterized in terms of aspect, pH and apparent viscosity (at 100 rpm, spindle n.°6, $\tau = 90\%$) by using a DV-I+ Viscometer (Brookfield Engineering Labs. Inc., Middleboro, MA, USA). BTMA-loaded NP formulation was applied to the dorsal surface of the rats (500 mg formulation/ animal), by gently rubbing the formulation 50 times with the index finger for each treatment. The presence of BTMA in serum was measured at 0, 16, 24, 32, 40 and 48 h, after considering the time period and the results for the amount of drug released obtained in the *in vitro* release studies and according to previous studies, that demonstrated a maximum peak in plasma for BTMA at approximately 1.5 h (i.m., s.d.) and $T_{1/2}$ around 12 h (Salem and Najib, 2012). Serum samples (300 μL) were treated and the drug extracted from the serum according to Goyal et al. (2008). BTMA extracted from serum was determined by HPLC described in Section 2.5.

2.15. *Statistical methodology*

Results were expressed as mean ± SD. The significance of differences was assessed using paired sample *T*-test for mean comparisons between the physicochemical parameters of the formulation control for the stability assay and One-Way ANOVA for multiple comparisons between different systems, for the same concentration, in case of *in vitro* cytotoxicity. A 0.05 significance level was adopted for every test.

Table 1
Physicochemical characterization of BTMA-loaded OA NP, empty core NP (no oleic acid) and empty OA NP (without the drug). A comparison is made between a direct and an indirect method for determination of drug encapsulation. Results are expressed as mean of measurements on independent nanoparticle batches ±SD, expect for polydispersity index (PI), (only means are expressed, $n = 3$).

Systems	Size (nm)	PI	Zeta potential (mV)	pH	Direct method (EE, %)	Indirect method (EE, %)
BTMA-loaded OA NP	306.5 ± 15.3	0.244	−7.9 ± 9.5	4.3 ± 0.2	85.9 ± 10.3	96.8 ± 1.9
Core NP	335.5 ± 48.7	0.192	−13.5 ± 9.6	7.1 ± 0.3	–	–
Empty OA NP	328.2 ± 17.2	0.190	−5.3 ± 1.3	3.7 ± 0.1	–	–

3. Results and discussion

3.1. Nanoparticle characterization and drug encapsulation efficiency

Nanoparticles (NP) were formulated consisting of a hydrophobic poly-ε-caprolactone–stearic acid core, containing the hydrophobic drug betamethasone-21-acetate, followed by the formation of a hydrophobic shell of oleic acid (OA). It was anticipated that the combination of a synthetic polymer and fatty acid core, in combination with a fatty acid shell would enable long term controlled release of the drug when applied as a topical dressing, and at the same time facilitate tissue absorption of the drug when released from the formulation. Characterization of the NP consisted in the determination of size, surface charge, drug loading, and rate of drug release.

Physicochemical characterization is an important aspect of determining the basic structure and behavior of the NP. The mean size and other physicochemical characteristics of the NP are presented in Table 1. Fig. 2 illustrates the differential volume size distribution of BTMA-loaded OA NP and empty NP (core NP and OA-coated NP). Mean diameter of the BTMA-loaded OA NP was 307 nm, but slightly larger diameters were observed for empty NP, and empty NP lacking the oleic acid outer shell (i.e., core NP). The presence of drug or of the oleic acid outer shell did not appear to have an important effect on diameter. For all nanoparticle formulations, PI was kept at a value of 0.2, demonstrating that the suspensions were monodisperse. Zeta potential of the nanoparticles presented in Table 1, show a surface charge of −7.9 mV for BTMA-loaded OA NP. A similar charge was observed for NP lacking drug, while nanoparticles lacking both shell and drug material had a much more strongly negative surface potential, to −13 mV. This may be due to the fact that the oleic acid shell masks the strongly negative charge associated with the polycaprolatone (PCL) making up the core material (Shah et al., 2012). Thus, nanoparticles lacking the shell material better reflected the negative charge of the main core polymer. Also, differences in pH were observed between the various formulations. For example, the pH for the formulation suspension of the BTMA-loaded OA NP was 4.6, and slightly less in the absence of shell material at pH 3.7, while nanoparticle cores lacking drug showed a higher pH of 7.1.

Encapsulation efficiency was high, measured at either 86 or 97%, depending on whether the drug was measured in the supernatant of the formulation suspension (direct method), or measured following rupture of nanoparticles and measurement of released drug (indirect method), respectively. The actual drug loading can be obtained from the encapsulation efficiencies. A value of 3.3% on a mass basis was calculated based on the encapsulation efficiency determined using the direct method. Following formulation, empty and BTMA-loaded OA NP were weighed, showing mass of 209 ± 42 and 215 ± 45 mg, respectively. This represents an overall yield of essentially 100% for both formulations, based on the mass of components used to make up the nanoparticle suspensions.

3.2. Nanoparticle morphology

The morphology of drug loaded and empty nanoparticles, containing the shell material, are illustrated in Fig. 3. It may be seen that empty OA NP showed a spherical shape and a smooth surface (Fig. 3A and B), while BTMA-loaded OA NP exhibited a rough surface (Fig. 3C and D), which may suggest the presence of some drug at the nanoparticle surface. After one month following preparation, a significant amount of the drug was released and the degradation of the NP structure was visible (Fig. 3E and F). For empty nanoparticles in presence of shell material, the Ostwald ripening phenomenon was also visible (Fig. 3E), as small particles tended to form larger aggregates, to reach a stable thermodynamic state over time (Sharma et al., 2011).

3.3. Drug release studies and drug degradation

After production, BTMA-loaded NP were freeze-dried and dispersed into phosphate buffer solution pH 5.5. At appropriate time intervals, aliquots of supernatant were collected and BTMA quantified by HPLC. The drug release profile of BTMA-loaded OA NP is presented in Fig. 4. BTMA-loaded OA NP supported the release of BTMA for one month, with an initial burst after the first 10 h (around 50% of BTMA release), followed by a controlled phase (around 75% release until 72 h) and finally, a slow release stage until the end of the one month period. Similarly, in a previous study conducted by Rafienia et al. (2007), a long-term release of BTMA from polymeric implants made of PLGA was also described to have a three-phase discharge profile in phosphate buffer solution (pH 7.4, 37 °C), defined as: burst phase (I), controlled

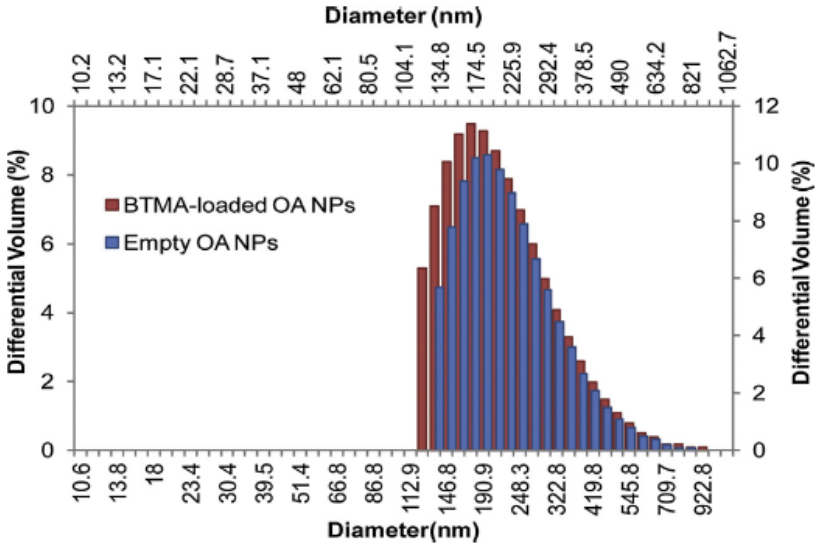

Fig. 2. Size distribution, as volume, of empty and BTMA-loaded OA NP ($n = 3$, for each sample), obtained after measurement of concentrated aqueous nanoparticle suspensions with a Coulter Nano-sizer Delsa™ Nano C.

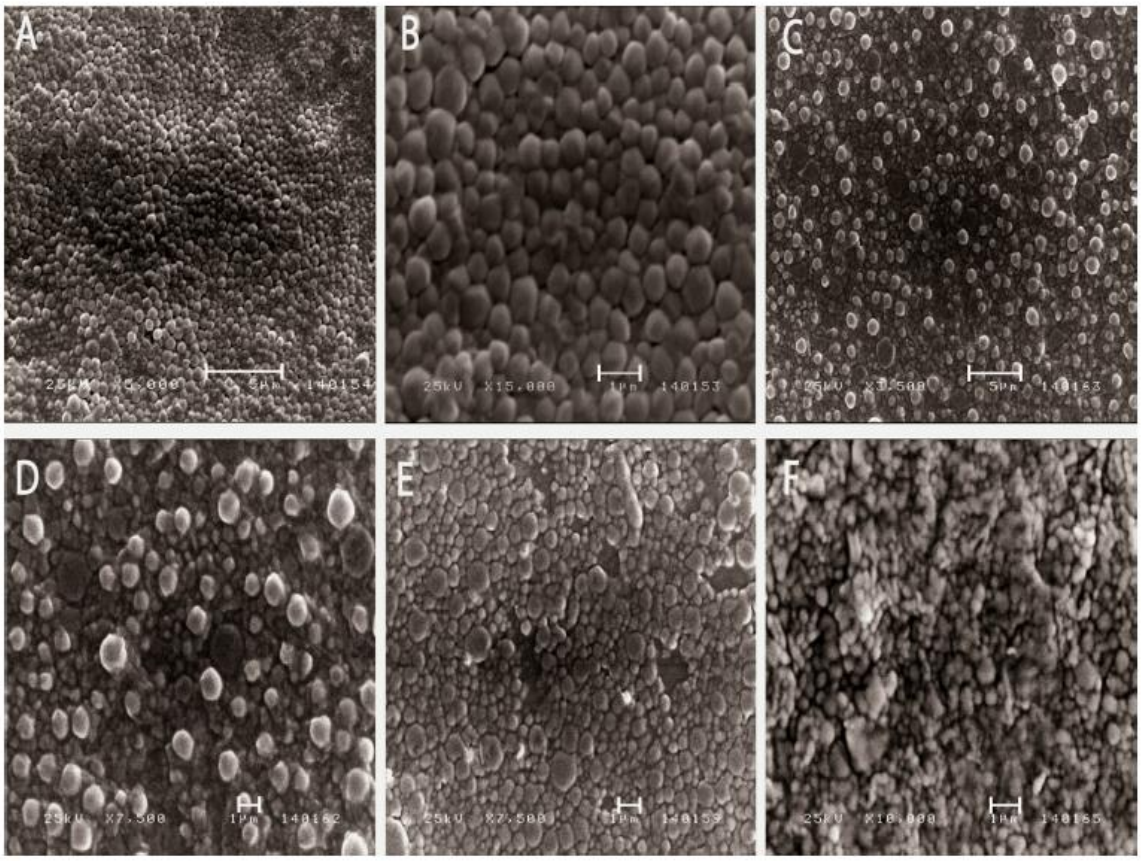

Fig. 3. SEM micrographs of freshly prepared nanoparticles: (A), (B), empty OA NP. (C), (D), BTMA-loaded OA NP. Nanoparticles after one month of preparation: (E), empty OA NP. (F), BTMA-loaded OA NP. Scale bars: 1 μm, except for A and C, which scale is 5 μm.

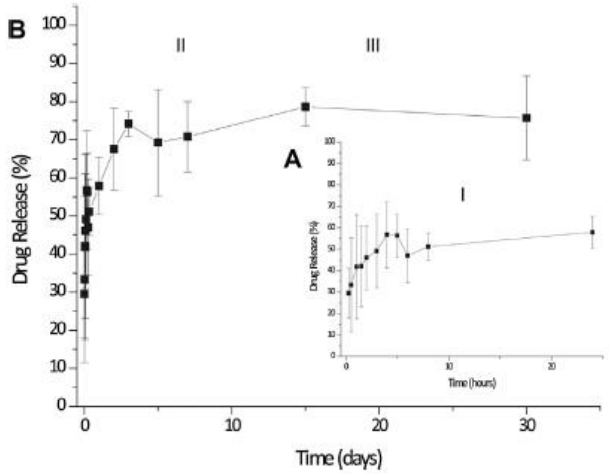

Fig. 4. *In vitro* drug release of BTMA-loaded OA NP for: (A) 24 h and (B) one month, in phosphate buffer pH 5.5 solution. Triple-phase release profile is observed: burst phase (I), controlled phase (II) and depletion phase (III). Results are expressed as mean of measurements of three independent nanoparticle batches ±SD ($n = 3$).

phase (II) and depletion phase (III) where the drug was fully released after 20 days. Comparably, our OA NP improved the release profile of BTMA, achieving a more controllable and linear drug release with after the initial burst release. Polycaprolactone degrades at a slower rate so it can be a more suitable polymer for topical delivery to control of the drug permeation into the skin. Another advantage in our studies is that, at a pH 5.5, the depot effect of NP after topical application onto the skin surface is also better mimicked (Knor et al., 2011).

BTMA degradation into betamethasone during the release study was also evaluated by TLC and HPLC. The degradation of BTMA in the supernatant (i.e., in direct contact with the phosphate buffer solution pH 5.5) was compared with the BTMA encapsulated inside the nanoparticles. After one month of release, the BTMA-loaded OA NP were destroyed and the remaining BTMA inside the nanoparticles was quantified. The chromatograms of both BTMA in the supernatant (Fig. 5A) and inside the OA NP (Fig. 5B) show that almost no betamethasone (less than 9% of BTMA degradation into betamethasone) is formed while BTMA is entrapped inside the nanoparticles, during the one month. Therefore, after the release period, BTMA could still be quantified inside the NP. Since BTMA shows a less polar nature than betamethasone, as betamethasone appears first with a retention time of 3 min, while BTMA appears only at 5 min, the retention and protection of the drug by the NP may have hindered the contact of BTMA with the aqueous solution medium, avoiding greater degradation.

3.4. Stability of nanoparticles over time

The stability of the empty OA NP and BTMA-loaded OA NP was evaluated under different ambient conditions: three months at room temperature (25 ± 5 °C, RT) and 60% of residual humidity, and six months at 4 ± 2 °C (refrigeration conditions, RC) and 70% of residual humidity. Mean size, polydispersity index (PI), zeta

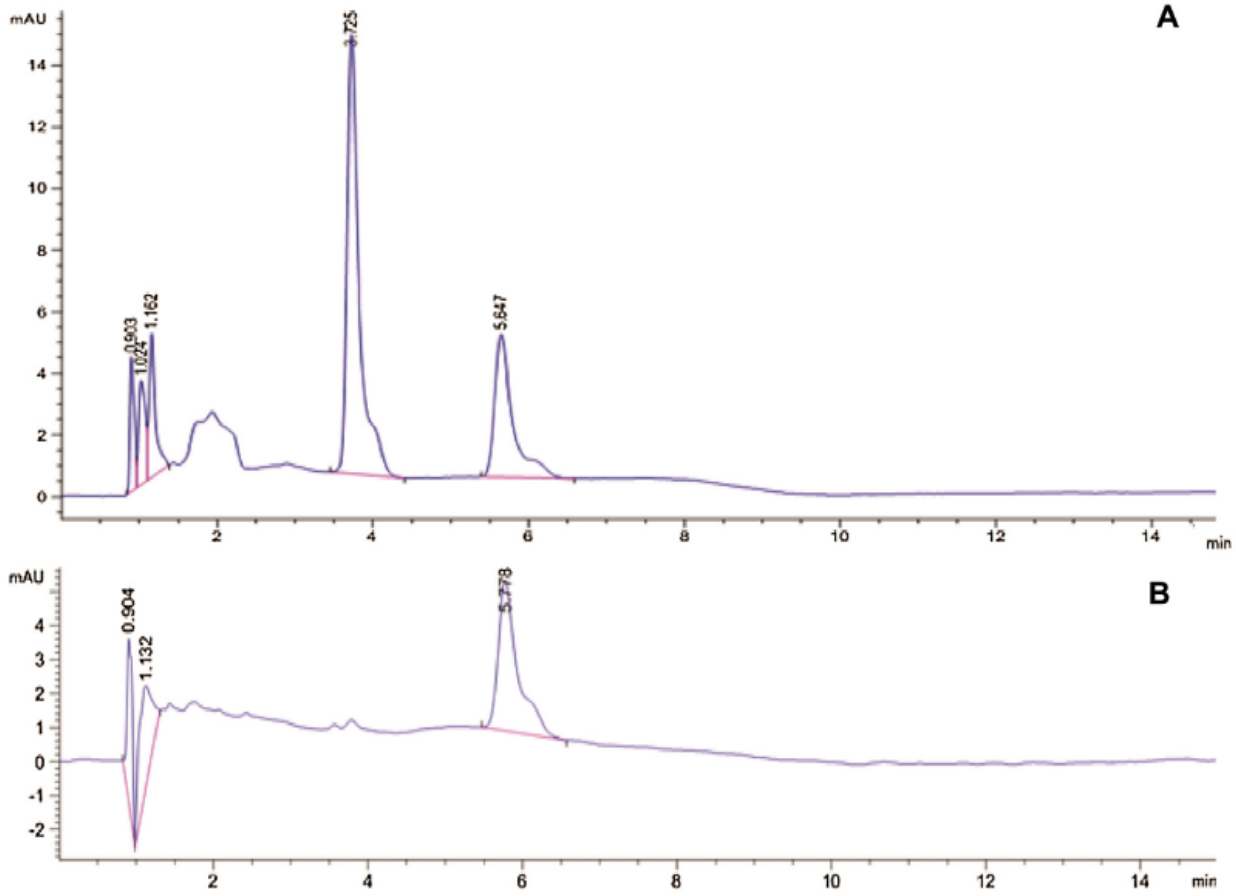

Fig. 5. BTMA conversion into betamethasone conducted after one month *in vitro* BTMA-loaded OA NP release assay in phosphate buffer pH 5.5 solution, compared with the free drug: (A) chromatogram for BTMA present in the supernatant: betamethasone appears at 3.725 min, and BTMA at 5.647 min, (B) chromatogram for BTMA extracted from BTMA-loaded OA NP: BTMA appears at 5.778 min, but no betamethasone signal is detected.

potential and pH were measured and results are presented in Fig. 6. Over 75 days, at room temperature, empty OA NP and drug loaded NP show an increase in the mean size of 35 nm and 50 nm, respectively (Fig. 6A). Since nanoparticles were stored as aqueous suspensions, swelling of the polymeric core of empty nanoparticles may occur, as the water molecules permeate though the porous structure of poly-ε-caprolactone (Pohlmann et al., 2013). After six months, at 4 ± 2 °C, empty OA NP increase 40 nm in the mean size, while BTMA-loaded OA NP showed a slight decrease of 10 nm in the mean size (Fig. 6A). The polydispersity index (PI) varied between 0.15 and 0.25 for both empty and loaded nanoparticles stored at 4 ± 2 °C, while the nanoparticles stored at room temperature showed a PI variation between 0.35 and 0.45 (Fig. 6B). The pH of all formulations varied from 3 to 5, over the three months in case of nanoparticles stored at room temperature and six months for the nanoparticles stored at 4 ± 2 °C (Fig. 6C). Zeta potential also varied with time, starting from lower negative values to higher ones, probably as a result of the coating with OA and loss from the NP over time, exposing the PCL-SA core (Fig. 6D).

Another key issue is the stability of the drug to light. Betamethasone and its ester derivatives have been investigated as photochemical degradable substances (Görög 2011; Takács et al., 1991). In the current study, drug stability was followed by TLC and HPLC, showing that OA NP can protect BTMA from degradation by exposure to UV and visible light (data not shown). The introduction of PCL nanoparticles as delivery systems of BTMA improves the stability, reducing the formation of photoproducts.

3.5. Interactions between drug and nanoparticles

Regarding the complexity of the nanoparticles developed in this work, it was important to study the interactions between all the three components that make the nanoparticles, namely: the core (composed of poly-ε-caprolactone and stearic acid), the coating (oleic acid) and the drug (BTMA and its main degradation/hydrolysis product, betamethasone). The spectra obtained with fourier transform infrared spectroscopy (FTIR), representing all the components of the nanoparticles, are shown in Fig. 7 (Panels A and B).

In Panel A, the presence of the shell material (i.e, oleic acid, OA) on the surface of the nanoparticles was confirmed by FTIR analysis (Fig. 7). The OA coating was confirmed by the bands IR (KBr) ν: 2926, 2855 cm^{-1}, respectively for the asymmetric CH_2 stretch and the symmetric CH_2 stretch, which show a shift for 2925/2927 cm^{-1} and 2856 cm^{-1}, when associated with the NP, as described previously for the adsorption of oleic acid onto the surface of NP (Zhang et al., 2006). Also in our work and, as referenced in the literature, the peak for 1710 cm^{-1} disappeared in the spectrum of OA NP and two peaks appeared between 1300 and 1450 cm^{-1}, indicating the presence of carboxylic acid salts, probably formed by adsorption at the surface of NP (Inoue et al., 2004 Zhang et al., 2006). This may indicate that the lipid on the surface of OA NP is not exclusively influenced by ionic strength, but may also result in desorption over time. Further, the addition of another coating material adhering to OA (such as a polysaccharide or another polymer), could be an alternative to enhance the bridges between

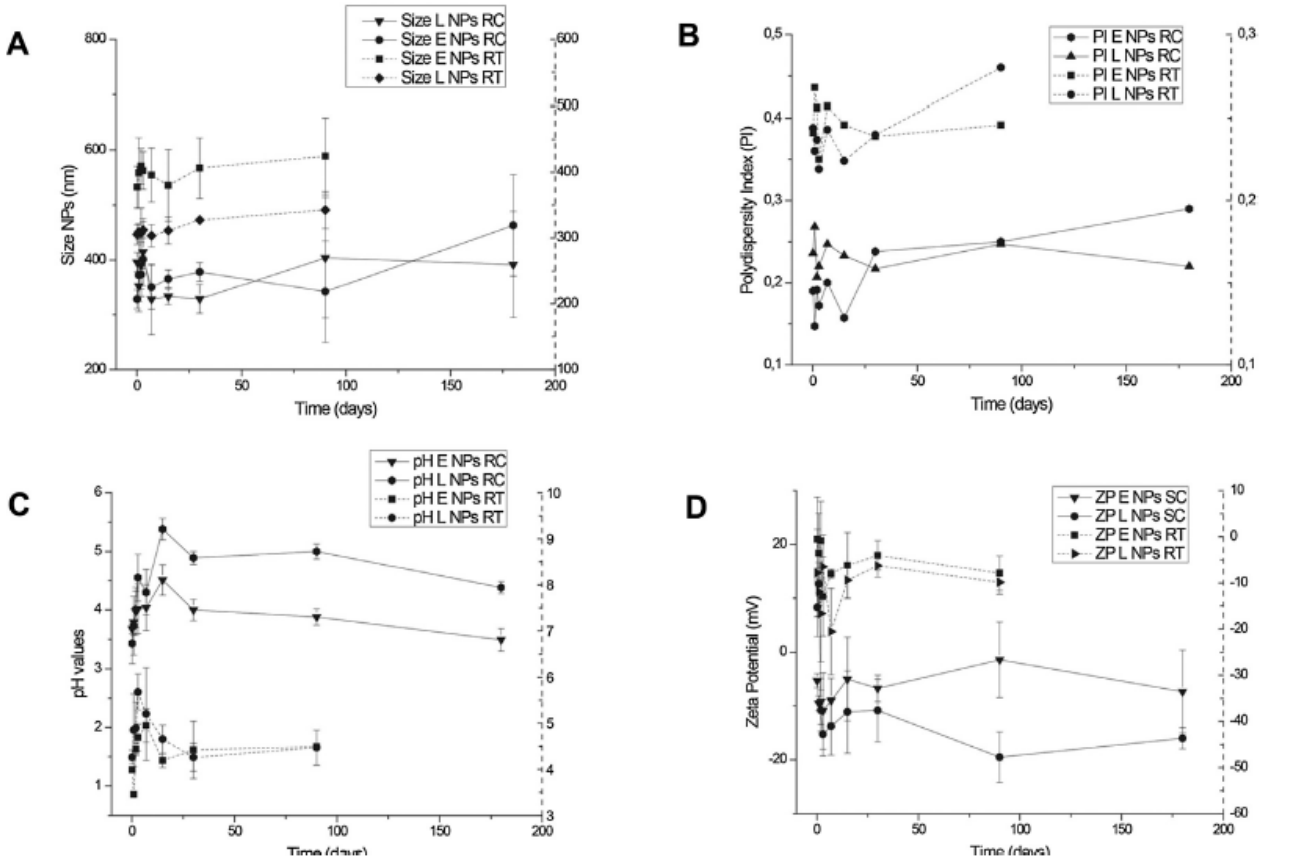

Fig. 6. Nanoparticle physicochemical parameters: (A) size, (B) polydispersity index, PI, (C) pH and (D) zeta potential, ZP, of empty and BTMA-loaded OA NP over three months (90 days) for nanoparticles stored at room temperature (25 ± 5 °C, RT) (dotted line; correspondent *y*-axis with dotted line) and six months (180 days) for nanoparticles stored at a temperature of 4 ± 2 °C and a residual humidity (RH) of 60% (refrigeration conditions, RC) (continuous line; correspondent *y*-axis with continuous line). Results are expressed as mean of measurements of three independent NP batches ±SD ($n = 3$).

NP core and OA coating. Several spectra were performed to evaluate BTMA-loaded OA NP and drug interaction (compared to pure betamethasone, as the degradation product), empty and BTMA-loaded OA NP stability and the presence of betamethasone after one month, the interaction between all components of NP and, finally, between BTMA and empty OA NP (1:1, w/w) in comparison with BTMA-loaded OA NP.

In Panel B, results show that BTMA was incorporated inside the OA NP, mainly by fade of the specific band for the drug at 3404 cm^{-1} that appears in the mixture of empty OA NP and BTMA. Other characteristic bands for BTMA are described as IR (KBr) ν: 2955 cm^{-1}, 2936 cm^{-1}, 1723 cm^{-1}, 1656 cm^{-1}, 1604 cm^{-1}, 1405 cm^{-1}, 1262 cm^{-1}, 1123 cm^{-1}, 1047 cm^{-1}, 891 cm^{-1} (Attia Shafie and Mohammed Fayek, 2013). The peaks between 1400 and 1000 cm^{-1}, which are associated with hydrogen bonding between drug and polymer, tend to disappear, after drug encapsulation. When comparing the spectra for free drug (BTMA) and physical mixture of drug and empty OA NP (Fig. 8, Panel B), the bands between 1400 and 1000 cm^{-1} are visible in both cases. Empty OA NP + BTMA (1:1, w/w) showed both specific bands for BTMA (IR (KBr) ν 3404 cm^{-1}, 1657 cm^{-1}, 1605 cm^{-1}, and 1047 cm^{-1}) and for NP (IR (KBr) ν 1726 cm^{-1} and 1187 cm^{-1}). Specific band for polycaprolactone (1730 cm^{-1} for C=O stretching) was visible for every sample with nanoparticles, varying from 1326 to 1327 cm^{-1}, which may indicate a carbonyl bond interaction site (Verma et al., 2006). This was the main visible band for the nanoparticles, since polycaprolactone is the more abundant compound. In addition, when comparing the spectra of the raw polycaprolactone and the empty OA NP (mainly composed of polycaprolactone), it seems that the polymer may have changed its linear structure to another conformation when the NP were formed. Other specific bands for polycaprolactone are IR (KBr) ν: 1296 cm^{-1} (C—O, CC stretching in crystalline phase), 1106 cm^{-1} (C—O stretching), 1046 cm^{-1} (CC stretching), 732 cm^{-1} (CH_2 rocking) (Verma et al., 2006). After one month, the signal of the empty NP appears the same and it was not possible to distinguish betamethasone characteristic peaks (IR (KBr) ν 3448 cm^{-1}, 2936 cm^{-1}, 1710 cm^{-1}, 1661 cm^{-1}, 1615 cm^{-1}, 1453 cm^{-1}, 1371 cm^{-1}, 1296 cm^{-1}, 1248 cm^{-1}, 1054 cm^{-1}, 1045 cm^{-1}), as a consequence of gradual degradation of the drug after release from the NP. Some residual BTMA was still inside the OA NP after one month preparation, which is shown by the presence of drug specific bands with less intensity between 1400 and 1000 cm^{-1}. Finally, characteristic peaks for SA are IR (KBr) ν: 2915 cm^{-1}, 2849 cm^{-1}, 2655 cm^{-1}, 1702 cm^{-1}, 1464 cm^{-1}, 1298 cm^{-1}, ~900 cm^{-1}, 719 cm^{-1} (Inoue et al., 2004). However, we could not observe clearly the formation of these bands, which may indicate that the lipid (presented in lower concentrations than the other compounds, such as polycaprolactone or oleic acid) is entrapped inside the NP, as desired for drug encapsulation enhancement.

3.6. Thermal stability of nanoparticles

Differential scanning calorimetry (DSC) was conducted to analyze the thermal transformations of the free drug in comparison to when it is encapsulated in or is part of an association (i.e., mixture) with the nanoparticles (Fig. 8). BTMA shows three polymorphic forms (II, Iα and Iβ) and a hydrate with an

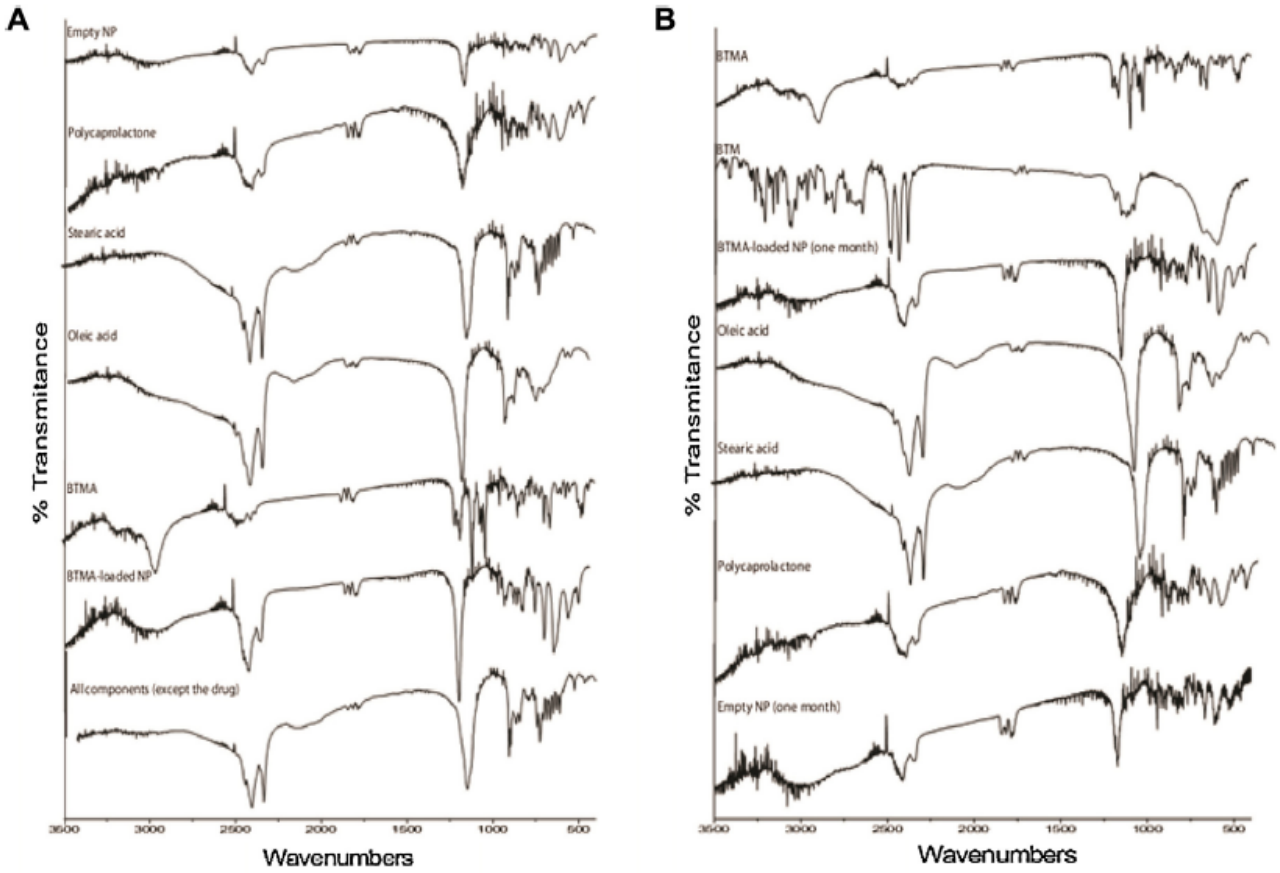

Fig. 7. FTIR spectra at 3500–400 cm^{-1} for the following samples: in Panel A, fresh empty OA NP were compared with raw polymer (poly-ε-caprolactone) and fatty acids (stearic acid and oleic acid), and free BTMA was compared with fresh BTMA-loaded OA NP, as well as a physical mixture of raw components (i.e., poly-ε-caprolactone, stearic acid, oleic acid at 1:1:1, w/w) of the nanoparticle formulation (except the drug); in Panel B, free BTMA was compared with BTM and one-month old BTMA-loaded OA NP and the raw polymer (poly-ε-caprolactone) and fatty acids (stearic acid and oleic acid) was compared with one-month old empty OA NP.

enantiotropic relationship, which means these polymorphisms can revert their state (Ke et al., 2005). Transformation and energy states of polymorphic forms under different stress conditions (e.g., heating) has already been studied for this drug (Ke et al., 2005). Forms II, Iα and Iβ are described to have a melting point at 150–156 °C, 210–212 °C and 222–224 °C, respectively (Ke et al., 2005). In our studies, BTMA showed a T_m around 228 °C (Fig. 8). At higher temperatures, BTMA Iβ form is the most hydrodynamically stable form, while BTMA form II (i.e., the crystalline form) is the most active (Perrier et al., 1981). In Fig. 8, we can observe that BTMA form II appears with a T_m around 150–160 °C; however, the formation of this transition is immediately followed by an exothermic peak at 170 °C, due to BTMA re-crystallization. A complete different behavior is observed for BTMA-loaded OA NP. Stearic acid (SA) acts as a lipid carrier, entrapping the drug inside the lipid solid matrix, avoiding drug crystallization (Chen et al., 2001; Hu et al., 2005). For the BTMA-loaded OA NP, the fatty acid seems to have avoided the crystallization of BTMA, as the peaks for BTMA crystallization are no longer visible and the drug appears to be inside the core when compared to a physical mixture of empty nanoparticles and BTMA. Therefore, SA may create a less ordered modification to the OA NP, promoting drug entrapment.

3.7. In vitro *permeation studies*

Parallel artificial membrane permeability assay (PAMPA) recreates drug passive transport and helps to predict permeability characteristics of the free drug compared to the drug encapsulated into nanoparticles. Most PAMPA studies present permeability assays for short periods (<8 h) (Markovic et al., 2012). However, we have prolonged these assays for 24 h to understand if there were changes in BTMA behavior, especially when entrapped into the OA NP. In Table 2 are the expressed results of the PAMPA study including: drug retention (R), permeation parameter ($C_A(t)/C_D(0)$), permeability coefficients (log P_e) and degradation percentage in acceptor/ donor compartments.

After penetrating the skin epidermis, in general, steroids pass through an enzymatic transformation into inactive substances (Abidi et al., 2012). On the other hand, we observed in this study that OA NP influenced the drug retention (R, %) but also may protect the BTMA from degradation (BTMA to betamethasone), when in contact with the phosphate buffer pH 5.5 solution in the acceptor compartment. Higher retention (R, %) associated with a small value for permeation parameters are characteristic of C_{21} esters, as their hydrophobicity increased; also, they show log permeability coefficients below −6.0, indicating affinity for the hydrophobic membrane (Markovic et al., 2012). In spite of this, our small nanoparticles (around 300 nm) easily permeate through artificial membrane especially when associated with permeation enhancers, such as oleic acid, and they may make use of other pathways and capabilities of the skin structure, such as hair follicles and skin ducts (Zhang et al., 2013). Another reason of the high permeability of BTMA when associated to NP would be by exchange of lipids between the NP and the epidermis, resulting in

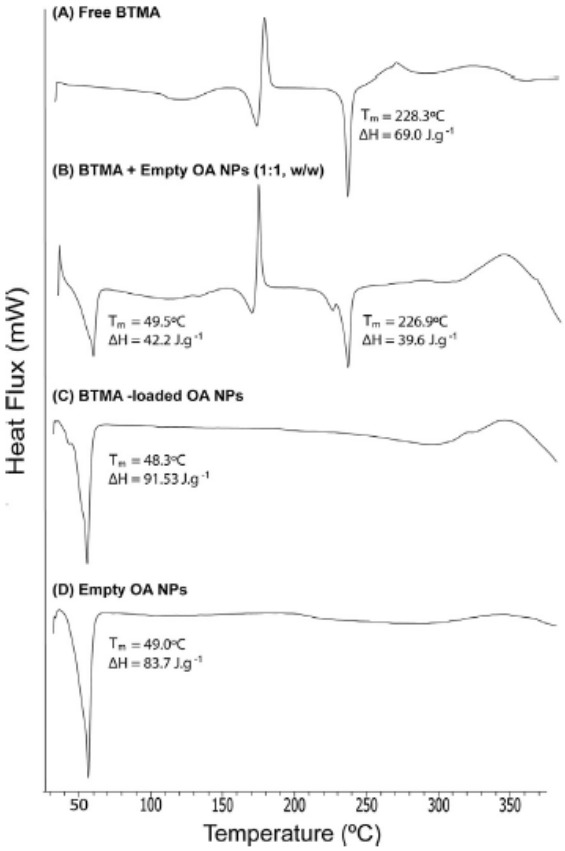

Fig. 8. DSC thermal transformations for: (A) free BTMA, (B) free BTMA and empty OA NP (1:1, w/w), (C) BTMA-loaded OA NP and (D) Empty OA NP. Experiments were conducted with a temperature range from 25 to 375 °C, at a heating rate of 10 °C/min. The number of thermal transitions, the melting point (T_m, °C) and difference in Gibbs energy (ΔH, $J g^{-1}$), for each sample, are also represented.

greater permeation by disruption of the *stratum corneum* barrier (Lin et al., 2013). Fatty acids, mainly long-chain unsaturated ones like oleic acid, were previously described as vital for epidermis differentiation and permeation enhancement (Lin and Khnykin, 2014; Naik et al., 1995). Thus, this overall permeation enhancement seems possible through the association of fatty acids and the depot capacity of the core polycaprolactone. Those nanoparticles may also work as reservoirs on superficial skin layers like other previous works (Campbell et al., 2012) mainly due to the slow release characteristics of polycaprolactone. The low value of degradation percentage of BTMA-loaded OA NP shows the stability enhancement of the NP over 24 h period when BTMA is encapsulated inside the NP core and not on the shell surface of NP. This fact can potentially improve the patient compliance during the treatment with BTMA for dermatological diseases, decreasing the number of applications of the dosage form on the skin.

3.8. Toxicity assays

Cytotoxicity assays were conducted in human keratinocytes cell line (HaCaT) and in yeast *S. cerevisiae* model in order to verify their behavior in biologic unicellular systems. *A. salina* was selected as a multicellular invertebrate model also for the toxicity evaluation. We believe that the comparison between different models for toxicity evaluation of NP can be a simple and useful tool for predicting the experimental conditions for *in vivo* testing.

Firstly, for the HaCaT model, MTT assays were conducted. In terms of the cytotoxicity profiles, BTMA showed an IC_{50} = 168.8 μg/mL and BTMA-loaded nanoparticles showed an IC_{50} = 14.5 μg/mL (Fig. 9). Empty nanoparticles also demonstrated a concentration-dependent toxic effect on human keratinocytes HaCaT cell line (IC_{50} = 18.0 μg/mL). DMSO 5% (v/v) was used as positive control and decreased cell viability to 9.28 ± 0.91% (data not shown). Results for BTMA IC_{50} values were in accordance with the expected and described in the literature for other derivatives (Zulfakar et al., 2012). For the same concentration of BTMA (50 μg/mL), there were significant statistical differences ($p < 0.05$), as expected, between the free drug and both empty and BTMA-loaded OA NP. Although nanoparticles' concentration was below 1 mg/mL, the decrease in cell viability observed with NP was probably related with an occlusive effect of our nanoparticles (ranging size of 300 nm) on the keratinocytes. This occlusive effect of nanosystems has been investigated (Doktorovova et al., 2014) but the cytotoxicity profiles for nanosystems are not yet well understood. It seems that particle size is an important issue in cell cytotoxicity although there is no clear relationship established. A recent review demonstrate that lipidic NP with a size range between 200 and 300 nm and within a concentration range similar to ours (10–100 μg/mL) show lowest viability values (Doktorovova et al., 2014). Another influencing factor of cell viability can be related to the NP composition. Our excipients are environmental friendly and biocompatible. As an example, we used OA as permeation enhancer and as shell material for NP. As previously reported, metallic nanoparticles coated with different fatty acids, including OA, showed lower cytotoxicity in macrophages, lower reactive oxygen species (ROS) formation and higher uptake (Jebali et al., 2014). Moreover, OA is widely used for production of nanoparticles for topical delivery, as it further demonstrates to increase drug accumulation and absorption *in vivo*, without causing irritation to the viable skin (Gupta and Vyas, 2012; Verma et al., 2014).

In the *S. cerevisiae* model, the assays with free BTMA showed a concentration dependent inhibitory effect on the yeast proliferation rate. BTMA-loaded OA NP had a greater inhibitory effect on the yeast cell proliferation rate than the unloaded ones (Table 3). In addition, cytotoxicity testing of NP on the *S. cerevisiae* model was also limited by the amount of particles in suspension due to their strong contribution to the background absorption at 525 nm, conducting at the later growth phase to absorptions higher than 0.9. The results showed a direct relationship between BTMA concentrations and the magnitude of cytotoxic effects. The concentration-effect relationship can be also due to the presence of similar mammalian GC receptors in yeast (Popovic et al., 2010).

Table 2
Parallel artificial membrane permeability assay (PAMPA) permeation studies: permeation parameters ($C_A(t)/C_D(0)$), retention factors (R), permeability coefficients (log P_e) and degradation (%) in acceptor/ donor compartments for free BTMA, empty OA NP + free BTMA (1:1, w/w) and BTMA-loaded OA NP. Results are expressed as mean ± SD (n = 5 except for empty OA NP + free BTMA (1:1, w/w) with n = 3 for retention, R%).

Systems	$C_A(t)/C_D(0)$ (%)	R (%)	log P_e (cm/s)	Degradation in acceptor and donor compartments (%)
Free BTMA	5.4 ± 7.4	69.8 ± 9.8	−7.1 ± 0.8	78.0 ± 25.4
BTMA-loaded OA NP	9.6 ± 8.4	56.0 ± 14.6	−6.5 ± 0.6	34.5 ± 14.5
Empty OA NP + free BTMA (1:1, w/w)	5.4 ± 4.3	14.2 ± 4.3	−6.7 ± 0.4	39.5 ± 16.8

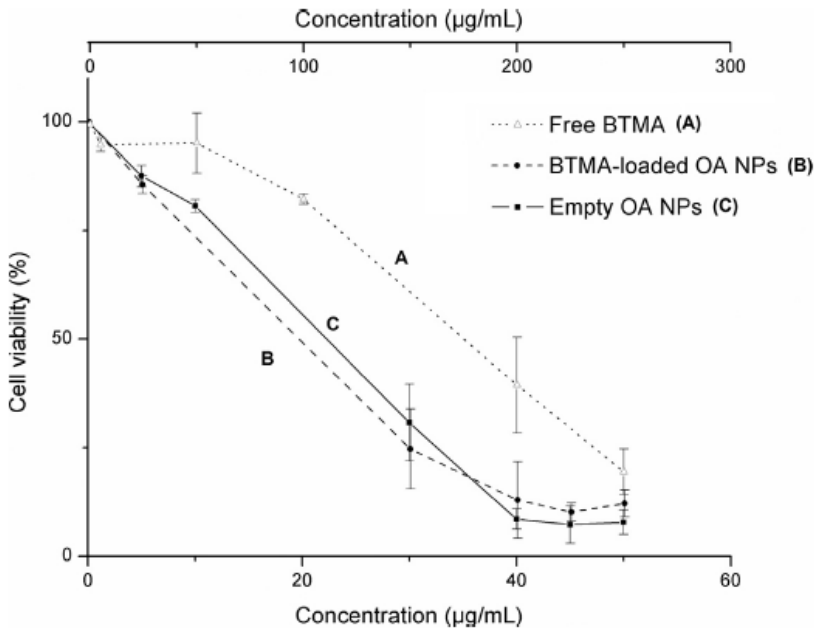

Fig. 9. Cytotoxic effect of (A) free BTMA, (B) BTMA-loaded OA NP and (C) empty OA NP on the viability of human keratinocytes HaCaT evaluated by the MTT assay. Results are expressed as percentages of the untreated control cultures (mean ± SD; $n = 3$).

Table 3
Growth inhibition (%) of *Saccharomyces cerevisiae* exposed to the test systems: free BTMA, BTMA-loaded OA NP and empty OA NP. Results are expressed as mean ± SD ($n = 4$), for three independent assays. All tested concentrations exhibit a cellular growth inhibitory effect that is statistically significant ($P < 0.05$).

Systems	Concentrations (μg/mL)	Growth inhibition (%)
Free BTMA	5	8 ± 3.8
	25	21 ± 4.4
	50	31 ± 2.3
	100	92 ± 5.6
BTMA-loaded OA NP	2	12 ± 6.0
	4	31 ± 5.3
Empty OA NP	4	10 ± 6.5

However, further studies on the toxicity mechanisms are needed to clarify how BTMA exerts the inhibitory effect observed on the growth proliferation rate. The tested concentration of empty OA NP inhibited the growth rate almost as much as the lower concentration of the BTMA-loaded OA NP did. Corresponding concentrations of BTMA in the loaded OA NP were more than ten times lower than the concentrations of free BTMA tested, and reduced *S. cerevisiae* cell proliferation rate at the same extent.

Finally, a higher mortality of *A. salina* was observed with the exposure to BTMA-loaded OA NP than the one with empty OA NP or free BTMA (Table 4). Other studies with some steroidal compounds (mainly progesterone derivatives) have suggested that their cytotoxic effects on *A. salina* may be related with the presence of more complex aromatic rings than progesterone (Fan et al., 2013a,b).

3.9. *Preliminary* in vivo *studies*

Preliminary safety and permeation *in vivo* studies were conducted in Wistar rats by applying BTMA-loaded OA NP incorporated in a Carbopol® 940 gel. Carbopol® gel was used in this study in order to keep the semisolid formulations containing the BTMA-loaded OA NP and the free BTMA, in a specific skin area, like suggested in previous studies (Bonacucina et al., 2004; Bregni et al., 2008). In addition, the use of this gel is also justified mainly due to its mucoadhesive and rheological properties of Carbopol® gels. After incorporation of the NP, the gel became white in color, odorless, with some solid aggregates that were easily homogenized with a spatula. The pH of the final formulation was 6 and the apparent viscosity was around 2500 mPa. No inflammatory skin reaction was observed in the Wistar rats 48 h after application of the gel containing the BTMA-loaded NP. HPLC analysis of the plasma samples showed that BTMA (and betamethasone by natural hydrolysis after entering blood circulation), could be detected after 48 h in contrast to free BTMA or non-encapsulated (not detectable in all samples). In this case, we obtained a retention time of 1.5 min and 3.2–3.4 min for betamethasone and BTMA, respectively (Fig. 10). Although these preliminary results need

Table 4
Mortality (%) of *A. salina*, when exposed to different concentrations of test systems for 24 h and 48 h: free BTMA, BTMA-loaded OA NP and empty OA NP. Results are expressed as mean ± D, for four replicate groups of ten nauplii ($n = 4$).

Systems	Concentrations (μg/mL)	Mortality after 24 h (%)	Mortality after 48 h (%)
Free BTMA	50	8 ± 5.0	40 ± 27.1
	100	73 ± 20.6	73 ± 20.6
BTMA-loaded OA NP	2	78 ± 33.0	95 ± 10.0
	4	100 ± 0.0	100 ± 0.0
Empty OA NP	4	15 ± 5.8	65 ± 33.2

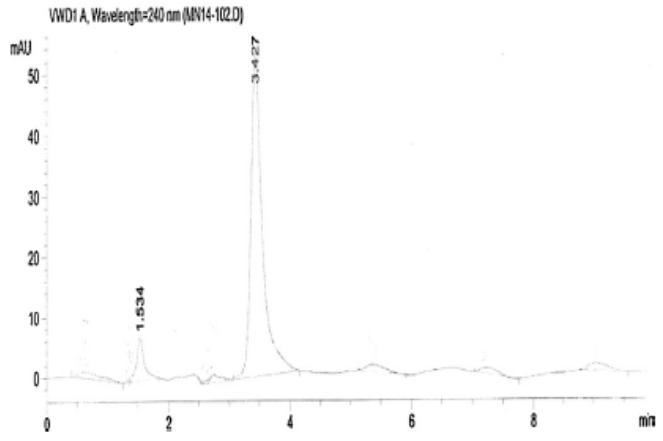

Fig. 10. Chromatogram for BTMA obtained by HPLC. Retention times were determined at 3.246 min (peak area: 196 mAU) for sample after BTMA extraction from plasma, 48 h after application of BTMA-loaded OA NP gel, and 3.427 min (peak area: 796 mAU) for free BTMA standard solution with a concentration of 20 μg/mL.

corroboration, they indicate that our formulation is capable of permeating the skin but more *in vivo* studies will be conducted, respecting the 3R's (replacement, refinement and reduction) for animal research and the project directives.

4. Conclusion

In this study, we reported the development and evaluation of oleic acid (OA) coated NP as transdermal delivery systems. For the manufacture, we selected different materials, like lipids and well-known polymers, described as biocompatible and accepted for pharmaceutical applications. The association of those materials, and their respective properties, confirmed the huge possibilities behind drug delivery and how can we guide therapies to a specific context. Our NP demonstrated to be stable for several months, with and without steroid entrapment, and promoted a long-term drug release. Further, it is also our ambition to manipulate other biomolecules as targeting moieties.

Conflict of interest statement

The authors declare there are no conflicts of interest.

Acknowledgements

The authors would like to thank Hovione FarmaCiência SA for kindly offering us the corticosteroids used in this work and Fundação para a Ciência e Tecnologia (FCT) for the partial financial support under the project reference PTDC/BBB-BMC/0611/2012. Finally, we would like to thank Ph.D. student Filipe Pereira and Professor Marisa Nicolai from CBiOS-ULHT for the help with HPLC studies, Arife Jiyan Baysal from Uppsala University, Fábio Branco and Rita Pereira from Coimbra's University for the help with *in vitro* toxicity studies and *in vivo* studies and Professor Dr. Ronald Neufeld from Queen's University (Ontario, Canada) for his help.

References

Abdel-Mottaleb, M.M.A., et al., 2012. Nanoparticles enhance therapeutic outcome in inflamed skin therapy. Eur. J. Pharm. Biopharm. 82 (1), 151–157.
Abidi, A., et al., 2012. Comparison of reservoir effect of topical corticosteroids in an experimental animal model by histamine-induced wheal suppression test. Indian J. Phamacol. 44 (6), 722–725.
Al Abood, R.M., et al., 2013. Microemulsion as a tool for the transdermal delivery of ondansetron for the treatment of chemotherapy induced nausea and vomiting. Coll. Surf. B: Biointer. 101 (0)), 143–151.
Arica, B., Lamprecht, A., 2005. In vitro evaluation of betamethasone-loaded nanoparticles. Drug Develop. Ind. Pharm. 31 (1), 19–24.
Attia Shafie, M.A., Mohammed Fayek, H.H., 2013. Formulation and evaluation of betamethasone sodium phosphate loaded nanoparticles for ophthalmic delivery. J. Clin. Exphthalmol. Ophthal. 4, 1–11.
Banciu, M., et al., 2006. Anti-angiogenic effects of liposomal prednisolone phosphate on B16 melanoma in mice. J. Control. Release 113 (1), 1–8.
Bennet, D., et al., 2012. Dual drug-loaded nanoparticles on self-integrated scaffold for controlled delivery. Int. J. Nanomed. 7, 3399–3419.
Bonacucina, G., Martelli, S., Palmieri, G.F., 2004. Rheological, mucoadhesive and release properties of Carbopol gels in hydrophilic cosolvents. Int. J. Pharm. 282 (1), 115–130.
Bregni, C., et al., 2008. Release study of diclofenac from new carbomer gels. Pak. J. Pharm. Sci. 21 (1), 12–16.
Calvo, P., et al., 1997. Chitosan and chitosan/ethylene oxide-propylene oxide block copolymer nanoparticles as novel carriers for proteins and vaccines. Pharm. Res. 14 (10), 1431–1436.
Campbell, C.S.J., et al., 2012. Objective assessment of nanoparticle disposition in mammalian skin after topical exposure. J. Control. Release 162 (0), 201–207.
Chen, D.-B., et al., 2001. In vitro and in vivo study of two types of long-circulating solid lipid nanoparticles containing paclitaxel. Chem. Pharm. Bull. 49 (11), 1444–1447.
Doktorovova, S., Souto, E.B., Silva, A.M., 2014. Nanotoxicology applied to solid lipid nanoparticles and nanostructured lipid carriers—a systematic review of *in vitro* data. Eur. J. Pharm. Biopharm. 87 (1), 1–18.
Fan, N.-J., et al., 2013a. Synthesis and cytotoxicity of some novel 21E-benzylidene steroidal derivatives. Steroids 78 (9), 874–879.
Fan, N.-J., et al., 2013b. Synthesis and cytotoxic activity of some novel steroidal C-17 pyrazolinyl derivatives. Eur. J. Med. Chem. 69 (0), 182–190.
Ference, J.D., Last, A.R., 2009. Choosing topical corticosteroids. Am. Fam. Physician 79 (2), 135–140.
Gomes, A., et al., 2013. Evaluation of a new topical treatment for acne with azelaic acid-loaded nanoparticles. Microsc. Microanal. 19 (S4), 59–60.
Görög, S., 2011. Advances in the analysis of steroid hormone drugs in pharmaceuticals and environmental samples (2004–2010). J. Pharm. Biomed. Anal. 55 (4), 728–743.
Goyal, N., et al., 2008. Simultaneous determination of dexamethasone, dexamethasone 21-acetate, and paclitaxel in a simulated biological matrix by RP-HPLC: assay development and validation. J. Liq. Chrom. Rel. Technol. 31 (10), 1478–1491.
Gupta, M., Vyas, S.P., 2012. Development, characterization and *in vivo* assessment of effective lipidic nanoparticles for dermal delivery of fluconazole against cutaneous candidiasis. Chem. Phys. Lipids 165 (4), 454–461.
Hayashi, S., Sakaguchi, T., Ozawa, O., 1974. Parmacokinetic investigation of 17a-dexoxymethasone (A 41 304) in rats. Chem. Pharm. Bull. 22 (12), 2771–2777.
Herman, A., Herman, A.P., 2015. Essential oils and their constituents as skin penetration enhancer for transdermal drug delivery: a review. J. Pharm. Pharmacol. 67, 473–485.
Hu, F.Q., et al., 2005. Preparation and characterization of stearic acid nanostructured lipid carriers by solvent diffusion method in an aqueous system. Coll. Surf. B: Biointer. 45 (0), 167–173.
Inoue, T., et al., 2004. Solid–liquid phase behavior of binary fatty acid mixtures: 1. Oleic acid/stearic acid and oleic acid/behenic acid mixtures. Chem. Phys. Lipids 127 (2), 143–152.
Jebali, A., Hekmatimoghaddam, S., Kazemi, B., 2014. The cytotoxicity of silver nanoparticles coated with different free fatty acids on the Balb/c macrophages: an *in vitro* study. Drug Chem. Toxicol. 37 (4), 433–439.
Kabasakalian, P., Britt, E., Yudis, M.D., 1966. Solubility or some steroids in water. J. Pharm. Sci. 55 (6), 642.
Ke, X., Ping, Q.N., Shi, H., 2005. Interconversion studies of betamethasone acetate polymorphs. Drug Develop. Ind. Pharm. 31 (8), 813–818.
Knor, T., Meholjić-Fetahović, A., Mehmedagić, A., 2011. Stratum corneum hydration and skin surface pH in patients with atopic dermatitis. Acta Dermatovenerol. Croat. 19 (4), 242–247.
Lebwohl, M.G., et al., 2013. Pathways to managing atopic dermatitis: consensus from the experts. J. Clin. Aesthet. Dermatol. 6 (7) Suppl. S18, S2-S18..
Lee, J.-H., et al., 2003. Polymeric nanoparticle composed of fatty acids and poly (ethylene glycol) as a drug carrier. Int. J. Pharm. 251 (1–2), 23–32.
Lin, M.-H., Khnykin, D., 2014. Fatty acid transporters in skin development, function and disease. BBA Mol. Cell Biol. Lipids 1841 (3), 362–368.
Lin, Y.-K., et al., 2013. Squalene-containing nanostructured lipid carriers promote percutaneous absorption and hair follicle targeting of diphencyprone for treating alopecia areata. Pharm. Res. 30 (2), 435–446.
Markovic, B.D., et al., 2012. A PAMPA assay as fast predictive model of passive human skin permeability of new synthesized corticosteroid C-21 esters. Molecules 17 (1), 480–491.
Naik, A., et al., 1995. Mechanism of oleic acid-induced skin penetration enhancement *in vivo* in humans. J. Control. Release 37 (3), 299–306.
Perrier, R., Chauvet, A., Masse, J., 1981. Etude thermoanalytique de quelques steroides. II. Derives de la cortisone. Thermochim. Acta 44 (0), 189–201.
Petersen, M.C., Nation, R.L., Ashley, J.J., 1980. Simultaneous determination of betamethasone, betamethasone acetate and hydrocortisone in biological fluids

using high-performance liquid chromatography. J. Chromatogr. B. Biomed. Sci. Appl. 183 (2), 131–139.
Pinto Reis, C., et al., 2011. Design and transdermal delivery of indomethacin nanosystem. J. Mater. Sci. Eng. A: Struct. Mater. Prop. Microstr. Process. 1 (4), 531–537.
Pinto Reis, C.P., et al., 2013. Development and evaluation of a novel topical treatment for acne with azelaic acid-loaded nanoparticles. Microsc. Microanal. 19 (5), 1141–1150.
Pohlmann, A.R., et al., 2013. Poly(ε-caprolactone) microcapsules and nanocapsules in drug delivery. Exp. Opin. Drug Deliv. 10 (5), 623–638.
Popovic, N., et al., 2010. Site-specific and dose-dependent effects of glucocorticoid receptor phosphorylation in yeast Saccharomyces cerevisiae. Steroids 75 (6), 457–465.
Rafienia, M., et al., 2007. In vitro evaluation of drug solubility and gamma irradiation on the release of betamethasone under simulated in vivo conditions. J. Bioact. Compat. Polym. 22 (4), 443–459.
Rijo, P., et al., 2014. Antimicrobial plant extracts encapsulated into polymeric beads for potential application on the skin. Polymers 6 (2), 479–490.
Roberto, A., Caetano, P.P., 2005. A high-troughput screening method for general cytotoxicity part I chemical toxcity. Res. Lus. Cienc. Tecnol. Saúde 2 (2), 95–100.
Rosado, C., Silva, C., Reis, C.P., 2012. Hydrocortisone-loaded poly(ε-caprolactone) nanoparticles for atopic dermatitis treatment. Pharm. Develop. Technol. 18 (3), 710–718.
Salem, I.I., Najib, N.M., 2012. Pharmacokinetics of betamethasone after single-dose intramuscular administration of betamethasone phosphate and betamethasone acetate to healthy subjects. Clin. Ther. 34 (1), 214–220.
Shah, P.P., et al., 2012. Skin permeating nanogel for the cutaneous co-delivery of two anti-inflammatory drugs. Biomaterials 33 (5), 1607–1617.
Sharma, V.K., et al., 2011. Solid lipid nanoparticles system: an overview. Int. J. Res. Pharm. Sci. 2 (3), 450–461.
Shen, W.W., et al., 2000. Polymer-supported lipid bilayers on benzophenone-modified substrates. Biomacromolecules 2 (1), 70–79.
Slominski, A., et al., 2013. Steroidogenesis in the skin: implications for local immune functions. J. Steroid Biochem. Mol. Biol. 137 (0), 107–123.
Takács, M., et al., 1991. The light sensitivity of corticosteroids in crystalline form. Pharm. Acta Helv. 66 (5–6), 137–140.
Verma, D., Katti, K., Katti, D., 2006. Experimental investigation of interfaces in hydroxyapatite/polyacrylic acid/polycaprolactone composites using photoacoustic FTIR spectroscopy. J. Biomed. Mater. Res. Part A 77A (1), 59–66.
Verma, S., et al., 2014. Oleic acid vesicles: a new approach for topical delivery of antifungal agent. Artif. Cells Nanomed. Biotechnol. 42 (2), 95–101.
Zhang, J., Smith, E., 2010. Percutaneous permeation of betamethasone 17-valerate incorporated in lipid nanoparticles. J. Pharm. Sci. 100 (3), 896–903.
Zhang, Ling, He, Rong, Gu, Hong-Chen, 2006. Oleic acid coating on the monodisperse magnetite nanoparticles. App. Surf. Sci. 253 (5), 2611–2617.
Zhang, Y., et al., 2012. An improved brine shrimp larvae lethality microwell test method. Toxicol. Mech. Methods 22 (1), 23–30.
Zhang, Z., et al., 2013. Polymeric nanoparticles-based topical delivery systems for the treatment of dermatological diseases. WIREs Nanomed. Nanobiotechnol. 5 (3), 205–218.
Zulfakar, M.H., Ong, C.M.Y., Heard, C.M., 2012. The effects of betamethasone dipropionate and fish oil on HaCaT proliferation and apoptosis. Int. J. Pharm. 434 (0), 399–405.

Article III

Lysozyme Photochemistry as a Function of Temperature. The Protective Effect of Nanoparticles on Lysozyme Photostability.

Catarina Oliveira Silva[1,2], Steffen B. Petersen[3], Catarina Pinto Reis[1,4,*], Patrícia Rijo[1], Jesús Molpeceres[2], Henrik Vorum[5] and Maria Teresa Neves-Petersen[6,*]

[1]CBiOs, Research Center for Biosciences & Health Technologies, Universidade Lusófona, Lisboa, 1749-024, Portugal.
[2]Department of Biomedical Sciences, Faculty of Pharmacy, University of Alcalá, 28871 Alcalá de Henares, Spain.
[3]Medical Photonics Lab, Department of Health Science and Technology, Faculty of Medicine, Aalborg University, Fredrik Bajers vej 7, DK-9220, Aalborg, Denmark.
[4]IBEB, Biophysics and Biomedical Engineering, Faculty of Sciences, University of Lisbon, 1749-016, Lisbon, Portugal.
[5]Department of Ophthalmology, Aalborg University Hospital, Hobrovej 18-22, 9000 Aalborg, Denmark.
[6]Department of Clinical Medicine, Aalborg University Hospital, Hobrovej 18-22, 9000 Aalborg, Denmark.

Corresponding Authors: Prof. Dr. Catarina Pinto Reis and Prof. Dr. Teresa Neves-Petersen.

PLoS One 10(12):e0144454 (2015)

doi: 10.1371/journal.pone.0144454.

PLOS ONE

RESEARCH ARTICLE

Lysozyme Photochemistry as a Function of Temperature. The Protective Effect of Nanoparticles on Lysozyme Photostability

Catarina Oliveira Silva[1,2], Steffen B. Petersen[3], Catarina Pinto Reis[1,4]*, Patrícia Rijo[1], Jesús Molpeceres[2], Henrik Vorum[5], Maria Teresa Neves-Petersen[6]*

1 Research Center for Biosciences & Health Technologies, Universidade Lusófona, Lisboa, 1749–024, Portugal, **2** Department of Biomedical Sciences, Faculty of Pharmacy, University of Alcalá, 28871 Alcalá de Henares, Spain, **3** Medical Photonics Lab, Department of Health Science and Technology, Faculty of Medicine, Aalborg University, Fredrik Bajers vej 7, DK-9220, Aalborg, Denmark, **4** IBEB, Biophysics and Biomedical Engineering, Faculty of Sciences, University of Lisbon, 1749–016, Lisbon, Portugal, **5** Department of Ophthalmology, Aalborg University, Hobrovej 18–22, 9000 Aalborg, Denmark, **6** Department of Clinical Medicine, Aalborg University, Søndre Skovvej 15, 9000 Aalborg, Denmark

* nevespetersen@gmail.com (MTNP); catarinapintoreis@gmail.com (CPR)

OPEN ACCESS

Citation: Oliveira Silva C, Petersen SB, Pinto Reis C, Rijo P, Molpeceres J, Vorum H, et al. (2015) Lysozyme Photochemistry as a Function of Temperature. The Protective Effect of Nanoparticles on Lysozyme Photostability. PLoS ONE 10(12): e0144454. doi:10.1371/journal.pone.0144454

Editor: Jamshidkhan Chamani, Islamic Azad University-Mashhad Branch, Mashhad, Iran, ISLAMIC REPUBLIC OF IRAN

Received: June 9, 2015

Accepted: November 18, 2015

Published: December 14, 2015

Data Availability Statement: All relevant data are within the paper.

Funding: The authors would like to thank Fundação para a Ciência e Tecnologia (FCT) for the financial support under the project reference PTDC/BBB-BMC/0611/2012. The authors acknowledge the funding from the European Commission through the project H2020-644242-SAPHELY. The funders had no role in study design, data collection and analysis, decision to publish, or preparation of the manuscript.

Abstract

The presence of aromatic residues and their close spatial proximity to disulphide bridges makes hen egg white lysozyme labile to UV excitation. UVB induced photo-oxidation of tryptophan and tyrosine residues leads to photochemical products, such as, kynurenine, N–formylkynurenine and dityrosine and to the disruption of disulphide bridges in proteins. We here report that lysozyme UV induced photochemistry is modulated by temperature, excitation power, illumination time, excitation wavelength and by the presence of plasmonic quencher surfaces, such as gold, and by the presence of natural fluorescence quenchers, such as hyaluronic acid and oleic acid. We show evidence that the photo-oxidation effects triggered by 295 nm at 20°C are reversible and non-reversible at 10°C, 25°C and 30°C. This paper provides evidence that the 295 nm damage threshold of lysozyme lies between 0.1 μW and 0.3 μW. Protein conformational changes induced by temperature and UV light have been detected upon monitoring changes in the fluorescence emission spectra of lysozyme tryptophan residues and SYPRO® Orange. Lysozyme has been conjugated onto gold nanoparticles, coated with hyaluronic acid and oleic acid (HAOA). Steady state and time resolved fluorescence studies of free and conjugated lysozyme onto HAOA gold nanoparticles reveals that the presence of the polymer decreased the rate of the observed photochemical reactions and induced a preference for short fluorescence decay lifetimes. Size and surface charge of the HAOA gold nanoparticles have been determined by dynamic light scattering and zeta potential measurements. TEM analysis of the particles confirms the presence of a gold core surrounded by a HAOA matrix. We conclude that HAOA gold nanoparticles may efficiently protect lysozyme from the photochemical effects of UVB light and this nanocarrier could be potentially applied to other proteins with clinical relevance. In addition, this study confirms that the temperature plays a critical role in the photochemical pathways a protein enters upon UV excitation.

Competing Interests: The authors have declared that no competing interests exist.

Introduction

The fluorescence of aromatic amino acids in proteins can be used to monitor protein conformational changes, to determine the protein's melting temperature, to detect solvent accessibility changes and to unravel the onset of photochemical pathways. Their fluorescence spectral properties can be modulated by solvent polarity (tryptophan in particular) and by the presence of fluorescence quenchers. Spectral shifts are monitored in order to probe, e.g., for protein-receptor binding, protein-protein dimerization and protein-metal binding [1]. Extrinsic fluorescence probes such as SYPRO® Orange and 8-Anilinonaphthalene-1-sulfonic acid (ANS) can also reveal protein conformation changes induced by, e.g., ligand binding, temperature, pH and UV light, as their fluorescent emission is enhanced upon binding to hydrophobic regions of the protein [2]. On the other hand, water strongly quenches their fluorescence.

UVB induced photo-oxidation of tryptophan (Trp) and tyrosine (Tyr) residues leads to the formation of photochemical products, such as, kynurenine (Kyn), N—formylkynurenine (NFK), singlet oxygen, 3α-hydroperoxypyrroloindole, 3α-dihydroxypyrroloindole, hydroxyl radicals and dityrosine (DT) [3, 4]. The presence and the kinetics of formation of NFK, Kyn and DT can be monitored by fluorescence spectroscopy (Table 1). Furthermore, UVB induced photo-oxidation of Trp, Tyr and Phenylalanine (Phe) residues leads to electron ejection from their side chains [5]. Such electron can be captured by disulphide (SS) bridges, leading to a transient disulphide electron adduct, and ultimately to the reduction of the SS bridges [5]. Since SS bridges are one of the best quenchers of protein fluorescence, this can lead to a fluorescence emission intensity increase [5, 6, 7]. On the other hand, the conversion of Trp and Tyr into their photoproducts leads to a decrease of the original fluorescence emission intensity [8]. Different photochemical pathways will lead to an increase or a decrease of the protein's fluorescence emission intensity. The triggered pathways will depend on, e.g., the excitation wavelength, the irradiance level (power per unit area) and the temperature [9], leading lead to reversible [8] or irreversible changes [10].

Hen egg white lysozyme (LYZ) is a small size (129 amino acids) monomeric catalytic enzyme displaying 4 SS, 6 Trp and 3 Tyr residues (see Fig 1). LYZ structural changes induced by temperature, UVB light, pH and ionic strength haves been previously reported [2, 9–12]. LYZ is described to show a two-stage denaturation induced by temperature and a melting temperature ranging from 52°C to 77°C, depending on pH [10, 13]. The studies done by Neves-Petersen et al. confirmed that UVB excitation of aromatic residues leads to the disruption of SS bridges. Such disruption leads to changes in the proteins fluorescence emission intensity and to the formation of photo products of Trp and Tyr residues [5, 6, 8, 14, 15].

There is an interest in protecting proteins from photo damage, since some of these proteins might be used as biosensors, drugs or simply as enzymes. Protein photochemistry can be modulated by the presence of plasmonic surfaces such as gold [16, 17] and by the presence of fluorescence quenchers such as hyaluronic acid (HA, [18]) and oleic acid (OA, [19]). HA is reported to be a very good fluorescence quencher, as well as to confer structural stability to proteins [20]. LYZ has a high isoelectric point (pI) value around 11.1 [21]. This allows for LYZ binding onto

Table 1. Absorption and fluorescence spectral characteristics of N-formylkynurenine (NFK), dityrosine (DT) and kynurenine (Kyn), according to the literature [25–27].

Photo degradation product	Absorption (nm)	Fluorescence emission (nm)
NFK: N-formylkynurenine	261, 322	400–440
DT: Dityrosine	284, 316	400–409
Kyn: Kynurenine	258, 360	434–480

doi:10.1371/journal.pone.0144454.t001

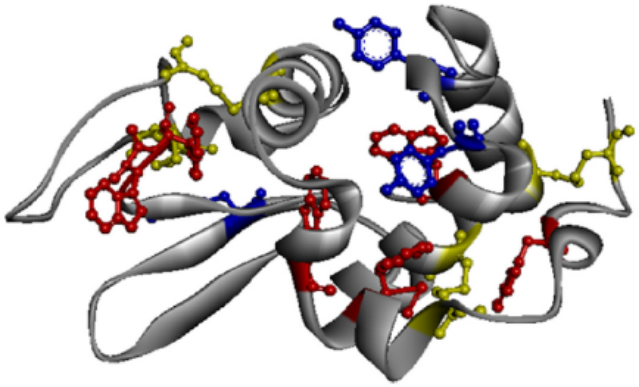

Fig 1. LYZ molecular structure, according to (2LYZ.pdb). Aromatic residues are represented by different colors: Trp (red), Tyr (blue), Cys (yellow).

doi:10.1371/journal.pone.0144454.g001

the surface of negative charged multifunctional gold nanoparticles via electrostatic attractive interactions (at pH < pI), putatively protecting it from UVB induced photochemistry.

In this study we have monitored the time dependent effect of continuous 295 nm excitation of LYZ on the protein's fluorescence emission intensity, as a function of irradiance level, temperature and excitation wavelength. The kinetics of such processes are analysed and compared. The reversibility of the light induced pathways is observed to be temperature dependent in the chosen temperature range from 10–30°C. Protein conformational changes induced by 295 nm and temperature have been monitored using Trp as an intrinsic molecular probe and SYPRO® Orange as an extrinsic molecular probe. The formation of photoproducts such as NKF and Kyn has been monitored as a function of excitation time. Furthermore, LYZ has been coupled to gold nanoparticles coated with HA and OA. The putative protective effect of the coated gold nanoparticles against photochemistry is investigated. The kinetics and extent of light induced processes and the protein fluorescence lifetimes alone and when coupled to the gold nanoparticles are compared.

Materials and Methods

Materials

Gold (III) chloride trihydrate ($HAuCl_4$) (PubChem ID: 24895143; Product number: G4022), sodium citrate dihydrate ($C_6H_5Na_3O_7$) (PubChem ID: 24901436; Product number: W302600), L-ascorbic acid (L-AA) (PubChem ID: 24891246; Product number: A7506), silver nitrate ($AgNO_3$) (PubChem ID: 24852543; Product number: S0139), hyaluronic acid (HA) sodium salt from *Streptococcus equi* (MW: 7,000–250,000 $g.mol^{-1}$) (PubChem ID: 24878223; Product number: 53747), oleic acid (OA) (MW: 282.46 $g.mol^{-1}$) (PubChem ID: 24886786; Product number: 75090), Lysozyme from hen egg white, in powder form, (LYZ, MW: 14.3 kDa) (Enzyme number:3.2.1.17; Product number: L6876) were all supplied by Sigma-Aldrich (Steinheim, Germany). SYPRO® Orange Protein Gel Stain (5,000X Concentrate in DMSO) was purchased from Life Technologies as the molecular probe for protein conformational studies. The water used for buffer preparation was purified through a Millipore system.

Preparation of LYZ stock solution and LYZ-conjugated gold nanoparticles

A 10 μM (0.15 mg/mL) stock solution of LYZ was prepared in 2 mM Phosphate Buffer Saline (PBS) at pH 7.4. After mixing directly the protein with the buffer, the solution had pH 6.0. In

order to prepare LYZ-conjugated gold nanoparticles, the stock solution of the protein at 10 μM was mixed with the gold nanoparticles solution (0.22 mM) and hyaluronic acid-oleic acid (HAOA) polymer solution at a 1:1:1 (v/v/v, concentration of 1 mg/mL, for each polymer) ratio and allowed to interact for 30 min at room temperature. Gold nanoparticles were prepared using produced by seed-growth method, described elsewhere [22], with some modifications (paper in preparation). The solution was centrifuged twice at 500 g for 20 min in a FV2400 Microspin (BioSan, Riga, Latvia) to remove unbound peptides. The pellet was re-suspended in PBS buffer (pH 7.4). LYZ stock solution was stored at 4–8°C until further use.

LYZ structure analysis and gold nanoparticles structure design

The crystallographic data used for the display of the 3D protein structure (Fig 1) was extracted from (2LYZ.pdb) (structure of hen egg-white lysozyme, [23]) using Discovery Studio 4.1 (Accelrys Software, San Diego, CA, USA). Distances between protein residues were obtained by using the monitor tool in the program to determine the distance between atoms in the 3D structure (see Table 2). As for LYZ-conjugated HAOA gold nanoparticles structural design, Adobe Illustrator CS5 (Adobe Systems Software Ireland Ltd.) was used as the graphic design software.

Steady-state fluorescence spectroscopy studies

Steady-state fluorescence emission spectra were collected upon excitation of the aromatic pool of the protein at 295 nm. Excitation spectra, with a fixed wavelength at 330 nm (or 350 nm, for thermal ramp), were also monitored. All measurements were conducted on a Felix fluorescence RTC 2000 spectrometer (Photon Technology International, Canada, Inc.347 Consortium Court London, Ontario N6E 2S8) with a T-configuration, using a 75-W Xenon arc lamp coupled to a monochromator. The samples were analyzed in a cuvette of 1 cm light path and were magnetically stirred at 200 rpm in order to secure homogeneous excitation. All slits were set to 5 nm.

Thermal unfolding studies and melting point of LYZ. LYZ thermal unfolding studies were conducted in order to determine the melting point of the protein prior to illumination (see Fig 2). The fluorescence emission intensity at 350 nm (exc. 295 nm) of fresh LYZ sample (non-illuminated) was monitor from 45°C to 90°C. The heating rate was fixed at 1°C/min. Excitation slit size was set at 0.1 mm (equivalent lamp power of 0.1 μW). Trp emission is

Table 2. Shortest spatial distances between disulphide bonds and aromatic residues (tryptophan and tyrosine) in LYZ (2LYZ.pdb). The shortest distances (< 12 Å) between atoms of each pair of elements (Trp, Tyr and disulphide bonds) were considered. For Trp and Tyr residues, only one of the atoms belonging to the indole and benzene rings were considered, and for SS bonds one of SG atoms. (W = Trp; Y = Tyr).

Disulphide Bond	Aromatic Residue	Distance (Å)
C30-C115	W123 (CD1)	3.3
	W111(CD1)	5.6
	W23 (CD1)	10.7
	W28 (CD2)	10.2
C6- C127	W123 (CD2)	9.2
C76-C94	W108(CH2)	8.0
	Y20 (CD2)	11.9
	W63 (CH2)	6.6
C64-C80	Y53 (CD2)	4.1
	W62 (CD2)	10.7
	W63 (CD2)	7.7

doi:10.1371/journal.pone.0144454.t002

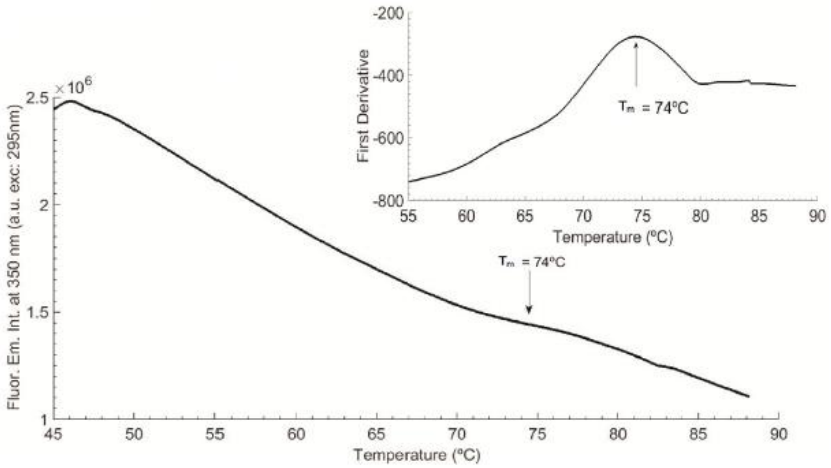

Fig 2. LYZ thermal ramp and data first derivative from 45–90°C (T_m = 74°C), with heating rate fixed at 1°C/min. Fluorescence excitation was fixed at 295 nm and fluorescence emission at 350 nm and excitation slit was set at 0.1 mm (0.1 μW).

doi:10.1371/journal.pone.0144454.g002

usually used as a probe for protein conformational changes and can be used to determine the melting temperature of the protein. First derivative was conducted in Matlab version R2014b (MathWorks, Massachusetts, USA) for calculation of the melting temperature, according to the mid-point value in°C. Fluorescence excitation (em. fixed at 350 nm) and emission (exc. fixed at 295 nm) spectra of LYZ were analysed before and after thermal unfolding and changes in fluorescence intensity were quantified (see Fig 3).

Continuous 295 nm illumination of LYZ. Continuous 295 nm illumination of LYZ (fresh sample, 10 μM) was carried out for 2 hours and the protein's fluorescence emission intensity at 330 nm was monitored (see Fig 4). The excitation slit was set at 0.1 mm, with an equivalent lamp power of 0.1 μW, as in the thermal ramp experiment. The illumination spot was approximately 0.35 cm^2. Irradiance was 0.343 $W.cm^{-2}$. The excitation and emission spectra of LYZ prior and after the 2 hours continuous 295 nm excitation were analyzed (see Fig 5).

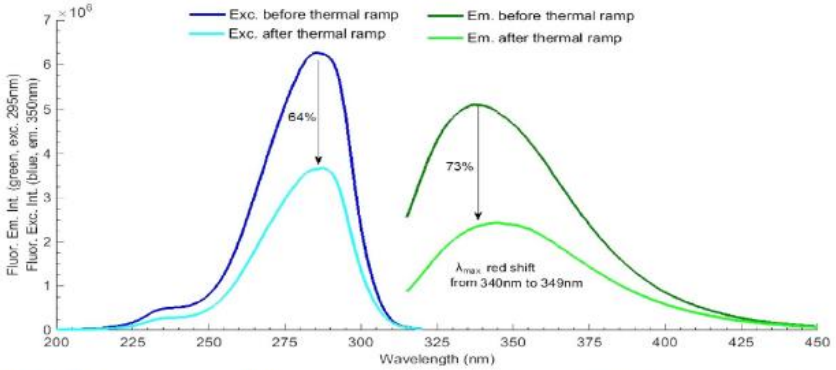

Fig 3. LYZ fluorescence excitation and emission spectra, before and after the thermal ramp at 45–90°C. Fluorescence excitation was fixed at 295 nm and fluorescence emission at 350 nm and excitation slit was set at 0.1 mm (0.1 μW).

doi:10.1371/journal.pone.0144454.g003

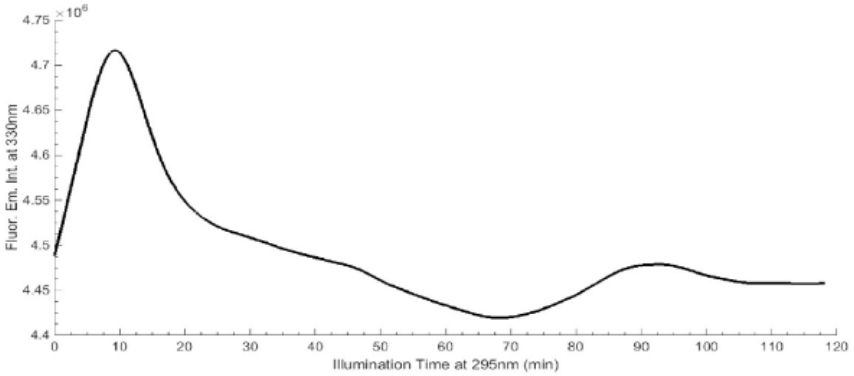

Fig 4. Continuous 295 nm excitation of LYZ at 20°C, for 2 hours. Fluorescence emission at 330 nm and excitation slit was set at 0.1 mm (0.1 μW).

doi:10.1371/journal.pone.0144454.g004

The fluorescence emission intensity of LYZ at 330 nm was monitored upon continuous 2 hours excitation at six selected excitation wavelengths: 250 nm, 265 nm, 285 nm, 295 nm, 305 nm and 310 nm (see Fig 6). The excitation slit was fixed at 0.5 mm, corresponding to a 1.0 μW excitation power. The temperature of the solution was kept at 20°C using a Peltier element at the cuvette holder location. A fresh sample was used for each illumination run. The emission and excitation intensity values obtained were corrected in real-time for oscillations in the intensity of the excitation lamp.

SYPRO® Orange for probing LYZ conformation changes

SYPRO® Orange is used as a molecular probe in order to monitor protein conformational changes, since its fluorescence is greatly enhanced upon contact with hydrophobic environments [24]. A 3μL aliquot (dilution 1:1000) of SYPRO® Orange stock solution (5,000X Concentrate in DMSO) was added to a cuvette containing a fresh sample of LYZ (10 μM, 3 mL) prior to the 295 nm continuous illumination experiment. The sample was gently shaken to mix both solutions. The fluorescence emission spectrum of SYPRO® Orange, with excitation fixed at 470 nm and the fluorescence excitation spectrum of SYPRO® Orange, with emission fixed at 580 nm, were acquired prior and after continuously illuminating LYZ at 295 nm for 70 min.

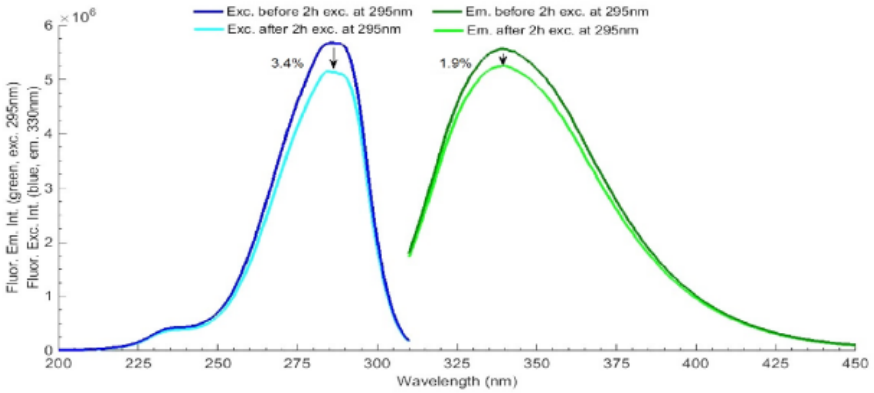

Fig 5. LYZ fluorescence excitation and emission spectra, before and after 295 nm continuous excitation for 2 hours. Fluorescence excitation was fixed at 295 nm and fluorescence emission at 330 nm and excitation slit was set at 0.1 mm (0.1 μW).

doi:10.1371/journal.pone.0144454.g005

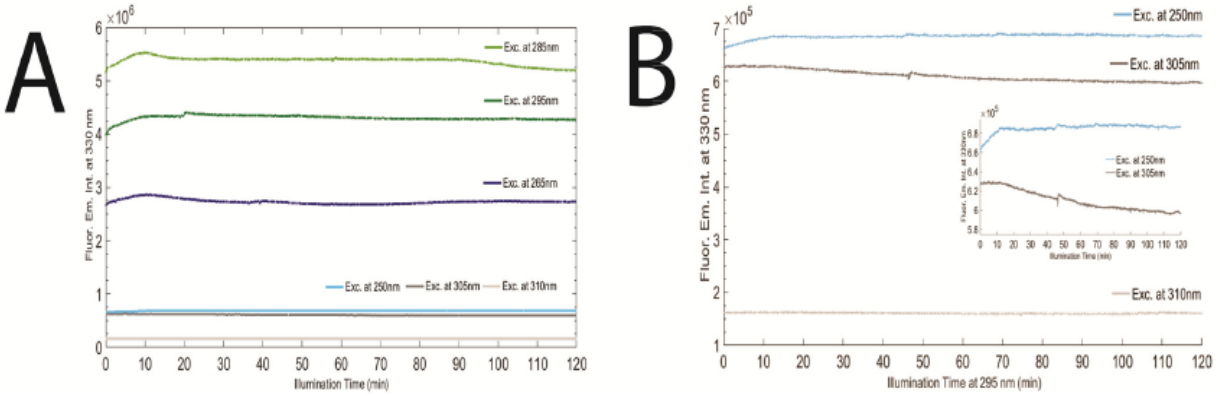

Fig 6. A) LYZ 2 hours excitation from 250 nm until 310 nm, at 20°C. Fluorescence emission wavelength was fixed at 330 nm, while excitation wavelengths were selected as following: at 250 nm (light blue), at 265 nm (dark blue), at 285 nm (light green), at 295 nm (dark green), at 305 nm (dark grey) and at 310 nm (light grey). **B)** Closer look at LYZ 2hours excitation at 250 nm, 305 nm and 310 nm, at 20°C. For all excitation wavelengths, fluorescence emission wavelength was fixed at 330 nm and slit fixed at 0.5 mm (1.0 μW).

doi:10.1371/journal.pone.0144454.g006

Changes in LYZ fluorescence intensity and spectral shifts were quantified. The fluorescence emission intensity of SYPRO® Orange at 580 nm (exc. at 470 nm) was monitored after every ten minutes of LYZ excitation at 295 nm for 70 min (see Fig 7). The excitation slit size was set at 0.5 mm (equivalent power lamp of 1.0 μW). The wavelength corresponding to the maximum fluorescence emission intensity of SYPRO® Orange was monitored in order to detect the occurrence of possible spectral shifts during the illumination of LYZ at 295 nm (see Table 3).

295 nm excitation power effect on LYZ fluorescence emission. Firstly, the dependence of the excitation slit size versus excitation power was determined by measuring the power level at the cuvette location with a power meter (Ophir Photonics StarLite Meter ASSY ROHS, P/N7Z01565, Jerusalem, Israel), used with a power head (Ophir Photonics, 30A-BB-18 ROHS, P/N7Z02692, Jerusalem, Israel) upon varying the excitation slit size. The effect of 295 nm illumination power on the fluorescence emission intensity at 330 nm of LYZ was acquired using

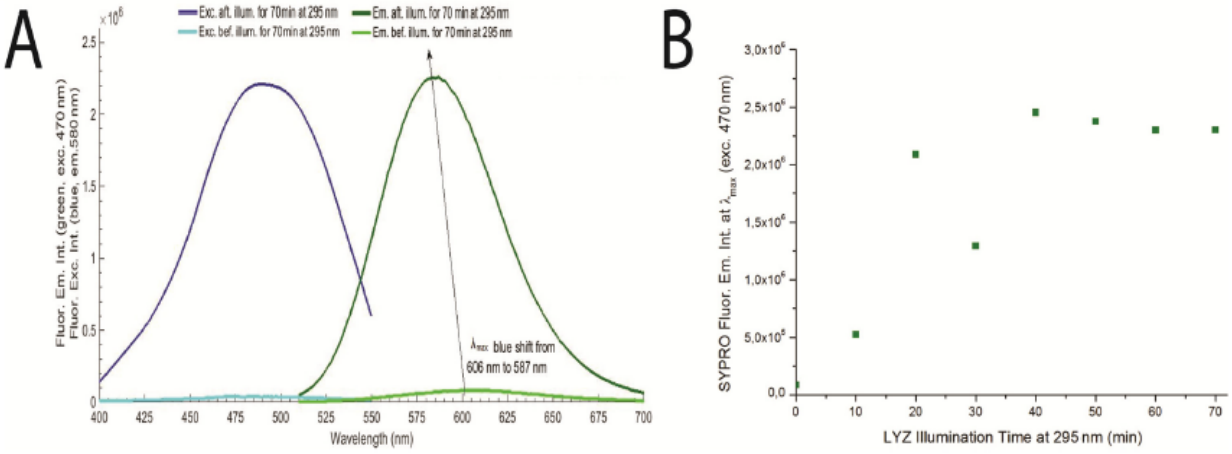

Fig 7. A) Monitoring LYZ with SYPRO® Orange spectra before and after 70 min 295 nm excitation of LYZ at 20°C, with excitation slit fixed at 0.5 mm (1.0 μW). Fluorescence intensity of SYPRO® Orange was fixed at 580 nm and excitation at 470 nm. **B)** SYPRO® Orange emission intensity (excitation wavelength fixed at 470 nm) for every 10 min of LYZ 295 nm excitation for 70 min.

doi:10.1371/journal.pone.0144454.g007

Table 3. Wavelengths corresponding to maximum fluorescence emission intensity of SYPRO® Orange after consecutive 10 min excitation cycles of LYZ at 295 nm.

Time (min)	λ_{max} (nm)	$\Delta(\lambda_{t=0}-\lambda_{t=t})$ (nm)
0	606	0
10	580	26
20	584	22
30	584	22
40	583	23
50	584	22
60	587	19
70	587	19

doi:10.1371/journal.pone.0144454.t003

different excitation slit openings: 0.1 mm, 0.3 mm, 0.4 mm and 0.5 mm corresponding to 0.1 μW, 0.5 μW, 0.7 μW and 1.0 μW, respectively (see Fig 8). The temperature of the solution was kept at 20°C using a Peltier element at the cuvette holder location. A fresh sample was used for each illumination session. Fluorescence excitation (em. fixed at 330 nm) and emission (exc. fixed at 295 nm) spectra of LYZ were acquired before and after LYZ illumination with 0.1 mm and 0.5 mm excitation slit. The fluorescence intensity changes were quantified (see Fig 9).

Temperature effect on LYZ photochemistry. The fluorescence emission intensity of LYZ at 330 nm was monitored upon 295 nm excitation. After 10 min of illumination the shutter was closed for another 10 min, remaining the protein in the dark. This excitation scheme was repeated four times. In total the protein was illuminated for 50 min and remained in the dark during 40 min. This experiment was repeated at four different temperatures: 10°C, 20°C, 25°C and 30°C. Four open/close cycles have been carried out. The excitation slit size was set at 0.5 mm (equivalent power lamp of 1.0 μW). A fresh sample was used for each experiment (see Fig 10).

SYPRO® Orange was used in order to monitor putative LYZ conformational changes due to 295 nm illumination at different temperatures. Fluorescence emission spectra (exc. fixed at

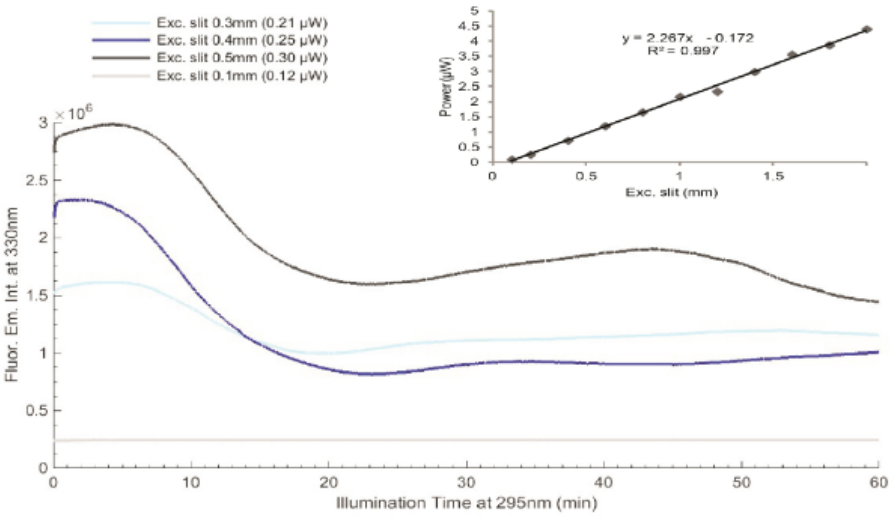

Fig 8. LYZ fluorescence 295 nm 2hours excitation at 20°C, using different excitation slit openings: 0.1 mm (0.1 μW), 0.3 mm (0.5 μW), 0.4 mm (0.7 μW) and 0.5 mm (1.0 μW). Fluorescence emission wavelength was fixed at 330 nm. At the upper corner is displayed the equation of the dependence of the excitation slit size (x) versus excitation power (y).

doi:10.1371/journal.pone.0144454.g008

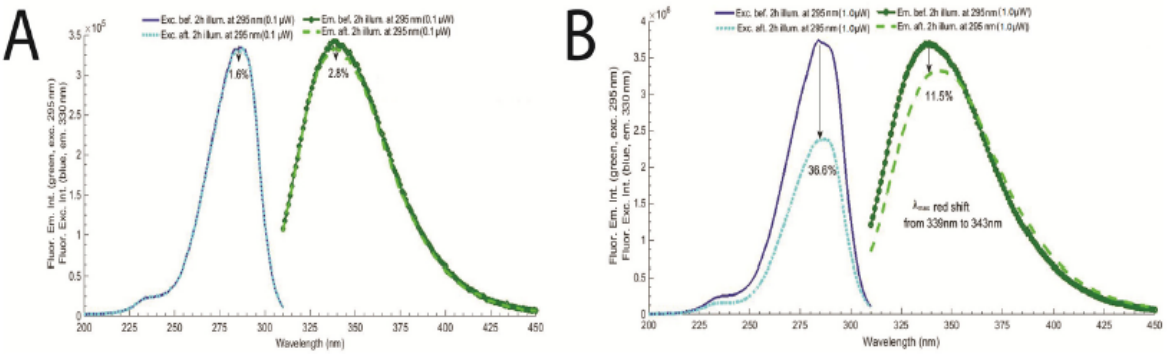

Fig 9. A) LYZ fluorescence excitation and emission spectra before and after LYZ 295 nm 2hours excitation, with slit opening fixed at 0.1 mm (0.1 μW). **B)** LYZ fluorescence excitation and emission spectra before and after LYZ 295 nm 2hours excitation, with slit opening fixed at 0.5 mm (power: 1.0 μW). Fluorescence excitation was fixed at 295 nm and fluorescence emission at 330 nm.

doi:10.1371/journal.pone.0144454.g009

470 nm) were acquired before and after the four open/close cycles (as described above) of 295 nm illumination of LYZ at each temperature (see Fig 11). Afterwards, the reversibility of the light induced processes at 10°C and 20°C were investigated. The fluorescence emission intensity at 330 nm of a four LYZ samples were monitored (exc. at 295 nm): a) fresh, non-illuminated sample, b) LYZ sample after 30 min of continuous 295 nm illumination (0.5mm slit size, with an equivalent power lamp of 0.30 μW), c) LYZ sample after 30 min of continuous 295 nm illumination followed by 48 hours in the dark and, d) LYZ sample after 30 min of continuous 295nm illumination followed by 48 hours in the dark and subsequent further 30 min of continuous 295 nm (see Fig 12).

Photochemistry of LYZ conjugated with HAOA gold nanoparticles. The effect of continuous 295 nm excitation of LYZ has been investigated for LYZ conjugated to gold nanoparticles covered by natural polymers (hyaluronic acid, HA) and oleic acid (OA). Results have been compared with the data obtained with free LYZ (see Fig 13). Four samples have been continuously illuminated with 295 nm light for 2 hours at 20°C and their fluorescence emission intensity at 330 nm had been monitored: a) conjugated LYZ, b) free LYZ, c) plain non-coated gold

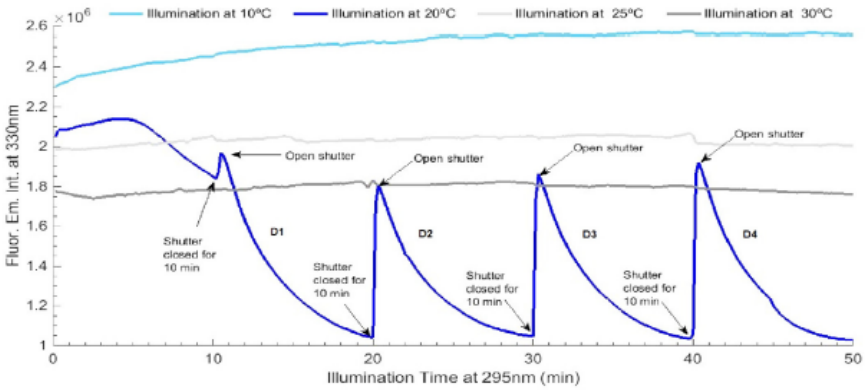

Fig 10. Temperature effect on LYZ photochemistry: at 10°C (light blue), 20°C (dark blue), 25°C (light grey) and 30°C (dark grey), for four open/close cycles of periods of 10 min of excitation followed by 10 min in the dark. Fluorescence excitation and emission wavelengths were fixed at 295 nm and 330 nm, respectively. Excitation slit size was set at 0.5 mm (1.0 μW) for all experiments.

doi:10.1371/journal.pone.0144454.g010

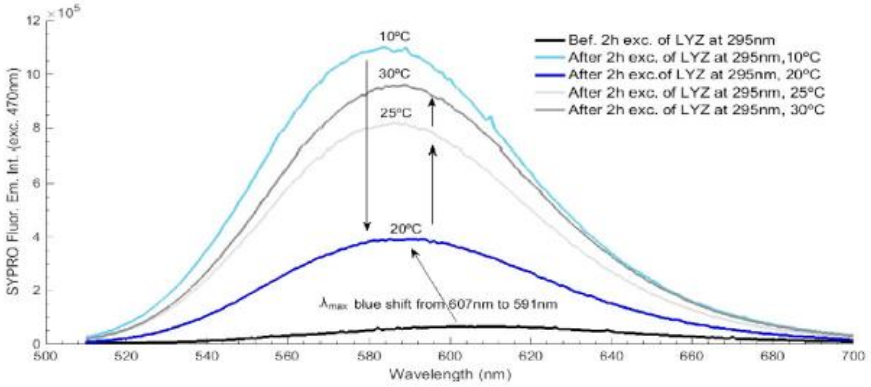

Fig 11. SYPRO® Orange emission intensity spectra before and after LYZ 295 nm excitation at different temperatures (10°C, 20°C, 25°C and 30°C). SYPRO® fluorescence excitation wavelength was fixed at 470 nm and acquired before and after the four open/close cycles. Excitation slit size was set at 0.5 mm (1.0 μW).

doi:10.1371/journal.pone.0144454.g011

nanoparticles and d) HAOA coated gold nanoparticles. The excitation slit was set at 2.0 mm (equivalent power of 4.4 μW at the sample location). The conjugation of LYZ onto the HAOA gold nanoparticles (see Fig 14) has been confirmed using steady state fluorescence spectroscopy. The fluorescence excitation (em. fixed at 330 nm) and emission (exc. fixed at 295 nm) spectra of non-conjugated LYZ, of the supernatant after centrifugation of the solution containing conjugated and non-conjugated LYZ, and of conjugated LYZ onto HAOA gold nanoparticles have been acquired in order to detect the presence of protein (see Fig 15). The formation of Trp photo degradation products upon 295 nm excitation of free LYZ and LYZ-conjugated

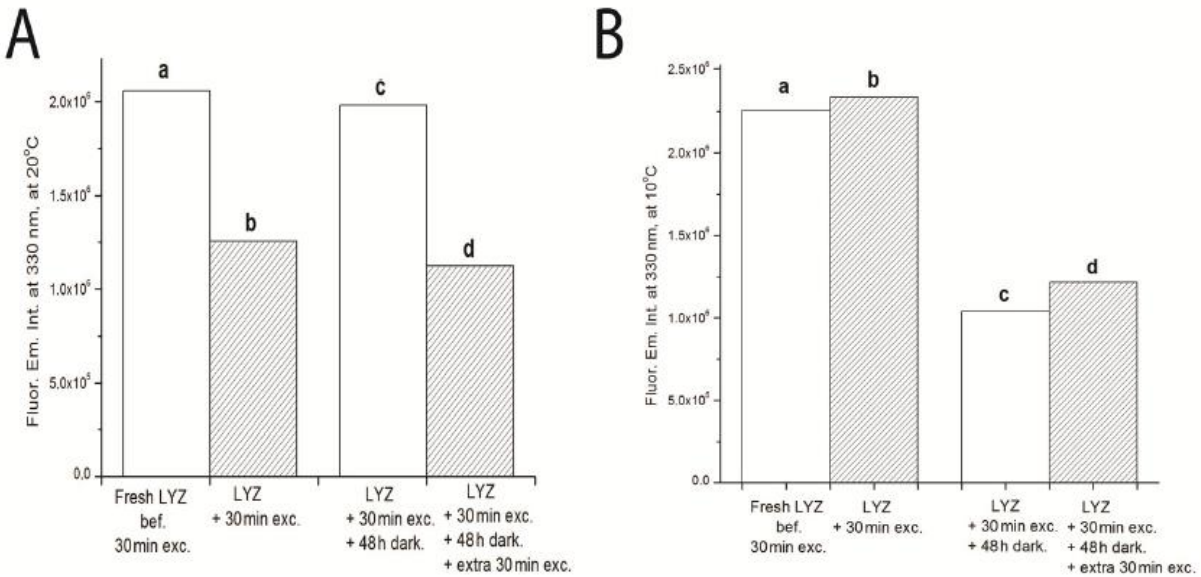

Fig 12. A) LYZ fluorescence emission intensity at 330nm monitored at 20°C; and **B)** at 10°C. Samples are described as: a) fresh LYZ never previously illuminated, b) LYZ after 30 min of continuous 295 nm illumination, c) LYZ after 30 min of continuous 295 nm illumination followed by 48 hours in the dark, d) LYZ after 30 min of continuous 295 nm illumination followed by 48 hours in the dark and subsequent further 30 min of continuous 295 nm. LYZ excitation was fixed at 295 nm with a slit size was set at 0.5 mm (1.0 μW).

doi:10.1371/journal.pone.0144454.g012

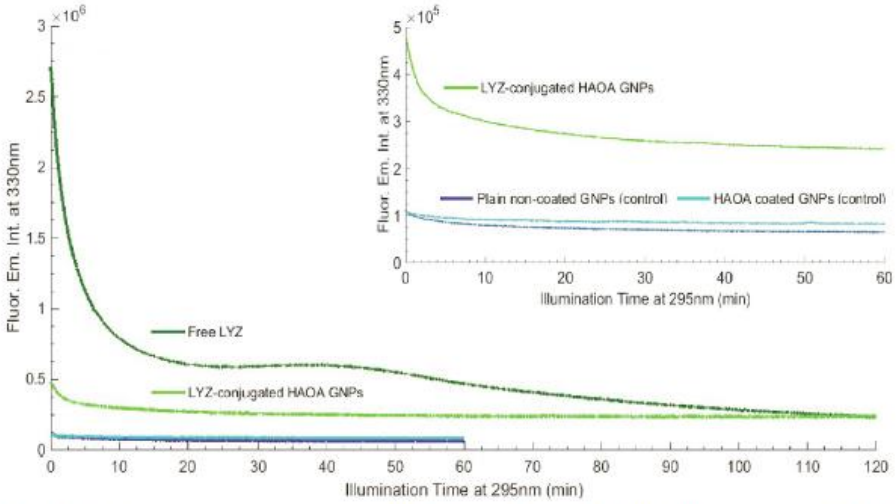

Fig 13. LYZ fluorescence emission intensity at 330 nm for free LYZ (2 h 295 nm excitation), LYZ-conjugated HAOA GNPs (2 h 295 nm excitation), and empty HAOA gold nanoparticles (GNPs) and non-coated plain GNPs (1h 295 nm excitation). All samples were analyzed at 20°C and excitation slit size fixed at 2.0 mm (4.4 μW). At the upper corner, LYZ-conjugated HAOA GNPs excited for 2 hours is compared to HAOA GNPs and plain GNPs.

doi:10.1371/journal.pone.0144454.g013

HAOA gold nanoparticles has been confirmed using steady state fluorescence spectroscopy. In order to verify the formation of DT and NFK, fluorescence emission spectra were acquired upon 320 nm excitation of the solution before and after 2 hours of continuous excitation at 295 nm (see Fig 16A). In order to verify the presence of Kyn, emission spectra were obtained upon 360 nm excitation before and after 295 nm continuous excitation. Fluorescence changes have been quantified and compared for free and conjugated LYZ. A fresh sample was used for each illumination run (see Fig 16B).

Time resolved fluorescence spectroscopy

The fluorescence lifetimes of free and conjugated LYZ have been acquired with fluorescence TCSPC lifetime spectrometer (DeltaPro, Horiba Scientific, Kyoto, Japan). A 280 nm and a 295 nm light emitting diode, <200 picoseconds FWHM with PPD and laser diode Horiba Scientific, Kyoto, Japan) was used to excite the samples. The fluorescence emission intensity at 330 nm was detected at the magic angle (54.7°) by a GaAs detector (Hamamatsu H7422P-40). The temperature of the solution was kept at 20°C using a Peltier element at the cuvette holder

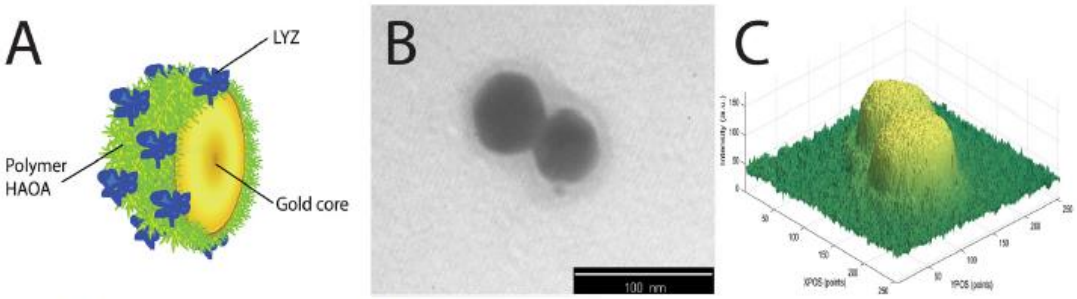

Fig 14. A) Representative illustration of LYZ-conjugated HAOA coated gold nanoparticles; **B)** TEM image of HAOA coated gold nanoparticles (non-conjugated) at scale bar: 100 nm; and **C)** Intensity analysis of the HAOA gold nanoparticles TEM image.

doi:10.1371/journal.pone.0144454.g014

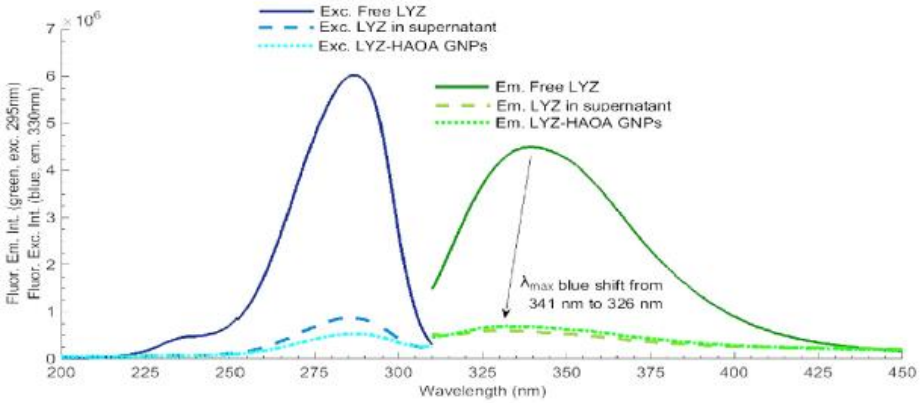

Fig 15. Conjugation effect: LYZ in supernatant (after conjugation) compared with free LYZ and LYZ-conjugated HAOA gold nanoparticles (GNPs). Fluorescence excitation spectra was fixed at 330 nm and fluorescence emission spectra was fixed at 295 nm. Experiments were conducted at 20°C and excitation slit size fixed at 2.0 mm (4.4 μW). LYZ was not continuously excited and only the necessary UV light was used for obtaining the displayed spectra.

doi:10.1371/journal.pone.0144454.g015

location. A fresh sample was used for each illumination run. A 300 nm long-pass filter (Semrock) was used in the emission channel. A solution of Ludox (colloidal silica) in Millipore water was used in order to acquire the instrument response function (IRF). Such response function has been used to deconvolve the protein decay. The decay times (τ) and pre-exponential factors (f_i) recovered from the time resolved intensity decays for free LYZ and LYZ-conjugated HAOA gold nanoparticles at pH 7.4.

HAOA gold nanoparticles physical characterization

The mean particle size, polydispersity index (PI) and zeta potential (ZP) for HAOA gold nanoparticles (non conjugated with LYZ) were also determined with a Coulter Nano-sizer Delsa Nano™C (Fullerton, CA). A low value of PI factor (< 0.25) indicates a more stable and less dispersed nanoparticles distribution in size. "D-value" was determined to describe the particle size distribution of 10%, 50% and 90% of the nanoparticles population.

TEM analysis

HAOA gold nanoparticles structure and surface morphology were analyzed by Transmission Electron Microscopy (TEM, Zeiss M10, Germany). Samples were prepared through "sequential

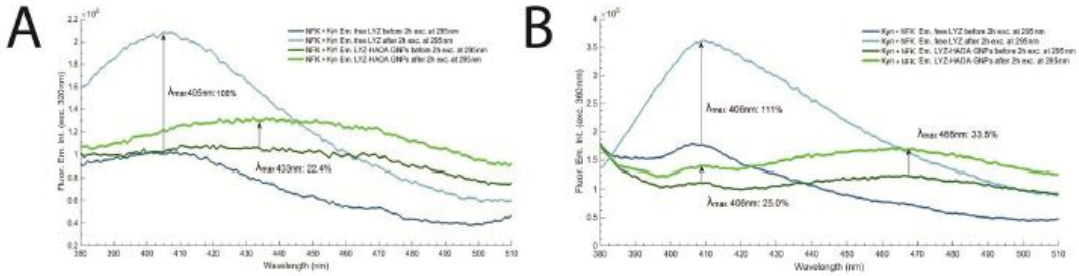

Fig 16. A) Fluorescence emission spectra for NFK + Kyn, before and after excitation of free LYZ and LYZ-conjugated HAOA gold nanoparticles (GNPs), at a fixed wavelength of 320 nm. Experiments were conducted at 20°C and excitation slit size fixed at 2.0 mm (4.4 μW); **B)** Fluorescence emission spectra for Kyn + NFK, before and after excitation of free LYZ and LYZ-conjugated HAOA gold nanoparticles (GNPs), at a fixed wavelength of 360 nm. Experiments were conducted at 20°C and excitation slit size fixed at 2.0 mm (4.4 μW).

doi:10.1371/journal.pone.0144454.g016

two-droplet" method by re-suspending the HAOA gold nanoparticles in distilled water and placing a drop (5–10 μL) of the suspension on to a formvar grid for 30–60 seconds. When the HAOA gold nanoparticles suspension had partly dried, the grid was washed three times with distilled water and the excess of water removed with a filter paper. Then, sodium phosphotungstate (PTA, 2%, w/v) was applied to the grid for 10 seconds, the excess of stain removed with a filter paper and the grid was left to dry at room temperature for 24 hours. Samples were analyzed at an accelerated voltage of 10–20 kV. Different fields of the images were recorded digitally, by using Matlab version R2014b (MathWorks, Massachusetts, USA), for determination of the intensity distribution of polymer HAOA and gold nanoparticles.

Data Analysis

All data analysis, plotting and fitting procedures were done using Origin 8.1 (OriginLab Corporation, Northampton, MA, USA).

Emission Spectra and Excitation Spectra. Emission and excitation spectra were first smoothed using a 10 points adjacent averaging. All fluorescence spectra obtained were first Raman corrected by subtracting the spectra recorded for the buffer in solution. Normalized emission and excitation spectra were obtained by dividing each data point by the maximum intensity value in each spectrum.

Fitting Procedures

LYZ fluorescence emission kinetic traces (em. at 330 nm) upon 295 nm continuous excitation. Each of the four decay curves observed upon 10 min of continuous 295 nm illumination after LYZ has been kept for 10 min in the dark at 20°C (see Fig 10), were fitted using a single exponential decay model given by the function $F(t) = C_1{}^*exp(-x/k_1) + y_0$. $F(t)$ is the fluorescence emission intensity at 330 nm (a.u.) upon 295 nm at excitation time t (min), y_0 and C_1 are constants and k_1 is the rate constant of fluorescence emission intensity decrease (min^{-1}). y_0 value was fixed to 0. The root mean square error R^2 was > 0.99 for all traces. The fitted parameter values and corresponding errors, and root mean square error values obtained after fitting the 330 nm emission kinetic trace are displayed in Table 4.

Free LYZ and LYZ conjugated HAOA gold nanoparticles fluorescence kinetics (em. at 330 nm) upon 295 nm excitation. The fluorescence emission intensity kinetic traces observed for free LYZ, plain non-coated gold nanoparticles, HAOA gold nanoparticles and LYZ-conjugated HAOA gold nanoparticles samples and displayed in Fig 13, after continuous 295 nm illumination for 2 hours, except for plain gold nanoparticles and HAOA gold nanoparticles without LYZ (60 min), at 20°C, were fitted using a double exponential decay model according to the formula $F(t) = y_0+C_1{}^*exp(-k_1{}^*x)+C_2{}^*exp(-k_2{}^*x)$. $F(t)$ is the fluorescence emission intensity at 330 nm (a.u.) upon 295 nm excitation at time t (min), y_0, C_1 and C_2 are

Table 4. Single exponential fit using model $F(t) = C_1{}^*exp(-x/k_1) + y_0$ for each decay curve of LYZ at 20°C (D1, D2, D3 and D4; *D* stands for decay) (see Fig 10). Fit parameters are displayed in this table. Red. χ^2 and Adj. R^2 are reduced Qui-Square and Adjusted R- Square, respectively.

Decay curve	Parameters			Statistics	
	y_0	C_1	k_1	Red. χ^2	Adj. R^2
D1	974297.8±3850.8	1.168E6±3954.1	21.1±0.2	4.61E7	0.999
D2	1.01E6±2172.9	887338.9±2627.9	18.9±0.2	2.22E7	0.999
D3	981472.1±2585.9	977520.3±2751.6	20.3±0.2	2.52E7	0.999
D4	949274.3±5964.5	1.09E6±6196.2	20.7±0.4	1.28E8	0.998

doi:10.1371/journal.pone.0144454.t004

Table 5. Double exponential fit using model $F(t) = yo + C_1 * exp(-k_1 * x) + C_2 * exp(-k_2 * x)$ for plain non-coated gold nanoparticles (GNPs), HAOA coated GNPs, free LYZ and LYZ-conjugated GNPs (see Fig 13).

Samples	Constants (y_0, k_1, k_2)	R^2	Pre-exponential factors (C_1, C_2)
Free LYZ	*For first 30min decay*:	0.999	C_1 = 7.34E5 ± 7.10E3
	y_0 = 5.84E5 ± 0.40E3		
	k_1 = 1.42E-2 ± 0.20E-2		C_2 = 1.42E6 ± 0.80E3
	k_2 = 3.24E-3 ± 1.30E-5		
LYZ—conjugated HAOA GNPs	y_0 = 9.83E4 ± 2.68E3	0.997	C_1 = 1.44E4 ± 0.50E3
	k_1 = 2.03E-3 ± 1.28E-4		C_2 = 2.02E4 ± 2.14E3
	k_2 = 1.22E-4 ± 2.78E-5		
Plain non coated GNPs (control)	y_0 = 6.31E4 ± 9.00E1	0.998	C_1 = 1.91E4 ± 1.70E2
	k_1 = 6.20E-3 ± 1.09E-4		C_2 = 2.46E4 ± 1.20E2
	k_2 = 7.14E-4 ± 1.00E-5		
HAOA coated GNPs (control)	y_0 = 7.93E4 ± 3.70E2	0.988	C_1 = 1.40E4 ± 2.90E3
	k_1 = 5.05E-3 ± 1.69E-4		C_2 = 1.44E4 ± 2.6E3
	k_2 = 4.23E-4 ± 2.83E-5		

doi:10.1371/journal.pone.0144454.t005

constants and k_1 *and* k_2 is the rate constant of fluorescence emission intensity decrease (min^{-1}). y_0 value was fixed to 0. The root mean square error R^2 was > 0.99 for all kinetics. The fitted parameter values and corresponding errors, and root mean square error values obtained after fitting the 330nm emission kinetic trace are displayed in Table 5.

Time resolved fluorescence. The fluorescence decay was analyzed by a routine based on the Marquardt least-squares minimization. The main equations for the time-resolved intensity decay data were assumed to be a sum of discrete exponentials as in:

$$F(t) = \sum_i \alpha_i . \exp(-t/\tau_i)$$

where $F(t)$ is the intensity decay, α_i is the amplitude (pre-exponential factor), τ_i the fluorescence lifetime of the i-th discrete component, and $\Sigma\alpha\tau_i = 1.0$.

The fractional intensity *fi* of each decay time is given by:

$$f_i = \frac{\alpha_i \tau_i}{\sum_i \alpha_i \tau_i}$$

and the mean lifetime is:

$$\langle \tau \rangle = \sum_i f_i \tau_i$$

The fluorescence lifetimes of free LYZ and LYZ-conjugated HAOA gold nanoparticles acquired upon 280 nm and 295 nm excitation are summarized in Table 6.

Results

In Table 1 are listed the absorption and fluorescence spectral characteristics of N-formylkynurenine (NFK), dityrosine (DT) and kynurenine (Kyn) [25–27].

In Fig 1 is displayed the 3D molecular structure of hen egg white LYZ (2LYZ.pdb), highlighting Trp and Tyr residues and disulphide bridges. Trp residues are displayed in red, Tyr residues in blue and Cystines in yellow. LYZ has in total 6 Trp residues, 3 Tyr residues and 4 disulphide bridges. In Table 2 are listed the shortest distances between each Trp and Tyr

Table 6. Recovered fluorescence lifetimes (τ_i), pre-exponential factors (α_i), intensity fraction (f_i) and average lifetime ($<\tau>$) for free LYZ and LYZ-conjugated HAOA gold nanoparticles (GNPs), at pH 7.4 obtained by a nonlinear fit using the PTI software. Excitation has been carried out using a 280 nm and 295 nm diodes.

Lifetime (ns)		Intensity fraction		Pre-exponential factor	
Free LYZ (280 nm diode)					
τ_1	0.41±0.03	f_1	0.21	α_1	1.02±0.04
τ_2	1.53±0.08	f_2	0.48	α_2	0.63±0.02
τ_3	3.33±0.13	f_3	0.31	α_3	0.19±0.03
$<\tau>$	1.86				
LYZ-conjugated HAOA GNPs (280 nm diode)					
τ_1	0.17±0.008	f_1	0.50	α_1	3.97±0.16
τ_2	1.58±0.04	f_2	0.36	α_2	0.31±0.01
τ_3	9.20±0.76	f_3	0.14	α_3	0.02±0.002
$<\tau>$	1.91				
Free LYZ (295 nm diode)					
τ_1	0.27±0.02	f_1	0.26	α_1	1.85±0.06
τ_2	1.05±0.05	f_2	0.41	α_2	0.74±0.04
τ_3	3.02±0.06	f_3	0.33	α_3	0.21±0.01
$<\tau>$	1.50				
LYZ- conjugated HAOA GNPs (295 nm diode)					
τ_1	0.046±0.009	f_1	0.41	α_1	9.62±1.21
τ_2	0.38±0.01	f_2	0.50	α_2	1.44±0.08
τ_3	2.77±0.38	f_3	0.03	α_3	0.01±0.002
τ_4	36.0±6.30	f_4	0.06	α_4	0.002±0.0002
$<\tau>$	1.43				

doi:10.1371/journal.pone.0144454.t006

residues and the nearby disulphide (SS) bonds. The shortest distance between Trp123 and SS bridge C30-C115 is 3.326 Å. All considered distances were < 12 Å.

In Fig 2 is displayed the fluorescence emission intensity at 350 nm, upon continuous excitation at 295 nm (0.1 μW) of a 10 μM LYZ solution as a function of temperature, from 45°C and 90°C. The heating rate was fixed at 1°C/min. The first derivative is represented in the upper right corner. The melting temperature (T_m) of LYZ was determined to be 74°C, consistent with literature values obtained under similar physicochemical conditions [28, 29]. The fluorescence emission intensity at 350 nm decreased from 2.4E6 to 1.1E6 counts (56%) during the thermal scan from 45–90°C.

The fluorescence excitation and emission spectra of LYZ, before and after thermal unfolding, are displayed in Fig 3. While acquiring the fluorescence excitation spectra the emission was fixed at 350 nm. The fluorescence emission spectra were acquired upon 295 nm excitation. After thermal unfolding, the fluorescence emission intensity of LYZ at the wavelength where maximum emission is observed (340 nm) has decreased by 73% and the fluorescence excitation intensity at the wavelength where maximum excitation is observed (285 nm) has decreased by 64%. Furthermore, the fluorescence emission spectrum of LYZ has been red shifted from 340 nm to 349 nm, after protein unfolding.

In Fig 4 is displayed the fluorescence emission intensity kinetic trace at 330 nm upon continuous illumination of a fresh LYZ sample (10 μM) at 295 nm, for 2 hours with a excitation slit of 0.1 mm (equivalent power: 0.1 μW). Two transitions are visible: the first one at 10 min and the second one, smaller, at 90 min. The fluorescence emission intensity increases 1.0% in

the initial 10 min of illumination, followed by a decay in the fluorescence emission intensity until 70 min, reaching an intensity level lower than the initial one. Afterwards, the fluorescence emission intensity increases peaking around 90–95 min of illumination and stabilizes thereafter.

The fluorescence excitation and emission spectra of LYZ, before and after 120 min of continuous 295 nm illumination (excitation slit at 0.1 mm, 0.1 μW) are displayed in Fig 5. While acquiring the fluorescence excitation spectra the emission was fixed at 330 nm. The fluorescence emission spectra were acquired upon 295 nm excitation. After 2 hours of continuous 295 nm excitation the fluorescence emission intensity of LYZ at 330 nm decreased 3.4% and the fluorescence excitation intensity decreased 1.9%. No shift has been observed in the fluorescence emission spectrum. The same spectra were acquired after 2 hours of excitation at 295 nm using a larger excitation power of 1.0 μW (exc. slit 0.5 mm) (data not shown). Both spectra show that the effect of 295 nm continuous excitation on the fluorescence emission and excitation spectra of LYZ is smaller than the effect of thermal unfolding.

In Fig 6 (panel A and B) is displayed the fluorescence emission of LYZ at 330 nm upon continuous 2 hours illumination, at 20°C, at six selected wavelengths: 250 nm, 265 nm, 285 nm, 295 nm, 305 nm and 310 nm. At 250 nm, 265 nm, 285 nm and 295 nm the kinetic traces are similar. An initial increase in the fluorescence emission intensity is followed by a plateau like region with smaller oscillations. The initial fluorescence emission intensity upon 250 nm, 265 nm, 285 nm and 295 nm illumination increases by 3.7%, 6.9%, 6.7%, 8.6%, respectively. Continuous illumination with 305 nm light leads to a 4.7% decrease in the fluorescence emission intensity after 2 hours of continuous illumination (Fig 6, panel B). Continuous illumination with 310 nm light does not lead to fluorescence emission intensity changes.

In Fig 7A is displayed the fluorescence emission spectrum of SYPRO® Orange, upon 470 nm excitation and the fluorescence excitation spectrum of SYPRO® Orange, with emission fixed at 580 nm, prior and after continuously illuminating LYZ at 295 nm for 70 min (1.0 μW). SYPRO® Orange fluorescence emission intensity at the wavelength where maximum emission is observed (580 nm) has increased by 25.5-fold and the fluorescence excitation intensity at the wavelength where maximum excitation is observed (470 nm) has increased by 52.3-fold. Furthermore, the fluorescence emission spectrum of SYPRO® Orange exhibits a 19 nm blue shift after 295 nm continuous excitation of LYZ. The wavelength at maximum SYPRO® Orange fluorescence emission intensity has shifted from 606 nm to 587 nm after 70 min of illumination. As a control, the fluorescence emission of SYPRO® Orange at 580 nm, upon excitation at 470 nm, was monitored after SYPRO® Orange has been continuously illuminated at 295 nm for 70 min. A bleaching effect of 18% was observed (data not shown), and no blue shift was observed.

LYZ was exposed to 10min continuous 295 nm excitation cycles (0.5 mm; 1.0 μW). After each excitation period, the fluorescence excitation and emission spectra of SYPRO® Orange were acquired. In total, LYZ was excited with 295 nm light for 70 min. In Fig 7B is displayed the fluorescence emission intensity of SYPRO® Orange (upon exc. at 470 nm) after each 10 min excitation period of LYZ at 295 nm. The SYPRO® Orange emission intensity is observed to increase 23.6-fold after the initial 20 min of LYZ excitation, followed by a decrease in the third round of LYZ excitation. Afterwards, SYPRO® Orange fluorescence emission intensity increases once again and stabilizes after 40 min of 295 nm excitation. Wavelengths corresponding to the maximum fluorescence emission intensity of SYPRO® as a function of LYZ illumination time are displayed in Table 3.

The effect of 295 nm excitation power on the fluorescence emission profile of LYZ is displayed in Fig 8. The power has been controlled using different excitation slit openings: 0.1 mm, 0.3 mm, 0.4 mm and 0.5 mm corresponding to 0.1 μW, 0.5 μW, 0.7 μW and 1.0 μW,

respectively. The equation displaying the dependence of the excitation slit size (x) versus excitation power (y) was found to be $y = 2.267x - 0.172$, with $R^2 = 0.997$ (see insert in Fig 8). At the lower power level (0.1 μW) almost no changes are observed in the fluorescence emission intensity of LYZ upon continuous excitation at 295 nm. For all other power levels, an initial increase in the fluorescence emission intensity is observed, followed by a decrease in intensity and subsequent weak increase.

The effect of increasing the power from 0.1 μW to 1.0 μW (exc. slit increase from 0.1 mm to 0.5 mm) in the fluorescence emission and excitation spectra of LYZ after 2 hours of continuous 295 nm excitation is displayed in Fig 9 (panels A and B, respectively). When carrying out the illumination with 0.1 μW, a slight decrease in the excitation and emission intensity spectra is observed. At the wavelength of maximum fluorescence intensity, the fluorescence excitation and emission intensities dropped 1.6% and 2.8%, respectively (Fig 9A). When carrying out the illumination with 1.0 μW, the fluorescence excitation and emission intensities dropped 36.6% and 11.5%, respectively, at the wavelength of maximum fluorescence intensity (Fig 9B).

In Fig 10 is displayed the fluorescence emission intensity of LYZ at 330 nm upon non continuous 295 nm illumination for 90 min at four different temperatures: 10°C, 20°C, 25°C and 30°C. After each 10 min excitation period, the shutter has been closed for 10 min, followed by another 10 min excitation at 295 nm. Four open/close cycles have been carried out. The observed kinetic traces are very dependent on temperature. At 10°C, LYZ fluorescence emission intensity increases by 11% after 90 min (a total of 50 min of non continuous excitation and a total of 40 min in the dark). The periods of darkness do not lead to changes in the fluorescence emission intensity of LYZ when the new 10 min excitation cycle starts. At 20°C, LYZ shows a very different response: the protein's fluorescence emission intensity decreases exponentially upon continuous excitation at 295 nm, except during the first 10 min where the fluorescence emission intensity increases during the first 5 min prior to decreasing. A 49.7% drop in fluorescence emission intensity is observed after the four last 10 min excitation cycles. After being kept in the dark for 10 min, LYZ recovers the lost fluorescence emission intensity. This experiment was repeated three times in order to confirm its reproducibility and the reversibility of the process (data not shown). Every time fluorescence recovery was observed at 20°C. Each of the four decay curves observed after the initial 10 min of excitation have been fitted by a single exponential decay model given by $y = C_1{}^*\exp(-x/k_1) + y_0$. The fitted parameter values (C_1, k_1, y_0) and corresponding errors, as well as root mean square error values, were obtained after fitting each kinetic trace. The results are displayed in Table 4. At last, continuous 295 nm excitation of LYZ at 25°C and 30°C does not significantly change the fluorescence emission intensity of the protein.

SYPRO® Orange was used to monitor possible conformational changes of LYZ at the end of the excitation/darkness cycles described above. In Fig 11 is displayed the SYPRO® Orange fluorescence emission intensity spectra, upon 470 nm excitation, acquired before and after the full 295 nm illumination of LYZ at each temperature as shown in Fig 10. SYPRO® Orange fluorescence emission intensity increased after each experiment. An intensity increase of 15.1-fold, 4.6-fold, 11.1-fold and 14.6-fold is observed at 10°C, 20°C, 25°C, and 30°C, respectively. The larger fluorescence emission intensity increase is observed at 10°C and the smallest fluorescence increase is observed at 20°C. Furthermore, the wavelength at maximum fluorescence emission intensity of SYPRO® Orange is observed to be 16 nm blue shifted from 607 nm to 591 nm after each experiment.

In order to confirm the observed reversibility of the process at 20°C and the lack of reversibility at 10°C the fluorescence emission intensity at 330 nm of the following samples has been monitored at 20°C and 10°C (Fig 12, panels A and B, respectively): a) fresh LYZ never previously illuminated, b) LYZ after 30 min of continuous 295 nm illumination, c) LYZ after 30 min

of continuous 295 nm illumination followed by 48 hours in the dark, d) LYZ after 30 min of continuous 295 nm illumination followed by 48 hours in the dark and subsequent further 30 min of continuous 295 nm. The results are presented in Fig 12 (panels A and B display the data acquired at 20°C and at 10°C, respectively). It can be seen that LYZ has lost fluorescence emission intensity when illuminated for 30 min at 295 nm. However, it has recovered its original fluorescence emission intensity after left in the dark for 48 hours, confirming the results at 20°C displayed in Fig 10. On the other hand, at 10°C it can be observed that continuous 295 nm excitation leads to a slight increase of protein fluorescence emission, as displayed in Fig 10. However, 48 hours in the dark did not lead to the recovery of the initial fluorescence emission intensity values.

The response of conjugated LYZ and non-conjugated LYZ to 295 nm continuous excitation has been investigated in order to infer the possible protective effect of gold nanoparticles covered by natural polymers (hyaluronic acid, HA) and oleic acid (OA) towards photochemistry. LYZ has been conjugated to HAOA coated gold nanoparticles. The fluorescence emission intensity at 330 nm as a function of continuous 295 nm excitation of conjugated LYZ, free LYZ, plain non-coated gold nanoparticles and HAOA coated gold nanoparticles is displayed in Fig 13. The initial fluorescence emission of conjugated LYZ is quenched by one order of magnitude when compared to the initial fluorescence emission intensity of free LYZ. After 2 hours of continuous 295 nm excitation the fluorescence emission intensity of free LYZ has dropped by 91.3% while the fluorescence emission intensity of conjugated LYZ has only dropped by 50.0%. Interestingly, both samples end up with the same fluorescence intensity level after 2 hours excitation. Both kinetic traces have been fitted with a double exponential decay model according to the formula $F(t) = y_0 + C_1 * exp(-k_1 * x) + C_2 * exp(-k_2 * x)$. In Table 5 are displayed the fitting parameters and corresponding errors as well as the root mean square error values for double exponential decay curves. For free LYZ, k_1 and k_2 were, respectively, 1.42E-2 ± 0.20E-2 and 3.24E-3 ± 1.30E-5 (for the first 30 min of the decay), while for LYZ-conjugated HAOA coated gold nanoparticles, k_1 and k_2 were, respectively, k_1 = 2.03E-3 ± 1.28E-4 and k_2 = 1.22E-4 ± 2.78E-5. We could confirm the protective effect of HAOA coated gold nanoparticles towards LYZ since the decay constants for conjugated LYZ were lower compared to the ones for free LYZ. The fluorescence emission intensities at 330 nm displayed by the plain or HAOA coated gold nanoparticles are only residual and do not change significantly upon continuous 295 nm illumination.

In Fig 14A is displayed a graphical representation of the HAOA coated gold nanoparticles. We have confirmed the HAOA gold nanoparticles structure and coating formation by TEM, as represented in Fig 14B. The mean particle size and polydispersity index (PI) for HAOA gold nanoparticles (non-conjugated with LYZ) was also determined to be around 300 nm (PI: 0.2) and a zeta potential (ZP) of -19 mV. However, the volume distribution for 90% of HAOA gold nanoparticles (D90%) was higher for smaller sized particles (D90% = 149 nm), as confirmed in TEM analysis. Here we observe that HAOA gold nanoparticles show a size around 50–100 nm. This variation could be explained by the presence of some aggregated in suspension. Finally, we have analyzed the image intensity by using Matlab version R2014b (MathWorks), as plotted in Fig 14C. We can observe that there is a core substrate, which is probably the gold core of the nanoparticles, while on top of this substrate there is a matrix, which we assign to the polymer HAOA distributed around the gold nanoparticles.

In Fig 15 is displayed the fluorescence excitation (emission at 330 nm) and emission (excitation at 295 nm) spectra of free LYZ, of the supernatant after centrifugation of the solution containing conjugated and free LYZ, and of conjugated LYZ HAOA gold nanoparticles. Data confirm the conjugation of LYZ onto the HAOA gold nanoparticles. Free LYZ shows the highest fluorescence excitation intensity, followed by LYZ present in the supernatant (that didn't

conjugate with HAOA gold nanoparticles) and, finally, LYZ conjugated HAOA gold nanoparticles. In the case of the fluorescence emission spectra, the emission intensity of LYZ conjugated HAOA gold nanoparticles was slightly higher than free LYZ in the supernatant, after nanoparticles isolation.

In Fig 16A is displayed the fluorescence emission spectra of four samples upon excitation at 320 nm: a) non-illuminated free LYZ, b) free LYZ excited with 295nm for 2 hours, c) non-illuminated LYZ-HAOA gold nanoparticles, d) LYZ-HAOA gold nanoparticles excited with 295 nm for 2 hours. The 320 nm excitation is intended to detect the presence of NFK and DT, a Trp and Tyr photoproduct, respectively. However, 320 nm light can still excite Kyn, despite its maximal excitation at 360 nm. For the free enzyme, a peak centred at 405 nm is observed upon 320 nm excitation. The fluorescence emission intensity of the peak increases 108% after continuous excitation with 295 nm for 2 hours. For the conjugated enzyme, a broad peak centred at 433 nm is observed. After continuous excitation with 295 nm for 2 hours, the fluorescence emission intensity is observed to increase by 22.4% for the peak centred at 433 nm.

In Fig 16B is displayed the fluorescence emission intensity spectra of four samples upon excitation at 360 nm: a) non-illuminated free LYZ, b) free LYZ excited with 295 nm for 2 hours, c) non-illuminated LYZ-HAOA gold nanoparticles, d) LYZ-HAOA gold nanoparticles excited with 295 nm for 2 hours. The 360 nm excitation is intended to excite Kyn, a Trp photoproduct. However, this wavelength will also excite NFK but not excite DT. For the free enzyme, a peak centred at 406 nm is observed upon 360 nm excitation. The fluorescence emission intensity of the peak increases 111% after continuous excitation with 295 nm for 2 hours. For the conjugated enzyme, two main peaks are observed: one centred at 406 nm and another centred at 466 nm. After 295 nm excitation for 2 hours, the fluorescence emission intensity is observed to increase by 25.0% and by 33.5% for the peaks centred at 406 nm and 466 nm, respectively.

In Table 6 are displayed the fluorescence lifetimes (τ_i) distribution and the associated pre-exponential factors (f_i) recovered from the time resolved intensity decays for non-illuminated LYZ and LYZ-conjugated HAOA gold nanoparticles (diode excitation wavelengths: 280 nm and 295 nm; emission wavelength: 330 nm) at pH 7.4. The structural changes induced in free LYZ and conjugated LYZ are visible in fluorescence lifetime distribution, as the lifetime for the free LYZ is shorter than for LYZ-conjugated HAOA gold nanoparticles, for both diodes studies. For free LYZ, at 280 nm and 295 nm, 3 lifetimes are present, as well as for the LYZ-conjugated HAOA gold nanoparticles, except for LYZ-conjugated HAOA gold nanoparticles at 295 nm with 4 lifetimes.

Discussion

The structure of lysozyme (LYZ) has been well characterized in literature [13, 23, 30, 31]. Its 3D structure displayed in Fig 1 shows the presence of four disulphide bonds (SS) in close spatial proximity to six Trp residues (Table 2). As previously published by Neves-Petersen et al. [8, 14, 15], excitation of the side chains of aromatic residues located in close spatial proximity to SS bridges may lead to the disruption of the SS bonds. SS bridges are known to be excellent quenchers of aromatic residues. Therefore, when the bridges are broken, Trp fluorescence intensity might increase [8]. The observed result will depend on the nature of the photochemical pathways that the protein enters after excitation (*vide infra*).

In this paper, we have investigated the effect of temperature and of 295 nm continuous excitation on LYZ. LYZ melting temperature has been determined with temperature dependent steady-state fluorescence measurements and was found to be ~74°C, at pH 6.0 (Fig 2), which is close to the value reported by other research groups when carrying out thermal unfolding of LYZ at similar conditions [28, 29]. After thermal unfolding, the fluorescence emission of LYZ

is observed to be 9 nm red-shifted, indicating that the Trp moiety in LYZ became more solvent accessible (Fig 3). Trp fluorescence emission is known to be very sensitive to the dielectric constant and therefore to the polarity of the medium surrounding it. In polar environments the fluorescence emission is red shifted compared to Trp emission in apolar environments. Solvent relaxation prior to fluorescence emission is responsible for this observation. The drop in excitation and emission intensity of LYZ observed after thermal unfolding (64% and 73%, respectively) reveals that the Trp moiety is now more quenched due to solvent exposure and/or that upon 295 nm excitation some of the Trp residues have been converted into photoproducts, such as NFK and Kyn (see Table 1), which have their excitation and emission spectra shifted with respect to Trp. The latter is confirmed by the data displayed in Fig 16, which shows that NFK and Kyn are formed upon 295 nm excitation of LYZ.

During the thermal unfolding experiment (Fig 2) the protein has also been exposed to 295 nm light. The results of such experiment (Figs 2 and 3) are a combined effect of temperature and UV exposure. To minimize the effect of UV light on the observed results a small excitation slit opening of 0.1 mm has been selected. In order to investigate the sole effect of 295 nm light on the observed fluorescence changes, LYZ has been continuously excited by 295 nm light for 2 hours, at 20°C, using an excitation slit opening of 0.1 mm (0.1 μW) (Fig 4). After 2 hours illumination, the fluorescence excitation and emission intensities at the respective wavelength corresponding to maximum intensity have decreased by only 3.4% and 1.9%, respectively and no spectral shift was observed (Fig 5). It is likely that these changes would be even smaller upon 45 min continuous excitation at 295 nm (the illumination time used during the thermal unfolding assay). This shows that the effect of temperature during the thermal unfolding experiment exceeds the effect of 295 nm illumination when a 0.1 mm slit is used. This also confirms that thermal unfolding studies should always be carried out using low excitation power in order to minimize photochemistry, which will influence the recovered T_m value.

The time dependent fluorescence emission kinetic traces of LYZ acquired upon continuous illumination with different UV wavelengths (250 nm, 265 nm, 285 nm, 295 nm, 305 nm and 310 nm) at 20°C are displayed in Fig 6. Excitation at 250 nm is known to cause direct photolysis of SS bonds [12]. 250 nm also excites Trp residues but marginally excites Tyr and Phe residues (see Table 7). This means that excitation of LYZ with 250 nm will lead to the disruption of SS bridges, according to literature [32–35]. In addition, 265 nm excites Tyr and Trp and marginally excites Phe, 285 nm excites Trp and Tyr, 295 nm excites Trp residues and very marginally excites Tyr residues, and finally, 305 nm and 310 nm marginally excites Trp and Tyr residues. Taking into consideration that SS bonds are very good quenchers of protein fluorescence, it is likely that their direct or indirect disruption [5–8, 15, 36, 37] leads to an increase of LYZ

Table 7. Molar extinction coefficients ($cm^{-1}.M^{-1}$) at different wavelengths (250 nm, 265 nm, 285 nm, 295 nm, 305 nm and 310 nm) studied for Trp, Tyr and Phe.

	Molar Extinction Coefficients ($cm^{-1}.M^{-1}$)		
Wavelength (nm)	Trp	Tyr	Phe
250	2240	274	136
265	4650	921	103
285	4544	675	1
295	1532	61	0
305	150	39	0
310	61	32	0
Number aromatic residue/ protein	6	3	3

doi:10.1371/journal.pone.0144454.t007

fluorescence emission intensity when illuminated with wavelengths that lead to direct photolysis of SS (~254 nm) or when illuminated with wavelengths that excite their aromatic residues. The excitation of Trp and Tyr aromatic residues has the highest probability to induce SS disruption since the yield of electron ejection is higher for Trp and Tyr than for Phe residues [6, 36, 37]. Therefore, it is likely that 285 nm and 295 nm excitation of LYZ leads to the largest initial increase of protein fluorescence, followed by 265 nm and 250 nm. It is important to underline "initial increase" since any prolonged excitation of proteins will allow photochemical pathways that can end up bleaching the protein´s fluorescence output. It is likely that 305 nm and, in particular, 310 nm excitation of LYZ does not lead to particular changes of the fluorescence output since these wavelengths lead to a very marginally excitation of LYZ. The data displayed in Fig 6A and 6B corroborates our interpretation.

SYPRO® Orange was selected as a probe in order to monitor LYZ conformational changes, which results in solvent exposure of hydrophobic surfaces [2]. After 70 min of continuous 295 nm excitation of LYZ, SYPRO® Orange fluorescence emission and excitation intensities have increased 25.5-fold (Fig 7A). The increase in fluorescence emission intensity of SYPRO® Orange indicates that this extrinsic probe is in contact with hydrophobic surfaces rendered accessible due to light induced conformational changes in LYZ. Furthermore, continuous excitation leads to a 19 nm blue-shift in the fluorescence emission peak of SYPRO® Orange (Fig 7A). This has also been observed for Nile Red—another hydrophobic fluorescent probe—used to monitor LYZ under stress induced by heat shock (heating at 70°C for 10 min, at pH 5.0), alone and in presence of stabilizers (e.g., betain, hydroxyectoine and trehalose) [2]. The fluorescence emission intensity of SYPRO® Orange at the wavelength where maximum fluorescence emission is observed has been plotted after consecutive 10min illumination periods of LYZ at 295 nm (Fig 7B). After the first and second initial illumination cycles the fluorescence emission intensity of SYPRO® increases by 5.2-fold and 23.5-fold, respectively, indicating that LYZ is in two different conformational states that have in common the fact that hydrophobic surfaces of LYZ became accessible to SYPRO® Orange and, therefore, were solvent accessible. The third cycle of LYZ illumination (30 min) leads to a conformation with a smaller area of hydrophobic surface accessible to the solvent than the area accessible at the end of the second cycle (20 min). After 40 min of illumination the fluorescence emission intensity of SYPRO® Orange at 580 nm increased and stabilized (Fig 7B) indicating that the conformation of LYZ is most likely not to exhibit further changes.

The dependence of the fluorescence emission intensity trace upon continuous 295 nm excitation on excitation power is displayed in Fig 8. At higher power levels (0.7 μW and 1.0 μW) two significant changes in fluorescence emission intensity is observed. Data displayed in Fig 9A clearly show that illumination carried out with the lowest power (0.1 μW) does not lead to significant photochemistry and damage of the Trp pool of residues due to the fact that the fluorescence excitation and emission spectra prior and after 2 hours illumination are very similar. Furthermore, no spectral shift is observed in the fluorescence emission spectrum of LYZ, indicating that the solvent accessibility of the Trp residues in LYZ has not changed (Fig 9A). On the other hand, when illumination is carried out with 1.0 μW power (Fig 9B) it is clear that 295 nm excitation has induced structural changes in LYZ. The intensity of the fluorescence excitation and emission spectra has decreased (36.6% and 11.5%, respectively) after 2hours illumination and the fluorescence emission has been 4 nm red shifted (Fig 9B), indicating that the Trp moiety in LYZ has been rendered more solvent accessible due to light induced protein conformation changes. Wu et al. 2008 [9] reported the photo induced degradation of LYZ (280 nm) as a function of illumination time, at pH 8.0 and 25°C, showing that Trp fluorescence emission intensity increased as a result of continuous excitation, which is correlated with the disruption of SS bridges. A red-shift was also observed. The drop in fluorescence emission intensity is

correlated with the formation of Trp photoproducts like NFK and Kyn upon 295 nm excitation of LYZ, as shown in Fig 16A and 16B. Data confirm that the light induced structural damage is dependent on the power of the light used to excite the molecules [8]. Our data indicate that LYZ is not exhibiting photo-oxidation changes at 0.1 μW at 295 nm illumination. However, an increase to 0.5 μW leads to distinct changes.

The study of the effect of temperature (10°C, 20°C, 25°C and 30°C) on LYZ fluorescence emission intensity as a function of 295 nm illumination time, at a fixed slit size (0.5 mm, or 1.0 μW), has been carried out. The reversibility of the processes has also been investigated upon exposing LYZ to repeated 10 min cycles of alternated excitation and darkness. LYZ kinetic traces showed a clear temperature-dependent behaviour. At 20°C the light induced a reversible loss of fluorescence emission intensity. As displayed in Fig 10, after each 10 min dark period LYZ has recovered the fluorescence emission intensity value at the 20 min previous moment where the shutter have been open. This was not observed at any other tested temperature. At 10°C the fluorescence emission intensity increases with illumination time and at 25°C and 30°C the observed increase is minimal.

SYPRO® Orange has been used to monitor the conformational changes of LYZ as a function of temperature. Data show that 2 hours-excitation of LYZ at 295 nm at four different temperatures induces different conformational changes in LYZ (Fig 11). SYPRO® Orange showed highest fluorescence emission intensity at 10°C and lowest fluorescence emission intensity at 20°C. The conformational changes that led to the largest exposure of hydrophobic areas in LYZ has occurred at 10°C, followed by 30°C, 25°C and finally 20°C. At 20°C the lowest exposure of hydrophobic patched in LYZ has occurred. Interestingly, this is the temperature at which the loss of fluorescence emission intensity seems to be reversible upon keeping LYZ in the darkness (Fig 10). In order to confirm such reversible process, we have recorded the fluorescence emission intensity of the following samples: a) fresh LYZ sample, b) fresh sample after being excited for 30 min at 295 nm, c) fresh sample after being excited for 30 min at 295 nm and kept in the dark for 48 hours, d) fresh sample after being excited for 30 min at 295 nm, kept in the dark for 48 hours and further excited for another 30 min with 295 nm. Such experiments took place at 10°C and 20°C. Data displayed in Fig 12A and 12B confirm that the loss of protein fluorescence after the first 30 min of excitation is reversible if the sample is kept in the dark and the experiment is carried out at 20°C and non-reversible if the experiments have been carried out at 10°C.

In the present study we have also immobilized LYZ onto gold nanoparticles coated with hyaluronic acid (HA) and oleic acid (OA). Since gold, HA and OA are known to be fluorescence quenchers, we have investigated if the presence of such quenchers decreased the rate of the observed photochemical reactions and if it induced a preference for short fluorescence decay lifetimes in the case of the conjugated LYZ compared to free LYZ. Data displayed in Figs 13 and 15 show that the presence of gold nanoparticles coated with HAOA (Fig 14A) quenches LYZ fluorescence. The results summarised in Table 5 and the kinetic traces displayed in Fig 13 confirm that the rates of fluorescence emission intensity loss (k1 and k2 values, Table 5) as a function of 295 nm illumination time are one order of magnitude slower for the conjugated LYZ compared to free LYZ. Furthermore, analysis of the fluorescence lifetimes' distribution of free LYZ compared to LYZ conjugated to HAOA gold nanoparticles (upon pulsed excitation with 280 nm and 295 nm diodes) reveals that upon conjugation, the percentage of molecules that decays with lifetimes in the picosecond range increases, while the percentage of the population that decays with lifetimes in the nanosecond range decreases (see Table 6). When exciting with a 280 nm diode it is observed that for free LYZ, 21% of the population decays with a picosecond lifetime and 79% of the population decays with a nanosecond lifetime. When conjugated to HAOA gold nanoparticles it is observed that 50% of the population decays with a

picosecond lifetime and 50% of the population decays with a nanosecond lifetime. When exciting the samples with a 295 nm diode it is observed that for free LYZ, 26% of the population decays with a picosecond lifetime and 74% of the population decays with a nanosecond lifetime. When conjugated to HAOA gold nanoparticles it is observed that >91% of the population decays with a picosecond lifetime and only 9% of the population decays with a nanosecond lifetime. LYZ proximity to the HAOA gold nanoparticles creates a different physico-chemical environment that promotes a faster decay from LYZ excited state. It is known that both silver and gold nanoparticles quench protein fluorescence [16, 38] and that the presence of nanoparticles leads to protein conformational changes revealed by shifts in the fluorescence emission spectrum of the protein [39]. Furthermore, it is known that both HA and OA are good fluorescence quenchers and that their presence leads to shorter fluorescence lifetime components [18, 19]. The protonated forms of carboxylic, hydroxyl and amine groups are known to be fluorescence quenchers of proteins [40]. These groups are present in the glucuronic acid and N-acetyl-glucosamine monomers in the hyaluronic acid (HA) polymer and in oleic acid (OA) and will therefore promote shorter fluorescence lifetime decays in proteins.

Furthermore, as observed in Fig 15, the conjugation of LYZ to HAOA gold nanoparticles leads to protein conformational changes since a blue shift (from 341 nm to 326 nm) in the fluorescence emission spectra is observed upon conjugation. The observed blue indicates that the Trp moiety in LYZ is in a more hydrophobic environment upon conjugation. The hydrophobic environment can be created by the presence of aliphatic chains in OA and by the presence of HA. Such new conformational states might also be responsible for the observed shorter lifetime decays in conjugated LYZ due to a putative closer spatial distance between the aromatic residues and neighboring quencher residues.

In addition, other studies involving binding of drugs (e.g., ciprofloxacin and lomefloxacin) and other molecules (e.g, kynurenine) to LYZ are likely to induce conformational changes on this protein, through formation of aggregates [40] and complexes [39, 41]. These complexes modify the rate of lifetime decay compared to the equivalent components in their non-complex state.

The average fluorescence lifetime (at 330 nm) for free LYZ at pH 6.0 was 1.86 nanosecond and 1.5 nanosecond upon 280 nm and 295 nm excitation, respectively. The fluorescence decay data was best fitted with a 3 exponential decay model. When changing from a 2 lifetime decay model to a 3 lifetime decay model the statistics of the fitting routine improved considerably. For example, the Durbin-Watson parameter improved from being to 1.3 to being 1.8, being a value close to 2 ideal since it shows that the residual are not autocorrelated [42]. Choosing a 4 exponential decay model did not improve the statistics of the fitting routine, except for LYZ-conjugated gold nanoparticles excited at 295 nm. Free LYZ has been previously reported to be best fitted by a three exponential decay model, at a similar pH (5.5) and at 340 nm emission, with an average lifetime of 1.16 nanosecond [43]). Quenching of other proteins besides LYZ by nanocarriers has been reported in literature [16, 44, 45]. In our study both the gold nanoparticles and the coating polymers act as quenchers, contributing to the prevalence of short lifetime components. It has been previously described that the attachment of LYZ to gold nanostructures leads to the appearance of a shorter fluorescence lifetime than the shortest lifetime observed for free LYZ and that the longest fluorescence lifetime becomes longer compared with native LYZ, upon 280 nm excitation and when emission is fixed at 360 nm [44]. Our results are in accordance with this observation (Table 6). This effect can be associated with the quenching effect of gold nanoparticles associated with energy transfer to the gold surface [44].

The quenching effect by HAOA gold nanoparticles on LYZ fluorescence emission intensity (Fig 15), the shorter fluorescence lifetime components observed (Table 6) in the presence of the nanocarriers and the slower kinetics observed on conjugated LYZ upon continuous 295 nm

illumination compared to free LYZ (Fig 13 and Table 5) indicates that these particles protect LYZ against photochemistry. It is likely that the structure of LYZ when conjugated to the HAOA gold nanoparticles will be able of being UV excited for longer time prior to possible loss of structure and function. Furthermore, as displayed in Fig 16A and 16B, the amount of photoproducts formed (NFK and Kyn) upon continuous 295 nm excitation of LYZ is reduced in the presence of the nanoparticles.

Previous studies using LYZ mounted on silver nanoparticles also report that quenching can occur as a result of complexation between protein and nanocarrier, as the presence of increasing concentration of silver nanoparticles decreases LYZ fluorescence intensity [38]. LYZ can be linked to gold nanoparticles by non-covalent interactions such as hydrophobic, van der Waals, electrostatic and hydrogen bond interactions [45]. When conjugated to HAOA gold nanoparticles, LYZ will also bind to the HAOA polymer, as represented in Fig 14A. In Fig 14B a TEM image of HAOA gold nanoparticles (without LYZ) is displayed. The gold core (dark core) and the surrounding polymer can be observed. A 3D display of the TEM image shows such two regions in both particles (Fig 14C). Fig 14B and 14C confirm that the gold nanoparticles are covered by a polymer layer. Since LYZ shows a pI around 11.0 and HAOA gold nanoparticles have a superficial negative charge (-19 mV), attractive electrostatic interaction between the protein and the nanocarrier will occur at pH 7.4. Protein conjugation onto the particles has been confirmed by fluorescence spectroscopy (Fig 15). Conjugation has been made possible due to the electrostatic interaction between negatively charged HAOA polymer and positively charged LYZ. The fluorescence excitation (acquired fixing em. at 330 nm) and emission (upon exc. at 295 nm) intensity spectra of free LYZ, of the supernatant recovered after centrifugation of the solution containing conjugated and free LYZ, and of conjugated LYZ onto HAOA gold nanoparticles has been recorded (Fig 15). Data confirm the presence of LYZ onto the HAOA gold nanoparticles. A blue shift of 15 nm in the fluorescence emission spectrum was visible after conjugation of LYZ with HAOA gold nanoparticles. Ali et al. [38] have also described a similar effect (3 nm blue shift) after conjugation of LYZ onto silver nanoparticles. Both temperature and quenchers (i.e., HAOA gold nanoparticles) have an impact on LYZ conformation and structure. When LYZ is in the proximity of HAOA gold nanoparticles, we detect protein conformational changes that reveal that the Trp residues are in a more hydrophobic environment. This environment is provided by the HAOA gold nanoparticles and may increase the interactions and the binding affinity between the Trp moiety and the HAOA gold nanoparticles. This has also been referred by other authors in literature [16]. Concerning the thermal effect on LYZ, Trp residues become more solvent accessible, indicating that the hydrophobic core is more exposed to the solvent, which may increase the formation of inter-protein interactions [46].

Charged amine groups seem to play an important role in the conjugation, since they will interact with negatively charged acid groups present in the used polymer, hyaluronic acid, and present in oleic acid at pH 7.4 [20, 47]. The use of natural polymers has an important and advantageous role in the reduction and morphology of gold nanoparticles (e.g., can work as capping agents, activate "green" reduction of gold and are less toxic), as reported in literature [47]. Conjugation of LYZ onto gold nanorods for 2 hours at pH 6.2 and room temperature led to a blue shift in the nanorods absorbance spectrum and the nanorods acted as quenchers of Trp fluorescence [16]. When monitored at 35°C and pH 7.25, LYZ activity increased when conjugated with iron oxide superparamagnetic nanoparticles, which was observed to be correlated with an increase in the amount of β-sheets and α-helix coils [48]. Another study with iron oxide superparamagnetic nanoparticles demonstrated no change in aromatic residues of LYZ and protein activity after adsorption at the nanocarriers surface by incubation at 37°C for 60 min (200 rpm) [49].

The presence of oxidative conditions induced by light and by the presence of metallic surfaces can lead to the oxidation of the aromatic residues in proteins [5–7, 36, 50–52]. UVB excitation of aromatic residues in proteins leads to the disruption of SS bridges [5, 7, –8, 14, 36,37] and to the formation of photoproducts, such as NFK, Kyn [25, 53] and DT [26]. The spectral properties of these species are displayed in Table 1. In Fig 16A and 16B are displayed the fluorescence emission spectra obtained upon 320 nm and 360 nm excitation, respectively, of a fresh LYZ sample and of a LYZ-HAOA gold nanoparticles sample before and after 2 hours of 295 nm excitation. Since 295 nm excites specifically Trp residues, it is most likely that the photoproducts formed are Trp derivatives such as NFK and Kyn and not Tyr derivatives like DT. Furthermore, the emission spectrum of LYZ upon 295 nm leads to a fluorescence emission spectrum that peaks around 340 nm with a very small component below 290 nm. Therefore, it is unlikely that Tyr residues will be excited by LYZ emission. Two excitation wavelengths were used: 320 nm (Fig 16A) and 360 nm (Fig 16B). Light at 320 nm excites both NFK ($\varepsilon_{NFK(321nm)}$ = 3750 $M^{-1}cm^{-1}$ [54–57] and Kyn ($\varepsilon_{Kyn(321nm)}$ = 1812 $M^{-1}cm^{-1}$ [58]. At 315 nm DT has an extinction coefficient equal to 5200 $M^{-1}cm^{-1}$, but as explained above it is unlikely that we have DT formation [59, 60]. Light at 360 nm excites NFK ($\varepsilon_{NFK(360nm)}$ = 1607 $M^{-1}cm^{-1}$ [58] and Kyn ($\varepsilon_{Kyn(365nm)}$ = 4530 $M^{-1}cm^{-1}$ [61, 62]) but does not excite DT. Therefore, the peak with maximum fluorescence emission intensity at 405 nm in Fig 16B cannot be due to the presence of DT, since DT is not excited at 360 nm. This peak has to belong to a Trp photoproduct that can absorb light both at 320 nm and at 360 nm, since the peak is presence both in Fig 16A and 16B. It cannot be Kyn since the wavelength of maximum fluorescence emission of Kyn lies within 434–480 nm. According to Fukunaga et al., Kyn62LYZ (where Trp62 was converted into Kyn62 in lysozyme, [25]) fluoresces maximally at 470 nm and has broad fluorescence emission spectrum upon excitation at 360 nm. Thus, results are in accordance with ours since we see a broad fluorescence emission centered approximately at 466 nm (Fig 16B). Furthermore, it is reported that Kyn is quenched by protonated amino groups, leading to poor Kyn fluorescence [25]. The 466 nm broad peak in Fig 16B indeed displays poor fluorescence and LYZ at pH 7.4 has protonated amino groups (ARG61 and ARG112) that can quench Kyn. The closest distances between ARG61 (NE) and ARG112 (NE) to the nearby TRP62 (CZ2) and TRP111 (CZ3) are 4.3 Å and 7.5 Å, respectively. Our quest is to find the origin of the 406 nm peak observed in Fig 16A and 16B. NFK absorbs light both at 320 nm and 360 nm and NFK emission is reported to be more blue shifted (maximum emission between 400–440 nm) than Kyn (maximum emission between 434–480 nm). The NFK emission peak is very dependent on pH [25], and on the local dielectric constant (low dielectric medium leads to a blue shift of the maximum emission wavelength, [25]). When exposed to an alkaline pH, NFK emits maximally at 400 nm and when exposed to a neutral pH it emits maximally at 440 nm [25]. On the other hand, NFK emission is not quenched by protonated amino groups which lead to an enhancement of NFK fluorescence. The peak at 406 nm has indeed a large fluorescence emission intensity compared to the Kyn peak centered at 466 nm upon 360 nm excitation (Fig 16B). Summarizing, in Fig 16A and 16B it is likely that the peak at 405–406 nm is due to the formation of NFK upon 295 nm continuous excitation of both free LYZ (Fig 16A and 16B, blue spectra) and conjugated LYZ (Fig 16B, green spectra). According with the results of Fukunaga et al. [25], the broad peak with maximum fluorescence at 433 nm seen in Fig 16A for conjugated LYZ (green curves) is due to the presence of NFK.

In Fig 16A and 16B it can also be seen that the amount of photoproducts formed upon 295 nm excitation of LYZ is reduced when LYZ has been conjugated to HAOA gold nanoparticles. It again likely that the additional presence of fluorescence quenchers such as gold, HA and OA by reducing the fluorescence lifetime of LYZ, prevents that excited Trp residues enter photochemical pathways that lead to the formation of e.g. NFK and Kyn. As a result of LYZ close

vicinity to fluorescence quenchers it is likely that static quenching occurs due to the formation of complexes between LYZ and HAOA gold nanoparticles [39, 40]. Plasmonic surfaces such as the gold and biomolecules such as HA and OA are described to be good fluorescence quenchers [16, 18, 19]. In our studies, the occurrence of static quenching between LYZ and HAOA gold nanoparticles leads to the shorter fluorescence lifetimes for conjugated LYZ (Table 6), to the reduction of LYZ fluorescence intensity, to a fluorescence emission blue shift from 341 nm to 326 nm (Fig 15) after 2 hours continuous illumination at 295 nm and, finally, to the prevention of excited Trp residues to enter photochemical pathways that lead to the formation of NFK and Kyn, in the case of LYZ-conjugated HAOA gold nanoparticles (Fig 16A and 16B).

Conclusions

With this work, it has been demonstrated that the photochemical effects occurring during 295 nm UV excitation at 20°C are reversible, but not at 10°C, 25°C and 30°C. This paper also provides evidence that the UV-damage threshold is between 0.1 μW and 0.5 μW for LYZ. In addition, we have developed HAOA gold nanoparticles that can efficiently protect proteins like LYZ from 295 nm induced photochemistry. These results can be used for biomedical application, as gold nanoparticles gain a greater impact as drug delivery platforms, in areas such as targeting delivery and use of peptides and biomolecules as specific ligands for target cell pools or simply as enzyme carriers. Further, we will study the application of other peptides conjugated with the developed HAOA gold nanoparticles, as biologic triggers for application in cancer laser-based photothermal treatment.

Acknowledgments

The authors would like to thank Fundação para a Ciência e Tecnologia (FCT) for the financial support under the project reference PTDC/BBB-BMC/0611/2012. The authors acknowledge the funding from the European Commission through the project H2020-644242-SAPHELY.

Author Contributions

Conceived and designed the experiments: COS SBP MTNP. Performed the experiments: COS SBP MTNP. Analyzed the data: COS SBP MTNP JM CPR PR. Contributed reagents/materials/analysis tools: COS SBP MTNP JM CPR PR HV. Wrote the paper: COS MTNP SBP JM CPR PR HV.

References

1. Lakowicz JR. Principles of fluorescence spectroscopy. 2nd ed. New York: Academic/ Plenum Publishers; 1999.
2. Avanti C, Saluja V, van Streun ELP, Frijlink HW, Hinrichs WLJ. Stability of Lysozyme in Aqueous Extremolyte Solutions during Heat Shock and Accelerated Thermal Conditions. PLoS ONE. 2014; 9(1): e86244. doi: 10.1371/journal.pone.0086244 PMID: 24465983
3. Gracanin M, Hawkins CL, Pattison DI, Davies MJ. Singlet-oxygen-mediated amino acid and protein oxidation: formation of tryptophan peroxides and decomposition products. Free Radic Biol Med. 2009; 47 (1): 92–102. doi: 10.1016/j.freeradbiomed.2009.04.015 PMID: 19375501
4. Davies MJ. Singlet oxygen-mediated damage to proteins and its consequences. Biochem Biophys Res Commun. 2003; 305(3): 761–770. PMID: 12763058
5. Correia M, Neves-Petersen MT, Jeppesen PB, Gregersen S, Petersen SB. UV-Light Exposure of Insulin: Pharmaceutical Implications upon Covalent Insulin Dityrosine Dimerization and Disulphide Bond Photolysis. PLoS ONE. 2012; 7(12): e50733. doi: 10.1371/journal.pone.0050733 PMID: 23227203
6. Correia M, Snabe T, Thiagarajan V, Petersen SB, Campos SRR, Baptista AM, et al. Photonic Activation of Plasminogen Induced by Low Dose UVB. PLoS ONE. 2015; 10(1): e0116737. doi: 10.1371/journal.pone.0116737 PMID: 25635856

7. Correia M, Neves-Petersen M, Parracino A, di Gennaro A, Petersen S. Photophysics, Photochemistry and Energetics of UV Light Induced Disulphide Bridge Disruption in apo-α-Lactalbumin. J. Fluoresc. 2012; 22(1): 323–337. doi: 10.1007/s10895-011-0963-7 PMID: 21997288
8. Neves-Petersen MT, Gryczynski Z, Lakowicz J, Fojan P, Pedersen S, Petersen E, et al. High probability of disrupting a disulphide bridge mediated by an endogenous excited tryptophan residue. Protein Sci. Logo of prosci. 2002; 11(3): 588–600.
9. Wu L-Z, Sheng Y-B, Xie J-B, Wang W. Photoexcitation of tryptophan groups induced reduction of disulfide bonds in hen egg white lysozyme. J. Mol. Struct. 2008882(1–3): 101–106.
10. Chang J-Y, Li L. The unfolding mechanism and the disulfide structures of denatured lysozyme. FEBS Letters. 2002; 511(1–3): 73–78. PMID: 11821052
11. Shugar D. The measurement of lysozyme activity and the ultra-violet inactivation of lysozyme. Biochim Biophys Acta. 1952; 8(0): 302–309.
12. Xie J, Qin M, Cao Y, Wang W. Mechanistic insight of photo-induced aggregation of chicken egg white lysozyme: The interplay between hydrophobic interactions and formation of intermolecular disulfide bonds. Proteins. 2011; 79(8): 2505–2516. doi: 10.1002/prot.23074 PMID: 21661057
13. Maroufi B, Ranjbar B, Khajeh K, Naderi-Manesh H, Yaghoubi H. Structural studies of hen egg-white lysozyme dimer: Comparison with monomer. BBA Proteins and Proteomics. 2008; 1784(7–8): 1043–1049. doi: 10.1016/j.bbapap.2008.03.010 PMID: 18439436
14. Neves-Petersen MT, Klitgaard S, Pascher T, Skovsen E, Polivka T, Yartsev A, et al. Flash Photolysis of Cutinase: Identification and Decay Kinetics of Transient Intermediates Formed upon UV Excitation of Aromatic Residues. Biophys J. 2009; 97(1): 211–226. doi: 10.1016/j.bpj.2009.01.065 PMID: 19580759
15. Neves-Petersen MT, Snabe T, Klitgaard S, Duroux M, Petersen SB. Photonic activation of disulfide bridges achieves oriented protein immobilization on biosensor surfaces. Protein Sci. Logo of prosci.2006; 15(2): 343–351.
16. Moghadam TT, Ranjbar B, Khajeh K, Etezad SM, Khalifeh K, Ganjalikhany MR. Interaction of lysozyme with gold nanorods: conformation and activity investigations. Int. J. Biol. Macromol. 2011; 49(4): 629–636. doi: 10.1016/j.ijbiomac.2011.06.021 PMID: 21729718
17. Moghadam TT, Ranjbar B, Khajeh K. Conformation and activity of lysozyme on binding to two types of gold nanorods: A comparative study. International J. Biol. Macromol. 2012; 51(1–2): 91–96.
18. Neves-Petersen MT, Klitgaard S, Skovsen E, Petersen SB, Tømmeraas K, Schwach-Abdellaoui K. Biophysical Properties of Phenyl Succinic Acid Derivatised Hyaluronic Acid. J. Fluoresc. 2010 2010; 20(2): 483–492.
19. Yang F Jr, Zhang M, Chen J, Liang Y. Structural changes of α-lactalbumin induced by low pH and oleic acid. BBA Proteins and Proteomics. 2006; 1764(8): 1389–1396. PMID: 16920042
20. Water JJ, Schack MM, Velazquez-Campoy A, Maltesen MJ, van de Weert M, Jorgensen L. Complex coacervates of hyaluronic acid and lysozyme: Effect on protein structure and physical stability. Eur. J. Pharm. Biopharm. 2014; 88(2): 325–331. doi: 10.1016/j.ejpb.2014.09.001 PMID: 25218319
21. Anderson EA, Alberty RA. Homnogeneity and the Electrophoretic Behavior of Some Proteins. H. Reversible Spreading and Steady-State Boundary Criteria. J. Phys. Colloid Chem. 1948; 52(8): 1345–1364. PMID: 18100073
22. Murphy C, Sau T, Gole A, Orendorff C, Gao J, Gou L, et al. Anisotropic metal nanoparticles: Synthesis, assembly, and optical applications. J Phys Chem B. 2005; 109(29): 13857–13870. PMID: 16852739
23. Diamond R. Real-space refinement of the structure of hen egg-white lysozyme. J. Mol. Biol. 1974; 82 (3): 371–391. PMID: 4856347
24. Geerlof A, Brown J, Coutard B, Egloff M-P, Enguita FJ, Fogg MJ, et al. The impact of protein characterization in structural proteomics. Acta Crystallogr. D. 2006; 62(10): 1125–1136.
25. Fukunaga Y, katsuragi Y, Izumi T, sakiyama F. Fluorescence Characteristics of Kynurenine and N′-Formylkynurenine, Their Use as Reporters of the Environment of Tryptophan 62 in Hen Egg-White Lysozyme. J. Biochem. 1982; 92(1): 129–141. PMID: 7118867
26. Malencik D, Anderson S. Dityrosine as a product of oxidative stress and fluorescent probe. Amino acids. 2003; 25(3–4): 233–247. PMID: 14661087
27. Jacob JS, Cistola DP, Hsu FF, Muzaffar S, Mueller DM, Hazen SL, et al. Human Phagocytes Employ the Myeloperoxidase-Hydrogen Peroxide System to Synthesize Dityrosine, Trityrosine, Pulcherosine, and Isodityrosine by a Tyrosyl Radical-dependent Pathway. J. Biol. Chem. 1996; 271(33): 19950–19956. PMID: 8702710
28. Wimmer R, Olsson M, Neves Petersen MT, Hatti-Kaul R, Petersen SB, Müller N. Towards a molecular level understanding of protein stabilization: the interaction between lysozyme and sorbitol1. J. Biotech. 1997; 55(2): 85–100.

29. Blumlein A, McManus JJ. Reversible and non-reversible thermal denaturation of lysozyme with varying pH at low ionic strength. BBA Proteins and Proteomics. 2013; 1834(10): 2064–2070. doi: 10.1016/j.bbapap.2013.06.001 PMID: 23774197

30. Phillips DC. The hen egg-white lysozyme molecule. Proc. Natl. Acad. Sci. U.S.A.. 1967; 57(3): 483–495.

31. Canfield RE, Liu AK. The Disulfide Bonds of Egg White Lysozyme (Muramidase). J. Biol. Chem. 1965 May 1, 1965; 240(5): 1997–2002.

32. Anpo M, Kamat PV. Environmentally benign photocatalysts: applications of titanium oxide-based materials. 1st ed. New York: Springer Science & Business Media; 2010.

33. Kraemer KH. Photochemical and Photobiological Reviews (Book). J. Invest. Dermatol. 1978; 70(5): 299–300.

34. Cockell CS, Airo A. On the plausibility of a UV transparent biochemistry. Orig. Life Evol. Biosph. 2002; 32(3): 255–274. PMID: 12227430

35. Grossweiner L. Photochemical inactivation of enzymes. Curr. Top. Radiat. Res. 1976; 11(2): 141–199.

36. Correia M, Thiagarajan V, Coutinho I, Gajula GP, Petersen SB, Neves-Petersen MT. Modulating the Structure of EGFR with UV Light: New Possibilities in Cancer Therapy. PLoS ONE. 2014; 9(11): e111617. doi: 10.1371/journal.pone.0111617 PMID: 25386651

37. Neves-Petersen MT, Gajula GP, Petersen S. UV light effects on proteins: from photochemistry to nanomedicine: INTECH Open Access Publisher; 2012.

38. Ali MS, Al-Lohedan HA, Rafiquee MZA, Atta AM, Ezzat AO. Spectroscopic studies on the interaction between novel polyvinylthiol-functionalized silver nanoparticles with lysozyme. Spectrochim. Acta A. Mol. Biomol. Spectrosc.2015; 135(0): 147–152.

39. Ziyarat PF, Asoode A, Sharif Barfeh Z, Pirouzi M, Chamani J. Probing the interaction of lysozyme with ciprofloxacin in the presence of different-sized Ag nanoparticles by multispectroscopic techniques and isothermal titration calorimetry. J Biomol Struct Dyn. 2014; 32(4): 613–629. doi: 10.1080/07391102.2013.785919 PMID: 23659247

40. Sattar Z, Iranfar H, Asoodeh A, Saberi MR, Mazhari M, Chamani J. Interaction between holo transferrin and HSA—PPIX complex in the presence of lomefloxacin: An evaluation of PPIX aggregation in protein—protein interactions. Spectrochim Acta A Mol Biomol Spectrosc. 2012 97:1089–1100. doi: 10.1016/j.saa.2012.07.034 PMID: 22925987

41. Sherin PS, Grilj J, Kopylova LV, Yanshole VV, Tsentalovich YP, Vauthey E. Photophysics and photochemistry of the UV filter kynurenine covalently attached to amino acids and to a model protein. J Phys Chem B. 2010; 114(36):11909–11919. doi: 10.1021/jp104485k PMID: 20722363

42. Nerlove M, Wallis KF. Use of the Durbin-Watson statistic in inappropriate situations. Econometrica. 1966:235–238.

43. Yamashita S, Nishimoto E, Yamasaki N. The Steady State and Time-resolved Fluorescence Studies on the Lysozyme-Ligand Interaction. Biosci. Biotechnol. Biochem. 1995; 59(7): 1255–1261. PMID: 7670186

44. Volden S, Lystvet SM, Halskau Ø, Glomm WR. Generally applicable procedure for in situ formation of fluorescent protein-gold nanoconstructs. RSC Advances. 2012; 2(31): 11704–11711.

45. Du J, Xia Z. Interactions of Gold Nanoparticles and Lysozyme by Fluorescence Quenching Method. Analytical Letters. 2012; 45(15): 2236–2245.

46. Chanphai P, Bekale L, Tajmir-Riahi HA. Effect of hydrophobicity on protein—protein interactions. Eur Polym J. 2015; 67: 224–231.

47. Shen L, Rapenne L, Chaudouet P, Ji J, Picart C. In situ synthesis of gold nanoparticles in exponentially-growing layer-by-layer films. J. Colloid Interface Sci. 2012; 388(1): 56–66. doi: 10.1016/j.jcis.2012.06.079 PMID: 22981588

48. Shareghi B, Farhadian S, Zamani N, Salavati-Niasari M, Moshtaghi H, Gholamrezaei S. Investigation the activity and stability of lysozyme on presence of magnetic nanoparticles. J. Indust. Eng. Chem. 2015; 21(0): 862–867.

49. Sun J, Xu R, Yang Y. Conformational changes and bioactivity of lysozyme on binding to and desorption from magnetite nanoparticles. J. Chromatography B. 2011; 879(28): 3053–3058.

50. Si S, Mandal TK. Tryptophan-Based Peptides to Synthesize Gold and Silver Nanoparticles: A Mechanistic and Kinetic Study. Chemistry—A. 2007; 13(11): 3160–3168.

51. Durán N, Marcato PD, Durán M, Yadav A, Gade A, Rai M. Mechanistic aspects in the biogenic synthesis of extracellular metal nanoparticles by peptides, bacteria, fungi, and plants. Appl. Microbiol. Biotechnol.2011; 90(5):1609–1624. doi: 10.1007/s00253-011-3249-8 PMID: 21484205

52. Mitra RN, Das PK. In situ preparation of gold nanoparticles of varying shape in molecular hydrogel of peptide amphiphiles. J. Phys. Chem. C. 2008; 112(22): 8159–8166.

53. Kerwin BA, Remmele RL. Protect from light: photodegradation and protein biologics. J. Pharm. Sci. 2007; 96(6): 1468–1479. PMID: 17230445

54. Dooley M, Mudd J. Reaction of ozone with lysozyme under different exposure conditions. Arch. Biochem. Biophys. 1982; 218(2): 459–471. PMID: 7159096

55. Dreaden TM, Chen J, Rexroth S, Barry BA. N-formylkynurenine as a marker of high light stress in photosynthesis. J. Biol. Chem. 2011; 286(25): 22632–22641. doi: 10.1074/jbc.M110.212928 PMID: 21527632

56. Pryor WA, Uppu RM. A kinetic model for the competitive reactions of ozone with amino acid residues in proteins in reverse micelles. Journal of Biological Chemistry. 1993; 268(5): 3120–3126. PMID: 7679107

57. Mehler AH, Knox WE. The conversion of tryptophan to kynurenine in liver: Ii. The enzymatic hydrolysis of formylkynurenine. Journal of Biological Chemistry. 1950; 187(1): 431–438. PMID: 14794728

58. Pirie A. Fluorescence of N'-formylkynurenine and of protein exposed to sunlight. Biochem. J. 1972; 128 (5): 1365. PMID: 4674628

59. Marquez LA, Dunford HB. Kinetics of Oxidation of Tyrosine and Dityrosine by Myeloperoxidase Compounds I and II Implications for lipoprotein peroxidation studies. J. Biol. Chem. 1995; 270(51): 30434–30440. PMID: 8530471

60. Bayse GS, Michaels AW, Morrison M. The peroxidase-catalyzed oxidation of tyrosine. BBA Enzymology.1972; 284(1): 34–42.

61. Qian H, Howard R, Jianyong L. Biochemical identification and crystal structure of kynurenine formamidase from Drosophila melanogaster. Biochem. J. 2012; 446(2): 253–260. doi: 10.1042/BJ20120416 PMID: 22690733

62. Kurnasov O, Goral V, Colabroy K, Gerdes S, Anantha S, Osterman A, et al. NAD biosynthesis: identification of the tryptophan to quinolinate pathway in bacteria. Chem. Biol. 2003; 10(12); 1195–1204. PMID: 14700627

Article IV

Bio-production of gold nanoparticles for photothermal therapy

Catarina Oliveira Silva[1], Patrícia Rijo[1,2], Jesús Molpeceres[3], Lia Ascensão[4], Amílcar Roberto[1], Ana Sofia Fernandes[1,2], Ricardo Gomes[5], João M. Pinto Coelho[5,6], Ana Gabriel[7], Pedro Vieira[7] and Catarina Pinto Reis[1,6*]

[1]CBiOS, Research Center for Biosciences & Health Technologies, Universidade Lusófona, Campo Grande 376, 1749-024 Lisboa, Portugal.

[2]iMed.ULisboa, Instituto de Investigação do Medicamento, Faculdade de Farmácia, Universidade de Lisboa, 1649-003, Lisboa, Portugal.

[3]Department of Biomedical Sciences, Faculty of Pharmacy, University of Alcalá, Ctra. A2, km 33.600. Campus Universitario, 28871 Alcalá de Henares, Spain.

[4]CESAM, Universidade de Lisboa, Faculdade de Ciência s, CBV, Campo Grande, 1949-016, Lisboa, Portugal.

[5]Laboratório de Óptica, Lasers e Sistemas, Faculdade de Ciências, Universidade de Lisboa, 1649-038, Lisboa, Portugal.

[6]Instituto de Biofísica e Engenharia Biomédica, Faculdade de Ciências, Universidade de Lisboa, Campo Grande, 1749-016, Lisboa, Portugal.

[7]LIBPhys-UNL, Departamento de Física, Faculdade de Ciências e Tecnologia, Universidade Nova de Lisboa, 2829-516 Monte da Caparica, Portugal.

*** Corresponding Author:** Prof. Dr. Catarina Pinto Reis.

Therapeutic Delivery (Future Medicine), 7(5):287-304 (2016).

doi: 10.4155/tde-2015-0011.

Research Article

For reprint orders, please contact: reprints@futuremedicine.com

Therapeutic Delivery

Bioproduction of gold nanoparticles for photothermal therapy

Background: Photothermal response of plasmonic nanomaterials can be utilized for a number of therapeutic applications such as the ablation of solid tumors. **Methods & results:** Gold nanoparticles were prepared using different methods. After optimization, we applied an aqueous plant extract as the reducing and capping agent of gold and maximized the near-infrared absorption (650–900 nm). Resultant nanoparticles showed good biocompatibility when tested *in vitro* in human keratinocytes and yeast *Saccharomyces cerevisiae*. Gold nanoparticles were easily activated by controlled temperature with an ultrasonic water bath and application of a pulsed laser. **Conclusion:** These gold nanoparticles can be synthesized with reproducibility, modified with seemingly limitless chemical functional groups, with adequate controlled optical properties for laser phototherapy of tumors and targeted drug delivery.

First draft submitted: 5 January 2016; Accepted for publication: 4 March 2016; Published online: 14 April 2016

Keywords: bioproduction • gold nanoparticles • photothermal therapy

Catarina Oliveira Silva[1], Patrícia Rijo[1,2], Jesús Molpeceres[3], Lia Ascensão[4], Amílcar Roberto[1], Ana Sofia Fernandes[1,2], Ricardo Gomes[5], João M Pinto Coelho[5,6], Ana Gabriel[7], Pedro Vieira[7] & Catarina Pinto Reis*[,1,6]

[1]CBiOS, Research Center for Biosciences & Health Technologies, Universidade Lusófona, Campo Grande 376, 1749–024 Lisboa, Portugal
[2]iMed.ULisboa, Instituto de Investigação do Medicamento, Faculdade de Farmácia, Universidade de Lisboa, Portugal
[3]Department of Biomedical Sciences, Faculty of Pharmacy, University of Alcalá, Campus Universitario, Spain
[4]CESAM, Universidade de Lisboa, Faculdade de Ciências, Portugal
[5]Laboratório de Óptica, Lasers e Sistemas, Faculdade de Ciências, Universidade de Lisboa, Portugal
[6]Instituto de Biofísica e Engenharia Biomédica, Faculdade de Ciências, Universidade de Lisboa, Campo Grande, 1749–016, Lisboa, Portugal
[7]LIBPhys-UNL, Departamento de Física, Faculdade de Ciências e Tecnologia, Universidade Nova de Lisboa, Portugal
*Author for correspondence:
Tel.: +351 217 515 550
Fax: +351 2175 155 98
catarina.reis@ulusofona.pt

Cancer is considered one of the leading causes of morbidity and mortality worldwide [1]. The main goal of a cancer treatment program is to cure or, ultimately, to prolong the life of patients and ensure the best possible quality of life after survival. Photothermal therapy (PTT) of cancer is considered a minimally invasive treatment methodology compared to conventional chemotherapy treatments [2]. In PTT, the energy of the optical radiation is absorbed and transformed into heat, causing denaturation of proteins and tissue necrosis. Some intracellular constituents are released into the extracellular environment producing detrimental inflammatory response and, consequently, an irreversible damage to cells. The absorption of optical radiation for heat conversion can be significantly enhanced by gold nanostructures, owing to their strong surface plasmon band absorption. Light-absorbing metallic nanoparticles, such as gold nanoparticles, show promising therapeutic applications in cancer treatment, when showing improved characteristics (e.g., size, shape and plasmonic surface properties). In order to improve the PTT efficiency, gold nanoparticles can be biofunctionalized, for greater transport to the target tissues [3]. Near-infrared (NIR) lasers have demonstrated superior therapeutic value over visible light (532 nm) lasers, when combined with conjugated gold nanoparticles, by reducing the tumor growth without causing any collateral damage or inflammation of the surrounding normal tissues [4].

Herein we describe the preparation of gold nanoparticles according to three main production methods: the Turkevich method (1954) used to obtain spherical gold nanoparticles based on mild reduction with sodium citrate; the Brust–Schiffrin method (1994) based on stronger reduction agents like sodium borohydride; and the seed-mediated growth method (2001) consisted

FUTURE SCIENCE part of fsg

of different reducing and capping agents (i.e., shape modulators) [5]. Those gold nanoparticles exhibit suitable properties for photothermal therapy, but generally involve toxic chemicals as capping agents, which can cause some concerns *in vivo*. The use of polymers, with biocompatible and biodegradable features, have been described to promote the absorption of gold nanoparticles to longer wavelengths. Biogenic synthesis of nanomaterials show many advantages as it is cost-effectively, biocompatible, with low toxicity and based on easy methodologies [6]. Gold nanoparticles produced by these novel routes have been studied for their therapeutic value by easy synthesis, photostability, biofunctionalization with specific targeting moieties and combination of different morphologies [3,6,7]. Therefore, we have also prepared gold nanoparticles synthesized using green chemistry route and possessing NIR absorbance. The developed method in this work could be as an alternative synthesis method for metallic nanoparticles using both polysaccharides and phytochemicals as reducing and capping agents. All involved agents are easily available and completely safe, avoiding any toxicity on nontarget tissues. The addition of 'green' extracts from natural sources, as an alternative to more toxic substances such as hexadecyltrimethylammonium bromide (CTAB), is an ongoing approach through the use of the naturally antioxidant compounds, beyond their use as reducing agents and as capping agents [8–12]. Biopolymers (e.g., chitosan and hyaluronic acid [HA]) [13–15] or alternative methods, involving the use of UV and gamma radiation, for formation of gold nanoparticles, can be used to reduce the impact on viability of healthy cells [16].

Another important task is to promote the absorption of gold nanoparticles at the NIR window, also known as the 'optical therapeutic window' (wavelength range: around 650–900 nm), which has the lowest absorption by our tissues [17,18]. The use of this type of light (typically, laser radiation) allows higher penetration depths by minimizing the effect of absorption. In this region, the main attenuation cause becomes scattering, which has a major impact in reducing the in-depth irradiance (power/area) [19]. Since the interaction of NIR radiation with tissues is mainly thermal (for typical irradiation times), and regarding the relevant parameters, there is no major difference between healthy and unhealthy tissues. Photothermal therapy requires that an external element is added in order to increase the absorption in the zone where the heat generation is required. One solution is to take advantage of the new developments in the field of nanotechnology, in particular that of gold nanoparticles allowing easy biofunctionalization [20]. Nanoparticles are characterized by having high absorption in a specific wavelength band (or peak). This effect is known by surface plasmon resonance. Being a surface phenomenon, it depends on the size and shape of the nanoparticle but also of the materials (particle and medium). This is particularly critical in laser phototherapy of tumors and targeted drug delivery since just the functionalization of the nanoparticle can shift its initial resonance.

The cooperative application of photothermal therapy with gold nanoparticles have reached promising results, although a consensus approach of how to develop reproducible and biocompatible gold nanoparticles with a surface plasmon band resonance at NIR wavelength is still an ongoing issue. Based on these ideas, we aim to develop different multifunctional gold nanoparticles that will be activated by photothermal therapy and provide ablation of superficial cancers (e.g., skin and breast cancer) (Figure 1). Moreover, we have selected *Plectranthus saccatus* Benth. as our natural source for reducing and capping agents in gold nanoparticles production. Aqueous extracts of *P. saccatus* are rich in rosmarinic acid, caffeic acid and chlorogenic acid (1 mg of this extract contains 5.9, 0.26 and 0.042%, respectively, identified by HPLC-DAD) [10]. Currently, there are standard platforms that help to characterize natural products with biomedical activities. One of them is ORAC, an acronym that stands for oxygen radical absorbance capacity, being a high ORAC value indicative of a strong reducing capacity. Although there are no references available for *P. saccatus*, the related species rosemary shows great antioxidant properties as it shows, as well as its extract, a major content in rosmarinic acid and caffeic acid [21].

Gold nanoparticles were characterized in terms of particle size, polydispersity index (PI), zeta potential, morphology and also cytotoxicity profile in two different *in vitro* models: human keratinocytes (HaCaT cells) and yeast *Saccharomyces cerevisiae*. HaCaT model is a spontaneously transformed keratinocyte cell line from adult human skin with high capacity to proliferate *in vitro*. This cell line has been used for cytotoxicity assays with gold nanoparticles, allowing the characterization of these systems when size particle, gold concentration and reducing agents varied [22,23]. On the other hand, the main advantages of using *S. cerevisiae* as an *in vitro* model organism are the similarity with mammalian cells, the yeast fast growth, and the inexpensiveness and easy cultivation. Yeast can grow both in presence and absence of oxygen and, therefore, it is especially useful for toxicity studies involving oxidative stress-related mechanisms [24,25]. Throughout this study, we intend to select the best system for further functionalization with ligands with biological value and association with NIR light applied to photothermal therapy.

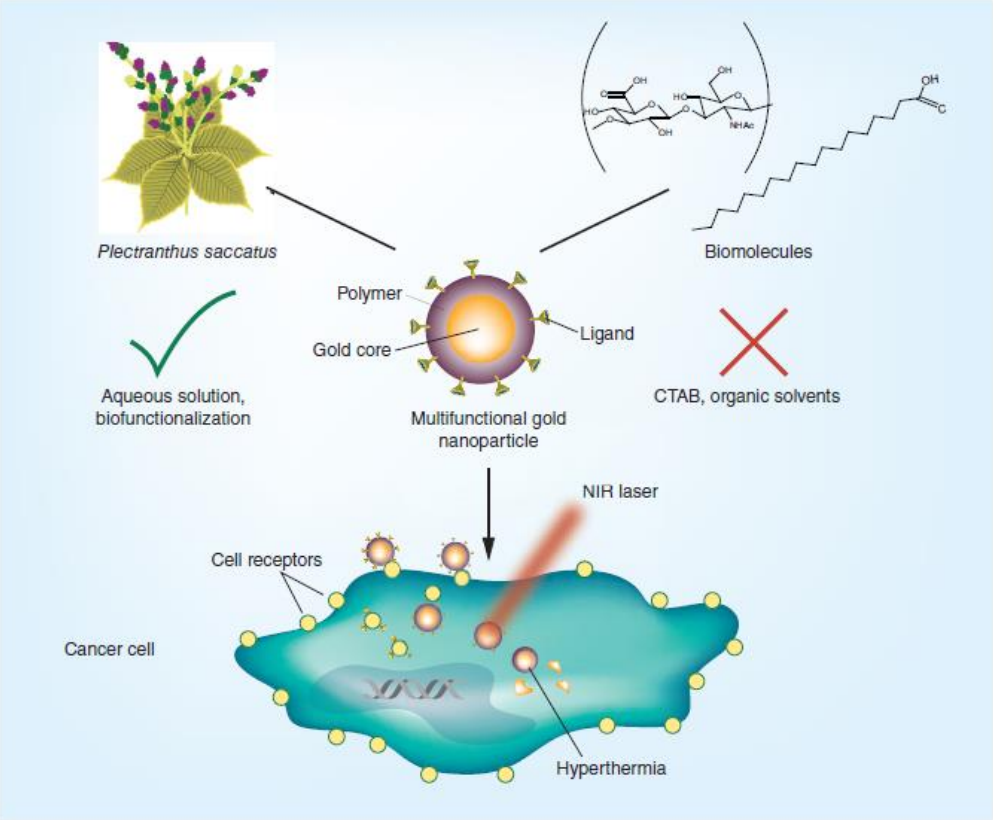

Figure 1. Methods for production of gold nanoparticles and their possible mechanism of action.

Materials & methods

Materials

Gold (III) chloride trihydrate ($HAuCl_4$), sodium citrate dihydrate ($C_6H_5Na_3O_7$), sodium borohydride ($NaBH_4$), hexadecyltrimethylammonium bromide (CTAB), L-ascorbic acid (L-AA), silver nitrate ($AgNO_3$), HA sodium salt from *Streptococcus equi* (MW: 7000–250,000 g/mol), oleic acid (OA) (MW: 282.46 g/mol), cholesterol-polyethylene glycol 600 sebacate (CHOL-PEG 600) were all supplied by Sigma-Aldrich (Steinheim, Germany). All reagents used for nanoparticles' preparation were of analytical grade. In addition, gold nanoparticles (diameter: 20 nm; Product Reference: 753610) and gold nanorods (Product Reference: 716820) were purchased from Sigma-Aldrich (Steinheim, Germany). The water used was purified (18.2 MΩ·cm at 25°C) through a Millipore system (Millipore, MA, USA). Thiazolyl Blue Tetrazolium Bromide (MTT), fetal bovine serum and penicillin/streptomycin were supplied by Sigma-Aldrich (Steinheim, Germany), as of cell culture grade. Dulbecco's Modified Eagle's medium was supplied by Biowest (Nuaillé, France) and DMSO was supplied by Merck (Darmstadt, Germany).

Production of gold nanoparticles by conventional methods

The Turkevich method was used to produce spherical gold nanoparticles previously described in the literature [26]. Briefly, in a round-bottom flask equipped with a condenser, 50 ml of 0.2 mM $HAuCl_4$ was brought to a rolling boil (~80°C), with vigorous stirring. To this solution, 5 ml of sodium citrate (4 mM) were added, resulting in a color change from pale yellow to dark red. Boiling was continued for 10 min; afterward, the heating mantle was removed and stirring was continued for 15 min. Further, a concentration of 1.0 mM $HAuCl_4$ was also tested, using the same method. The Brust–Schiffrin method for gold nanoparticles production was conducted according to a previous reference [27]. In summary, 0.1 M of $NaBH_4$ (0.6 ml) was used to reduce 0.2 mM $HAuCl_4$ (50 ml) for 18 h at 30°C. Finally, as the last classical method, the Seed-mediated Growth method was studied according to two differ-

ent procedures described in the literature [28,29]. Briefly, a first approach with CTAB (1 mM) and L-AA (2 mM) was studied by reducing 0.2 mM $HAuCl_4$ in a mixing reaction stirred vigorous for 4 h, at 30°C. Secondly, gold nanorods were also produced by preparing a seed solution with 0.6 ml iced-cooled $NaBH_4$ (0.1 M) and 5 ml CTAB (1 mM) to reduce 5 ml $HAuCl_4$ (0.2 mM). A Growth solution was prepared with 5 ml CTAB (1 mM), 70 µl L-AA (2 mM) and 280 µl $AgNO_3$ (1 mM) to reduce 5 ml $HAuCl_4$ (0.2 mM). The Seed solution (12 µl) was added to 10 ml and stirred vigorous for 4 h, at 30°C. Afterward, to continue the study of a novel method for formulation of gold nanoparticles, we selected the best conventional method for preparation of gold nanoparticles, according to the determination of the small mean particle size, polydispersity index and the specific absorbance spectra.

Novel method for gold nanoparticles preparation using an aqueous plant extract & biopolymers

The aqueous extract of *P. saccatus* was prepared according to the procedure described in the work developed by Rijo *et al.* using a microwave method [30]. Gold nanoparticles were produced based on the Seed-mediated Growth method developed by Murphy *et al.*, with some modifications [31]. First, citrate-coated gold nanoparticles were reduced with different molar ratios of *P. saccatus* aqueous extract (rosmarinic acid, as the main compound) with gold (2:1, 1:2, 1:4, 1:8, 1:10 and 1:20, molar ratio). The extract concentration necessary to get the higher reduction of gold nanoparticles was also selected. We tried to promote the development of gold nanoparticles with two curves for the surface plasmon band, typically a short wavelength band at about 520 nm (transverse oscillation) and a longer wavelength band at 700–800 nm (longitudinal oscillation) [32,33]. The aspect ratio of the gold nanoparticles (length/width) should be equal to 3–4 [34]. Further, we have selected the most suitable batch to proceed with the Seed-mediated Growth method for gold nanoparticles production. Briefly, the seed solution consisted on the previous formulation of the citrate-coated gold nanoparticles (1.0 mM $HAuCl_4$), isolated immediately with Milli-Q water. An aliquot (25 µl) of the seed solution was introduced into the growth solution consisting of $HAuCl_4$ (1 mM), aqueous extract of *P. saccatus* (1:4, molar ratio), L-AA (20 mM) and $AgNO_3$ (10 mM). Then, different parameters were evaluated for this preparation method: the time of the reaction (15 min, 1, 2, 3 and 24 h), the temperature (ice-cold reaction and sand-mantle at 60°C) and the pH of the growth solution (3 to 10). The addition of biopolymers was also studied: HA at 1 mg/ml; HA and oleic acid (HAOA) at 1 mg/ml (1:1, v/v), associated in a sand mantle at 60°C, pH = 10 for 24 h and 3) cholesterol-PEG 600 at 1 mg/ml. We allowed the gold nanoparticles to react with each polymer for 15 min [31,35]. Finally, we selected the best method for preparation of gold nanoparticles, according to the mean size, polydispersity index and potential zeta determination and the specific absorbance spectra.

Gold nanoparticles mean size, size distribution & zeta potential characterization

All gold nanoparticles produced in this study were recovered by centrifugation (Centrifuge High Speed Table Top Z 36 HK, Hermle Labortechnik, Germany) at speed rate of 33,768 g, at 4°C for 10 min and resuspended in the same water. Gold nanoparticles concentrated suspensions (10 ml) were characterized in terms of mean particle size, polydispersity index, by dynamic light scattering, in a Coulter Nano-sizer Delsa Nano C™ (Fullerton, CA, USA). A low value of polydispersity index factor (<0.3) indicates a less wide size distribution. For the gold nanoparticles prepared with the newly developed Seed-mediated Growth method (with and without biopolymers), the zeta potential was also measured in a Coulter Nano-sizer Delsa Nano C by applying an electrophoretic light scattering.

Absorbance spectra determination for gold nanoparticles

The maximum absorbance wavelength (λ_{max}) was determined and the gold nanoparticles concentration was determined according to the following formula (Equation 1):

$$\lambda_{max} = 450\ nm, Abs \times 0.416 = concentration\ (mM)$$

since at the mentioned wavelength, the absorbance is independent from size/shape [36].

Gold nanoparticles morphology characterization by scanning electron microscopy & by transmission electron microscopy

First, the morphology of the plain gold nanoparticles (i.e., uncoated) was obtained with a JEOL 5200LV scanning electron microscope (JEOL Ltd., Tokyo, Japan). Prior to examination, an aliquot of each sample was mounted on a glass coverslip and left to dry in a desiccator for 24 h. Afterward, the sample was coated with a thin layer of gold (100 nm thick) and observed at an accelerated voltage of 20 kV. Different fields of the images were recorded digitally.

For surface morphology characterization, samples of plain gold nanoparticles (i.e., uncoated) were observed by TEM, as well as samples of HA-coated gold nanoparticles, hyaluronic and oleic acids (HAOA)-coated gold nanoparticles and CHOL-PEG

600-coated gold nanoparticles. Samples were prepared through sequential two-droplet method by resuspending the gold nanoparticles in distilled water and placing a drop (5–10 µl) of the suspension for 30–60 s on a grid coated with Formvar. When the gold nanoparticles suspension had partly dried, the grid was washed with distilled water and the excess of water was removed with a filter paper. Then, sodium phosphotungstate (PTA, 2%, w/v) was applied to the grid for 10 s, and the excess of stain was removed with a filter paper. The grid was left to dry at room temperature for 24 h. The samples were analyzed at an accelerated voltage of 20 kV (TEM, Zeiss M10, Germany). Different fields of the images were recorded digitally.

Thermal activation of gold nanoparticles conjugated with two dyes, using an ultrasonic bath & a pulsed laser

First, dye release study was carried out using methylene blue, a hydrophilic dye, after association with HAOA-coated gold nanoparticles, detailed herein in the section titled 'Novel method for gold nanoparticles preparation using an aqueous plant extract & biopolymers'. Gold nanoparticles were incubated for 24 h, at pH = 7 and pH = 10, with methylene blue at 20 µg/ml, as described previously [37,38]. In addition, Sudan III, a hydrophobic dye, was also used for incorporation with HAOA-coated gold nanoparticles at pH =10 and at a concentration of 20 µg/ml. HAOA-coated gold nanoparticles conjugated with methylene blue and Sudan III were lyophilized (FreeZone 2.5 Liter Benchtop Freeze Dry System, Labconco, MO, USA) and incorporated, independently, in agar at 1% (w/v) inside glass cuvettes. These preliminary tests were used to observe the dye release after the gold nanoparticles re-suspension in Milli-Q water and exposure to ultrasounds water bath (Bandelin Sonorex Super Rk 510H, frequency of 45 kHz) varied in time (3 min until 3 h) and temperature (30–50°C). The cumulative percentage of Sudan III from the HAOA-coated gold nanoparticles (mean ± SD, n = 3) was determined by measurement of the absorbance over time (3 min until 3 h), at 516 nm, in the spectrophotometer (Thermo Scientific model Evolution 300 BB, UK). Moreover, the release of the dye from the nanoparticles, fixed in an agar phantom, was also observed by using a pulsed laser (frequency doubler Nd: YAG laser, emitting at a wavelength of 532 nm, 7 ns pulses, with an incident energy of 6.24 mJ), as a source of heat.

In vitro cytotoxicity studies

Cytotoxicity in human keratinocytes

Cell viability studies were conducted in human immortalized keratinocytes (HaCaT cells, CLS Cell Lines Service GmbH, Eppelheim, Germany) using the Thiazolyl blue tetrazolium bromide (MTT) assay [39,40], to assess the cytotoxicity of the extract of *P. saccatus* and HAOA-coated gold nanoparticles. Cells were cultured in Dulbecco's modified eagle's medium supplemented with 10% fetal bovine serum and 1% penicillin/streptomycin solution. HaCaT cells were seeded in a 96-well plate at a density of 5000 cells/well. After a 24 h-incubation, cells were exposed to aqueous extract of *P. saccatus* (10–500 µg/ml) or to HAOA-coated gold nanoparticles (1–80 µM, based on the gold's concentration). DMSO 5% (v/v) was used as the positive control group, while non treated cultures were the negative control group. After 24 h, cells were washed with PBS and incubated with MTT solution (0.5 mg/ml in culture medium) for 2.5 h at 37°C. Finally, the medium was removed and cells were washed with PBS. DMSO (200 µl/well) was added to dissolve the formazan crystals and absorbance was read at 595 nm (Thermo Scientific Multiskan FC, Shanghai, China). Two to six independent experiments were carried out, each comprising four replicate cultures (n = 2–6).

Cytotoxicity on S. cerevisiae *model*

Saccharomyces cerevisiae (ATCC® 9763™) grew in yeast extract peptone dextrose medium containing 1% yeast extract, 0.5% peptone and 2% glucose. Approximately 2.0 × 10^5 cells/ml were cultured in yeast extract peptone dextrose medium in disposable cuvettes, with a final volume of 2 ml. Non treated cultures were used as the negative control, while the positive one contained nystatin at 1 µg/ml. HAOA-coated gold nanoparticles were tested at two different concentrations (60 and 150 µM, based on gold's concentration). Before adding the HAOA-coated gold nanoparticles to the yeast cultures, an ultrasonic bath Bandelin SONOREX Super RK510 was used to homogenize the nanoparticles suspensions, for 2–5 min. Afterward, the method was carried out as described by Roberto *et al.* [25,41]. Briefly, the cultures were mized in a vortex before absorbance measurements, at 525 nm, in the spectrophotometer (Thermo Scientific model Evolution 300 BB, UK). The growth curve in the logarithmic phase for each tested group, as well as for the control group was conducted by correlating the logarithm of the cell concentration (number of cells/ml) against the time of incubation. Each group was tested in four replicates (n = 4) and the cells' concentration was calculated as previously described by Roberto *et al.* [25]. For each sample and corresponding concentration, the growth inhibition (GI, %) was calculated from the linear slope in the logarithmic phase of *S. cerevisiae* growth curve.

Statistical analysis

Results were expressed as mean ± SD. The significance of differences was assessed using a Student's t-test was conducted for independent (unpaired) samples for MTT studies with HaCaT cell line ($p < 0.01$ vs control, as the significance level).

Results

Production of gold nanoparticles by conventional methods

Herein, by using the materials described previously, we produced gold nanoparticles according to the three main conventional methods (i.e., Turkevich method, Brust–Schiffrin method and Seed-Growth method). The evaluation of the gold nanoparticles characterization according to their size, polydispersity index and surface plasmon band, obtained through UV-visible spectrometry, allowed us to select the best suitable way to produce gold nanoparticles with a small particle size, monodisperse particle size distribution (PI < 0.3) and maximum absorbance wavelength (λ_{max}) around the NIR range. Results for gold nanoparticles characterization are showed in Table 1 (n = 3, mean ± SD). In all cases, gold nanoparticles prepared by the above-mentioned conventional methods had small size (<100 nm) and were monodisperse. In terms of concentration, gold nanoparticles demonstrated a variation from 0.050 to 0.250 mM if the formulation had a light or dark red color, respectively.

Citrate-coated gold nanoparticles prepared by the Turkevich method showed higher stability with a size range from 20 to 30 nm, a PI around 0.3, with no aggregation, and a maximum absorbance peak at 525 nm. The concentration was also 0.173 and 0.160 mM, before and after exposure to an ultrasound water bath, respectively (data not shown). Further, we studied the physical characterization and concentration of citrate-coated gold nanoparticles for 1 month, in Milli-Q water medium, under storage conditions (6–8°C). This preliminary study on stability showed that the gold nanoparticles were stable for 1 month, maintaining a size between 10 and 30 nm (PI < 0.3). After 1 month, we confirmed the presence of some aggregates and a change to an acid pH of the solution, but a slight blueshift of the maximum absorbance peak from 352 to 350 nm (2 nm; data not shown). Besides, citrate is considered a mild and less toxic reducing agent. Therefore, we choose the citrate-coated gold nanoparticles to continue our studies. When manipulating gold concentration ($HAuCl_4$ at 0.2 mM and at 1.0 mM), we obtained a wide range of size distribution, with smaller and monodisperse nanoparticles (size <50 nm) or larger polydisperse nanoparticles (>50 nm), as demonstrated in Figure 2.

Novel method for gold nanoparticles preparation using a plant extract & biopolymers

After producing the desired gold nanoparticles formulation, based on the conventional methods described in the literature, we tested the introduction of several modifications to those preparation methods. The Seed-mediated Growth method was selected as the main production for our gold nanoparticles due to the great possibilities to modify and optimize this method. First, the previous selected formulation of citrate-coated gold nanoparticles (1.0 mM $HAuCl_4$), isolated immediately with Milli-Q water was used as seed solution. Gold nanoparticles produced by the citrate-based reduction method are normally used as seed solutions for growth of larger particles prepared by the Seed-mediated Growth method. In order to apply the citrate-coated gold nanoparticles as 'Seed' for production of larger gold nanoparticles, we selected the citrate-coated gold nanoparticles produced with a best citrate-gold ratio (1:4, $HAuCl_4$: citrate, molar ratio), showing a final mean size of 160.5 ± 50.3 (PI: 0.182) and a λ_{max} around 600 nm.

After preparing the seed solution, we dedicated efforts to develop a new growth method for production of gold nanoparticles with a maximum absorbance wavelength around 800 nm. To improve the biocompatibility profile of the gold nanoparticles and minimize the use of toxic reducing agents, we replaced the reducing and capping agent, CTAB, for an aqueous plant extract. Different molar ratios of an aqueous extract of *Plectranthus saccatus* and gold were evaluated to reduce citrate-coated gold nanoparticles, as demonstrated in Table 2. The reaction was stopped after 24 h, since the absorption at higher surface plasmon band only appeared after this time. Also, as showed in Table 2, for molar ratios above 1:4, two maximum absorbance wavelengths are detectable: transverse oscillation (short wavelength band, at 530–550 nm) and longitudinal oscillation (long wavelength band at 700–800 nm). In this case, 1:4 molar ratio showed higher gold nanoparticles concentration after reaction and, therefore, we used this formulation for further testing regarding the seed-mediated growth method.

To reduce the time of the reaction, the growth solution was improved with another natural and well-known reducing agent, L-ascorbic acid, and silver nitrate, in lower concentrations, as an additional capping agent (Table 3). We observed that the addition of both L-ascorbic acid and silver nitrate to solution containing the aqueous extract of *P. saccatus* led to the formation gold nanoparticles of small size, with low polydispersity index (PI = 0.12) and a maximum absorbance wavelength at the NIR range. Further,

Table 1. Characterization of gold nanoparticles produced by conventional methods, in terms of size (diameter), polydispersity index (PI) and maximum wavelength for absorbance spectra (λ_{max}), (mean ± SD).

Method	Size ± SD (nm)	PI	λ_{max} (nm)
Turkevich method	20.1 ± 12.9	0.304	525
Brust–Schiffrin method	14.2 ± 9.9	0.118	526
Seed-mediated growth method (reduction only with CTAB and L-AA)	91.4 ± 61.5	0.278	575
Seed-mediated growth method	57.2 ± 38.8	0.310	535

other parameters such as time, pH and temperature of the reaction, as well as the addition of different coating polymers were also evaluated. Results summarized in Table 3 show that gold nanoparticles had a higher mean size when the reaction time was reduced to 15 min, but also increased the maximum wavelength value at 830 nm. The absorbance spectra of these gold nanoparticles is represented in Figure 3A. If the reaction was prolonged until 24 h, gold nanoparticles size would increase, but the wavelength for the maximum absorbance would undergo a blueshift. The increase of the reaction pH and temperature did not show a great impact neither on the gold nanoparticles' size, nor on the maximum absorbance wavelength.

After changing the reaction parameters (time, pH and temperature), we defined the preparation method of the plain gold nanoparticles (i.e., uncoated) based on the modified Seed-mediated Growth method. The presence of the aqueous extract of *P. saccatus* in association with L-ascorbic acid and silver nitrate, as well as the time (15 min) and pH (= 10) of the Growth solution, seemed to be essential for obtaining gold nanoparticles with a maximum absorbance wavelength around 800–900 nm (Figure 3A). In addition, gold nanoparticles morphology observed by SEM shows that these nanoparticles have mainly a spherical form but rod-like particles also existed (Figure 3B).

At last, we tested the use of different biomolecules as coating polymers (Table 3). HA-coated gold nanoparticles, HAOA-coated gold nanoparticles and CHOL-PEG 600-coated gold nanoparticles were evaluated in terms of their size, polydispersity index, zeta potential, maximum absorbance wavelength (λ_{max}) and structure. As showed in Table 3, the coated gold nanoparticles showed a blueshift in their absorbance spectra and tuned to wavelengths of 500–600 nm, as the two longitudinal and transverse bands also merged into a single band. HAOA-coated gold nanoparticles showed an absorbance wavelength around 650–700 nm. In terms of size and polydispersity index, all systems showed a small particle diameter and a polydispersity index range from 0.1 to 0.3. Lastly, in terms of zeta potential, we found that plain gold nanoparticles (i.e., uncoated) showed a neutral surface charge (0.26 mV), but after addition of the biopolymers the surface charge of the gold nanoparticles changed, according to the polymer used. While HA-coated gold nanoparticles and CHOL-PEG 600-coated gold nanoparticles showed small variations (-0.17 and -3.32 mV, respectively), HAOA-coated gold nanoparticles demonstrated a greater impact on the nanoparticles surface charge, having a higher negative zeta potential of -19.25 mV.

By TEM we observe polydisperse gold nanoparticles populations and different structures, after the addition of biomolecules (Figure 4A–D). This feature is more visible after addition and reaction of the gold nanoparticles with HAOA and HA, leading to the formation of new structures with singular shapes. We may suggest that the compounds of the aqueous extract of *P. saccatus* (mainly rosmarinic acid) can work similarly to CTAB, while oleic acid (as a surfactant) and HA (as a polysaccharide) can be also capable of modulating the gold nanoparticles shape. HAOA addition led to the formation of structures with octahedral sections with an internal angle of ~110–120 degrees, while HA addition resulted specially in development of structures with triangular sections (almost equilaterals) with an internal angle of ~60–70 degrees. In addition, as showed in Figure 5A, HAOA-coated gold nanoparticles are present mainly as spheres but also nonspherical structures, such as octahedral and triangular forms. As for the absorption spectra (Figure 5B), when compared to commercial gold nanospheres of ~20 nm (525 nm) and gold nanorods (810 nm), a broad spectrum is observed at 650–700 nm (λ_{max}= 709 nm), but no peak at around 520–530 nm was visible. Lower absorption peak means high activation energy. For clinical application, the ideal system will require an adequate binomial relation between low activation energy and high depth.

Based on the overall evaluation of these four different coating for our gold nanoparticles, we have selected the HAOA-coated gold nanoparticles for further studies, regarding thermal activation and cytotoxicity assays.

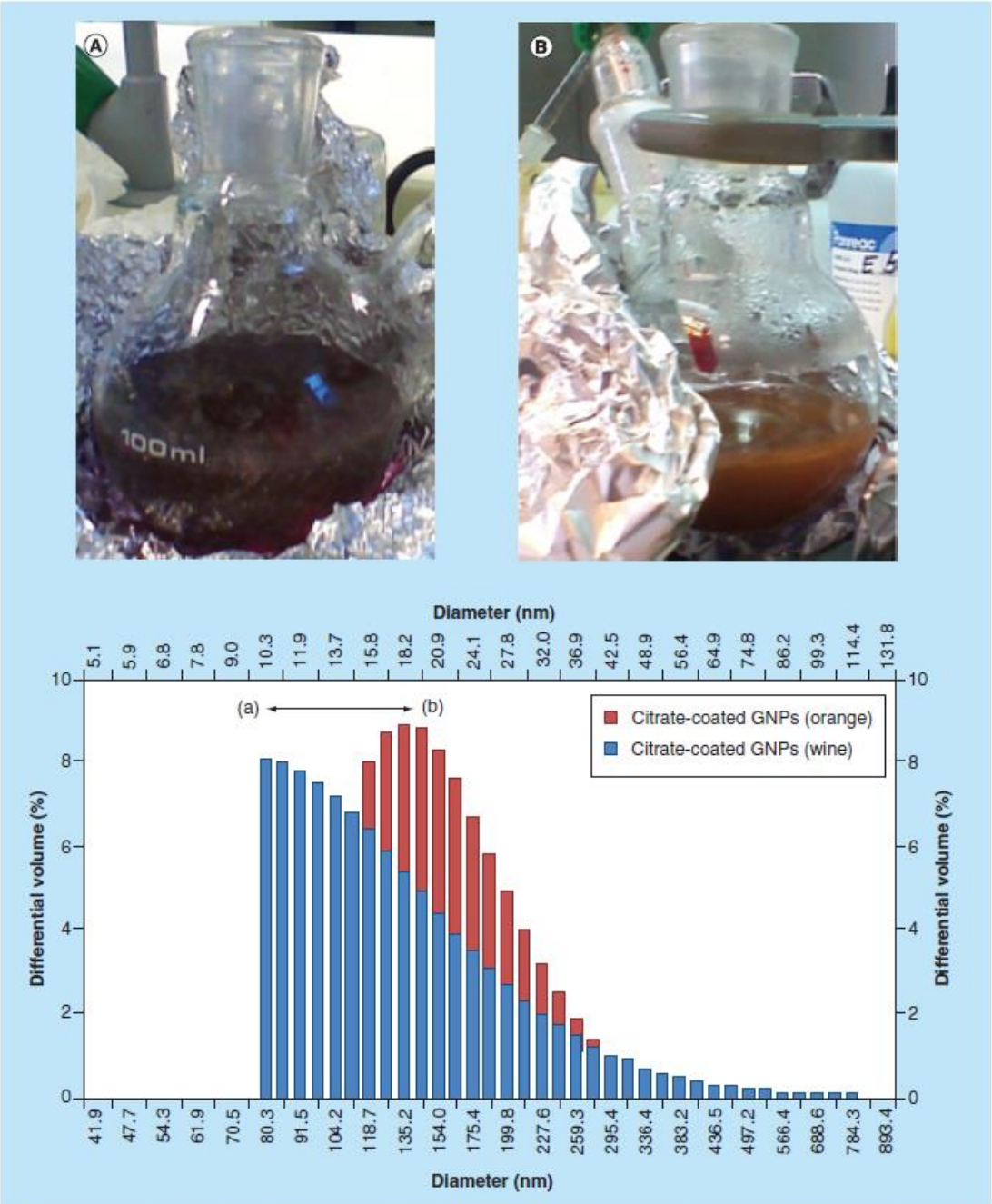

Figure 2. Size distribution (diameter as differential volume, %) for citrate-coated gold nanoparticles produced by the Turkevich method. Two different citrate-gold (HAuCl4) concentration ratios used: (A) 0.2 mM HAuCl4: 4.0 mM citrate; (B) 1.0 mM HAuCl4 : 4.0 mM citrate.

Thermal activation of gold nanoparticles conjugated with two dyes, using an ultrasonic bath & a pulsed laser

To test the thermal activation of the gold nanoparticles, we used, first, an ultrasonic bath (frequency: 45 kHz) and, second, a pulsed laser (frequency-doubled Nd: YAG laser, emitting at a wavelength of 532 nm). Two different dyes were selected for association with the HAOA-coated gold nanoparticles: Methylene Blue and Sudan III. Reaction with methylene blue and the nanoparticles at pH = 7 resulted in absence of conjugation. At pH = 10, a spectra of three peaks were obtained,

Table 2. Gold nanoparticles characterization for mean size, polydispersity index (PI) and maximum absorbance wavelength (λ_{max}) after reduction with different molar ratios of gold: aqueous extract of *Plectranthus saccatus* (mean ± SD).

Gold: *Plectranthus saccatus* (molar ratio)	Mean size ± SD (nm)	PI	λ_{max} (nm)
2:1	159.6 ± 65.9	0.146	532
1:2	71.8 ± 36.0	0.263	550
1:4	194.7 ± 76.2	0.195	570; 800
1:8	158.7 ± 55.7	0.182	548; 805
1:10	194.2 ± 37.5	0.199	550; 800
1:20	196.0 ± 36.3	0.102	543; 791

Table 3. Gold nanoparticle mean size, polydispersity index (PI) and λ_{max} according to parameters studied for the seed-mediated growth method (mean ± SD).

Parameters studied		Size ± SD (nm)	PI	λ_{max} (nm)
Reduction/capping agents	Silver nitrate	50.0 ± 5.4	0.288	537
	L-ascorbic acid	57.7 ± 37.9	0.280	540
	L-ascorbic acid and silver nitrate	62.1 ± 15.5	0.122	580; 988
Reaction time	15 min	194.2 ± 37.5	0.199	830
	30 min	21.9 ± 14.0	0.296	550
	2 h	26.0 ± 18.2	0.326	538
	24 h	74.1 ± 48.9	0.293	534
Reaction pH	4	99.1 ± 53.1	0.168	530
	5	137.7 ± 86.2	0.404	532
	6	127.5 ± 79.5	0.239	562
	7	99.4 ± 52.7	0.153	520
	8	116.6 ± 72.2	0.207	550
	9	83.1 ± 54.6	0.149	555
	10	119.8 ± 63.1	0.185	520
Reaction temperature	Ice-cold (< 0°C)	70.7 ± 48.0	0.209	525
	Sand mantle (60 ± 5°C)	86.3 ± 42.5	0.109	549
Polymers	HA	66.6 ± 41.8	0.284	543
	HAOA	139.3 ± 50.3	0.120	709
	CHOL-PEG 600	32.6 ± 21.1	0.328	531

as expected, for the HAOA-coated gold nanoparticles not conjugated (527 nm), methylene blue-conjugated HAOA-coated gold nanoparticles (613 nm) and methylene blue (664 nm), with higher absorbance at 613 nm [37]. Methylene blue conjugated HAOA-coated gold nanoparticles showed a size of 42.0 ± 24.3 nm (PI: 0.268). After exposure to ultrasounds water bath at a controlled temperature (3 h, 45 kHz, at 50°C), the dye was released immediately into the aqueous medium, as a result of heating the water and the initial pellet of nanoparticles was not detected. Even when a polymer was conjugated with the nanoparticles and after lyophilization, the dye naturally releases in the agar phantom, at room temperature (data not shown).

In contrast, results were different with the hydrophobic dye, Sudan III. HAOA-coated gold nanoparticles after conjugation with Sudan III showed a size of 56.9 ± 37.3 nm (PI: 0.375) and a smooth surface and shape, with some aggregates, as observed by SEM (Figure 6A). A single absorbance peak was observed, between the HAOA-coated gold nanoparticles λ_{max} of 595 nm and dye Sudan III of 507 nm, as referred previously [42], indicating that the nanoparticles successfully incorporated the dye, with a maximum absorbance wavelength of 516 nm. After ultrasounds water bath exposure (45 kHz, at 50°C, for 3 h), as a heat source, there was a decrease in the absorbance for the referenced wavelengths, which was quantified as the cumulative

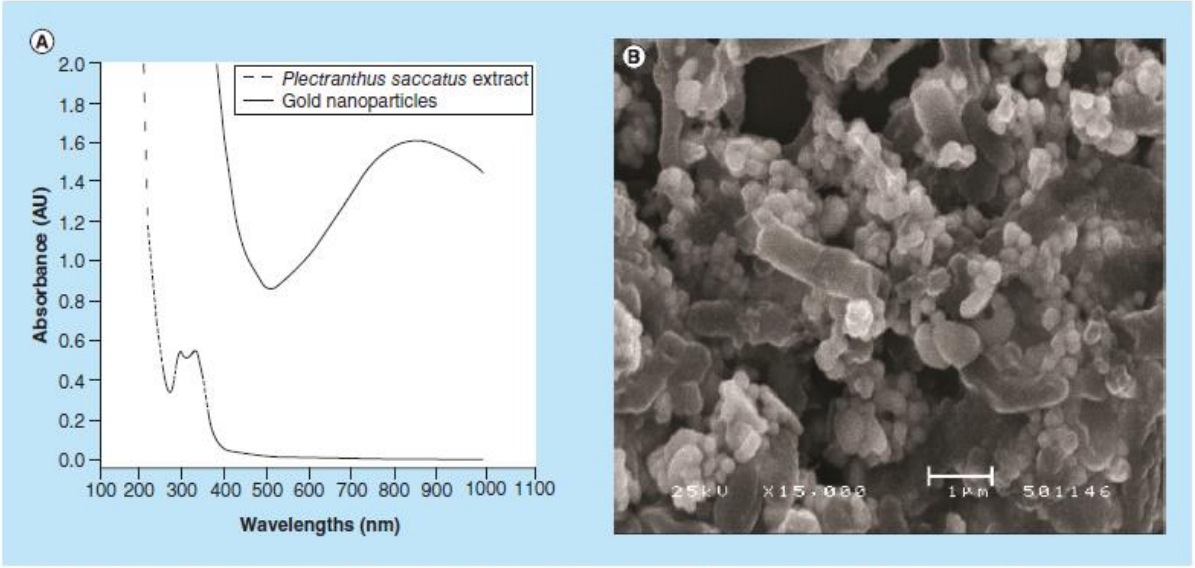

Figure 3. *Plectranthus saccatus* **aqueous extract and gold nanoparticles. (A)** Absorbance spectra of *P. saccatus* aqueous extract solution (dashed line) and plain gold nanoparticles after reduction with the same extract (continuous line); the formation of a surface plasmonic band for gold nanoparticles is visible around 830 nm. **(B)** SEM micrograph of plain gold nanoparticles produced according to the novel method using *P. saccatus* aqueous extract: gold molar ratio of 1:4.

percentage of dye release for 3 h (mean ± SD, n = 3) (Figure 6B). Better results were obtained with the laser experiments, since a clear dye release was observed each and after 6 shots with 7 ns and an incident energy of 6.24 mJ (Figure 7A & B). We expect that a higher amount of drug or dye would be released *in vivo*, because laser will be the source of energy.

In vitro cytotoxicity studies

Cytotoxicity in human keratinocytes

To evaluate the cytotoxicity, MTT assays on human keratinocytes (HaCaT) were first carried out with the aqueous extract of *P. saccatus,* within a concentration range suitable for the gold nanoparticles preparation. For the *P. saccatus* extract itself, HaCaT cells showed viability values over 80%, similar for all tested concentrations, as showed in Figure 8. As for HAOA-coated gold nanoparticles, concentrations ≤ 35 μM did not show to decrease cell viability. The highest concentration tested (80 μM) let to around 75% of cell survival ($p < 0.01$). No aggregates were visible after addition of the HAOA-coated gold nanoparticles to the wells.

Cytotoxicity on *Saccharomyces cerevisiae* model

The linear slope in the logarithmic phase for each sample was determined in order to allow the calculation of the growth inhibition percentage value (Figure 9). The exposure to HAOA-coated gold nanoparticles at lowest concentration (i.e., 60 μM) resulted in 6.0 ± 6.5% of growth inhibition and the highest concentration (i.e., 150 μM) resulted in 7.0 ± 3.3%. Conversely, nystatin used as positive control caused a growth inhibition of 64 ± 3.2%, while the negative control (no treatment) was assumed as producing zero percentage of growth inhibition (i.e., 100% yeast growth), in every experiment.

Discussion

In this study, we describe the sequential production and development of hybrid polymeric gold nanoparticles with a mean size around 100–200 nm and a low polydispersity index (PI < 0.3) and, foremost, with a maximum absorbance wavelength in the NIR range (650–900 nm), for further application in cancer photothermal therapy, activated with an 811 nm laser beam. First, we have evaluated the application of conventional methods for gold nanoparticles production (Table 1). Turkevich method is considered a simple one, as citrate works, as both as, reducing and the capping agent, creating negatively charged and spherical gold nanoparticles [16]. Citrate concentration ratio to gold is also an important factor for aggregation, as demonstrated in Figure 2, since at lower concentrations, this agent covers fewer gold nanoparticles and aggregation occurs; while at higher concentrations, smaller and stable gold nanoparticles are produced [16]. These physical modifications are also mentioned by other authors, which refer that when gold nanoparticles undergo aggregation, their electronic clouds overlap and, consequently, the maximum absorbance wavelength of the gold

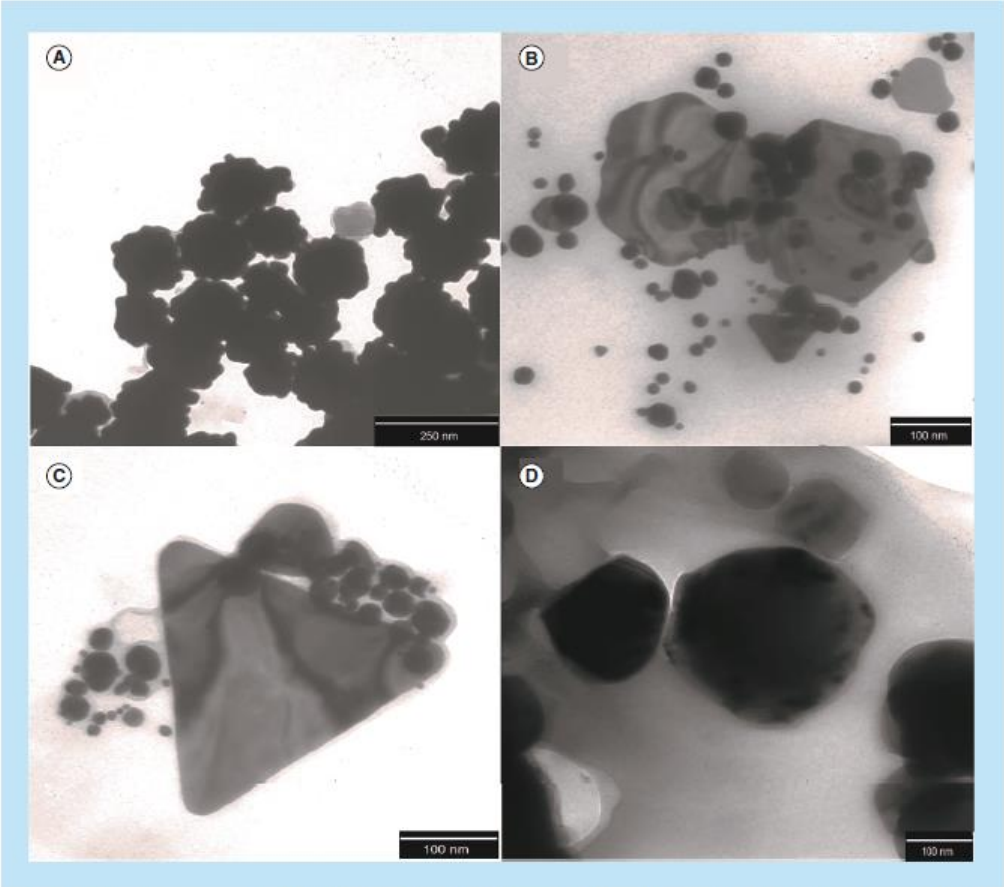

Figure 4. TEM micrographs. (A) Plain gold nanoparticles (uncoated); **(B)** HA-coated gold nanoparticles; **(C)** HAOA-coated gold nanoparticles; and **(D)** CHOL-PEG 600-coated gold nanoparticles.
HA: Hyaluronic acid; HAOA: Hyaluronic and oleic acids.

nanoparticles that behave as larger is redshifted [16,43]. Grabar *et al.* also followed the Turkevich method to develop small citrate-coated gold nanoparticles with a size of 13 nm, while aggregates redshifted to 600–800 nm, forming clusters made of spherical gold nanoparticles, which remain stable when kept in storage in water for 7 months [26]. Another interesting result of this study was accomplished with gold nanoparticles produced with sodium borohydride reduction, which are normally used as seeds for growing larger particles for the Seed-mediated Growth method. Through the Brust–Schiffrin method, developed to increase gold reduction by using stronger reducing agents (such as sodium borohydride), we have obtained the smallest gold nanoparticles, as expected and described in the literature [16]. However, due to the toxicity concerns involving this reducing agent, we selected the citrate-coated gold nanoparticles to continue our studies, since those gold nanoparticles also showed a small size and were stable for 1 month in aqueous solution.

After preparing the seed gold nanoparticles solution, we dedicated efforts to develop a new Seed-mediated Growth method, based on the reduction of gold using biomolecules and an aqueous extract of *P. saccatus*. Some of the reducing agents (e.g., sodium borohydride) and capping agents (e.g., CTAB) are generally toxic to cells and if not eliminated efficiently can increase cell death after interaction with gold nanoparticles [43,44]. Aiming to improve the biocompatibility of these gold nanoparticles we replaced CTAB for an aqueous extract of *P. saccatus* as the main reducing and capping agent. A lower ratio of the extract (1:4 molar ratio) was selected, as the reducing agent seemed enough to form gold nanoparticles (Table 2). In fact, it seems that the production of NIR-absorbing gold nanoparticles is obtained with low concentration of extracts, as reported in another study

using an extract of *Theobromo cacao* (cocoa) [21]. Also, we suggest that the gold nanoparticles are being reduced and formed with the aqueous extract of *P. saccatus* as the spectrum from the extract was completely different than the one from the gold nanoparticles (Figure 3A). SEM observations of plain gold nanoparticles (i.e., uncoated) allowed us to distinguish the formation of two different populations of nanostructures: nanorods and nanospheres (Figure 3B). Gold structures exhibit different shapes and presentations, such as spheres and clusters, as a result of the method used to prepare them. Spheres are the lowest-energy and bottom-up methods – which are the most frequent – cause a larger particle size distribution [45]. The use of impurities (i.e., low concentrated solution) of silver nitrate, is also reported in literature as an alternative method to control the yield of nanorods with the desired shape (short rods with ratio ~6), while L-ascorbic acid is applied as a mild reduction agent [34]. Anisotropic structures, like nanorods and other modified-surface structures, are a common features when gold nanoparticles production is based on biomolecules and natural extracts [21,46,47]. As the main advantages, gold anisotropic nanostructures show a controlled size and shape, mediated by the capping agents, as well as a large surface area and crystallographic facets good for biomolecules adsorption. Moreover, these

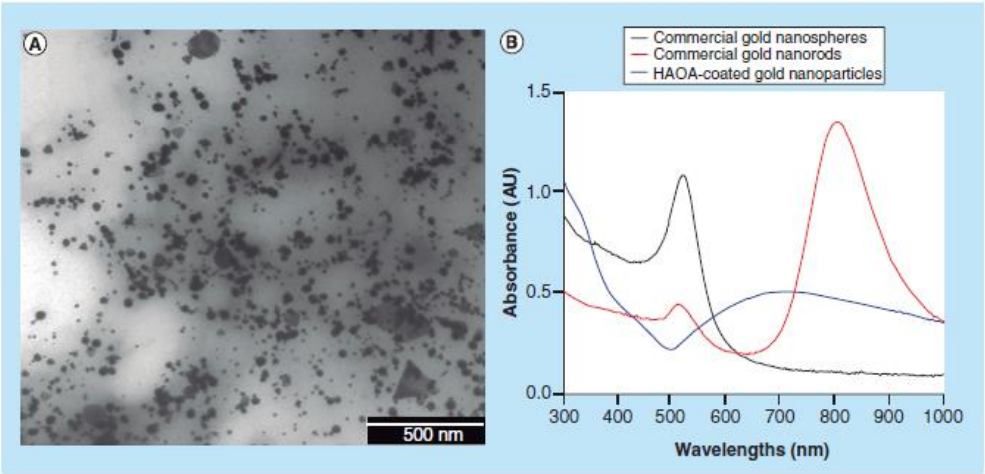

Figure 5. HAOA-coated gold nanoparticles. (A) TEM micrograph of hyaluronic and oleic acids (HAOA)-coated gold nanoparticles; **(B)** Absorbance spectra of commercial gold nanospheres (λmax= 525 nm) and nanorods (λmax= 520 nm + 810 nm) and HAOA-coated gold nanoparticles produced with *Plectranthus saccatus* extract and HAOA (λmax = 709 nm).

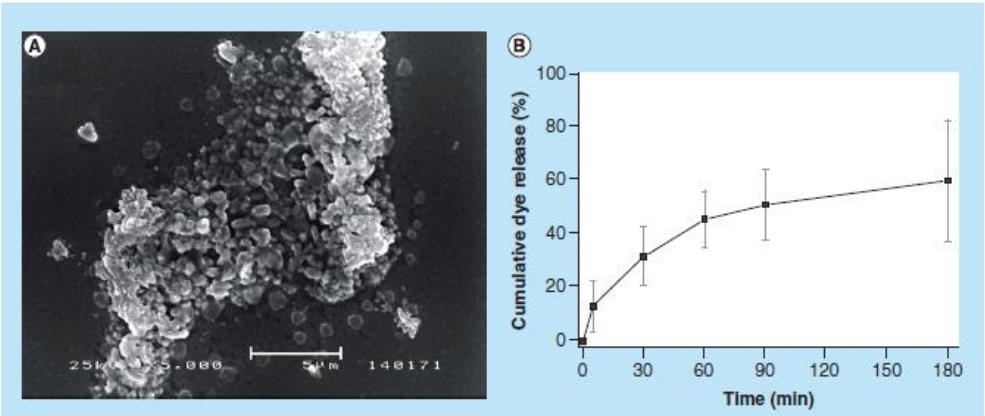

Figure 6. HAOA-coated gold nanoparticles conjugated with Sudan III. (A) SEM micrograph of HAOA-coated gold nanoparticles, conjugated with the hydrophobic dye Sudan III (SD) after lyophilization. **(B)** Cumulative dye release (%) after the gold nanoparticles exposure to ultrasound water bath (frequency of 45 kHz for 3 h) (mean ± SD, n = 3).

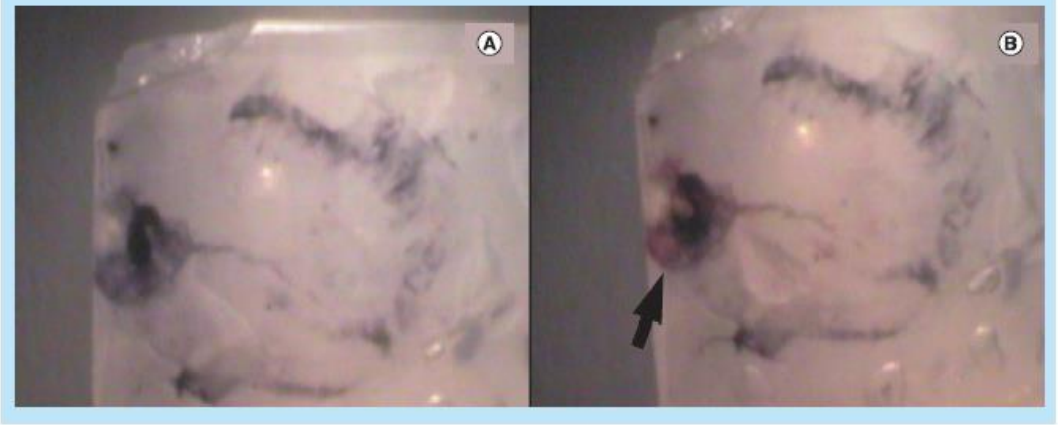

Figure 7. Agar phantom with HAOA-coated gold nanoparticles conjugated with Sudan III. (A) Before and **(B)** after irradiation with a laser pulsed beam (incident energy of 6.24 mJ after 6 shots of 7 ns duration). The arrow in **(B)** indicates the dye release zone.

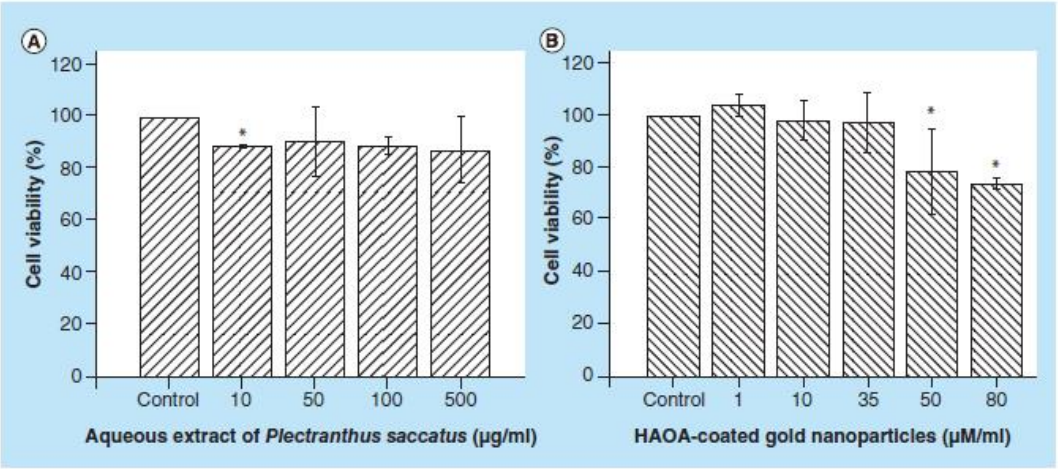

Figure 8. Thiazolyl blue tetrazolium bromide cytotoxicity assay in human keratinocytes HaCaT. (A) HaCaT cell viability (%) after 24 h exposure to the aqueous extract of *Plectranthus saccatus* up to 500 µg/ml. **(B)** HaCaT cell viability (%) after 24 h exposure to HAOA-coated gold nanoparticles up to 80 µM/ml (gold concentration; mean ± SD; n = 2–6) (Student's t-test, *p < 0.01 vs control).
HAOA: Hyaluronic and oleic acid.

structures possess optical and electronic features, such as an enhanced surface plasmon resonance band and tunable absorption from visible to NIR region, promoting their applicability in NIR phototherapy [7]. The assembly of these gold nanoparticles and their multiple interactions affects the surface plasmon band: side-by-side and end-to-end assemblies can cause spectra blueshifts (i.e., toward UV-Visible) or redshifts (i.e., toward NIR), respectively [45]. At last, monolayer coatings can be applied, considering a controlled drug release and avoiding the drug release before reaching the site of action [48]. In our experiments, we observed that the conjugation of three different biocompatible polymers (i.e., HA, HAOA and cholesterol-PEG 600) resulted in a redshift of the maximum absorbance wavelength to 650–900 nm (Table 3). Anisotropy creates species with higher surface to volume ratio (higher energy than spheres), but shows facets with lower surface energies [45], as we observed for our samples by TEM in Figure 4A–D. Capping molecules show adsorption to specific facets and can hinder or enhance the crystal growth in different directions and also increase production yield of monodisperse populations of nanoparticles [34,45]. As for pH and ionic strength, the addition of a basic solution to raise the pH of the growth solution, as we did in our experiments (Table 3), leads to more rapid growth due to forced reduction of gold ions and forms high-aspect-ratio nanorods [34,45]. In addition, and as verified in

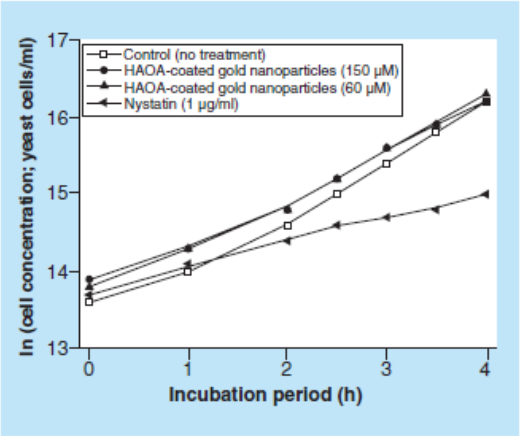

Figure 9. Growth curves of *Saccharomyces cerevisiae* cultures exposed to HAOA-coated gold nanoparticles (60 and 150 µM) or to nystatin (1 µg/ml), used as positive control. Yeast growth is presented as the natural logarithm of the cell concentration, which is expressed as number of yeast cells/ml. The interval 2–4 h was considered as the log growth phase (n = 4, mean ± SD).

this study (Table 3), low temperature (e.g., production in an ice-cooled bath) and fast addition of the reducing agent is also described for production of smaller and monodisperse gold nanoparticles [16]. Murphy *et al.* (2011) also described the formation of gold nanorods made through a silver-assisted Seed-mediated Growth method, which grow into structures with octahedrical sections, when exposed to ultrasonication (20 kHz, at 75°C) in an organic solvent and in combination with the polymer poly(vinylpyrrolidone) [34]. Highly anisotropic shapes are not consider favorable in terms of thermodynamics, but are also common when capping agents, such as CTAB, are present in the formulation [49]. In fact, biomolecules of extracts may simulate the CTAB bilayer effect for surface charge, preventing aggregation [44], while polymers such as poly(vinylpyrrolidone) can induce a shape-tunable effect on gold nanoparticles, determining the final structure and shape [49]. In this paper, we found evidence of anisotropic gold particles formation after the addition of HA and HAOA as coating polymers for the gold nanoparticles. It is known that both polysaccharides and phytochemicals act as reducing and capping agents in synthesis of metallic nanoparticles. The protonated forms of carboxylic, hydroxyl and amine groups, present in the compounds of natural plant extracts (e.g., terpenoids, polyphenols and flavonoids), are known to be capable of reducing gold and silver salts and also stabilizing the gold nanoparticles through surface binding [7,50,51]. Moreover, these functional groups are also present in the glucuronic acid and N-acetyl-glucosamine monomers of HA and in aliphatic chains of OA. Therefore, production of gold nanoparticles involving both HAOA, as well as the *Plectranthus saccatus* aqueous extract (easily available with high interest in scale-up for pharma industry) can promote an innovative synergistic approach for obtaining biocompatible nanostructures, with optimal size, surface charge and optical properties. In addition, HAOA-coated gold nanoparticles may surpass other formulations such as phospholipid and PEG gold nanoparticles, due to stability problems (conversion to nonbilayer structures) or blockage of targeting moieties, respectively [52,53].

Herein, we have study the production of gold nanoparticles in controlled conditions. Variations of these conditions, namely temperature, pH, stirring, extract concentration, gold salt concentration and addition of different biopolymers, allowed to obtain a controlled production of gold nanoparticles, mainly with spherical shape but also non-spherical structures, such as octahedral and triangular forms (Figure 5A). In addition, we compared the developed gold nanoparticles produced with phytochemicals and HAOA with commercial gold nanoparticles and gold nanorods with an absorbance spectrum in the visible (525 mn) and NIR region (810 nm), respectively (Figure 5B). HAOA-coated gold nanoparticles showed a peak for maximum absorption at 709 nm, indicating that after addition of biopolymers the gold nanoparticles still show an absorbance within the NIR range (i.e., 650–900 nm). Moreover, commercial gold nanorods showed a smaller peak at 520 nm, which is absent in developed HAOA-coated gold nanoparticles. Both commercial nanosystems will need more energy to be activated and non-target tissues (i.e., healthy cells) could be also irradiated by laser. HAOA-coated gold nanoparticles show a broad absorbance band instead of a narrow absorbance peak (lower activation energy). Although this first attempt for developing gold nanoparticles by 'green' synthesis, using both phytochemicals and biopolymers, show promising results for a future application in photothermal therapy, more investigation is needed to optimize this method.

Further, to test the activation of HAOA-coated gold nanoparticles with heat we exposed the systems to an ultrasounds water bath (45 kHz, at 50°C, for 3 h) and a pulsed beam with a frequency-doubler Nd: YAG laser, as heat sources. Photothermal therapy has demonstrated promising results for local cancer treatment-based hyperthermia applications, in association with gold nanoparticles absorbing in both visible and NIR range [20]. In this study, gold nanoparticles were successfully activated by temperature increase. According to previous reports, methylene blue is used to demonstrate the release profile from gold nanoparticles [38]; in this study, methylene blue was immediately released from the HAOA-coated nanoparticles, due to

its hydrophilic character and as a result of the heating. Therefore, we found that this dye was not suitable for our studies and we decided to use Sudan III, a hydrophobic dye, for the same type of experiments. Sudan III release was observed after exposure to the ultrasounds and determined as the dye release cumulative percentage (%) from the nanoparticles (Figure 6B) and to the pulsed laser at 532 nm (Figure 7A & B). In these preliminary experiments, we used a visible laser (i.e., green region of the spectra) as a first attempt to study the energy level and the thermal threshold for further application of these nanoparticles to a NIR-laser [54,55]. Thus, HAOA-coated gold nanoparticles appear to release the dye, according to a heat-dependent mechanism, probably associated with the disassembly of the polymeric coating [55]. However, besides the lower absorbance by tissue chromophores, reducing the damage by heating of the healthy tissue, NIR-lasers show efficient response in killing cancer cells with less power than the visible-lasers operate [20].

Additionally, the absence of toxicity of gold nanoparticles before the thermal activation is another key point of this study. For this, MTT assays in HaCaT and growth inhibition assays in yeast *S. cerevisiae* were helpful in determining the *in vitro* cytotoxicity profile of gold nanoparticles. Still, there were some restrictions that limited the range of the gold nanoparticles' concentrations tested. First, we faced a limitation of the production yield in terms of gold's concentration obtained after reduction, which limited the reachable concentration in the wells, when conducting the MTT assay with HaCaT cells. HAOA-coated gold nanoparticles tested were centrifuged before addition to cells' medium, in order to eliminate the absorption of the components involved in the gold reduction reaction, such as the polymers and the plant extract, and reduce the interferences, as recommended in the literature [56,57]. Hyaluronic acid present on the HAOA-coated gold nanoparticles may be responsible for pro-proliferating effects on cutaneous keratinocytes [58]. In addition, studying the cytotoxicity of the gold nanoparticles suspensions in *S. cerevisiae* model was restricted, because the HAOA-coated gold nanoparticles suspensions caused a background absorbance that limited the use of high concentrations in the experiment.

In terms of cytotoxicity, we observed that gold nanoparticles production with an aqueous extract of *P. saccatus* as the reducing agent, instead of CTAB, showed increased biocompatibility, in contrast to previous studies with conventional gold nanoparticles and nanorods [22,59,60]. Previously, the cytotoxicity of gold nanoparticles with different sizes, shapes and surface plasmon band characteristics (λ_{max} from 616 to 776 nm) were evaluated in HaCaT cell line, confirming again that the use of CTAB in formulation increased the *in vitro* toxicity of gold nanoparticles [22]. Moreover, other studies have reported the negative effect of CTAB attached to gold nanorods in human adenocarcinoma HT-29 cells, compared to other coating polymers such as polyacrylic acid and poly(allylamine) hydrochloride [60]. Similarly, for gold nanorods produced with CTAB when exposed to HEp-2 carcinoma cell line, an increased cytotoxicity was observed when compared to both free CTAB and polymeric (polystry renesulfonate [PSS] and poly(allylamine) hydrochloride [PAH]) coated nanorods [59]. Another issue is the adsorption of molecules from the growth media, to the gold nanoparticles surface, which is more likely to occur, due the increased surface area at nanoscale. As stated in literature, this phenomenon can also occur at *in vivo* conditions, when proteins, lipids and electrolytes are present; sometimes, these molecules change the surface charge of the gold nanoparticles, leading to the formation of aggregates [56]. Polymers coating and capping agents can surpass this disadvantage, as we observed that has occurred with our HAOA-coated gold nanoparticles. As referred before, similarly to the aqueous extract of *P. saccatus* used in the preparation of gold nanoparticles, plant extracts for production of metallic nanoparticles have been reported to have many other advantages, such as reduced environmental impact and an appropriate for large-scale production. The low cytotoxicity (less than 10% in both models) observed with our gold nanoparticles can be also related with the use of *P. saccatus* aqueous extract in alternative to conventional reducing and capping agents. As showed in this study, the aqueous extract of *P. saccatus* is devoid of relevant cytotoxicity. Considering *P. saccatus* components, such as rosmarinic and caffeic acids, we may anticipate that its antioxidant properties may enhance cell viability [6,24].

Finally, the obtained HAOA-coated gold nanoparticles could be further optimized for targeting drug delivery by ligand bioconjugation. Such strategy would allow the accumulation of the nanoparticles in cancer cells rather than normal cells. The best suitable system will be further conjugated to a specific natural ligand, such as the EGF (Silva O *et al.*, Submitted manuscript). EGF is the natural ligand for the EGFR, which belongs to the ErbB family of tyrosine kinases receptor and is overexpressed in several tumors, such as melanoma, increasing proliferation, migration and survival of tumor cells [61–63]. Biofunctionalization is now being conducted with the EGF targeting peptide, for further evaluation of its biological value in our formulation, in addition to a NIR laser beam irradiation for photothermal therapy.

Conclusion

In conclusion, we produced shape-tunable gold nanoparticles through gold reduction and conjugation with natural compounds and without the use of toxic agents, such as CTAB. This plant extract slightly increased the nanoparticle size and modified their shape. It also strongly influenced the gold nanoparticles' localized surface plasmon resonance band to reach the near-infrared wavelength (~800 nm) but did not increase the *in vitro* toxicity of gold nanoparticles before its thermal activation. Thus, this study provides evidence that this kind of gold nanoparticles could be an attractive system for photothermal therapy in cancer. Further research, now in progress, includes the incorporation of a specific ligand and the study of these nanoparticles in other *in vitro* and *in vivo* systems.

Future perspective

Novel potential targets and paths are being explored by clinicians and researchers to find better solutions and safer therapies that increase patient's compliance and life quality. Gold nanoparticles can help in molecular characterization and detection of cancerous or even precancerous tissues, with high accuracy and specificity. Therefore, gold nanoparticles are excellent platforms for *in vivo* tracking of biomolecules as a diagnostic mechanism and, furthermore, associated with chemotherapy. In the future, NIR light-based therapies will allow greater penetration depths, with minimal invasive approaches, reaching deeper tissues for an improved local treatment of the tumor site.

Financial & competing interests disclosures

The authors would like to thank to Fundação para a Ciência e Tecnologia (FCT) for the financial support under the projects references PTDC/BBB-BMC/0611/2012 and UID/BIO/00645/2013. We would also like to thank the master students Catarina Filipe and João Lopes, from CBiOS/ULHT, and Arife Jiyan Baysal, from Uppsala University, for the help with cytotoxicity assays in HaCaT and in *S. cerevisiae* models, respectively. The authors have no other relevant affiliations or financial involvement with any organization or entity with a financial interest in or financial conflict with the subject matter or materials discussed in the manuscript apart from those disclosed.

No writing assistance was utilized in the production of this manuscript.

Executive summary

Novel method for gold nanoparticles preparation

- Incorporation of biopolymers and natural reduction agents, obtained from an aqueous extract of *Plectranthus saccatus*, resulted in gold nanoparticles with mean size around 100–200 nm, a low polydispersity index (PI < 0.3) and, most importantly, with a maximum absorbance wavelength in the near infrared range (650–900 nm).
- Gold nanoparticles showed essentially round-shape morphology with the presence of other structures, in few amount, such as rod-like particles and with octahedral sections.

Thermal activation of gold nanoparticles

- Gold nanoparticles conjugated with a hydrophobic dye, Sudan III, were successfully incorporated into an agar phantom to simulate the desired optical conditions.
- Thermal activation of gold nanoparticles and dye release was possible with an ultrasound water bath (45 kHz, at 50°C, for 3 h) and a pulsed beam with a frequency-doubler Nd:YAG laser, as heat sources.

Biocompatibility of gold nanoparticles

- In terms of cytotoxicity, gold nanoparticles production with an aqueous extract of *Plectranthus saccatus* as the reducing agent showed increased biocompatibility with human skin cell line and yeast.

Ethical conduct of research

The authors state that they have obtained appropriate institutional review board approval or have followed the principles outlined in the Declaration of Helsinki for all human or animal experimental investigations. In addition, for investigations involving human subjects, informed consent has been obtained from the participants involved.

References

1 Siegel R, Ma J, Zou Z, Jemal A. Cancer statistics, 2014. *CA. Cancer J. Clin.* 64(1), 9–29 (2014).

2 Huang X, El-Sayed MA. Plasmonic photo-thermal therapy (PPTT). *Alexandria J. Med.* 47(1), 1–9 (2011).

3 Jabeen F, Najam-ul-Haq M, Javeed R, Huck CW, Bonn GK. Au-nanomaterials as a superior choice for near-infrared photothermal therapy. *Molecules* 19(12), 20580–20593 (2014).

4 Shao J, Griffin RJ, Galanzha EI *et al.* Photothermal nanodrugs: potential of TNF-gold nanospheres for cancer theranostics. *Sci. Rep.* 3 (2013).

5 Jana NR, Gearheart L, Murphy CJ. Wet chemical synthesis of high aspect ratio cylindrical gold nanorods. *Phys. Chem. B.* 105, 4065–4067 (2001).

6 Faramarzi MA, Sadighi A. Insights into biogenic and chemical production of inorganic nanomaterials and nanostructures. *Adv. Colloid Interface Sci.* 189, 1–20 (2013).

7 Kharissova OV, Dias HVR, Kharisov BI, Pérez BO, Pérez VMJ. The greener synthesis of nanoparticles. *Trends Biotechnol.* 31(4), 240–248 (2013).

8 Fazaludeen MF, Manickam C, Ashankyty IMA, Ahmed MQ, Beg QZ. Synthesis and characterizations of gold nanoparticles by *Justicia gendarussa* Burm F leaf extract. *J. Microbiol. Biotechnol. Res.* 2(1), 23 (2012).

9 Ajitha B, Ashok Kumar Reddy Y, Sreedhara Reddy P. Biosynthesis of silver nanoparticles using *Plectranthus amboinicus* leaf extract and its antimicrobial activity. *Spectrochim. Acta. A. Mol. Biomol. Spectrosc.* 128, 257–262 (2014).

10 Rijo P, Batista M, Matos M, Rocha H, Jesus S, Simões MF. Screening of antioxidant and antimicrobial activities on Plectranthus spp. extracts. *Biomed. Biopharm. Res.* 9(2), 225–235 (2013).

11 Noruzi M, Zare D, Davoodi D. A rapid biosynthesis route for the preparation of gold nanoparticles by aqueous extract of cypress leaves at room temperature. *Spectrochim. Acta. A. Mol. Biomol. Spectrosc.* 94, 84–88 (2012).

12 Sudip M, Sushma V, Sujata P *et al.* Green chemistry approach for the synthesis and stabilization of biocompatible gold nanoparticles and their potential applications in cancer therapy. *Nanotechnology* 23(45), 455103 (2012).

13 Sun I-C, Na JH, Jeong SY *et al.* Biocompatible glycol chitosan- coated gold nanoparticles for tumor-targeting CT imaging. *Pharm Res.* 31(6), 1418–1425 (2013).

14 Zhang G, Sun X, Jasinski J, Patel D, Gobin AM. Gold/chitosan nanocomposites with specific near infrared absorption for photothermal therapy applications. *J. Nanomater.* Article ID: 853416 (2012).

15 Boca SC, Potara M, Gabudean A-M, Juhem A, Baldeck PL, Astilean S. Chitosan-coated triangular silver nanoparticles as a novel class of biocompatible, highly effective photothermal transducers for *in vitro* cancer cell therapy. *Cancer Lett.* 311, 131–140 (2011).

16 Azzazy Hassan ME, Mansour Mai MH, Samir Tamer M, Franco R. Gold nanoparticles in the clinical laboratory: principles of preparation and applications. *Clin. Chem. Lab. Med.* 50(2), 193 (2012).

17 Hirsch LR, Stafford RJ, Bankson JA *et al.* Nanoshell-mediated near-infrared thermal therapy of tumors under magnetic resonance guidance. *Proc. Natl. Acad. Sci.* 100(23), 13549–13554 (2003).

18 Miwa M, Shikayama T. ICG fluorescence imaging and its medical applications. In: *International Conference of Optical Instrument and Technology. 7160(Session 4)*, International Society for Optics and Photonics, 71600K–71600K–9 (2008).

19 Jacques SL. Optical properties of biological tissues: a review. *Phys. Med. Biol.* 58(11), R37 (2013).

20 Kennedy LC, Bickford LR, Lewinski NA *et al.* A new era for cancer treatment: gold-nanoparticle-mediated thermal therapies. *Small* 7(2), 169–183 (2011).

21 Fazal S, Jayasree A, Sasidharan S, Koyakutty M, Nair SV, Menon D. Green synthesis of anisotropic gold nanoparticles for photothermal therapy of cancer. *ACS Appl. Mater. Interfaces*6(11), 8080–8089 (2014).

22 Wang S, Lu W, Tovmachenko O, Rai US, Yu H, Ray PC. Challenge in understanding size and shape dependent toxicity of gold nanomaterials in human skin keratinocytes. *Chem. Phys. Lett.* 463(1–3), 145–149 (2008).

23 Lu S, Xia D, Huang G, Jing H, Wang Y, Gu H. Concentration effect of gold nanoparticles on proliferation of keratinocytes. *Colloids Surf. B Biointerfaces* 81(2), 406–411 (2010).

24 Kwolek-Mirek M, ZadrAg-TEcza R, Bednarska S, Bartosz G. Yeast *Saccharomyces cerevisiae* devoid of Cu, Zn-superoxide dismutase as a cellular model to study acrylamide toxicity. *Toxicol. In Vitro* 25(2), 573–579 (2011).

25 Roberto A, Caetano PP. A high-troughput screening method for general cytotoxicity part I Chemical toxcity. *Rev Lusófona Ciências e Tecnol. da Saúde.* 2(2), 95–100 (2005).

26 Grabar KC, Freeman RG, Hommer MB, Natan MJ. Preparation and characterization of Au colloid monolayers. *Anal. Chem.* 67(4), 735–743 (1995).

27 Bouvrette P, Liu Y, Luong J, Male K. Process for producing gold nanoparticles. US Patent 20050153071 (2005).

28 Khan Z, Singh T, Hussain JI, Hashmi AA. Au(III)–CTAB reduction by ascorbic acid: Preparation and characterization of gold nanoparticles. *Colloids Surfaces B Biointerfaces* 104(0), 11–17 (2013).

29 Huang H-C, Yang Y, Nanda A, Koria P, Rege K. Synergistic administration of photothermal therapy and chemotherapy to cancer cells using polypeptide-based degradable plasmonic matrices. *Nanomedicine* 6(3), 459–473 (2011).

30 Rijo P, Falé PL, Serralheiro ML, Simões MF, Gomes A, Reis C. Optimization of medicinal plant extraction methods and their encapsulation through extrusion technology. *Measurement* 58(0), 249–255 (2014).

31 Murphy CJ, Sau TK, Gole AM *et al.* Anisotropic metal nanoparticles: synthesis, assembly, and optical applications. *J. Phys. Chem. B.* 109(29), 13857–13870 (2005).

32 Pustovalov VK, Pustovalov VK, Astafyeva LG, Zharov VP. Dependences of optical properties of spherical two-layered nanoparticles on parameters of gold core and material shell. *J. Quant. Spectrosc. Radiat. Transf.* (2013).

33 El-Brolossy TA, Abdallah T, Mohamed MB *et al.* Shape and size dependence of the surface plasmon resonance of gold nanoparticles studied by Photoacoustic technique. *Eur. Phys. J.* 153(1), 361–364 (2008).

34 Murphy CJ, Thompson LB, Chernak DJ *et al.* Gold nanorod crystal growth: From seed-mediated synthesis to nanoscale sculpting. *Curr. Opin. Colloid Interface Sci.* 16(2), 128–134 (2011).

35 Iqbal M, Chung Y-I, Tae G. An enhanced synthesis of gold nanorods by the addition of Pluronic (F-127) via a seed mediated growth process. *J. Mater. Chem.* 17(4), 335–342 (2007).

36 Khlebtsov NG. Determination of size and concentration of gold nanoparticles from extinction spectra. *Anal. Chem.* 80(17), 6620–6625 (2008).

37 Khan S, Alam F, Azam A, Khan AU. Gold nanoparticles enhance methylene blue-induced photodynamic therapy:

a novel therapeutic approach to inhibit *Candida albicans* biofilm. *Int. J. Nano.* 7(0), 3245–3257 (2012).

38 Roosta M, Ghaedi M, Daneshfar A, Sahraei R, Asghari A. Optimization of the ultrasonic assisted removal of methylene blue by gold nanoparticles loaded on activated carbon using experimental design methodology. *Ultrason. Sonochemistry* 21(1), 242–252 (2014).

39 Rijo P, Matias D, Fernandes A, Simões M, Nicolai M, Reis C. Antimicrobial plant extracts encapsulated into polymeric beads for potential application on the skin. *Polymers (Basel)* 6(2), 479–490 (2014).

40 Oliveira CA de, Peres DD, Graziola F *et al.* Cutaneous biocompatible rutin-loaded gelatin-based nanoparticles increase the SPF of the association of UVA and UVB filters. *Eur. J. Pharm. Sci.* 81, 1–9 (2015).

41 Reis CP, Martinho N, Rosado C, Fernandes AS, Roberto A. Design of polymeric nanoparticles and its applications as drug delivery systems for acne treatment. *Drug Dev. Ind. Pharm.* 40(3), 409–417 (2014).

42 Sabnis RW. *Handbook of Biological Dyes and Stains: Synthesis and Industrial Applications.* John Wiley & Sons, Inc., Hoboken, NJ, USA.

43 Murphy CJ, Gole AM, Stone JW *et al.* Gold nanoparticles in biology: beyond toxicity to cellular imaging. *Acc. Chem. Res.* 41(12), 1721–1730 (2008).

44 Alkilany AM, Thompson LB, Boulos SP, Sisco PN, Murphy CJ. Gold nanorods: their potential for photothermal therapeutics and drug delivery, tempered by the complexity of their biological interactions. *Adv. Drug Deliv. Rev.* 64(2), 190–199 (2012).

45 Sajanlal PR, Sreeprasad TS, Samal AK, Pradeep T. Anisotropic nanomaterials: structure, growth, assembly, and functions. *Nano Rev.* 2 (2011).

46 Philip D. Green synthesis of gold and silver nanoparticles using Hibiscus rosa sinensis. *Phys. E.* 42, 1417–1424 (2010).

47 Khalil MMH, Ismail EH, El-Magdoub F. Biosynthesis of Au nanoparticles using olive leaf extract. *Arab. J. Chem.* 5, 431–437 (2012).

48 Rana S, Bajaj A, Mout R, Rotello VM. Monolayer coated gold nanoparticles for delivery applications. *Adv. Drug Deliv. Rev.* 64, 200–216 (2012).

49 Carbó-Argibay E, Rodríguez-González B, Pacifico J, Pastoriza-Santos I, Pérez-Juste J, Liz-Marzán LM. Chemical sharpening of gold nanorods: the rod-to-octahedron transition. *Angew. Chemie Int. Ed.* 46(47), 8983–8987 (2007).

50 Park Y-S, Hong YN, Weyers A, Kim YS, Linhardt RJ. Polysaccharides and phytochemicals: a natural reservoir for the green synthesis of gold and silver nanoparticles. *IET Nanobiotechnol.* 5(3), 69–78 (2011).

51 Mittal AK, Chisti Y, Banerjee UC. Synthesis of metallic nanoparticles using plant extracts. *Biotechnol. Adv.* 31(2), 346–356 (2013).

52 Matthews JR, Payne CM, Hafner JH. Analysis of phospholipid bilayers on gold nanorods by plasmon resonance sensing and surface-enhanced raman scattering. *Langmuir* 31(36), 9893–9900 (2015).

53 Singh M, Harris-Birtill DCC, Markar SR, Hanna GB, Elson DS. Application of gold nanoparticles for gastrointestinal cancer theranostics: a systematic review. *Nanomed. Nanotechnol. Biol. Med.* 11(8), 2083–2098 (2015).

54 Huang X, Jain PK, El-Sayed IH, El-Sayed MA. Plasmonic photothermal therapy (PPTT) using gold nanoparticles. *Lasers Med. Sci.* 23(3), 217–228 (2008).

55 Huang J, Jackson KS, Murphy CJ. Polyelectrolyte wrapping layers control rates of photothermal molecular release from gold nanorods. *Nano Lett.* 12(6), 2982–2987 (2012).

56 Alkilany AM, Murphy CJ. Toxicity and cellular uptake of gold nanoparticles: what we have learned so far? *J. Nanoparticle Res.* 12(7), 2313–2333 (2010).

57 Ong KJ, MacCormack TJ, Clark RJ *et al.* Widespread nanoparticle-assay interference: implications for nanotoxicity testing. *PLoS One* 9(3), e90650 (2014).

58 Wohlrab J, Wohlrab D, Neubert RHH. Comparison of noncross-linked and cross-linked hyaluronic acid with regard to efficacy of the proliferative activity of cutaneous fibroblasts and keratinocytes *in vitro*. *J. Cosmet. Dermatol.* 12(1), 36–40 (2013).

59 Zhang Y, Xu D, Li W, Yu J, Chen Y. Effect of size, shape, and surface modification on cytotoxicity of gold nanoparticles to human HEp-2 and canine MDCK cells. *J. Nanomater.* 2012, 7 (2012).

60 Alkilany AM, Nagaria PK, Hexel CR, Shaw TJ, Murphy CJ, Wyatt MD. Cellular uptake and cytotoxicity of gold nanorods:molecular origin of cytotoxicity and surface effects. *Small* 5(6), 701–708 (2009).

61 Correia M, Thiagarajan V, Coutinho I, Gajula GP, Petersen SB, Neves-Petersen MT. Modulating the structure of EGFR with UV light: new possibilities in cancer therapy. *PLoS One* 9(11), e111617 (2014).

62 Boone B, Jacobs K, Ferdinande L *et al.* EGFR in melanoma: clinical significance and potential therapeutic target. *J. Cutan. Pathol.* 38(6), 492–502 (2011).

63 Bracher A, Cardona AS, Tauber S *et al.* Epidermal growth factor facilitates melanoma lymph node metastasis by influencing tumor lymphangiogenesis. *J. Invest. Dermatol.* 133(1), 230–238 (2013).

Article V

Functionalized diterpene Parvifloron D-loaded hybrid nanoparticles for targeted delivery in melanoma therapy

Catarina Oliveira Silva[1, 2], Jesús Molpeceres[2], Belén Batanero[3], Ana Sofia Fernandes[1,4], Nuno Saraiva[1], João Guilherme Costa[1, 4], Patrícia Rijo[1, 4], Isabel Vitória Figueiredo[5, 6], Pedro Faísca[7] and Catarina Pinto Reis[1, 8 *].

[1]CBiOS, Research Center for Biosciences & Health Technologies, Universidade Lusófona, Campo Grande 376, 1749-024 Lisboa, Portugal.
[2]Department of Biomedical Sciences, Faculty of Pharmacy, University of Alcalá, Ctra. A2, Km 33.600 – Campus Universitario, 28871 Alcalá de Henares, Spain.
[3]Department of Organic and Inorganic Chemistry, Faculty of Pharmacy, University of Alcalá, Ctra. A2, Km 33.600 – Campus Universitario, 28871 Alcalá de Henares, Spain.
[4]Research Institute for Medicines (iMed.ULisboa), Faculty of Pharmacy, Universidade de Lisboa, Av. Professor Gama Pinto, 1649-003 Lisboa, Portugal.
[5]Pharmacology and Pharmaceutical Care, Faculty of Pharmacy, Universidade de Coimbra, Azinhaga de Santa Comba, 3000-354 Coimbra, Portugal
[6]IBILI, Institute for Biomedical Imaging and Life Sciences, Universidade de Coimbra, Azinhaga de Santa Comba, 3000-548 Coimbra, Portugal
[7]Faculty of Veterinary Medicine – Universidade Lusófona Grande 376, 1749-024 Lisboa, Portugal
[8]IBEB, Biophysics and Biomedical Engineering, Faculty of Sciences, Universidade de Lisboa, 1749-016, Lisboa, Portugal.

***Corresponding Author**: Prof. Dr. Catarina Pinto Reis

Therapeutic Delivery (Future Medicine), 7(8): 521–544 (2016).
doi: 10.4155/tde-2016-0027

Research Article

Therapeutic Delivery

Functionalized diterpene parvifloron D-loaded hybrid nanoparticles for targeted delivery in melanoma therapy

Aim: Parvifloron D is a natural diterpene with a broad and not selective cytotoxicity toward human tumor cells. In order to develop a targeted antimelanoma drug delivery platform for Parvifloron D, hybrid nanoparticles were prepared with biopolymers and functionalized with α-melanocyte stimulating hormone. **Results/methodology:** Nanoparticles were produced according to a solvent displacement method and the physicochemical properties were assessed. It was shown that Parvifloron D is cytotoxic and can induce, both as free and as encapsulated drug, cell death in melanoma cells (human A375 and mouse B16V5). Parvifloron D-loaded nanoparticles showed a high encapsulation efficiency (87%) and a sustained release profile. *In vitro* experiments showed the nanoparticles' uptake and cell internalization. **Conclusion:** Hybrid nanoparticles appear to be a promising platform for long-term drug release, presenting the desired structure and a robust performance for targeted anticancer therapy.

First draft submitted: 17 April 2016; Accepted for publication: 15 June 2016; Published online: 22 July 2016

Keywords: α-melanocyte-stimulating hormone • cutaneous melanoma • hybrid nanoparticles • parvifloron D • sustained release • targeted delivery

Catarina Oliveira Silva[1,2], Jesús Molpeceres[2], Belén Batanero[3], Ana Sofia Fernandes[1,4], Nuno Saraiva[1], João Guilherme Costa[1,4], Patrícia Rijo[1,4], Isabel Vitória Figueiredo[5,6], Pedro Faísca[7] & Catarina Pinto Reis*[1,8]

[1]CBiOS, Research Center for Biosciences & Health Technologies, Universidade Lusófona, Campo Grande 376, 1749–024 Lisboa, Portugal
[2]Department of Biomedical Sciences, Faculty of Pharmacy, University of Alcalá, Spain
[3]Department of Organic & Inorganic Chemistry, Faculty of Pharmacy, University of Alcalá, Spain
[4]Research Institute for Medicines (iMed.ULisboa), Faculty of Pharmacy, Universidade de Lisboa, Portugal
[5]Pharmacology & Pharmaceutical Care, Faculty of Pharmacy, Universidade de Coimbra, Portugal
[6]IBILI, Institute for Biomedical Imaging & Life Sciences, Universidade de Coimbra, Portugal
[7]Faculty of Veterinary Medicine – Universidade Lusófona, Lisboa, Portugal
[8]IBEB, Biophysics & Biomedical Engineering, Faculty of Sciences, Universidade de Lisboa, Portugal
*Author for correspondence:
Tel.: +351 217 515 550
Fax: + 351 2175 155 98
catarinapintoreis@ulusofona.pt

Cutaneous melanoma is responsible for 90% of skin cancer mortality and incidence of primary disease has increased significantly over the last decades [1]. Survival is highly dependent on an early diagnosis, followed by surgical removal of local cancer and adjuvant systemic chemotherapy or radiotherapy [2]. Thus, treating primary cancer and avoiding its progression preferably by applying a less invasive local technique, is a challenge for the future of medicine. Nanomedicine plays an important role in the development of such techniques since it provides several potential advantages when applied as a local chemotherapy platform: controlled and sustained drug release; less side effects as a result of targeted delivery, by conjugation of specific ligands at the nanoparticle surface; reduced number of drug administrations, as a result of the increase in residence time and local drug concentration; and improved stability and anticancer activity [3–6].

When applied to more superficial cancers such as melanoma *in situ* (i.e., before formation of metastases), nanoparticles can improve antitumor therapies, preventing cancer evolution to metastatic stages [3,7–9]. Also, based on a review of commercially available topical formulations for skin cancer treatment, prolonged therapy is common (from 2 weeks to 7 months), with several times applications' daily or weekly [10]. For this approach, nanosystems that comprise specific targeting moieties are fundamental.

Hybrid nanoparticles made of polymers or natural substances such as modified polyesters, lipids, polysaccharides and proteins, hold multiple functionalities and a promising role in localized chemotherapy [4]. The benefits of the application of nanoparticles and

FUTURE SCIENCE part of fsg

other sophisticated delivery systems as local treatment for primary and localized cancers, have been reviewed in literature [3–4,10]. In terms of formulation design, longer lipid hydrophobic chains conjugated with amphiphilic molecules (e.g., surfactant) appear to form stable nanoparticles with tight cores, which retain the drug, create less ordered solid matrix for drug encapsulation (e.g., stearic acid [SA]) and promote a sustained drug release [11]. Indeed, hydrophobic moieties are considered an advantage as they promote interaction with the keratin present in cells, such as melanocytes [12]. Oleic acid (OA) works as a permeation enhancer and can function as a surfactant and coating element by chemical adsorption to the nanoparticle surface [13]. Previously, we have used this fatty acid as coating material for poly-ε-caprolactone (PCL) made nanoparticles, resulting in 1-month controlled release and *in vivo* drug permeation [14]. In the present paper, we increased the complexity of those nanoparticles, by adding hyaluronic acid (HA) and a peptide ligand, α-melanocyte stimulating hormone (α-MSH), to the nanoparticle surface. We anticipate that OA may function as a linker between the polymeric-lipid hydrophobic core and the hydrophilic HA coating [15]. HA has been extensively studied as a polysaccharide for coating and as a targeting biomolecule for cell receptors, such as CD44, which are overexpressed in melanoma cells [16]. In addition, HA has been studied as a transdermal carrier and permeation enhancer, adding flexibility and decreasing rigidity to nanosystems [17], as well as reporting a positive effect on increased skin permeability of molecules [18]. Furthermore, human melanoma cells show overexpression of melanocortin 1 receptors (MC1R), thus α-MSH can work as a natural binding peptide with high selectivity for these cells [19]. Therefore, besides improving accessibility, sustained drug release, local drug concentration and residence time *in situ*, these functionalized nanoparticles may also promote an efficient drug targeting due to the modifications of the nanoparticle surface [20–22].

Research attention is increasingly focused on the use of new and natural compounds for cutaneous melanoma prevention and treatment [23]. These compounds may hinder the drug multiresistance problem, since different molecular mechanisms and metabolic pathways can be explored. One example is the use of the natural compound curcumin, which shows multiple mechanisms of action against cancer, and it has been encapsulated into several delivery systems with promising outcomes [12]. Parvifloron D (PvD) isolated from *Plectranthus ecklonii* (Benth.) is one of the abietane diterpenes with royleanone motif (Figure 1), which shows broad spectra of antimicrobial and antitumor actions [24]. Other diterpenes have also demonstrated cytotoxic effects on human tumor cells, namely on human melanoma cell lines (SK-MEL-1) [25]. PvD has also promoted cell death on human leukemia cell lines [26]. However, PvD shows low water-soluble characteristics, as well as, an apparent lack of selectivity toward cancer cells. Thus, the encapsulation of PvD into hybrid nanoparticles as a drug delivery platform is studied in order to obtain a higher retention effect and accumulation at tumor site, drug stability protection and long-term delivery, as well as, continuous and prolonged therapeutic efficacy.

Herein, we demonstrate that PvD is cytotoxic to melanoma cells (human A375 and mouse B16V5 cell lines) but also to human 'normal-like' fibroblasts (Detroit 551 cell line). Therefore, in order to promote a targeted delivery of this drug toward melanoma, PvD was loaded into nanoparticles coated with hyaluronic and oleic acids (HAOA) and functionalized with α-MSH, for overexpressed CD44 and MC1R receptors in melanoma cell lines [27–29]. The nanosystems showed a size around 300 nm, negatively charged, at neutral pH, spherical morphology, high loading efficiency (~87%) and long-term stability at 4, 25 and 37°C, over 1 year. Also, we have studied the interactions between PvD and nanosystems, and confirmed the presence of HAOA coating and peptide conjugation by different techniques, demonstrating that the developed carriers present the ideal structure for targeted anticancer drug delivery. Moreover, we have demonstrated that α-MSH-conjugated HAOA-coated nanoparticles were capable of a receptor-mediated internalization into melanoma cells and maintained PvD cytotoxic action after loading.

Materials & methods

Materials

PvD was isolated from *P. ecklonii* Benth., according to a previous method described by Simões *et al.* (2010) [24]. α-MSH (MW: 1665 g.mol^{-1}) was supplied by Alfa Aesar GmbH&Co.KG (A Johnson Matthey Company, Karlsruhe, Germany). Rhodamine B (MW: 479 g.mol^{-1}), SA (MW: 284 g.mol^{-1}), OA (MW: 282 g.mol^{-1}), Pluronic® F-127 (Poloxamer 147), PCL (MW: 14,000 g.mol^{-1}), HA sodium salt from *Streptococcus equi* (MW: 7000–250,000 g.mol^{-1}), cyclohexyl isocyanide and acetaldehyde were supplied by Sigma-Aldrich (Steinheim, Germany). All reagents used for nanoparticle preparation were of analytical grade. Water was purified through a Millipore system (Millipore, MA, USA). Thiazolyl blue tetrazolium bromide (MTT), fetal bovine serum (FBS) and penicillin/streptomycin were supplied by Sigma-Aldrich (Steinheim, Germany), as of cell culture grade. Dulbecco's Modified Eagle's medium was supplied by Biowest

(Nuaillé, France) and DMSO was supplied by Merck (Darmstadt, Germany).

Flow cytometry: cell DNA content assay

The percentage of dead cells after treatment with PvD was assessed for melanoma cell lines (A375 and B16V5) by measuring the DNA content after propidium iodide stain of fixed cells [30]. Briefly, 3×10^5 cells/well were cultured in 6-well plates. After 24 h, cells were treated with PvD at 2.5 µg/ml and left to incubate for another 24 h. For sub-G1 (%) determination, floating and attached cells were harvested after incubation with 5 mM EDTA in phosphate-buffered saline (PBS). Cells were washed twice with cold PBS, centrifuged (160 × g, 8 min) in an Eppendorf centrifuge 5804 R (Eppendorf AG, Hamburg, Germany), resuspended, fixed with cold 80% ethanol, kept at 4°C for 2 h, washed twice with PBS and resuspended in PBS with 1% FBS. Cells were then stained for 20 min at 37°C with containing 12.5 µg/ml propidium iodide and 25 µg/ml RNase A in PBS. Finally, stained cells were incubated, mixed with 200 µl of PBS with 1% FBS and analyzed by flow cytometry using a BD FACSCalibur Cytometer (BD Biosciences, Singapore, Japan). Data acquisition and analysis was performed using CellQuest software (BD) and FlowJo (Tree Star, San Carlos, CA, USA), respectively. Experiments were conducted in triplicate and presented as mean ± standard deviation (SD).

Cytotoxicity assay

Cell viability studies for PvD and nanoparticles were conducted on human melanoma cells (A375, ATCC® CRL-1619™), murine melanoma cells (B16V5, CNIO, Madrid, Spain [31]) and 'normal-like' human fibroblasts (Detroit 551, ATCC® CCL-110™), using the MTT assay as previously described [32,33]. Briefly, cells were cultured in Dulbecco's Modified Eagle's medium supplemented with 10% FBS and 1% penicillin/streptomycin (P/S) solution and seeded onto a 96-well plate at a density of 5000 cells/well. Free PvD (0.1–10 µg/ml per well, MeOH < 0.05%, v/v) and nanoparticles were tested. In the case of the nanoparticles, several formulations were assessed, namely: PvD-loaded α-MSH-conjugated and non-conjugated HAOA-coated nanoparticles (PvD: 0.1–10 µg/ml) and empty α-MSH conjugated and non-conjugated HAOA-coated nanoparticles, as the equivalent weight of nanoparticles (without PvD). Cells were exposed to treatment for 24 h, washed with PBS and incubated with MTT solution (0.5 mg/ml in culture medium) for 2.5 h at 37°C. Finally, the medium was removed, cells were washed with PBS and DMSO (200 µl/well) was added to dissolve the formazan crystals. Absorbance

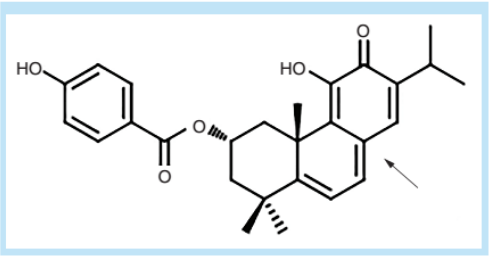

Figure 1. Molecular structure of parvifloron D.
The royleanone motif is pointed out by the arrow.

was read at 595 nm (Thermo Scientific Multiskan FC, Shanghai, China). IC_{50} values for PvD were determined by calculating the concentration of the samples that resulted in 50% inhibition of cell viability, using the software OriginPro 8.1 (OriginLab Corporation, MA, USA). Two to three independent experiments were carried out, each comprising four to eight replicate cultures. Results are represented as mean ± SD.

Preparation of hybrid nanoparticles

Hybrid nanoparticles were prepared according to a previously described solvent displacement method [14], with some modifications. First, 5 mg of HA and 20 µl of OA (HAOA 1:1, w/w) were incubated in aqueous solution at pH = 10 (NaOH 1 M, 0.3%, v/v), for 24 h at 60°C and 400 rpm. The non-coated nanoparticles were prepared in a sealed glass beaker (32 × 46 mm, capacity: 25 ml, Simax, Czech Republic), where an organic phase was prepared by mixing 100 mg of PCL and 4.975 ml of acetone, through 10-min ultrasound exposure (Bandelin Sonorex Super Rk 510H, frequency of 45 kHz). An SA solution in ethanol (0.025%, w/v) was added to the organic phase and allowed to mix for 5–10 min with magnetic stirring. This solution was immediately poured on 10 ml of an aqueous solution containing Pluronic® F127 (0.25%, w/v) and, for the coating formation, the polymer HAOA (0.05%, w/v) was added, in similar 25 ml glass beaker, under magnetic stirring (800 rpm) for 15 min, at room temperature. For loaded nanoparticles, PvD (0.0625 mg/ml in ethanol) was also dissolved in the organic phase before pouring to the aqueous solution. In addition, paclitaxel (PTX) at 0.06 mg/ml was used as an anticancer model drug for encapsulation into the nanoparticles. Nanoparticles were recovered under reduced pressure (Rotary evaporator from Heidolph type VV2000, Apeldoorn, The Netherlands) to 10 ml (final volume) and were isolated by centrifugation at 16,350 × g for 15 min (Hermle Labortechnik Gmbh type Z36HK, Wehingen, Germany) to remove unloaded drug. Formulations were made in triplicate to ensure the repeatability of the preparation method.

Conjugation of nanoparticles with α-MSH

In order to conjugate HAOA-coated nanoparticles with α-MSH, the peptide was prepared at a concentration of 1 mg/ml in PBS pH 7.4 (10 mM). First, HAOA-coated nanoparticles were prepared and concentrated under reduced pressure to a final volume of 10 ml as previously mentioned in the preparation of hybrid nanoparticles. Then, α-MSH was added to the formulation at a final concentration of 5 µg/ml. The peptide was allowed to interact with the HAOA-coated nanoparticles for 30 min, at 400 rpm, at room temperature and the suspension was kept for 24 h at 4°C. Finally, α-MSH conjugated HAOA-coated nanoparticles were isolated by centrifugation at 16,350 × g for 15 min (Hermle Labortechnik Gmbh type Z36HK, Wehingen, Germany) to remove unbound peptide. Formulations were made in triplicate to ensure the repeatability of the preparation method.

Physical characterization of the nanoparticles

Mean particle size, polydispersity index (PI) and zeta potential of the nanoparticles' concentrated suspension were measured with a Coulter Nano-sizer Delsa Nano™C (CA, USA). Experiments were performed in triplicate. In addition, D-value was determined to describe the particle size distribution of 10, 50 and 90% of the nanoparticles population. Measurement of pH was conducted with a pH electrode meter (827 pH Lab, Metrohm, Switzerland) calibrated daily with buffer solutions pH 4.00 ± 0.02 and 7.00 ± 0.02 (20°C) ST (Panreac, Barcelona, Spain).

Morphology of the nanoparticles: TEM & SEM

Morphology of freshly prepared non-coated nanoparticles (i.e., without HAOA), PvD-loaded HAOA-coated nanoparticles, α-MSH conjugated HAOA-coated nanoparticles and PTX-loaded HAOA-coated nanoparticles were also studied in terms of their structure and surface morphology by Transmission Electron Microscopy (TEM, Zeiss M10, Germany). Samples were prepared through a 'sequential two-droplet' method, by resuspending the nanoparticles in distilled water and placing a drop (5–10 µl) of the suspension on to a formvar grid for 30–60 s. When the nanoparticles suspension had partly dried, the grid was washed with distilled water and the excess of water was removed with a filter paper. Then, a small drop of sodium phosphotungstate (PTA, 2%, w/v) was applied to the grid for 10 s, the excess of stain was removed with a filter paper and the grid was left to dry at room temperature. Samples were analyzed at an accelerated voltage of 60 kV. Different fields of the images were recorded digitally (Zeiss M10 microscope camera).

For empty and PvD-loaded HAOA-coated nanoparticles, the morphology of freshly prepared samples was determined by Scanning Electron Microscopy (SEM, Zeiss DSM-950, Germany). Prior to SEM examination, an aliquot of each sample (10 µl) was mounted on a glass coverslip and left to dry at room temperature. Samples were coated with a thin layer of gold (500 nm thick) and analyzed at an accelerated voltage of 20 kV. Different fields of the images were recorded digitally (Olympus BH2 camera).

Long-term stability of the nanoparticles

Non-coated nanoparticles (i.e., without HAOA) and HAOA-coated nanoparticles were prepared and characterized in terms of size, polydispersity index (PI) and zeta potential, pH, morphology and UV-Visible absorbance spectra, over 1 year (see Supplementary Information). Samples of freshly prepared nanoparticles were kept (in triplicate) as suspensions in closed 10 ml glass vials at three different conditions: refrigeration conditions (T = 4 ± 2°C) and at residual humidity (RH) of 70%; room temperature (T = 25 ± 1°C) and at RH of 60%; body temperature (T = 37 ± 1°C) and at RH of 60%. Size, PI, zeta potential and pH were measured as described previously in the section 'Physical characterization of the nanoparticles'. Nanoparticle morphology was assessed by scanning electron microscopy (SEM, Zeiss DSM-950, Germany) (see section 'Morphology of nanoparticles'). UV–Visible absorbance spectra determination of HAOA-coated nanoparticles was conducted with a spectrophotometer (Thermo Scientific model Evolution 300 BB, UK).

HPLC method

PvD solubility, encapsulation efficiency (EE, %) and *in vitro* release studies were carried out using a reverse-phase HPLC chromatographic method for drug quantification [14]. The same method was used to quantify PTX, after entrapment into HAOA-coated nanoparticles, as a model anticancer drug. Briefly, a HPLC System Gold – Beckman Coulter (CA, USA) with a wavelength UV–VIS 166 model spectrophotometer detector was used with a mobile phase comprising acetonitrile (ACN) and Milli-Q water (60:40, v/v). A Supelcosil LC-18 column (4.6 × 150 mm, 5 µm particle size, Sigma-Aldrich, Spain) was used as stationary phase with a flow rate of 1.0 ml/min and a detection wavelength of 254 nm (PvD) and 227 nm (PTX). Column conditions were maintained at 25°C, with an injection volume of 20 µl and a run time of 20 min and 5 min, for PvD and PTX, respectively. Standards for PvD ranging from 0.1 to 10 µg/ml were evaluated and a calibration curve (y = 30.0 x + 2.4) was obtained with $R^2 > 0.998$. Standards for PTX between 0.1 µg ml and

10 µg/ml were also measured and a calibration curve ($y = 20.7 x - 0.98$) was obtained with $R^2 > 0.998$. LOD and LOQ) were determined for both PvD and PTX: LOD and LOQ for PvD were calculated to be 0.57 µg/ml and 1.89 µg/ml, respectively, while LOD and LOQ for PTX were determined to be 0.028 µg/ml and 0.093 µg/ml, respectively. Chromatographic data were processed using Gold-System Nouveau software. All measurements were carried out in duplicate.

Drug quantification & encapsulation efficiency

EE (%) was determined by measuring the retained drug by HPLC analysis. Retained drug was measured inside the PvD (0.0625 mg/ml) and PTX (0.06 mg/ml) loaded HAOA-coated nanoparticles (i.e., direct quantification), after exposure to organic solvents (ACN: water, 60:40, v/v), sonication (Braun ultrasonic sonicator at constant power of 160 watts [0.5 s cycles]) for 3 min and recovery after centrifugation (16,350 × g, 15 min). Measurements were carried out in triplicate and according to the described formula:

Amount of encapsulated drug/initial drug amount x 100%

In vitro release studies

First, PvD solubility in phosphate buffer solution pH 5.5 (USP XXX) was determined by measuring the amount of compound dissolved in a saturated solution (~40 µg/ml) after 8 h, at constant stirring (200 rpm), in order to maintain sink conditions during the *in vitro* release studies and as an approximation to the skin pH [34]. Then, PvD-loaded HAOA-coated nanoparticles and PTX-loaded HAOA-coated nanoparticles were lyophilized for 24 h at -50 ± 2°C (Freezone 2.5 L Benchtop Freeze Dry System, Labconco, MO, USA) and weighted according to the drug solubility limits. Each sample of weighted nanoparticles was placed in an amber-glass recipient, containing 30 ml of phosphate buffer solution pH 5.5 (USP XXX), under constant stirring (200 rpm), in order to simulate the human skin pH [34]. At appropriate time intervals, aliquots of the release medium were collected from three different points of the dissolution medium, in order to obtain a homogenous collection of the sample. Nanoparticles were isolated from the supernatant by centrifugation (16,350 × g for 15 min), mixed with organic solvents (ACN: Milli-Q water at 60:40, v/v), sonicated at constant power (160 watts; 0.5 s cycles) for 3 min and, finally, centrifuged again to separate the free drug from the nanoparticles residues. PvD amount at each time point, collected from the *in vitro* release medium, was determined by HPLC, according to the method described previously in the section 'HPLC method'. The assay was conducted for 2 months, until the total amount of PvD was released. Volume corrections were applied to the drug release profile curve. Three independent measurements of different nanoparticles batches were conducted (n = 3, mean ± SD).

Physicochemical characterization of nanoparticles' HAOA coating

Interaction analysis by Fourier transform infrared spectrometry

In order to study the possible interactions between PvD, polymers and peptide of the developed hybrid nanoparticles, Fourier transform infrared (FTIR) spectroscopy was conducted on lyophilized nanoparticles samples. KBr pellet method was chosen for this assay and the FTIR spectra were recorded by using a FT-IR Spectrum 2000 (Perkin Elmer, USA) from 4000 to 400 cm^{-1}. The pellet was prepared with a ratio of 1:10 (w/w) of KBr to sample (powder of nanoparticles or other component) and left to dry in a desiccator 24 h before analysis. The following samples were compared: empty HAOA-coated and non-coated nanoparticles (i.e., without HAOA), α-MSH-conjugated HAOA-coated nanoparticles and physical mixture of HAOA and non-coated nanoparticles (considering 100% HAOA coating), physical mixture of OA and HA (1:1, w/w) and the polymer HAOA, after preparation. PvD-loaded HAOA-coated nanoparticles, a physical mixture of free PvD and HAOA-coated nanoparticles (1:1, w/w) and a physical mixture of all components used for preparation of the nanoparticles, were also compared in the same proportion.

Differential scanning calorimetry

To check the purity of the drug and to confirm possible physicochemical interactions between nanoparticles and their raw components, including PvD, thermal transformations and phase transitions of the nanoparticles were studied by using a Mettler-Toledo DSC-30, TA 4000 Calorimeter (OH, USA). Indium was used to calibrate the instrument. Samples were previously lyophilized, weighted (2.0 mg) and sealed in an aluminium pan. First, free PvD thermal studies were carried out at three different heating rates: 5°C/min, 10°C/min and 25°C/min. Then, the same samples compared in FTIR analyses were studied. Results were demonstrated as curves of heat flux versus temperature (°C). A controlled heating rate of 10°C/min under a continuous nitrogen purge (20–30 ml/min) and over a temperature range from 25 to 375°C was selected. The number of thermal transitions, the melting point (T_m,°C) and difference in Gibbs energy (ΔH, $J.g^{-1}$) were determined.

NMR spectroscopy

In order to verify the possible interactions between encapsulated PvD and raw materials used to prepare the nanoparticles, ^{1}H NMR and ^{13}C NMR spectra were obtained and compared for non-coated nanoparticles (i.e., without HAOA), empty HAOA-coated nanoparticles and loaded HAOA-coated nanoparticles, by a 300 MHz spectrometer (Oxford Instruments, England). Three different solvents (i.e., D_2O, DMSO-d6 and $CDCl_3$) were used to dissolve all of the samples to identify and confirm the presence of the nanoparticles' main components, especially the HAOA coating and the presence of PvD inside the nanoparticles' core.

x-ray photoelectron spectroscopy

x-ray photoelectron spectroscopy (XPS) was used to assess the presence of the HAOA coating on the nanoparticles' surface, by comparing the spectra of non-coated (i.e., without HAOA) and HAOA-coated nanoparticles. A Multichamber XPS UHV system combined with a SPECS PHOIBOS 150 9MCD Hemispherical energy analyzer and equipped with both Al/Ag and Al/Mg x-ray source (SPECS GmbH, Berlin, Germany) was used. Briefly, samples previously lyophilized and forced under pressure to a pellet, were exposed to vacuum for approximately 45 h, before obtaining XPS spectra. XPS measurements of the nanoparticles were carried out using a nonmonochromatic Al-Mg radiation (200 W – 12 kV). Analyzer Energy mode was fixed at 50 eV pass energy for survey spectra and 25 eV pass energy for high-resolution spectra (regions). No electron flood gun was applied for minimizing surface charge. Surface elemental composition was determined by using CasaXPS software (Casa Software Ltd, UK).

In vitro permeation studies

A parallel artificial membrane permeability assay (PAMPA) was conducted as a preliminary characterization of the role of nanoparticles on drug permeability using a 96-well filter plate Millipore MultiScreen® IP 0.45 µm (Darmstadt, Germany). Previously lyophilized empty and PvD-loaded HAOA-coated nanoparticles (4 mg/ml), as well as free PvD (1.5 mg/ml), were re-suspended in Milli-Q water, to prepare the stock solutions for the assay. The concentration (C_0) in the starting solution was 20 µg/ml for the free PvD, PvD-loaded HAOA-coated nanoparticles and free PvD + empty HAOA-coated nanoparticles (1:1, w/w). These were added (150 µl, 5% DMSO, v/v) to the donor compartment, to achieve a homogenous covering of the hydrophobic polyvinylidene difluoride membrane. The acceptor compartment was filled with PBS pH 5.5. (USP XXX). The membrane solution was constituted of soybean lecithin at 2% (w/v) prepared in 5 µl dodecane. After 24-h and 72-h incubation, residual concentration in the donor compartment and retained in the membrane were determined [35].

Two measurements were carried out, each comprising four replicate samples (n = 4), using the same HPLC method described in section 'HPLC method' (methanol: water 60:40%, v/v, as the mobile phase, with Scharlau Kromasil C 18 column (4.6 × 150 mm, 5 µm, particle size) as the stationary phase). PvD standards in phosphate solution pH 5.5 were measured in duplicate. A calibration curve equation was found to be $y = 30.0x + 2.4$, with $R^2 > 0.998$. Results are expressed as mean ± SD.

Cell internalization of nanoparticles loaded with Coumarin-6-confocal microscopy

Cell internalization studies of HAOA-coated nanoparticles (i.e., without α-MSH) and α-MSH-conjugated HAOA-coated nanoparticles (concentration: 12.3 µg/ml per well) were carried out on Detroit 551 (not overexpressed CD44 and MC1R [36]), A375 (overexpressed CD44 and MC1R receptors [27,37]) and B16V5 cells (overexpressed CD44 and MC1R receptors [28,29]. Briefly, Coumarin-6 solution in ethanol at 2.5 µg/ml was encapsulated in both HAOA-coated nanoparticles, as targeting to CD44 receptors, and α-MSH-conjugated HAOA-coated nanoparticles, as targeting to both CD44 and MC1R receptors). Coumarin-6-loaded nanoparticles were centrifuged twice (16,350 × g for 15 min) for removal of unloaded dye. First, to quantify the dye release from the nanoparticles, they were incubated at 37°C for 24 h, in PBS pH 7.4. Coumarin-6 release was determined by fluorescence spectroscopy (λ_{cm}= 504 nm; λ_{ex}=460 nm; sensibility: 2), according to the calibration curve $y = 4.92\ x - 3.54$, $R^2 > 0.992$. Freshly prepared Coumarin-6-loaded nanoparticles (dye concentration/well: 1.2 µg/ml) were incubated for 2 h in 6-well plates containing each described cell line at a density of 3×10^5 cells/well. After incubation, cells were washed and visualized in a Confocal Microscope SP5 (40X, CLSM, Leica Microsystems, Barcelona, Spain) with an excitation laser He-Ne 460 nm and a λ_{em} of 300–600 nm (Coumarin-6, λ_{em} = 504 nm) to verify the internalization of the nanoparticles. Different fields of the images were recorded digitally (Nikon camera, LAS AF software; Leica Microsystems).

In vivo preliminary studies for nanoparticles

In this preliminary test, the *in vivo* anticancer effect of PvD and PvD-loaded α-MSH conjugated HAOA-coated nanoparticles was studied. Briefly, PvD stock solution in methanol was prepared and diluted with water 1:100 to reach a concentration of 100 µg/ml and kept in storage at

-20°C until the administration. This concentration was based on previously conducted *in vitro* cytotoxic assays (MTT, 24 h) and also, in the case of the nanoparticles, the amount of PvD released from the nanoparticles, as obtained with the *in vitro* release studies in PBS pH 5.5. Hairless 42-day-old male SHO-SCID mice (code: 474, Charles River, Barcelona, Spain), immunosuppressed for T and B cells were selected for the formation of melanoma xenografts models. The compatibility for implementing models of melanoma xenografts with A375 cells has been described in literature [38]. This study was conducted in accordance to the internationally accepted principles for laboratory animal use and care as found in Directive 2010/63/EU and the project was approved by the Portuguese Veterinary General Division. Animals were allowed to adapt to the laboratory for 7 days before testing and then they were maintained with food and water *ad libitum* and kept at 22 ± 1°C with controlled 12 h light/dark cycle at Faculty of Pharmacy, University of Coimbra. After this period, cells from section 2.2 were inoculated in the fold-back of the neck, using a 1 ml syringe (needle size: 25 G × 5/8 in.) at a concentration of 1 × 10^6 A375 cells/mouse in 200 µl of PBS pH 7.4 as described in the literature [9]. Animals were monitored twice a week for weight control, body conditions (body condition score, BCS), behavior and signs of tumor progression. The size of the tumor and rate of growth were measured until they reached the desired size (~1000 mm^3) for inclusion in the study. For histological evaluation, 24 h after each treatment previously described, the animals were sacrificed according to animal welfare principles. Tumors and organs (i.e., lungs, heart, liver, spleen and kidneys) were excised, weighed and measured. Then, organs were fixed in 10% formalin, paraffin embedded and cut into 5-µm sections for hematoxylin-eosin staining. Slices were examined under an Olympus BX51 microscope (Olympus Corporation, Tokyo, Japan) and images were taken using an Olympus U-TV1X-2 color camera and the extent of tumor necrosis was analyzed with Olympus analySIS software (Olympus Corporation, Tokyo, Japan).

Statistical analysis

The significance of differences between samples was assessed using one-way analysis of variance (ANOVA) for mean comparisons (Tukey's test). A 0.05 significance level was adopted for every test.

Results

PvD is cytotoxic & induces cell death on melanoma cells

To study the cytotoxicity of free PvD, MTT assays were conducted. Free PvD was slightly more cytotoxic to melanoma cell lines (i.e., A375 and B16V5) than to 'normal-like' skin fibroblasts, D551 cell line. PvD showed an IC_{50} of 3.91 ± 0.64 µg/ml for D551, and 2.71 ± 0.86 µg/ml and 2.98 ± 0.03 µg/ml for A375 and B16V5, respectively (Figure 2A). PvD (2.5 µg/ml) strongly induced cell death of melanoma cells (A375 and B16V5) as determined by the PvD induced increase in sub-G1 population when compared with the negative control (Figure 2B).

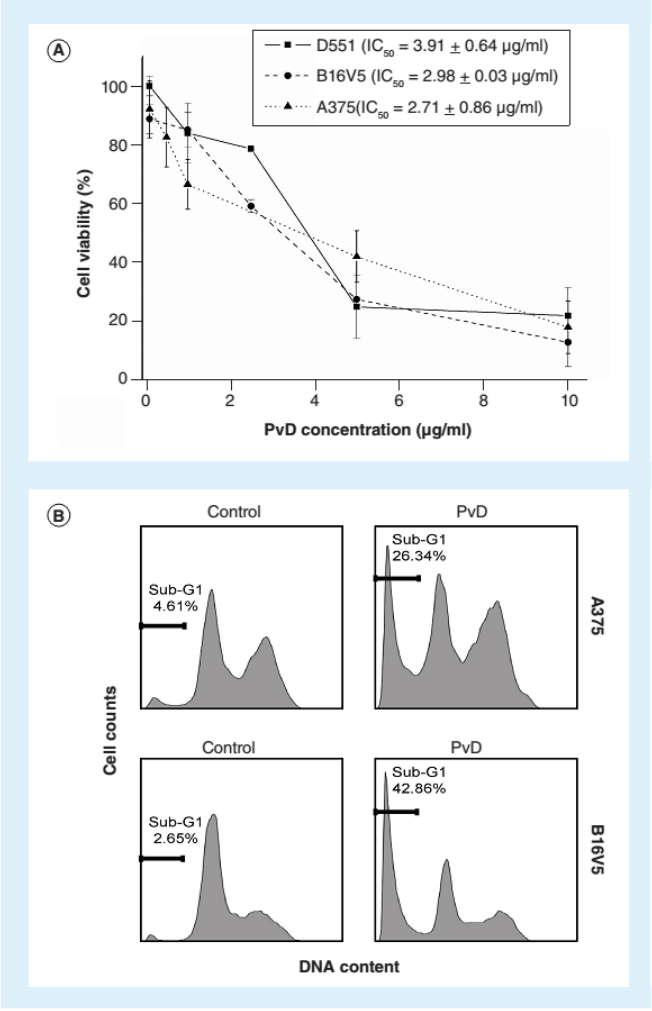

Figure 2. Parvifloron D is cytotoxic and induces cell death on melanoma cells. (A) Cytotoxic effect (MTT assay, 24h) of free PvD at a concentration range of 0.1–10 µg/ml on A375, B16V5 and D551 cells; results are expressed as percentages of the untreated control cultures (mean ± SD; n = 2–3). **(B)** The induction of cell death by PvD was assessed by sub-G1 (%) determination. Melanoma cell lines (A375, B16V5) incubated in absence or presence of 2.5 µg/ml of PvD for 24h were subjected to flow cytometry analysis following fixation and propidium iodide labeling. Results are representative of three independent experiments.
PvD: Parvifloron D.

Physicochemical characterization of nanoparticles

Considering the unselective cytotoxicity of PvD, its encapsulation into nanoparticles targeted to melanoma cells was attempted. Thus, nanoparticles loaded with PvD were coated with HAOA and functionalized with the peptide α-MSH. HA and α-MSH are natural ligands for CD44 and MC1R receptors, respectively, overexpressed in melanoma cells. For this purpose, several formulations of nanoparticles were prepared and characterized, sequentially, as the systems became more complex (i.e., after addition of the HAOA coating, drug loading and ligand α-MSH conjugation). Our aim was to obtain nano-sized particles, with a highly hydrophobic polymer-lipid core, for increased PvD encapsulation. Also, we expect core nanoparticles to be surrounded by HAOA, which would function as a polymeric net for conjugation with the α-MSH peptide. Therefore, parameters such as mean size, PI, zeta potential and pH were determined for the four types of nanoparticles studied: non-coated nanoparticles (i.e., without HAOA coating), HAOA-coated nanoparticles, PvD-loaded HAOA-coated nanoparticles and α-MSH-conjugated HAOA-coated nanoparticles (Figure 3).

Briefly, nanoparticles mean size increased after addition of HAOA coating, compared with the non-coated nanoparticles, made of PCL and SA core (Table 1). This increment (about 100 nm) was also visible after drug encapsulation, as the particle size distribution varied forming larger nanoparticles. However, in terms of mean size value, PvD-loaded HAOA-coated nanoparticles were slightly smaller than empty HAOA-coated nanoparticles (~60 nm), as well as PvD-loaded α-MSH-conjugated HAOA-coated nanoparticles (~90 nm). This fact is probably due to electrostatic interactions, which may reduce and compact the particle size. Nanoparticles also changed their color to orange, when PvD was entrapped inside the hydrophobic core. In addition, the pH value was around 7.0 for all four formulations. Zeta potential maintained its negative charge value, as both non-coated nanoparticles (mainly composed of PCL and SA), HAOA coating and α-MSH peptide naturally show a negative charge, in aqueous solutions.

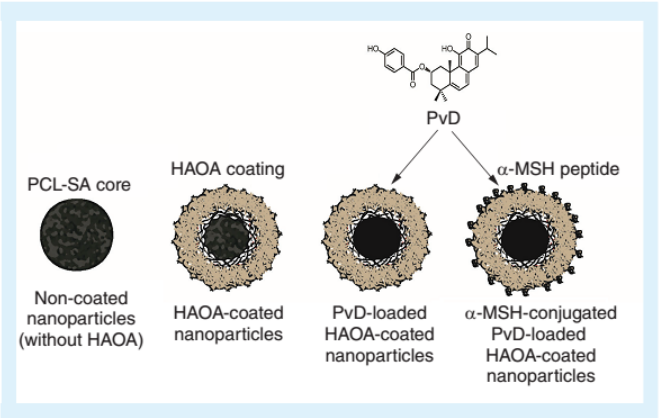

Figure 3. Illustrated scheme of hybrid nanoparticles progression, produced by solvent displacement method.
PvD: Parvifloron D.

The size and shape of the nanoparticles were also confirmed by electron microscopy (TEM and SEM). TEM images are presented in Figure 4A. Both non-coated and HAOA-coated nanoparticles showed a plain surface, a round shape and a broad distribution with different sizes of particles, mainly as according to the mean value around 300 nm. For empty non-coated nanoparticles, the core was heterogeneous with the appearance of lighter 'channels' in its interior. HAOA coating was visible by the presence of a shell around the nanoparticles' dark core, with a diameter of approximately 60–100 nm. In addition, α-MSH-conjugated HAOA-coated nanoparticles show a similar size and structure to HAOA-coated nanoparticles, not revealing an increment in the shell size after conjugation with the peptide. In order to evaluate the capacity of the nanosystem to incorporate another anticancer drug with different molecular weight, PTX was also encapsulated into α-MSH-conjugated HAOA-coated nanoparticles. Morphology of PTX-loaded nanoparticles was similar, with a round shape and coated with HAOA (Figure 4A). Furthermore, empty and PvD-loaded HAOA-coated nanoparticles were studied by SEM (Figure 4B). It was possible to observe that HAOA-coated nanoparticles tend to form aggregates as 'clusters' of nanoparticles, linked by the HAOA coating (Figure 4B). Both empty and PvD-loaded HAOA-coated nanoparticles showed a size varying from 300 to 500 nm. Also, the diameter of particles visualized by electronic microscopy is smaller. However, the D-value for 90% of the nanoparticle size distribution was determined to be around 430 nm for PvD-loaded α-MSH-conjugated HAOA coated nanoparticles and 330 nm for empty α-MSH-conjugated HAOA coated nanoparticles, confirming the actual size of the nanoparticles.

Long-term stability at different storage temperatures

Regarding the importance of developing stable formulations for drug delivery applications, we have assessed the stability of both non-coated and HAOA-coated nanoparticles at three different storage conditions: refrigeration temperature (4 ± 2°C), room

Table 1. Evaluation parameters for nanoparticles characterization, including mean size (nm), polydispersivity index, zeta potential (mV) and pH of: empty non-coated nanoparticles (i.e., without HAOA), empty HAOA-coated nanoparticles, parvifloron D-loaded HAOA-coated nanoparticles and α-melanocyte-stimulating hormone-conjugated HAOA-coated nanoparticles (mean value ± SD; n = 3).

Sample	Size (nm)	Polydispersivity index	Zeta potential (mV)	pH
Non-coated nanoparticles (without HAOA)	351 ± 41	0.192	-13 ± 10	7.1 ± 0.3
Empty HAOA-coated nanoparticles	478 ± 86	0.185	-12 ± 10	7.1 ± 0.5
HAOA-coated PvD-loaded nanoparticles	414 ± 60	0.240	-18 ± 11	7.2 ± 0.5
α-MSH-conjugated PvD-loaded HAOA-coated nanoparticles	389 ± 40	0.120	-18 ± 3	7.1 ± 0.2
α-MSH-conjugated PTX-loaded HAOA-coated nanoparticles	452 ± 74	0.234	-14 ± 7	–

α-MSH: α-melanocyte-stimulating hormone; HAOA: Hyaluronic and oleic acid; PTX: Paclitaxel; PvD: Parvifloron D.

temperature (25 ± 1°C) and body temperature (37 ± 1°C). Stability experiments were conducted in order to evaluate the longest period for stable nanoparticles and if the temporal stability was improved with the addition of the coating material. Therefore, the physicochemical characteristics and morphology of the nanoparticles were studied over 1 year, as suspensions. Graphics for UV–visible spectra and variation of the physiochemical parameters (size, PI, pH and zeta potential), as well as SEM images, are presented as Supplementary Table 1 and Supplementary Figures 1 & 2. Before measurements, all nanoparticle suspensions were easily redispersed by manual shaking. Briefly, morphology studies by SEM showed that the round shape and smooth surface of the nanoparticles is maintained mostly over the study period. However, swelling of the nanoparticles and aggregation was observed mainly for the non-coated nanoparticles, resulting in the formation of bigger particles. Non-coated nanoparticles were less stable than HAOA-coated nanoparticles at 4 and 25°C, starting to aggregate after 3 months. In spite of this, analysis of the size showed that all nanosystems maintained their original size around 300–400 nm, except for HAOA-coated nanoparticles, which had an initial size of 400 nm. Overall, both non-coated and HAOA-coated nanoparticles when stored at room temperature (25 ± 1°C) showed lower stability, forming aggregates after 1 month. PI was kept around 0.1 and 0.35 over the study period. As for pH values, both non-coated and HAOA-coated nanoparticles showed a decrease of the neutral suspension (pH ~7), reaching acid pH values around 3–4 at the end of the study period. In terms of zeta potential, nanoparticles surface charge was around -10 and -20 mV. HAOA-coated nanoparticles had approximately ten-times higher values for zeta potential than non-coated nanoparticles. Finally, UV-Visible spectra (200–1000 nm) of diluted (1:200, v/v) nanoparticles suspension showed that both non-coated and HAOA-coated nanoparticles absorb mostly in the UV-range (~200 nm) and, in general, the intensity in nanoparticles absorption decreased as time went by. Nanoparticles' size, pH values and zeta potential did not show significant statistical differences for each nanosystem (i.e., non-coated and HAOA-coated nanoparticles) stored at 4, 25 and 37°C.

PvD solubility, encapsulation efficiency (EE, %) & *in vitro* release studies

PvD is a hydrophobic compound that is easily hydrolyzed in aqueous solutions, resulting in a mixture of several decomposition products. Therefore, encapsulation into nanoparticles may be a suitable strategy to maintain the stability and activity of PvD. HPLC studies were conducted to determine the solubility of PvD in PBS (pH 5.5) before conducting *in vitro* release studies and evaluation of EE% of PvD after entrapment into the nanoparticles. PvD solubility after 8-h incubation in PBS pH 5.5 was 2–8 µg/ml (n = 3) and the EE% value for PvD was 86.7 ± 7.5% (mean value ± SD, n = 3). In addition, to compare the effect of encapsulation and *in vitro* release of other anticancer drugs from the HAOA-coated nanoparticles, PTX at 0.060 mg/ml was encapsulated in the HAOA-coated nanoparticles. PTX aqueous solubility has already been reported in literature as 0.3 µg/ml [39]. EE% for loaded PTX was determined to be 50.5 ± 3.2% (mean value ± SD, n = 3), a much lower value when compared with PvD.

In terms of *in vitro* release studies, all entrapped PvD was released from the HAOA-coated nanoparticles after 60 days in PBS pH 5.5; for PTX only ~30% of the drug was released after the same time period (Figure 5). After 24 h, only approximately 7% of PvD and of PTX was released from the HAOA-coated

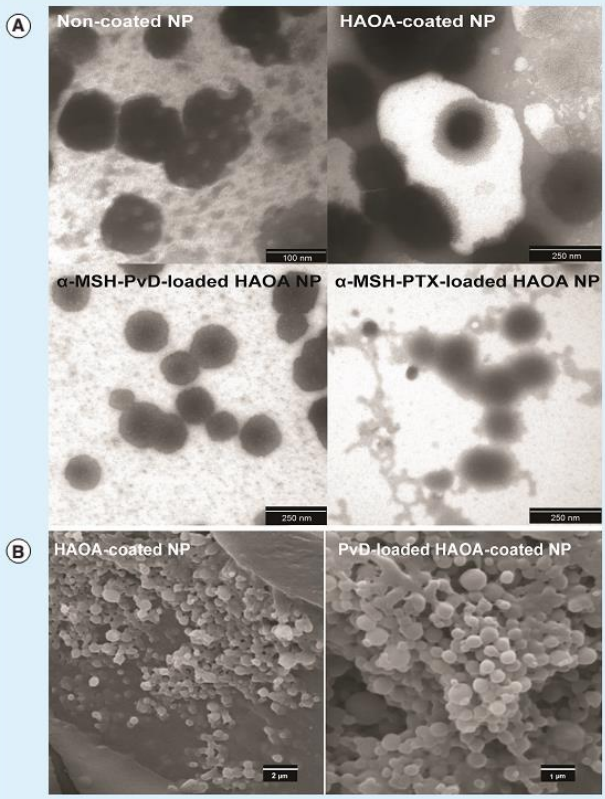

Figure 4. Morphology of the nanoparticles. (A) TEM micrographs of: empty non-coated nanoparticles (scale bar: 100 nm); Empty HAOA-coated nanoparticles (scale bar: 250 nm); α-MSH-conjugated PvD-loaded HAOA-coated nanoparticles (scale bar: 250 nm); α-MSH-conjugated PTX-loaded HAOA-coated nanoparticles (scale bar: 250 nm). **(B)** SEM micrographs of: Empty HAOA-coated nanoparticles (scale bar: 2 μm); PvD-loaded HAOA-coated nanoparticles (scale bar: 1 μm).
α-MSH: α-melanocyte-stimulating hormone; HAOA: Hyaluronic and oleic acids; NP: Nanoparticle; PTX: Paclitaxel; PvD: Parvifloron D.

nanoparticles and no burst release was observed. For both drugs, the release profile was continually sustained over the time of the experiment. Moreover, PvD degradation was assessed as the *in vitro* release studies went by. PvD retention time was around 13 min, while the main degradation product appeared at 5–6 min. By calculating the percentage of the peak area (at 5 min) in relation to the mean peak (at 13 min), it was determined that PvD degrades naturally inside the nanoparticles (14–35% over 1 month), while 70% of the PvD, in its original active state, was released in PBS pH 5.5. As for PTX, the slow release profile may be related to the fact that PTX shows high affinity to the hydrophobic core of HAOA-coated nanoparticles.

Physicochemical determination of nanoparticles' HAOA coating & of the presence of α-MSH in conjugated HAOA-coated nanoparticles

Interaction analysis by Fourier transform infrared spectrometry

FTIR has demonstrated to be a useful technique to interpret interactions between raw materials that compose the nanoparticles, since this physicochemical characterization is important to predict the nanoparticles behavior in *in vivo* conditions. All peaks are represented in Supplementary Table 2, as well as the corresponding functional groups described in the literature. HAOA coating was confirmed by the presence of three specific bands for amines (I, II and III) in both empty HAOA-coated nanoparticles and PvD-loaded HAOA-coated nanoparticles. Also, analysis of α-MSH-conjugated HAOA-coated nanoparticles shows that the peptide is present on the nanoparticles' surface. As for the interactions between drug and nanoparticles, it was possible to differentiate the spectra of PvD-loaded HAOA-coated nanoparticles and the physical mixture of free PvD and empty HAOA-coated nanoparticles (at 1:1, w/w). The drug was successfully entrapped inside the hydrophobic core of the nanoparticles since specific bands from PvD overlap probably due to the presence of nanoparticles. Finally, the physical mixture of nanoparticles' components showed distinct peaks compared with nanostructures, which may indicate that the raw components interact differently after formation of nanoparticles.

Differential scanning calorimetry

Differential scanning calorimetry studies allowed to evaluate different assets of the developed nanosystems, namely, PvD polymorphism, interactions between drug, HAOA coating and nanoparticles and the influence on their thermal events, comparing to raw materials, including PvD after encapsulation (Figure 6). First, it was verified that PvD is a polymorphic drug, since the drug shows an exothermic peak (i.e., crystallization effect) and an endothermic peak (i.e., melting effect) between 150–200°C and recrystallizes, melting again at higher temperatures. At different heating rates, PvD showed varied melting points indicating the presence of polymorphic forms by incomplete crystallization. At lower heating rate (5°C/min) this behavior is seen in detail, as the sample is exposed more time to heating, allowing the occurrence of more thermal events. To better understand the thermal behavior of PvD, more crystallographic studies will be conducted in the future. As for the thermal studies conducted with the produced HAOA coating material, new thermal events occur, compared with HAOA,

alone. Empty non-coated nanoparticles and HAOA-coated nanoparticles showed lower melting points (T_m = 50–52°C), when compared with the raw materials that compose them, especially PCL (T_m = 62°C). For α-MSH-conjugated HAOA-coated nanoparticles, a new peak was detected at around 43°C. PvD-loaded HAOA-coated nanoparticles did not show a clear melting peak for the drug, suggesting that PvD is successfully entrapped into HAOA-coated nanoparticles (T_m = 51°C), as a drug dispersion.

NMR spectroscopy

NMR is another technique usually applied in the nanoparticles chemical characterization. Although the developed nanoparticles were very complex systems, with an extended number of peaks, the present study confirmed the presence of HA and OA in empty HAOA-coated nanoparticles, when compared with the non-coated nanoparticles (i.e., without HAOA). In addition, the presence of the drug for the PvD-loaded HAOA-coated nanoparticles was also confirmed. The use of three different solvents was essential to dissolve the hydrophobic and hydrophilic components of the nanoparticles in each of the samples. By comparing the spectra, it was possible to verify that all components were present in the nanoparticles formulation, in spite of the complexity of these drug delivery systems. Therefore, in Supplementary Table 3 are represented the main NMR signals for ^{1}H-NMR and ^{13}C-NMR obtained, for each sample of nanoparticles, in D_2O, DMSO-d*6* and $CDCl_3$.

x-ray photoelectron spectroscopy

XPS is another technique used for chemical characterization of materials' surfaces. Thus, we have used it in order to corroborate the successful coating of the nanoparticles with HAOA. Therefore, non-coated (i.e., without HAOA) and HAOA-coated nanoparticles were compared. The binding energy (i.e. position of the signal) and full width at half-maximum intensity (FWHM), as counts eV, and the percentage of area of the element (%), for each XPS signal, corresponding to C 1s, N 1s and O 1s, in each sample, are represented in Supplementary Table 4. In summary, low nitrogen concentration was detected. Therefore, the presence of nitrogen associated to the presence of HAOA coating was quantified, as a result of the charge transfer of nitrogen to carbon, leading to an increase in C 1s binding energy level [40]. Broadening of C 1s band of non-coated nanoparticles (3.41 eV), when compared with C 1s of HAOA-coated nanoparticles (2.50 eV), was observed. Although it was not quantifiable, the presence of a peak at 290.7 eV position (1.7×10^4 counts/s) was visible, corresponding to amide C(O)N in the HAOA-coated nanoparticles sample (Figure 7). In addition, there was an increase of 15% of C 1s level for HAOA-coated nanoparticles, as expected, further corroborating the presence of HAOA coating.

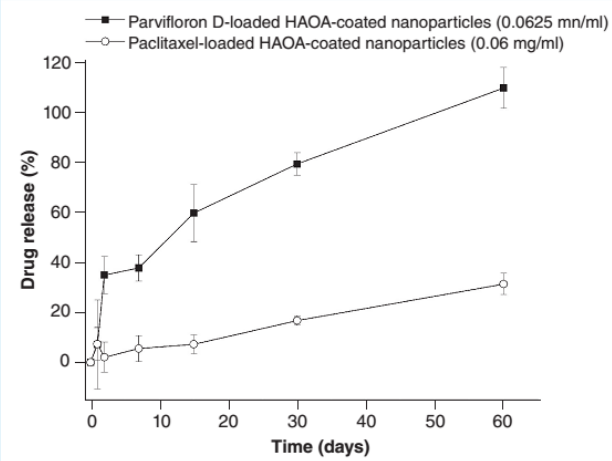

Figure 5. *In vitro* drug release of parvifloron D-loaded hyaluronic and oleic acids coated nanoparticles at 0.0625 mg/ml (black square) and paciltaxel-loaded hyaluronic and oleic acids coated nanoparticles at 0.060 mg/ml (open circle), for 60 days, in phosphate buffer pH 5.5 solution.
Results are expressed as mean of measurements of three independent nanoparticle batches ± SD (n = 3).
HAOA: Hyaluronic and oleic acid.

In vitro permeation studies

To help predict the *in vivo* permeation behavior of PvD as a free drug and after encapsulation into nanoparticles, when applied onto skin, PAMPA studies were conducted for 24 h and 72 h of incubation, with free PvD, PvD-loaded HAOA-coated nanoparticles and a mixture of free PvD and empty HAOA-coated nanoparticles at 1:1 (w/w). While conducting this experiment, it was very difficult to recover the drug for HPLC quantification, since PvD showed a high affinity to the permeation membrane. Therefore, very low recovery percentages (i.e., total amount of drug recovered from donor compartment, acceptor compartment and membrane) were obtained (around 22–48%). In addition, it was not possible to detect PvD presence, by HPLC, in the acceptor compartment (i.e., PBS solution at pH 5.5). Therefore, it was also not possible to calculate the retention factors (R) and permeability coefficients (log P_e) for tested samples. In spite of this, the percentage of PvD in the donor compartment ($C_A(t)/C_D(0)$, %) and the percentage of PvD retained in the membrane, were determined as represented in Figure 8.

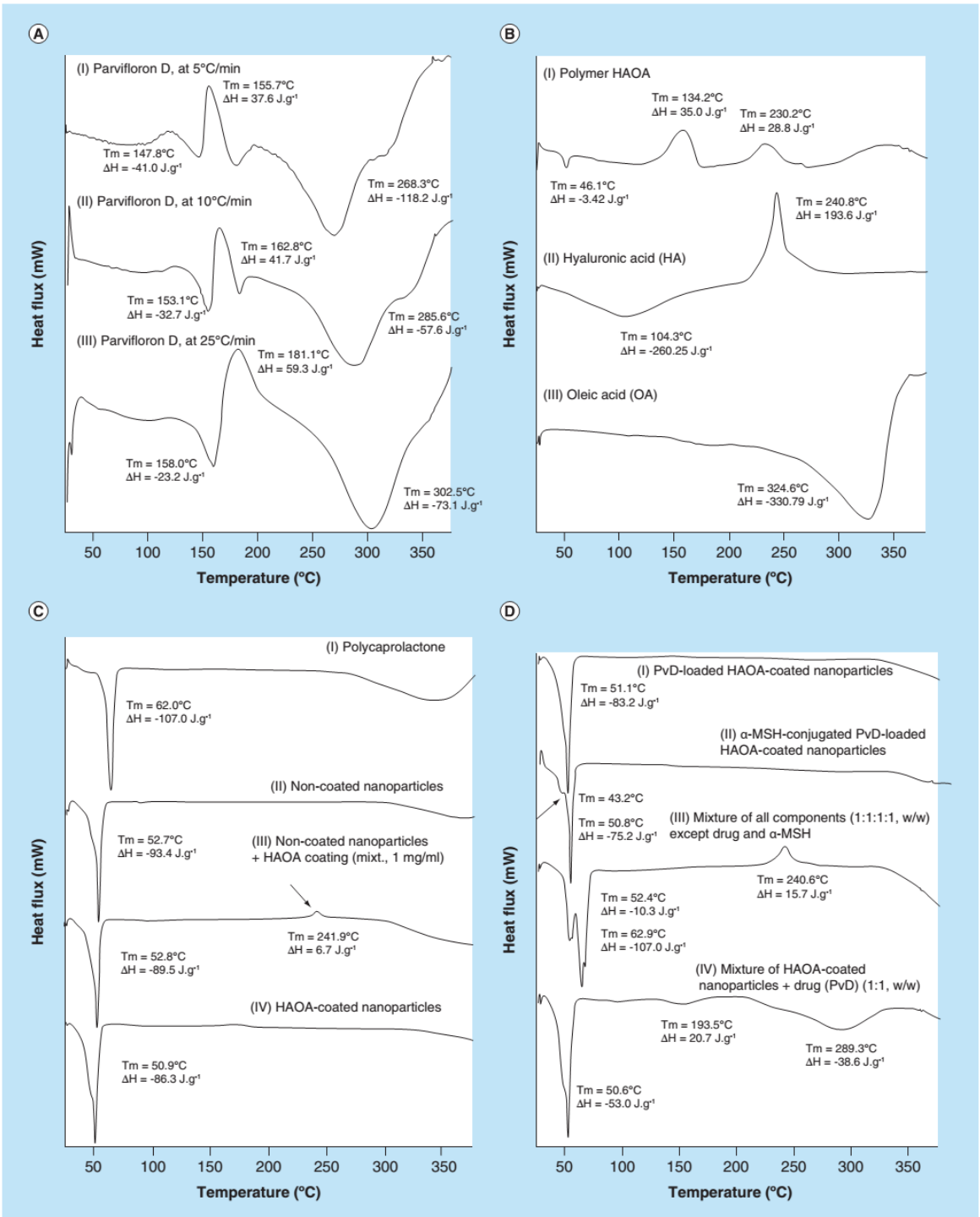
A
(I) Parvifloron D, at 5°C/min
Tm = 155.7°C
ΔH = 37.6 J.g-1
Tm = 147.8°C
ΔH = -41.0 J.g-1
Tm = 268.3°C
ΔH = -118.2 J.g-1
(II) Parvifloron D, at 10°C/min
Tm = 162.8°C
ΔH = 41.7 J.g-1
Tm = 153.1°C
ΔH = -32.7 J.g-1
Tm = 285.6°C
ΔH = -57.6 J.g-1
(III) Parvifloron D, at 25°C/min
Tm = 181.1°C
ΔH = 59.3 J.g-1
Tm = 158.0°C
ΔH = -23.2 J.g-1
Tm = 302.5°C
ΔH = -73.1 J.g-1
Heat flux (mW)
50 100 150 200 250 300 350
Temperature (°C)
B
(I) Polymer HAOA
Tm = 134.2°C
ΔH = 35.0 J.g-1
Tm = 230.2°C
ΔH = 28.8 J.g-1
Tm = 46.1°C
ΔH = -3.42 J.g-1
Tm = 240.8°C
ΔH = 193.6 J.g-1
(II) Hyaluronic acid (HA)
Tm = 104.3°C
ΔH = -260.25 J.g-1
(III) Oleic acid (OA)
Tm = 324.6°C
ΔH = -330.79 J.g-1
Heat flux (mW)
50 100 150 200 250 300 350
Temperature (°C)
C
(I) Polycaprolactone
Tm = 62.0°C
ΔH = -107.0 J.g-1
(II) Non-coated nanoparticles
Tm = 52.7°C
ΔH = -93.4 J.g-1
(III) Non-coated nanoparticles
+ HAOA coating (mixt., 1 mg/ml)
Tm = 241.9°C
ΔH = 6.7 J.g-1
Tm = 52.8°C
ΔH = -89.5 J.g-1
(IV) HAOA-coated nanoparticles
Tm = 50.9°C
ΔH = -86.3 J.g-1
Heat flux (mW)
50 100 150 200 250 300 350
Temperature (°C)
D
(I) PvD-loaded HAOA-coated nanoparticles
Tm = 51.1°C
ΔH = -83.2 J.g-1
(II) α-MSH-conjugated PvD-loaded
HAOA-coated nanoparticles
Tm = 43.2°C
Tm = 50.8°C
ΔH = -75.2 J.g-1
(III) Mixture of all components (1:1:1:1, w/w)
except drug and α-MSH
Tm = 240.6°C
ΔH = 15.7 J.g-1
Tm = 52.4°C
ΔH = -10.3 J.g-1
Tm = 62.9°C
ΔH = -107.0 J.g-1
(IV) Mixture of HAOA-coated
nanoparticles + drug (PvD) (1:1, w/w)
Tm = 193.5°C
ΔH = 20.7 J.g-1
Tm = 289.3°C
ΔH = -38.6 J.g-1
Tm = 50.6°C
ΔH = -53.0 J.g-1
Heat flux (mW)
50 100 150 200 250 300 350
Temperature (°C)

Figure 6. (facing page) Differential scanning calorimetry thermal transformations. (A) PvD thermal studies: free PvD at a heating rate of 5°C/min, free PvD at a heating rate of 10°C/min and free PvD at a heating rate of 25°C/min; **(B)** HAOA polymer formation: polymer HAOA, hyaluronic acid and oleic acid; **(C)** Nanoparticles coating: PCL, non-coated nanoparticles (i.e., bare core), mixture of non-coated nanoparticles and HAOA polymer, as 1 mg/ml (100% coating material) and HAOA-coated nanoparticles; **(D)** PvD loading and α-MSH conjugation: PvD-loaded HAOA-coated nanoparticles, α-MSH-conjugated PvD-loaded HAOA-coated nanoparticles, mixture of all components of the nanoparticles (1:1:1:1, w/w), except PvD and α-MSH, mixture of HAOA-coated nanoparticles and free PvD (1:1, w/w). Experiments were conducted with a temperature range from 25 to 375°C, at a heating rate of 10°C/min (except for PvD thermal studies, as described). The number of thermal transitions, the melting point (T_m,°C) and difference in Gibbs energy (ΔH, $J.g^{-1}$), for each sample, are also represented.
α-MSH: α-melanocyte-stimulating hormone; HAOA: Hyaluronic and oleic acids; PTX: Paclitaxel; PvD: Parvifloron D.

Cell internalization of nanoparticles loaded with Coumarin-6

To determine if α-MSH-conjugated HAOA-coated nanoparticles and HAOA-coated nanoparticles were able to enter melanoma and non-melanoma cancer cells, both nanoparticulate systems were incubated for 2 h in complete media with Detroit 551, A375 and B16V5. Melanoma cells overexpress MC1R and CD44 receptors, which natural ligands (i.e., α-MSH and HA, respectively) are present in surface of the nanoparticles [28,41–43]. Both HAOA-coated and α-MSH-conjugated HAOA-coated nanoparticles entered melanoma cells, A375 and B16V5, reaching the cytoplasm; but, in case of Detroit 551 'normal-like' fibroblasts, the nanoparticles were also retained in the cell surface (Figure 9). Internalization of α-MSH-conjugated HAOA-coated nanoparticles seems to be equivalent in all cells.

In vitro cytotoxicity studies for nanoparticles

Regarding the cytotoxic effect of encapsulated PvD, MTT assays were conducted with α-MSH-conjugated and non-conjugated PvD-loaded HAOA-coated nanoparticles, and also with α-MSH-conjugated and non-conjugated empty HAOA-coated nanoparticles (Figure 10). For PvD-loaded nanoparticles, the concentration range for PvD in these studies was defined based on the percentage of PvD released from the nanoparticles after 24 h. Briefly, in accordance with *in vitro* drug release study (Figure 5), after 24 h, 2.8 µg of PvD is released. Therefore, we tested concentrations from 0.1 to 10 µg/ml to cover the drug release range, since it takes 2 months to achieve 100% drug release. It is observed that α-MSH-conjugated HAOA-coated nanoparticles, especially, empty ones, generally showed a smaller reduction in cell viability than their non-conjugated counterparts. Hybrid nanoparticles developed in this work are composed of biocompatible and biodegradable materials, such as peptides, lipids, biopolymers and polysaccharides. Previously, we have reported a similar cytotoxic effect, concentration-dependent, for the non-coated nanoparticles (i.e., without HAOA coating), referring the occlusive effect of the nanoparticles as the main reason for these results (cellular asphyxia) [14]. The incorporation of PvD in the nanoparticles system generally increased the cell toxicity. At concentration of 1 µg/ml for A375 cell line and of 2.5 µg/ml for both D551 and B16V5, there was a statistically significant difference between samples.

In vivo preliminary studies for nanoparticles

In vivo preliminary studies conducted with the anti-cancer compound, PvD, showed that the tumors had an extensive area of necrosis and were also highly hemorrhagic (> 90%) (Figure 11). However, we could not observe a significant and immediate reduction on the tumor volume, after treatment when compared with phototherapy. Organs removed for analysis after necropsy (i.e., heart, kidney, liver, spleen and lung) showed no morphologic changes of these tissues, except in spleen, which was extensively hemorrhagic. PvD-loaded HAOA-coated nanoparticles also demonstrated to cause multiple foci of necrosis (>20%), but no reduction in tumor size.

Discussion

Although the primary treatment choice for cutaneous melanoma is surgery, reoccurrences are frequent [2]. Application of nanoparticles could turn out to be a promising tool for sustained delivery of anticancer drugs. Local chemotherapy could limit the extension of surgery and improve the overall patient response to the treatment and, thus, topical chemotherapy is currently considered as an advantageous choice in recent guidelines [1,44]. In addition, an extended exposure of cancer cells to local chemotherapy, during multiple cell cycles, appears to be more toxic than systemic chemotherapy over short-term administrations [3,8–9].

Herein, HAOA-coated nanoparticles, conjugated with α-MSH capable of transporting anticancer drugs were produced. PvD was selected as a natural diterpene due to its great cytotoxic activity, at low micromolar concentrations, against cancer cell lines but with low selectivity [25,26]. PvD shows lack of specificity, with dramatic cytotoxic effects on noncancerous cell lines (e.g., skin keratinocytes, HaCaT; Fernandes *et al.*, Unpublished Data). Also, PvD has been tested for

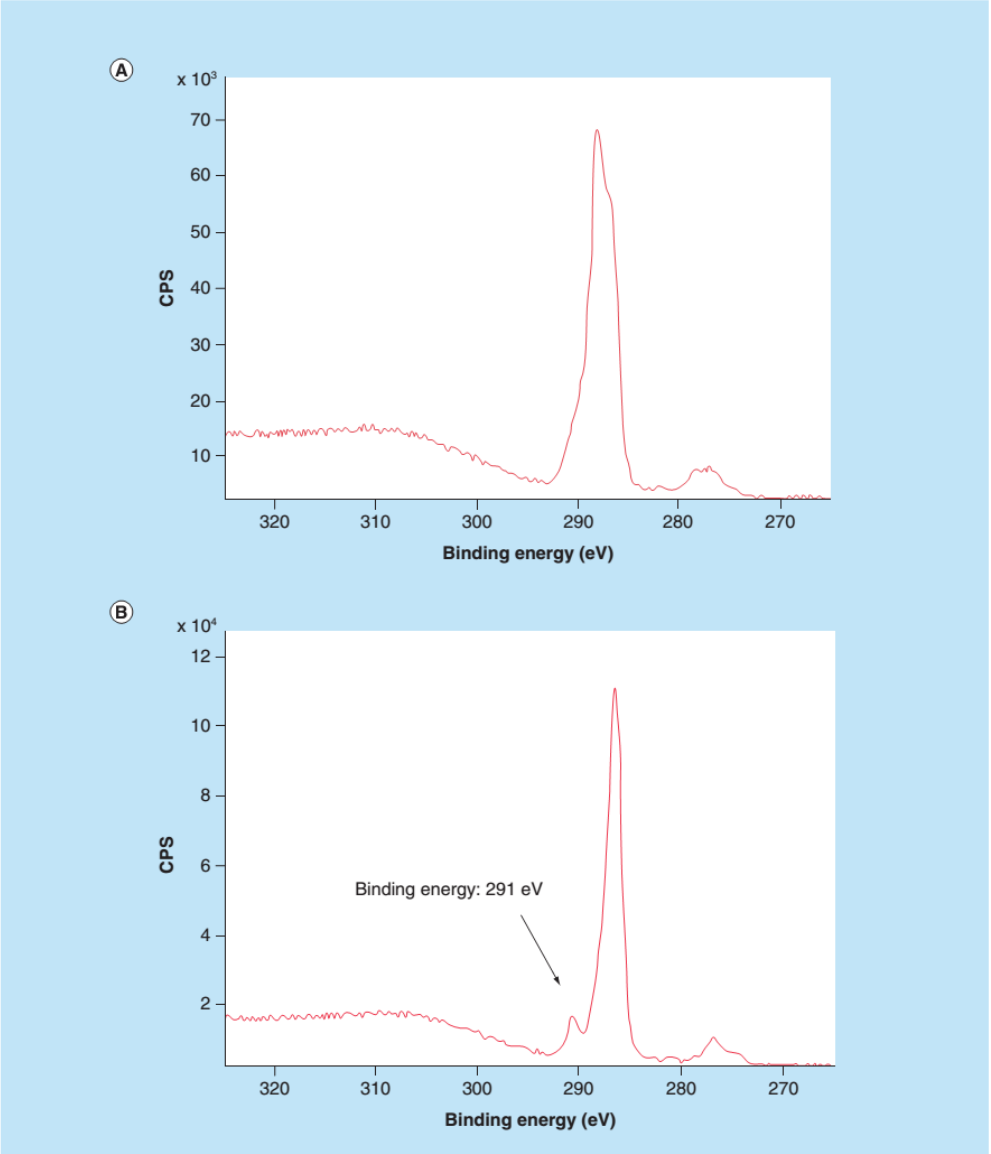

Figure 7. High-resolution XPS C1s spectra for region 325–265 eV. (A) Non-coated nanoparticles; **(B)** HAOA-coated nanoparticles. HAOA-coated nanoparticles spectra show the presence of amide (C(O)N) at 290.7 eV of biding energy position (1.7 × 10^4 counts/s).
HAOA: Hyaluronic and oleic acid; XPS: x-ray photoelectron spectroscopy.

its anticancer activity on human myeloid leukemia cell lines (HL-60, U-937, K652), lymphoid cell line (MOLT-3), human melanoma (SK-MEL-1) and breast cancer (MCF-7) cell lines, showing a significant inhibitory action on cancer proliferation (at concentration of 3 µM), through a concentration-dependent manner and by apoptosis induction, after 4 h or 24 h in contact with cells [25,26]. Recently, a semipurified fraction (DW-F5) isolated from *Wrightia tinctoria* (Roxb.) showed a high cytotoxicity (MTT assay, 72 h) against melanoma cells, especially A375 cell line, which IC_{50} was 8.8 µg/ml [45]. In the present study, lower IC_{50} values (<3 µg/ml) were obtained for PvD for A375 and B16V5 cells, while IC_{50} approximately 4 µg/ml was

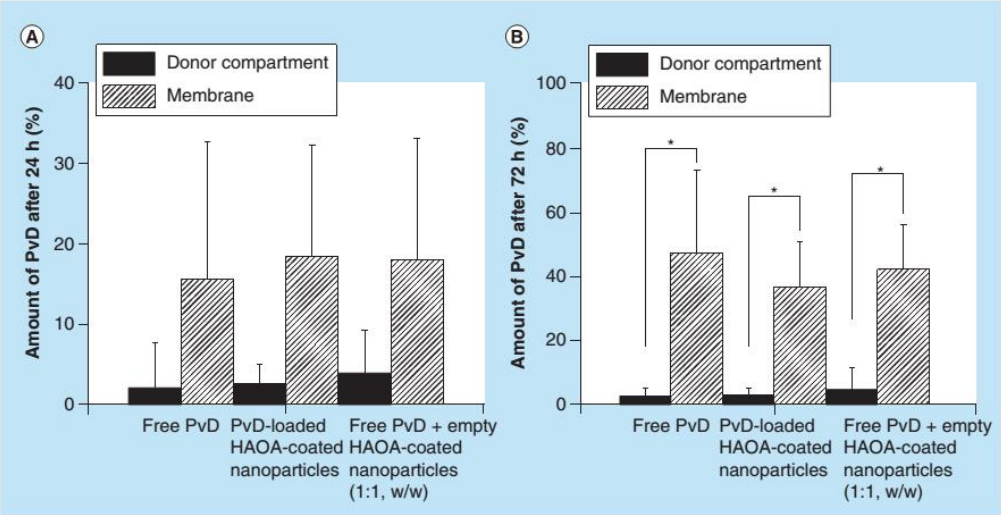

Figure 8. Amount of PvD in the donor compartment ($C_A(t)/C_D(0)$) and retained in the membrane after *in vitro* PAMPA studies with free PvD, PvD-loaded HAOA-coated nanoparticles and a mixture of free PvD and empty HAOA-coated nanoparticles, at 1:1 (w/w). (A) After 24-h incubation; **(B)** After 72-h incubation. PvD concentration per well, for each sample, was 20 μg/ml. No PvD was detected in the acceptor compartment after 24 h and 72 h. Results are expressed as mean ± SD (n = 4). *$p < 0.05$, ANOVA, Tukey's test.
HAOA: Hyaluronic and oleic acid; PAMPA: Parallel artificial membrane permeability assay; PvD: Parvifloron D.

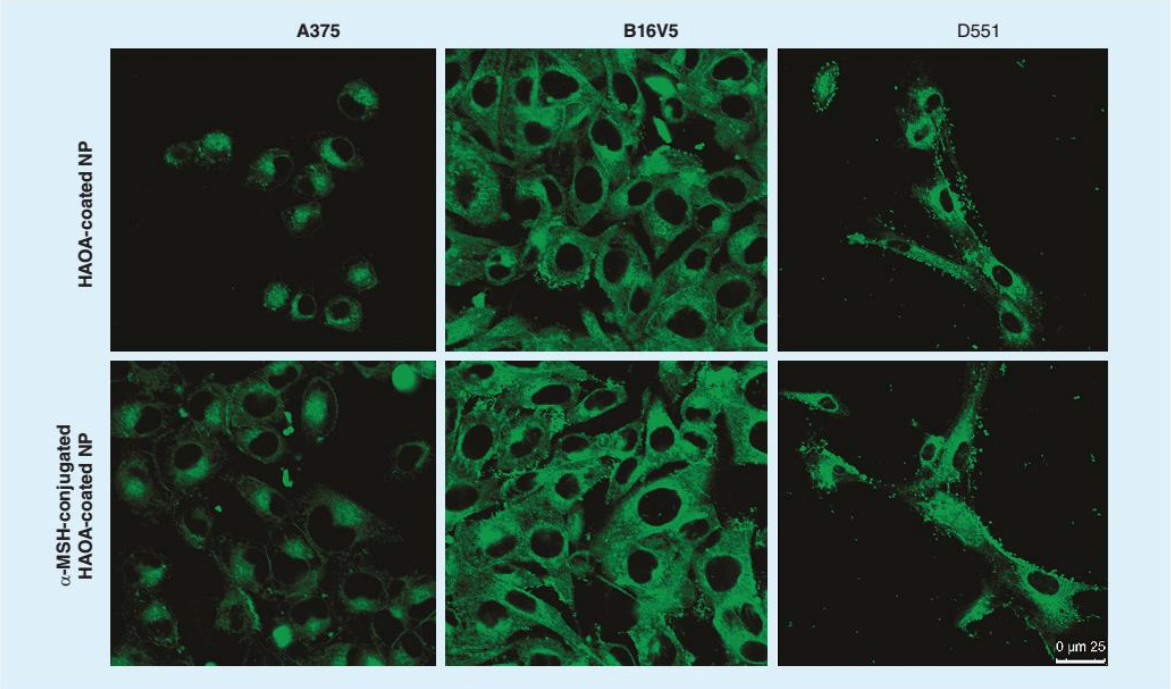

Figure 9. Particle cell internalization. A375, B16V5 and D551 cells were incubated for 2 h with Coumarin-6 dyed nanoparticles. For each cell line, the following images are represented: HAOA-coated nanoparticles and α-MSH-conjugated HAOA-coated nanoparticles (scale bar: 25 μm).
HAOA: Hyaluronic and oleic acid.

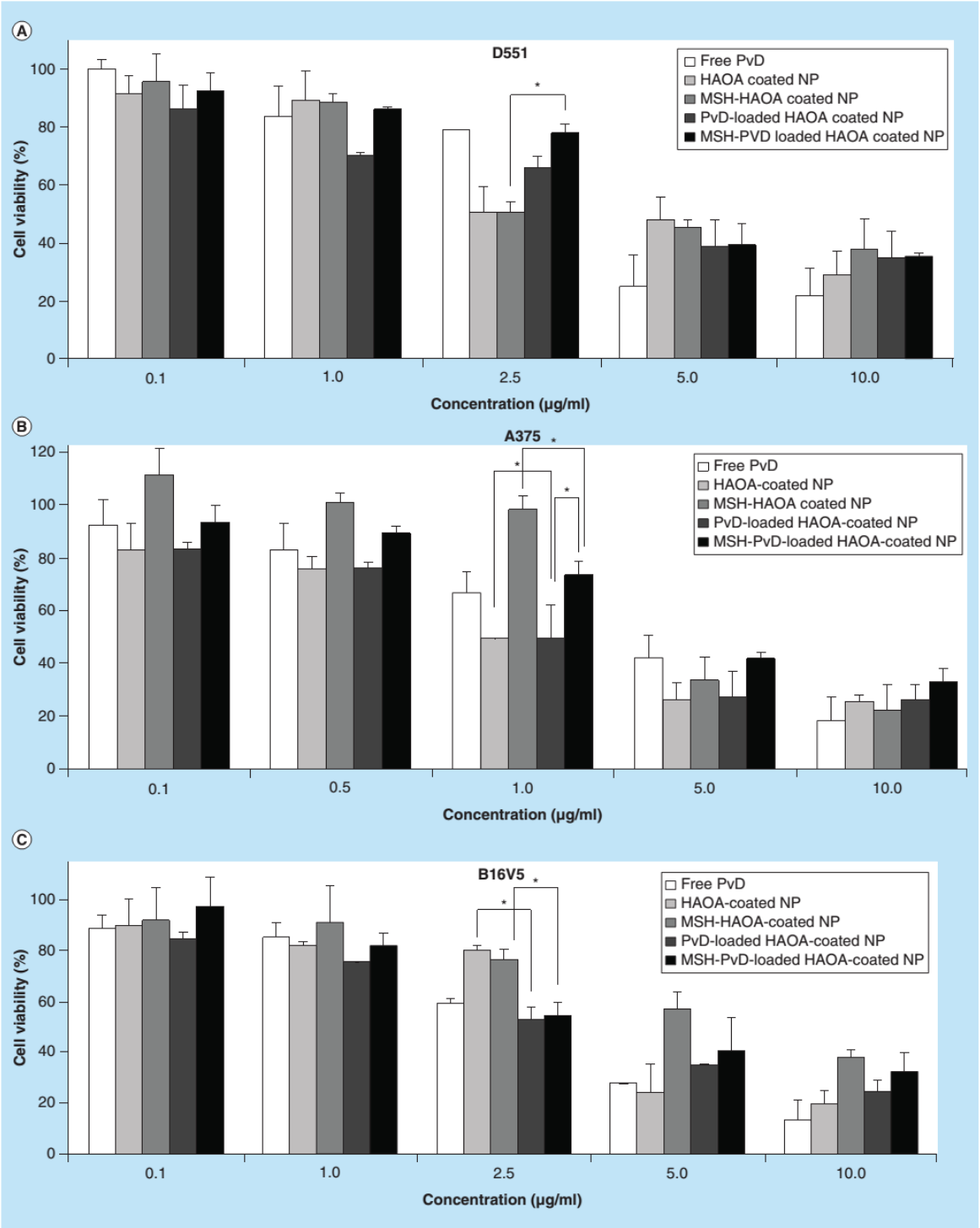
A
D551
Free PvD
HAOA coated NP
MSH-HAOA coated NP
PvD-loaded HAOA coated NP
MSH-PVD loaded HAOA coated NP
Cell viability (%)
Concentration (µg/ml)
0.1
1.0
2.5
5.0
10.0
B
A375
Free PvD
HAOA-coated NP
MSH-HAOA coated NP
PvD-loaded HAOA-coated NP
MSH-PvD-loaded HAOA-coated NP
Cell viability (%)
Concentration (µg/ml)
0.1
0.5
1.0
5.0
10.0
C
B16V5
Free PvD
HAOA-coated NP
MSH-HAOA-coated NP
PvD-loaded HAOA-coated NP
MSH-PvD-loaded HAOA-coated NP
Cell viability (%)
Concentration (µg/ml)
0.1
1.0
2.5
5.0
10.0

Figure 10. (facing page) Cytotoxic effect of HAOA-coated nanoparticles, MSH-conjugated HAOA-coated nanoparticles, PvD-loaded HAOA-coated nanoparticles and PvD-loaded MSH-conjugated HAOA-coated nanoparticles, at a range of PvD concentration of 0.1–10 µg/ml (and equivalent mass of empty nanoparticles). In **(A)** A375, **(B)** B16V5 and **(C)** Detroit 551 cells. Results for MTT assays are expressed as percentages of the untreated control cultures (mean ± SD; n = 2–3). * $p < 0.05$, ANOVA, Tukey's test.
HAOA: Hyaluronic and oleic acid; MSH: Melanocyte-stimulating hormone; MTT: Thiazolyl blue tetrazolium bromide; PvD: Parvifloron D.

obtained for D551 cells. In addition, and as expected, PvD was able to promote cell death of both A375 and B16V5 melanoma cells, increasing sub-G1 (%) population compared with the control. Due to its highly hydrophobic character, PvD is insoluble and apparently unstable in water. Still, this fact is only critical when the drug is in contact with aqueous solutions, for long periods, which did not occur during the cell culture assays. Stability studies with free and encapsulated PvD are still ongoing. Therefore, PvD is an interesting anticancer drug to test for encapsulation into nanoparticles in order to promote a local and sustained release targeted for melanoma cancer cells.

Briefly, nanoparticles were prepared according to a traditional solvent displacement method [46], with several improvements. Core nanoparticles (i.e., non-coated nanoparticles) were conjugated firstly with HAOA and secondly with a specific ligand for melanoma cells, α-MSH. As demonstrated previously, PCL and SA, as the materials for the core nanoparticles, can improve drug encapsulation to greater values (>90%) and promote a controlled and prolonged drug release [14]. OA was applied as the coating fatty acid. OA is described as a skin permeation enhancer, a membrane fluidizing agent and capable of reducing nanoparticle aggregation [47]. In addition, as the coating material, a natural non-sulfated high molecular weight HA was selected. HA is considered a nontoxic, biodegradable, biocompatible and water soluble polysaccharide, which is also anti-angiogenic and non-immunogenic [48]. Moreover, it is reported that lipid nanoparticles coated with high molecular weight HA show higher binding affinity without dissociation to the CD44 receptors [48]. However, some aggregates of HAOA-coated nanoparticles were visible as the HA tend to form cross-link bridges between them, creating 'clusters' that are difficult to resuspend [49]. This phenomenon is observed when the concentration of HA is low [50].

Zeta potential is also an important feature of nanoparticle formulations, with high impact on stability and drug entrapment efficiency. Lower values for zeta potential (< 20–30 mV) are indicative of low stability and faster aggregation of the nanoparticles. Still, high molecular materials used to stabilize the nanosystems, such as HA as the surface coating, act by steric stabilization, maintaining an efficient colloidal stability but reducing the value of surface charge [51]. This fact was later confirmed throughout the long-term stability studies, with non-coated and HAOA-coated nanoparticles, where the stability of coated nanoparticles was kept for longer periods, despite the lower value of zeta potential. In addition, zeta potential may vary with the position of the drug inside or closer to the surface, after entrapment [51].

TEM micrographs showed the difference between non-coated nanoparticles and HAOA-coated nanoparticles was clear and quite similar to other HA-coated nanoparticles described in the literature [50,52–53]. Empty non-coated nanoparticles showed a size around 100 nm less than HAOA-coated nanoparticles and small, low density 'channels' inside the PCL core, which may be attributed to SA presence. The formation of these fatty acid compartments is described in literature and may promote a controlled drug release as it stays stably entrapped inside them [54]. In this work, PTX was also used as model drug to evaluate the entrapment and release from HAOA-coated nanoparticles, and to study the nanosystems' flexibility to incorporate multiple drugs. PTX is a natural diterpenoid with potential application in melanoma treatment [52,55], which is ~2.2-fold bigger molecule (MW: 854 $g.mol^{-1}$) than PvD. Comparing PvD- and PTX-loaded HAOA-coated nanoparticles, it was observed that they are very similar in terms of size, PI, potential zeta and morphology.

PvD is a highly hydrophobic drug, with low solubility in PBS (2–8 µg/ml), and affinity to the hydrophobic PCL–SA core of the nanoparticles. As expected, after addition of the HAOA coating we have promoted a prolonged and sustained release, from 1 to 2 months, when comparing to what we have obtained previously, when encapsulating another hydrophobic molecule [14]. Also, as described previously, a slow drug release can be associated with crystallization of the nanoparticles' core, made PCL and SA, due to high drug concentration [56] or indeed by the presence of coating that prevents the drug to escape the nanoparticles [50]. However, it seems that HAOA-coated nanoparticles can mostly entrap small hydrophobic drugs, but it is less efficient for large anticancer molecules such as PTX.

Nanosystems (i.e., empty non-coated and HAOA-coated nanoparticles, α-MSH conjugated nanoparticles and PvD-loaded nanoparticles) were extensively studied in terms of physicochemical characterization. By stability studies over 1 year, we could conclude that refrigeration conditions (i.e., temperature of 4 ± 2°C

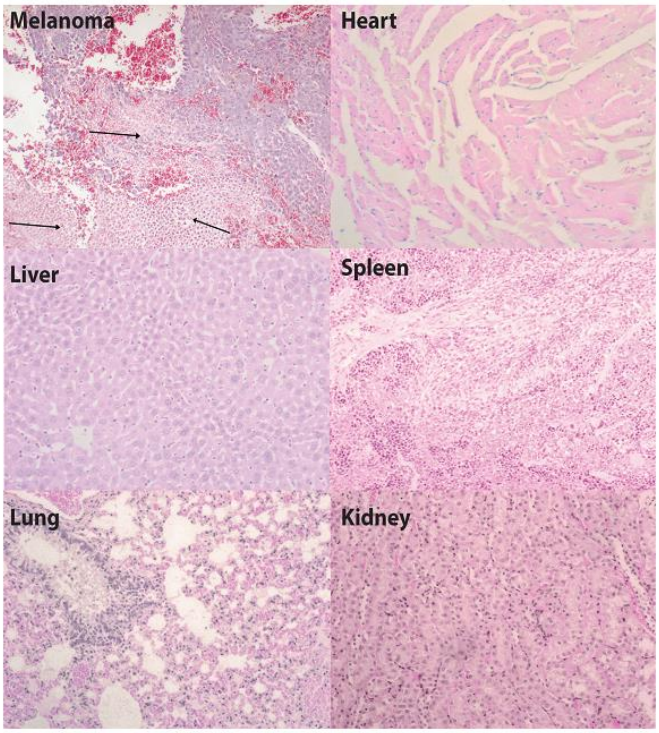

Figure 11. Histological images (100× microscopic approach) of the tumor treated with parvifloron D and the organs also removed for analysis after necropsy (i.e., heart, kidney, liver, spleen and lung). Each image is representative of the organs removed for analysis after necropsy (i.e., heart, kidney, liver, spleen, lung and tumor). Necrosis regions in tumor sample are indicated with black arrows. All tissues were marked by hematoxylin-eosin staining (H&E staining).

and residual humidity of 70%) were the best for storage of HAOA-coated nanoparticles and non-coated nanoparticles (see Supplementary Information). However, HAOA-coated nanoparticles showed also great stability over 1 year at body temperature (37 ± 1°C). When colloidal properties were compromised or apparent microbial growth was detected, the measurements were suspended; thus, at 25 ± 1°C the assay was stopped at 6 months, for both non-coated and HAOA-coated nanoparticles, and at 37 ± 1°C, the assay was finished for non-coated nanoparticles at 3 months of storage. Especially non-coated nanoparticles tend to be unstable and aggregate after 3–6 months, as a result of the water molecules permeation though the porous structure of PCL, which is directly exposed to the aqueous medium [57]. Also, PCL degrades quickly at 37°C due to ester bonds cleavage [58]; thus, HAOA coating, as a shell for PCL core nanoparticles, can protect them and improve the stability of the nanoparticles for more than 6 months. However, stability at 25 ± 1°C was disappointing for both systems. Non-coated nanoparticles and HAOA-coated nanoparticles showed a faster disintegration probably as a result of PCL and HA fast degradation process at room temperature [59]. Both nanosystems maintained as an suspension of nanoparticles showed an increasing acidic pH, which is associated with PCL slow degradation by acid catalysis [57]. In terms of physicochemical characteristics (namely size, PI and zeta potential), 1-year-old nanoparticles remained similar to freshly prepared ones, as described for different polymeric nanoparticles [60,61]. Stability (shelf-life) of well-defined nanostructures is one very important issue regarding the application of these nanoparticles for long term release of drugs, as, for example, local implants based on the tumor site.

FTIR is a useful technique to interpret interactions between raw materials that compose the nanoparticles [62]. The presence of HAOA coating on both empty HAOA-coated nanoparticles and PvD-loaded HAOA-coated nanoparticles was identified by the three specific bands for amines of HA [62,63]. In addition, the band at 1700 cm^{-1} related with C=O stretching vibration of carboxyl groups confirms the polymer formation with OA [62,64], which is absent for HA and OA mixture and isolated raw materials. The specific band for PCL at 1730 cm^{-1}, corresponding to the -C=O stretching, was also extremely visible, as the polymer constitutes the main percentage of both non-coated and HAOA-coated nanoparticles' composition. PvD-loaded HAOA-coated nanoparticles showed that some characteristics bands from the drug overlapped due to the nanoparticles matrix that involves it (e.g., 2945 cm^{-1} for methylene C-H stretching and 1727 cm^{-1} due to the dominant C=O stretching of PCL), and different peaks (e.g., 1049 and 773 cm^{-1}) appear in this sample, but not in the physical mixture. These results may indicate that the drug is successfully entrapped inside the hydrophobic core of the nanoparticles and that they interact in a different manner than their physical mixture [65]. Furthermore, α-MSH-conjugated HAOA-coated nanoparticles also show that the peptide is present, especially due to appearance of band at 1645 cm^{-1} (random coiled α-MSH), which is absent in non-conjugated HAOA-coated nanoparticles. Another characteristic band from α-MSH ~1670 cm^{-1} (amide I) was not seen, probably due to overlap by PCL dominant band at 1730 cm^{-1} [66,67].

Differential scanning calorimetry studies demonstrated that PvD is a polymorphic drug. At lower heating rate (5°C/min) we can see this behavior in detail, as there is more time for the different effects to occur [68,69]. To better understand the thermal behavior of PvD, more crystallographic studies will be conducted in the future. With regard to the nanoparticles thermal behavior, and as described in other studies,

PvD-loaded HAOA-coated nanoparticles didn't show a clear melting peak for the drug, suggesting that PvD was converted from the crystalline state to the amorphous state after loading into HAOA-coated nanoparticles [49,53]. Interestingly, all nanosystems (i.e., non-coated nanoparticles, HAOA-coated nanoparticles and PvD-loaded HAOA-coated nanoparticles) showed a lower melting point (50–52°C), in comparison with the raw materials that compose them. This effect can be attributed to the dimensions and high-surface-volume-ratio of nanoparticles, as well as the incorporation of lipids into the nanoparticles' core [53,54]. Also for PCL, the major component of the core, the raw polymer showed higher endothermic temperature (T_m = 62°C) compared with nanoparticles (T_m = 50 –52°C), as observed previously [14]. In spite of this, the values of the heats of fusion of PCL (107 J/g) and non-coated nanoparticles (93.4 J/g) were similar, indicating that the polymer maintained its semi-crystalline characteristics [70]. In relation to HAOA polymer formation and coating, three thermal events were detected, at 46°C (endothermic), 134°C and 230°C (exothermic), comparing to individual raw components (i.e., HA and OA). Those peaks showed a reduced height and sharpness, which can be associated with formation of new polymer, with a lower degree of crystallinity [62,69]. α-MSH conjugated HAOA-coated nanoparticles showed small endothermic peak at 43°C and, as expected, only apparent [67].

In terms of NMR Spectroscopy studies, the use of three different solvents was essential to see the dissolution of the hydrophobic and hydrophilic components of our nanoparticles in each of the samples [56,71]. First, both ^{13}C and ^{1}H were compared for organic solvents such as $CDCl_3$ and DMSO-*d6*, which allowed to identify peaks related to stearic and OAs, PCL, Pluronic F-127 (longer hydrophobic chain [72]) and PvD, while D_2O was essential to identify peaks from Pluronic F-127 (two hydrophilic chains [72]) and HAOA (mainly HA). Non-coated nanoparticles showed the presence of SA (CH_2 and CH_3) [73], Pluronic F-127, mostly the lipophilic central polypropyleneoxide (PPO moiety,C_2H_4) [73] and, predominantly, PCL as the core polymer of the nanoparticles, identified by hydroxyl end groups and methyl groups [74]. When HAOA coating was added to the nanoparticles, HA and OAs were also identified. Briefly, in $CDCl_3$ and DMSO-*d6*, HA peaks were minimal but in D_2O, anomeric H were present (4.60 and 4.70 ppm) [56]. As for PvD-loaded HAOA-coated nanoparticles, specific peaks for the drug were found mostly in analysis conducted on $CDCl_3$ and DMSO-*d6* solvents. Some shifts in the peaks from ^{13}C and ^{1}H ($CDCl_3$) were detected (e.g., 21.6 to 22.66 ppm (C-17 or C-18), 67.87 to 69.06 ppm (C-2) and 127.45 to 129.7 ppm (C-8)) [75].

XPS is an X-ray technique that focuses only on the elements' determination at the surface of the nanoparticles, which may increase our possibility to determine the presence of nitrogen elements in HAOA nanoparticles in comparison with non-coated nanoparticles. The presence of an amide group (i.e., C[O]N) at 290.7 eV position and an increase of C1s level (>15%) was observed for HAOA-coated nanoparticles. This increase may occur as a result of the charge transfer of nitrogen to carbon and a change of the sample surface and confirms the coating presence [39,76].

PAMPA was conducted to obtain a preliminary characterization of the nanoparticles system and drug permeability, showing that no significant permeation occurred after 24 h or 72 h, and that almost all drug was retained on the membrane. The membrane was made of hydrophobic polyvinylidone difluoride membrane and soybean lecithin (2%, w/v), which confirms the highly hydrophobic character of the drug. This value also increased with time, indicating that the drug is slowly released from the nanoparticles and do not permeate easily. Further experiments should focus on other *in vitro* or *in vivo* models that allow long-term drug permeation studies [77]. In spite of this, it is expectable that in biologic medium the nanoparticles are capable of entering the cells and interacting with membranes, due to the presence of two specific ligands at the nanoparticles surface. Therefore, we have conducted several *in vitro* studies with two melanoma cell lines (human A375 and murine B16V5) and non-melanoma cell line from skin (fibroblasts Detroit 551) to understand the internalization and cytotoxic mechanisms of the drug and nanoparticles.

Melanoma cells show several overexpressing membrane receptors, which promote growth, differentiation and invasion of tumor cells, at early stages. Therefore, polymeric nanoparticles in this study were functionalized with two natural ligands, α-MSH and HA, with affinity for MC1R and CD44 receptors, respectively. First, α-MSH is an interesting targeting ligand, since it is a small molecule, natural ligand showing higher affinity toward specific receptors and is less immunogenic than antibodies [66,78]. When α-MSH interacts with MC1R-positive melanoma cells proliferation and migration are inhibited [28]. As for CD44 receptor, although it is not specific for melanoma, this receptor acts in signalling of MIF, which is a cytokine widely expressed in melanoma cells (e.g., A375 and B16V5), responsible for increased cancer migration and progression [41,42]. CD44 receptors are comprised within the glycoprotein family, expressed ubiquitously in melanoma cells membrane and showing multifunctional actions related with cell migration, proliferation and drug resistance [16,29].

HA, used as coating for nanoparticles, is a natural mediator for CD44 and its binding to melanoma cells is mainly a CD44-dependent mechanism [16,27]. Therefore, both murine B16V5 and human A375 melanoma cell lines, used in the present work, have overexpressed CD44 and MC1R receptors. Internalization studies showed that both HAOA-coated nanoparticles, conjugated or not with α-MSH, were able to enter melanoma cells, but did not enter the nucleus. Other studies have demonstrated that agonist α-MSH conjugated nanoparticles show higher binding affinity and promote MC1R-mediated endocytosis into melanoma cells (B16F10) [79]. However, we have observed that for noncancerous fibroblasts Detroit 551, nanoparticles also entered into the cells. Dermal fibroblasts do not express MC1R receptors [80], but express some CD44 receptors on the cell membrane, which may cause HAOA-coated nanoparticles internalization by receptor-mediated endocytosis [36] or other non-mediated internalization mechanisms. In addition to cell internalization studies, cytotoxicity studies were conducted demonstrating that the use of ligand-mediated nanoparticles for cell uptake associated with PvD delivery can reduce cell viability of melanoma cells. Since nanoparticles have a large surface area, they can adsorb a protein corona from the biologic environment, such as cell culture medium with FBS. This effect can cause a concentration nondependent cytotoxicity profile, showing an increased cell viability at lower nanoparticle concentrations. Pluronic-F127 can reduce the formation of the protein corona, which may reflect the results obtained for the MTT assays with α-MSH-conjugated HAOA-coated nanoparticles [81]. Therefore, a small growth effect was observed, especially for α-MSH-conjugated nanoparticles, as a result of interaction between the peptide and the overexpressed MC1R receptors, before PvD release. As previously reported for gemcitabine-loaded nanoparticles [82], the cytotoxicity of our nanoparticles was similar to the free drug. Polymeric nanoparticles are ideal anticancer drug carriers, since they allow a sustained controlled and targeted delivery of these drugs for long periods. The goal of applying these nanosystems to cancer treatment provides an increased stability of drugs, reduce the adverse effects of chemotherapy and maintain or, eventually, improve the efficacy of the chemotherapy [83]. In this context, biodegradability and biocompatibility are important features, as well as, higher permeability to tumor cells. Several studies have demonstrated that polymeric nanoparticles work as excellent carriers and promoted a sustained drug release; however, without improving the *in vitro* cytotoxicity of the drug when loaded [83,84]. The prolonged release is pointed out as the main reason for not reaching an effective drug concentration in cells. In spite of this, nanoparticles improve pharmacokinetics of drugs [84] and greater anticancer activity [82]. The application of polymeric nanosystems to local cancer treatment improves the conventional treatments for subcutaneous tumors. Preliminary *in vivo* studies conducted in immunosuppressed hairless SCID mice for human melanoma (A375 cells) xenograft models, with the anticancer compound, as free PvD and PvD-loaded nanoparticles, showed that the tumors had an extensive area of necrosis and were also highly hemorrhagic. Therefore, this can be a preliminary approach for targeting cutaneous melanoma that may reduce cancer growth.

Conclusion

Through this experimental work, we have formulated α-MSH-conjugated HAOA-coated nanoparticles, characterized the systems in terms of their physical characteristics (size dimensions, charge, structural layers and morphology), raw materials and drug–nanoparticles interactions, ligand-conjugation with α-MSH, drug encapsulation, *in vitro* release profile and permeation and, finally, cell internalization and cytotoxicity studies. These nanosystems appear to be promising platforms for a long-term drug release, presenting the desired structure and a robust performance for a targeted and local (i.e., intra-tumor) antitumor therapy in cutaneous melanoma *in situ*.

Future perspective

Hybrid nanoparticles for cancer treatment are innovative nano-sized carriers, which can provide a stable and biocompatible possibility to improve the efficacy of drugs. Further experiments should focus on the development of nanosystems comprising different therapeutic strategies, based on distinct core structures and surface functionalization, with multiple targeting ligands, for a broad and potential application in heterogeneous cancers, such as cutaneous melanoma.

Acknowledgements

The authors would like to thank P Cavaco, É Viegas and F Falcão from Serviços Farmacêuticos do Centro Hospitalar de Lisboa Ocidental (CHLO, E.P.E.) for kindly offering us the paclitaxel used in this study and the Spanish National Cancer Research Center, CNIO (Madrid, Spain) for kindly donating the murine melanoma B16V5 cell line. The authors would also like to thank IT Jiménez from the Cell Culture Unit from University of Alcalá de Henares (UAH) for the help with the cell culture studies. Also, the authors would like to thank Spanish National Research Council (CSIC) for conducting XPS analysis.

Ethical conduct of research

The authors state that they have obtained appropriate institutional review board approval or have followed the principles outlined in the Declaration of Helsinki for all human or animal experimental investigations. In addition, for investigations involving human subjects, informed consent has been obtained from the participants involved.

Financial & competing interests disclosure

The authors thank Fundação para a Ciência e Tecnologia (FCT) for the partial financial support under the project reference PTDC/BBB-BMC/0611/2012. The authors have no other relevant affiliations or financial involvement with any organization or entity with a financial interest in or financial conflict with the subject matter or materials discussed in the manuscript apart from those disclosed. No writing assistance was utilized in the production of this manuscript.

Executive summary

Parvifloron D is cytotoxic to melanoma cells

- Parvifloron D (PvD) showed an IC_{50} of 2.71 ± 0.86 μg/ml and 2.98 ± 0.03 μg/ml for A375 and B16V5, respectively, and increased sub-G1 (%) in those melanoma cell lines.

Characterization HAOA-coated nanoparticles

- Hyaluronic and oleic acid (HAOA)-coated nanoparticles showed consistent results, confirming the presence of coating at the surface of the nanoparticles and an average diameter increase of 100 nm, comparing with non-coated nanoparticles.
- Stability (shelf-life) of HAOA-coated nanoparticles for over 1 year was greater at refrigeration conditions (4 ± 2°C) and 37 ± 1°C.

Sustained drug release & local action

- PvD-loaded HAOA-coated nanoparticles showed an encapsulation efficiency value of around 87% and a sustained release profile, over 2 months, while *in vitro* permeation studies show that PvD does not permeate easily.

Cell internalization & cytotoxicity

- Ligand-mediated nanoparticles for cell uptake associated with PvD delivery can reduce cell viability of melanoma cells.
- Preliminary *in vivo* studies conducted showed that the tumors had an extensive area of necrosis.

References

Papers of special note have been highlighted as:
• of interest; •• of considerable interest

1 Garbe C, Peris K, Hauschild A *et al.* Diagnosis and treatment of melanoma. European consensus-based interdisciplinary guideline – Update 2012. *Eur. J. Cancer.* 48(15), 2375–2390 (2012).

2 Eggermont AMM, Spatz A, Robert C. Cutaneous melanoma. *Lancet* 383(9919), 816–827.

•• **Describes the major advances in diagnosis and treatment of cutaneous melanoma.**

3 Wolinsky JB, Colson YL, Grinstaff MW. Local drug delivery strategies for cancer treatment: gels, nanoparticles, polymeric films, rods, and wafers. *J. Control. Rel.* 159(1), 14–26 (2012).

•• **Reviews the applications of polymer-based drug delivery nanosystems in cancer therapy.**

4 d'Angelo I, Conte C, Miro A, Quaglia F, Ungaro F. Core–shell nanocarriers for cancer therapy. Part I: biologically oriented design rules. *Expert Opin. Drug Deliv.* 11(2), 283–297 (2014).

5 Dianzani C, Zara GP, Maina G *et al.* Drug delivery nanoparticles in skin cancers. *Biomed. Res. Int.* 2014, Article ID 895986, (2014).

6 Simões MCF, Sousa JJS, Pais A. Skin cancer and new treatment perspectives: a review. *Cancer Lett.* 357(1), 8–42 (2015).

7 Zhao Q-H, Zhang Y, Liu Y *et al.* Anticancer effect of realgar nanoparticles on mouse melanoma skin cancer *in vivo* via transdermal drug delivery. *Med. Oncol.* 27(2), 203–212 (2010).

8 Weinberg BD, Blanco E, Gao J. Polymer implants for intratumoral drug delivery and cancer therapy. *J. Pharm. Sci.* 97(5), 1681–1702 (2008).

9 Liu R, Wolinsky J, Walpole J *et al.* Prevention of local tumor recurrence following surgery using low-dose chemotherapeutic polymer films. *Ann. Surg. Oncol.* 17(4), 1203–1213 (2010).

10 Micali G, Lacarrubba F, Nasca MR, Ferraro S, Schwartz RA. Topical pharmacotherapy for skin cancer: part II. Clinical applications. *J. Am. Acad. Dermatol.* 70(6), 979.e1–979.e12 (2014).

11 Ma M, Hao Y, Liu N *et al.* A novel lipid-based nanomicelle of docetaxel: evaluation of antitumor activity and biodistribution. *Int. J. Nanomedicine* 7, 3389–3398 (2012).

12 Mangalathillam S, Rejinold NS, Nair A, Lakshmanan V-K, Nair SV, Jayakumar R. Curcumin loaded chitin nanogels for skin cancer treatment via the transdermal route. *Nanoscale* 4(1), 239–250 (2012).

13 Zhang L, He R, Gu H-C. Oleic acid coating on the monodisperse magnetite nanoparticles. *Appl. Surf. Sci.* 253(5), 2611–2617 (2006).

14 Silva CO, Rijo P, Molpeceres J *et al.* Polymeric nanoparticles modified with fatty acids encapsulating betamethasone

for anti-inflammatory treatment. *Int. J. Pharm.* 493(1–2), 271–284 (2015).

15 Park J-H, Cho H-J, Yoon HY *et al.* Hyaluronic acid derivative-coated nanohybrid liposomes for cancer imaging and drug delivery. *J. Control. Rel.* 174(0), 98–108 (2014).

16 Ahrens T, Assmann V, Fieber C *et al.* CD44 is the principal mediator of hyaluronic-acid-induced melanoma cell proliferation. *J. Invest. Dermatol.* 116(1), 93–101 (2001).

17 Kong M, Chen XG, Kweon DK, Park HJ. Investigations on skin permeation of hyaluronic acid based nanoemulsion as transdermal carrier. *Carbohydr. Polym.* 86(2), 837–843 (2011).

18 Yang J-A, Kim E-S, Kwon JH *et al.* Transdermal delivery of hyaluronic acid – human growth hormone conjugate. *Biomaterials* 33(25), 5947–5954 (2012).

19 Carlson JA, Linette GP, Aplin A, Ng B, Slominski A. Melanocyte receptors: clinical implications and therapeutic relevance. *Dermatol. Clin.* 25(4), 541–557 (2007).

20 Abdel-Mottaleb MMA, Neumann D, Lamprecht A. Lipid nanocapsules for dermal application: a comparative study of lipid-based versus polymer-based nanocarriers. *Eur. J. Pharm. Biopharm.* 79(1), 36–42 (2010).

21 Bombelli FB, Webster CA, Moncrieff M, Sherwood V. The scope of nanoparticle therapies for future metastatic melanoma treatment. *Lancet Oncol.* 15(1), e22–e32 (2014).

22 Gonçalves AS, Macedo AS, Souto EB. Therapeutic nanosystems for oncology nanomedicine. *Clin. Transl. Oncol.* 14(12), 883–890 (2012).

23 Madhunapantula SV, Robertson GP. Chapter twelve – chemoprevention of melanoma. In: *Advances in Pharmacology.* Keiran SMS (Ed.). Academic Press, Cambridge, USA 361–398 (2012).

24 Simões MF, Rijo P, Duarte A, Matias D, Rodríguez B. An easy and stereoselective rearrangement of an abietane diterpenoid into a bioactive microstegiol derivative. *Phytochem. Lett.* 3(4), 234–237 (2010).

25 Burmistrova O, Simões MF, Rijo P, Quintana J, Bermejo J, Estévez F. Antiproliferative activity of abietane diterpenoids against human tumor cells. *J. Nat. Prod.* 76(8), 1413–1423 (2013).

26 Burmistrova O, Perdomo J, Simões MF, Rijo P, Quintana J, Estévez F. The abietane diterpenoid parvifloron D from *Plectranthus ecklonii* is a potent apoptotic inducer in human leukemia cells. *Phytomedicine* 22(11), 1009–16 (2015).

• **Reports the cytotoxicity character of the natural compund parvifloron D on several cancer cell lines.**

27 Scodeller P, Catalano PN, Salguero N, Duran H, Wolosiuk A, Soler-Illia GJAA. Hyaluronan degrading silica nanoparticles for skin cancer therapy. *Nanoscale.* 5(20), 9690–9698 (2013).

28 Chung H, Lee J, Jeong D, Han I-O, Oh E-S. Melanocortin 1 receptor regulates melanoma cell migration by controlling syndecan-2 expression. *J. Biol. Chem.* 287 (23), 19326–19335 (2012).

29 Dou J, Pan M, Wen P *et al.* Isolation and identification of cancer stem-like cells from murine melanoma cell lines. *Cell. Mol. Immunol.* 4(6), 467–472 (2007).

30 Nicoletti I, Migliorati G, Pagliacci MC, Grignani F, Riccardi C. A rapid and simple method for measuring thymocyte apoptosis by propidium iodide staining and flow cytometry. *J. Immunol. Methods* 139(2), 271–279 (1991).

31 Froidevaux S, Calame-Christe M, Schuhmacher J *et al.* A gallium-labeled DOTA-α-melanocyte-stimulating hormone analog for PET imaging of melanoma metastases. *J. Nucl. Med.* 45 (1), 116–123 (2004).

32 Rijo P, Matias D, Fernandes A, Simões M, Nicolai M, Reis C. Antimicrobial plant extracts encapsulated into polymeric beads for potential application on the skin. *Polymers (Basel)* 6(2), 479–490 (2014).

33 Oliveira CA de, Peres DD, Graziola F *et al.* Cutaneous biocompatible rutin-loaded gelatin-based nanoparticles increase the SPF of the association of UVA and UVB filters. *Eur. J. Pharm. Sci.* 81, 1–9 (2015).

34 Knor T, MeholjiĆ-FetahoviĆ A, MehmedagiĆ A. *Stratum corneum* hydration and skin surface pH in patients with atopic dermatitis. *Acta Dermatovenerol. Croat.* 19(4), 242–247 (2011).

35 Markovic BD, Vladimirov SM, Cudina OA, Odovic JV, Karljikovic-Rajic KD. A PAMPA assay as fast predictive model of passive human skin permeability of new synthesized corticosteroid C-21 esters. *Molecules* 17(1), 480–491 (2012).

36 Yoshida H, Nagaoka A, Kusaka-Kikushima A *et al.* KIAA1199, a deafness gene of unknown function, is a new hyaluronan binding protein involved in hyaluronan depolymerization. *Proc. Natl Acad. Sci.* 110 (14), 5612–5617 (2013).

37 Jonsson AL, Granqvist A, Elvin J, Johansson ME, Haraldsson B, Nyström J. Effects of melanocortin 1 receptor agonists in experimental nephropathies. *PLoS One* 9(1), e87816 (2014).

38 Cassard L, Cohen-Solal JFG, Galinha A *et al.* Modulation of tumor growth by inhibitory Fcγ receptor expressed by human melanoma cells. *J. Clin. Invest.* 110(10), 1549–1557 (2002).

39 Nam K, Nam HY, Kim P-H, Kim SW. Paclitaxel-conjugated PEG and arginine-grafted bioreducible poly (disulfide amine) micelles for co-delivery of drug and gene. *Biomaterials* 33(32), 8122–8130 (2012).

40 Muhl S, Méndez JM. A review of the preparation of carbon nitride films. *Diam. Relat. Mater.* 8(10), 1809–1830 (1999).

41 Oliveira CS, de Bock CE, Molloy TJ *et al.* Macrophage migration inhibitory factor engages PI3K/Akt signalling and is a prognostic factor in metastatic melanoma. *BMC Cancer* 14(1), 1–14 (2014).

42 Clawson GA, Matters GL, Xin P *et al.* Macrophage-tumor cell fusions from peripheral blood of melanoma patients. *PLoS One* 10(8), e0134320 (2015).

43 Haycock JW, Wagner M, Morandini R, Ghanem G, Rennie IG, Mac Neil S. α-Melanocyte-stimulating hormone inhibits NF-κB activation in human melanocytes and melanoma cells. *J. Invest. Dermatol.* 113(4), 560–566 (1999).

44 Bichakjian CK, Halpern AC, Johnson TM *et al.* Guidelines of care for the management of primary cutaneous melanoma. *J. Am. Acad. Dermatol.* 65(5), 1032–1047 (2011).

45 Antony J, Saikia M, V V *et al.* DW-F5: A novel formulation

against malignant melanoma from *Wrightia tinctoria*. *Sci. Rep.* 5, 11107 (2015).

46 Calvo P, Remunan-Lopez C, Vila-Jato JL, Alonso MJ. Chitosan and chitosan/ethylene oxide-propylene oxide block copolymer nanoparticles as novel carriers for proteins and vaccines. *Pharm. Res. [Internet]*. 14(10), 1431–1436 (1997).

47 Bennet D, Marimuthu M, Kim S, An J. Dual drug-loaded nanoparticles on self-integrated scaffold for controlled delivery. *Int. J. Nanomedicine* 7(3399–3419) (2012).

48 Mizrahy S, Raz SR, Hasgaard M *et al.* Hyaluronan-coated nanoparticles: the influence of the molecular weight on CD44-hyaluronan interactions and on the immune response. *J. Control. Release* 156(2), 231–238 (2011).

49 Liu Y, Sun J, Cao W *et al.* Dual targeting folate-conjugated hyaluronic acid polymeric micelles for paclitaxel delivery. *Int. J. Pharm.* 421(1), 160–169 (2011).

50 Song S, Chen F, Qi H *et al.* Multifunctional tumor-targeting nanocarriers based on hyaluronic acid-mediated and pH-sensitive properties for efficient delivery of docetaxel. *Pharm. Res.* 31(4), 1032–1045 (2014).

51 Honary S, Zahir F. Effect of zeta potential on the properties of nano-drug delivery systems-a review (Part 2). *Trop. J. Pharm. Res.* 12(2), 265–273 (2013).

52 Yang X, Li Y, Li M, Zhang L, Feng L, Zhang N. Hyaluronic acid-coated nanostructured lipid carriers for targeting paclitaxel to cancer. *Cancer Lett.* 334(2), 338–345 (2013).

53 Ramasamy T, Tran TH, Choi JY *et al.* Layer-by-layer coated lipid–polymer hybrid nanoparticles designed for use in anticancer drug delivery. *Carbohydr. Polym.* 102(0), 653–661 (2014).

54 Hu F-Q, Jiang S-P, Du Y-Z, Yuan H, Ye Y-Q, Zeng S. Preparation and characterization of stearic acid nanostructured lipid carriers by solvent diffusion method in an aqueous system. *Colloids Surf. B Biointerfaces* 45(0), 167–173 (2005).

55 Shen H, Shi S, Zhang Z, Gong T, Sun X. Coating Solid lipid nanoparticles with hyaluronic acid enhances antitumor activity against melanoma stem-like cells. *Theranostics* 5(7), 755 (2015).

56 Jeong Y-I, Kim DH, Chung C-W *et al.* Self-assembled nanoparticles of hyaluronic acid/poly(dl-lactide-co-glycolide) block copolymer. *Coll. Surf. B Biointerfaces* 90(0), 28–35 (2012).

57 Pohlmann AR, Fonseca FN, Paese K *et al.* Poly(e-caprolactone) microcapsules and nanocapsules in drug delivery. *Expert Opin. Drug Deliv.* 10(5), 623–638 (2013).

58 Coffin MD, McGinity JW. Biodegradable pseudolatexes: the chemical stability of poly(D,L-Lactide) and poly (ε-caprolactone) nanoparticles in aqueous media. *Pharm. Res.* 9(2), 200–205.

59 Simulescu V, Kalina M, Mondek J, PekaŘ M. Long-term degradation study of hyaluronic acid in aqueous solutions without protection against microorganisms. *Carbohydr. Polym.* 137, 664–668 (2016).

60 Morris GA, Castile J, Smith A, Adams GG, Harding SE. The effect of prolonged storage at different temperatures on the particle size distribution of tripolyphosphate (TPP) – chitosan nanoparticles. *Carbohydr. Polym.* 84(4), 1430–1434 (2011).

61 das Neves J, Amiji M, Bahia MF, Sarmento B. Assessing the physical–chemical properties and stability of dapivirine-loaded polymeric nanoparticles. *Int. J. Pharm.* 456(2), 307–314 (2013).

62 Jain A, Jain SK, Ganesh N, Barve J, Beg AM. Design and development of ligand-appended polysaccharidic nanoparticles for the delivery of oxaliplatin in colorectal cancer. *Nanomedicine* 6(0), 179–190 (2010).

63 de la Fuente M, Seijo B, Alonso MJ. Novel hyaluronan-based nanocarriers for transmucosal delivery of macromolecules. *Macromol. Biosci.* 8(5), 441–450 (2008).

64 Li Y-Y, Li L, Dong H-Q, Cai X-J, Ren T-B. Pluronic F127 nanomicelles engineered with nuclear localized functionality for targeted drug delivery. *Mater. Sci. Eng. C* 33(5), 2698–2707 (2013).

65 Natarajan V, Krithica N, Madhan B, Sehgal PK. Formulation and evaluation of quercetin polycaprolactone microspheres for the treatment of rheumatoid arthritis. *J. Pharm. Sci.* 100(1), 195–205 (2011).

66 Go DP, Hung A, Gras SL, O'Connor AJ. Use of a short peptide as a building block in the layer-by-layer assembly of biomolecules on polymeric surfaces. *J. Phys. Chem. B* 116(3), 1120–1133 (2012).

67 Contreras LM, de Almeida RFM, Villalaín J, Fedorov A, Prieto M. Interaction of α-melanocyte stimulating hormone with binary phospholipid membranes: structural changes and relevance of phase behavior. *Biophys. J.* 80(5), 2273–2283 (2001).

68 Tan CP, Che Man YB. Differential scanning calorimetric analysis of palm oil, palm oil based products and coconut oil: effects of scanning rate variation. *Food Chem.* 76(1), 89–102 (2002).

69 Giron D. Thermal analysis and calorimetric methods in the characterisation of polymorphs and solvates. *Thermochim. Acta* 248, 1–59 (1995).

70 de la Ossa DHP, Ligresti A, Gil-Alegre ME *et al.* Poly-ε-caprolactone microspheres as a drug delivery system for cannabinoid administration: development, characterization and *in vitro* evaluation of their antitumoral efficacy. *J. Control. Release* 161(3), 927–932 (2012).

71 Šmejkalová D, Nešporová K, Hermannová M *et al.* Paclitaxel isomerisation in polymeric micelles based on hydrophobized hyaluronic acid. *Int. J. Pharm.* 466(1–2), 147–155 (2014).

72 Liu F, Park J-Y, Zhang Y *et al.* Targeted cancer therapy with novel high drug-loading nanocrystals. *J. Pharm. Sci.* 99(8), 3542–3551 (2010).

73 Gao Q, Liang Q, Yu F, Xu J, Zhao Q, Sun B. Synthesis and characterization of novel amphiphilic copolymer stearic acid-coupled F127 nanoparticles for nano-technology based drug delivery system. *Coll. Surf. B Bioint.* 88(2), 741–748 (2011).

74 Shi S, Guo Q, Kan B *et al.* A novel poly(epsilon-caprolactone)-pluronic-poly(epsilon-caprolactone) grafted polyethyleneimine(PCFC-g-PEI), Part 1, synthesis, cytotoxicity, and *in vitro* transfection study. *BMC Biotechnol.* 9(1), 65 (2009).

75 Patrícia Dias de Mendonça Rijo. Phytochemical study and biological activities of Diterpenes and derivatives from *Plectranthus* species. *PhD Thesis.* University of Lisbon, Portugal (2010).

76 Chang MC, Tanaka J. XPS study for the microstructure development of hydroxyapatite–collagen nanocomposites cross-linked using glutaraldehyde. *Biomaterials.* 23(18), 3879–3885 (2002).

77 Selzer D, Abdel-Mottaleb MMA, Hahn T, Schaefer UF, Neumann D. Finite and infinite dosing: difficulties in measurements, evaluations and predictions. *Adv. Drug Deliv. Rev.* 65(2), 278–294 (2013).

78 Delehanty JB, Boeneman K, Bradburne CE, Robertson K, Bongard JE, Medintz IL. Peptides for specific intracellular delivery and targeting of nanoparticles: implications for developing nanoparticle-mediated drug delivery. *Ther. Deliv.* 1(3), 411–433 (2010).

79 Lu W, Xiong C, Zhang R *et al.* Receptor-mediated transcytosis: a mechanism for active extravascular transport of nanoparticles in solid tumors. *J. Control. Rel.*doi:10.1016/j.jconrel.2012.05.014 (2012) (Epub ahead of print).

80 Roberts DW, Newton RA, Beaumont KA, Helen Leonard J, Sturm RA. Quantitative analysis of MC1R gene expression in human skin cell cultures. *Pigment Cell Res.* 19(1), 76–89 (2006).

81 Tedja R, Lim M, Amal R, Marquis C. Effects of serum adsorption on cellular uptake profile and consequent impact of titanium dioxide nanoparticles on human lung cell lines. *ACS Nano* 6(5), 4083–4093 (2012).

82 Arias JL, Reddy LH, Couvreur P. Polymeric nanoparticulate system augmented the anticancer therapeutic efficacy of gemcitabine. *J. Drug Target* 17(8), 586–598 (2009).

83 Jeevitha D, Amarnath K. Chitosan/PLA nanoparticles as a novel carrier for the delivery of anthraquinone: synthesis, characterization and *in vitro* cytotoxicity evaluation. *Colloids Surf. B Biointerfaces* 101, 126–134 (2013).

•• **Reports the use of polymeric drug-delivery systems as carriers for phytochemicals with anticancer activity.**

84 de Mattos AC, Altmeyer C, Tominaga T, Khalil NM, Mainardes RM. Polymeric nanoparticles for oral delivery of 5-fluorouracil: formulation optimization, cytotoxicity assay and pre-clinical pharmacokinetics study. *Eur. J. Pharm. Sci.* 84, 83–91 (2016).

Supporting Materials

Table S1. SEM images of non-coated nanoparticles (i.e. bare core nanoparticles) and HAOA-coated nanoparticles, as an aqueous suspension, exposed to 4 ºC, 25 ºC and 37 ºC, for over 12 months. Scale bars range from 500 nm to 10 µm.

Time (months)	Non-coated nanoparticles	HAOA-coated nanoparticles
T = 4 ºC ± 2 ºC		
1	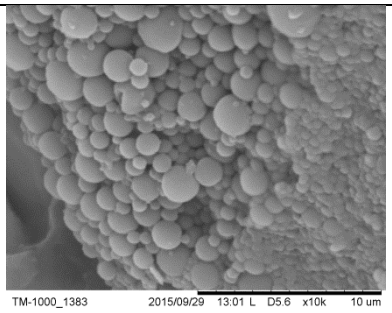	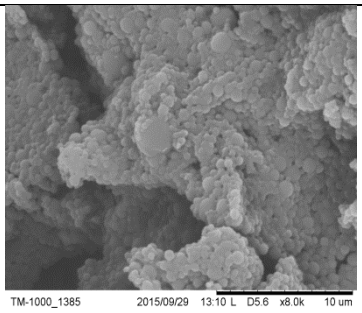
3	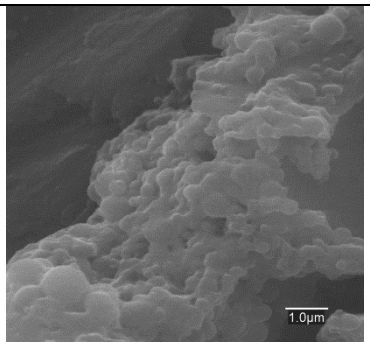	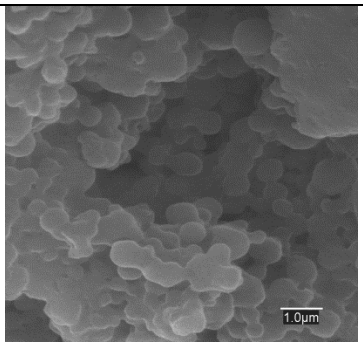
6	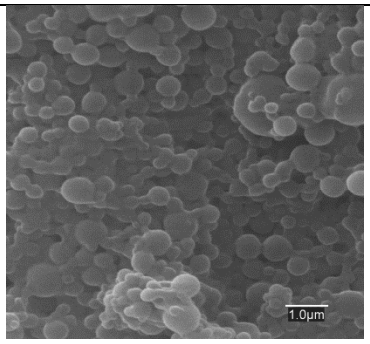	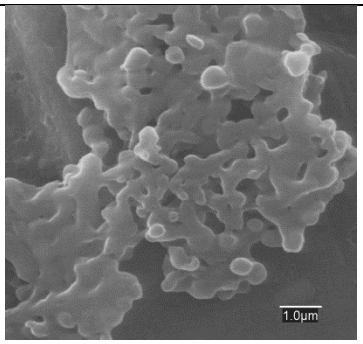

9	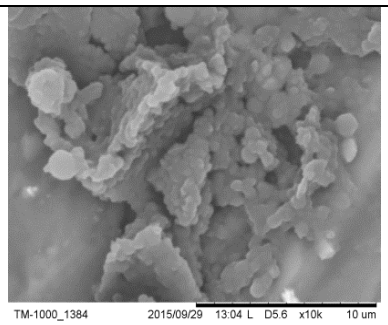	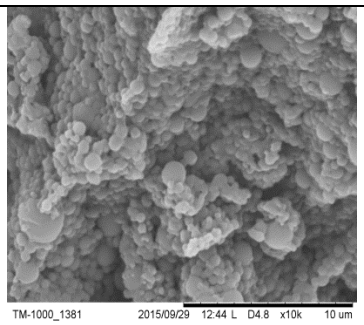
12	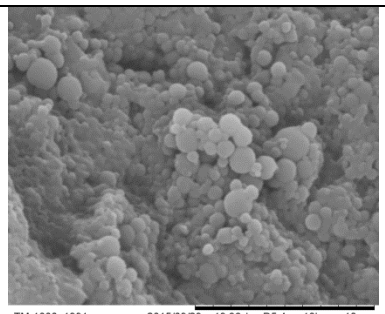	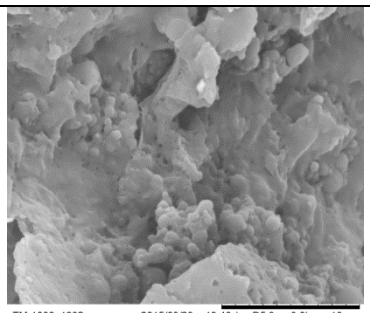
T = 25 ºC ± 2 ºC		
1	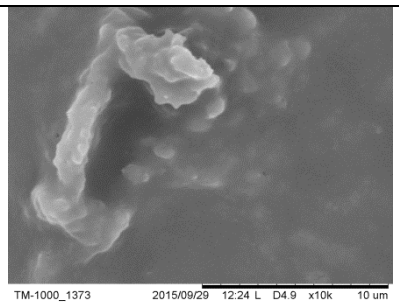	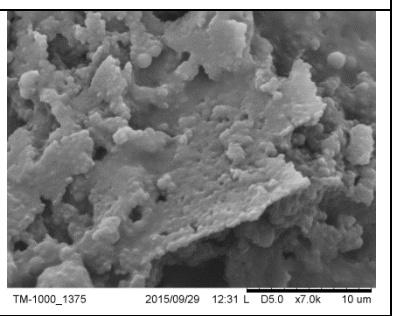
3	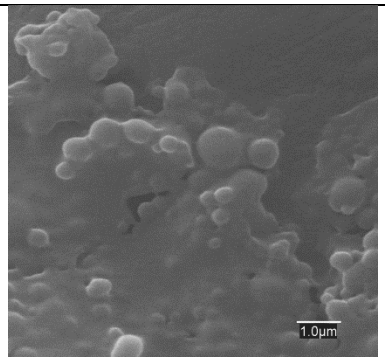	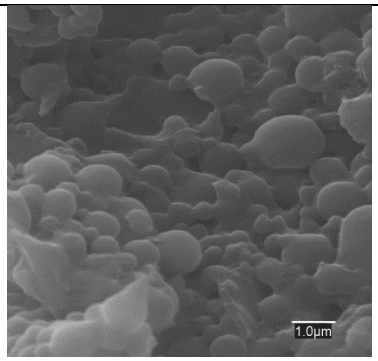
6	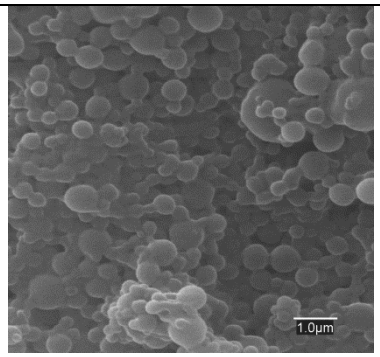	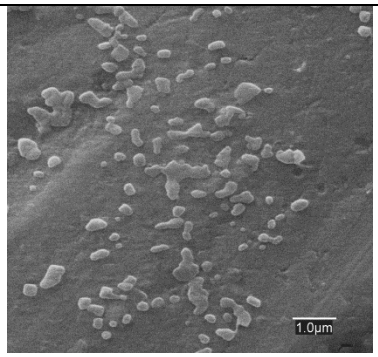
9	**x**	**x**

12	x	x
T = 37 ºC ± 2 ºC		
1	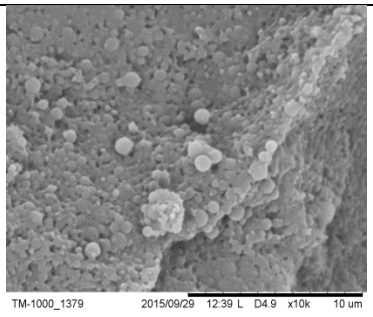	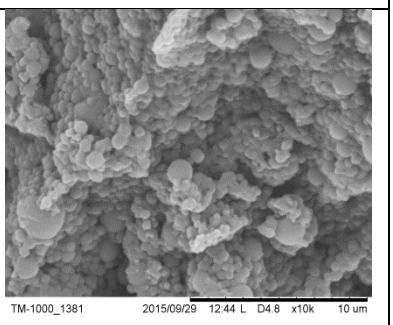
3	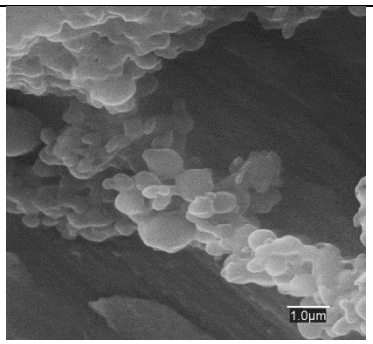	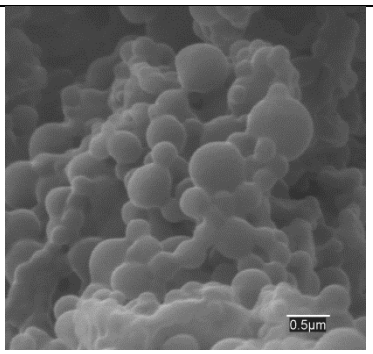
6	**x**	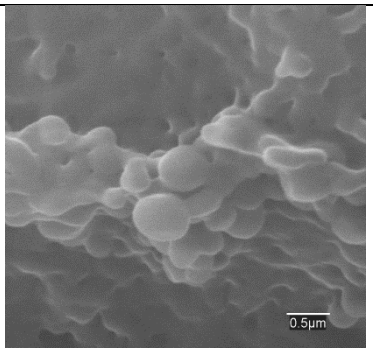
9	**x**	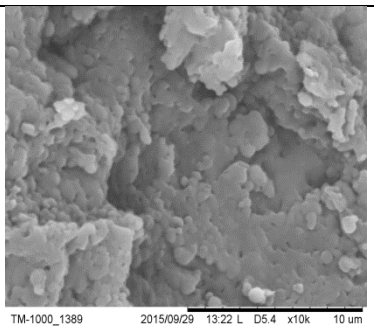
12	**x**	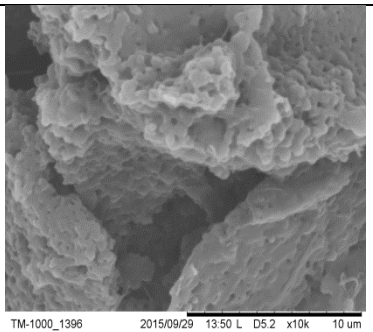

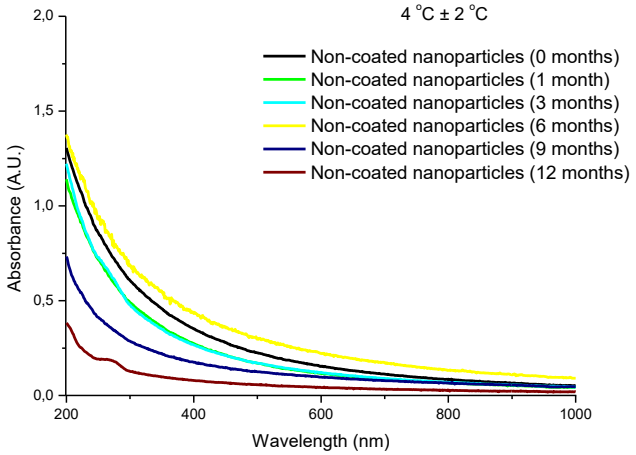
4 °C ± 2 °C
Non-coated nanoparticles (0 months)
Non-coated nanoparticles (1 month)
Non-coated nanoparticles (3 months)
Non-coated nanoparticles (6 months)
Non-coated nanoparticles (9 months)
Non-coated nanoparticles (12 months)
Absorbance (A.U.)
Wavelength (nm)

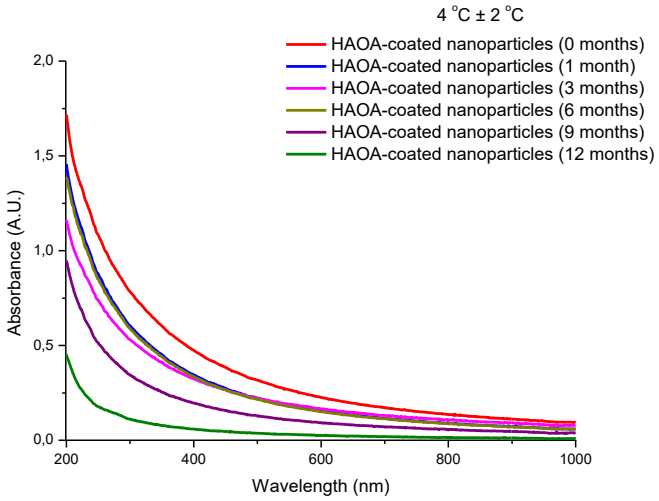
4 °C ± 2 °C
HAOA-coated nanoparticles (0 months)
HAOA-coated nanoparticles (1 month)
HAOA-coated nanoparticles (3 months)
HAOA-coated nanoparticles (6 months)
HAOA-coated nanoparticles (9 months)
HAOA-coated nanoparticles (12 months)
Absorbance (A.U.)
Wavelength (nm)

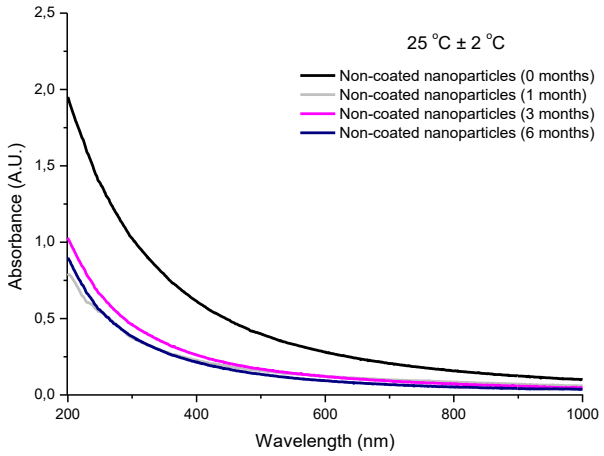
25 °C ± 2 °C
Non-coated nanoparticles (0 months)
Non-coated nanoparticles (1 month)
Non-coated nanoparticles (3 months)
Non-coated nanoparticles (6 months)
Absorbance (A.U.)
Wavelength (nm)

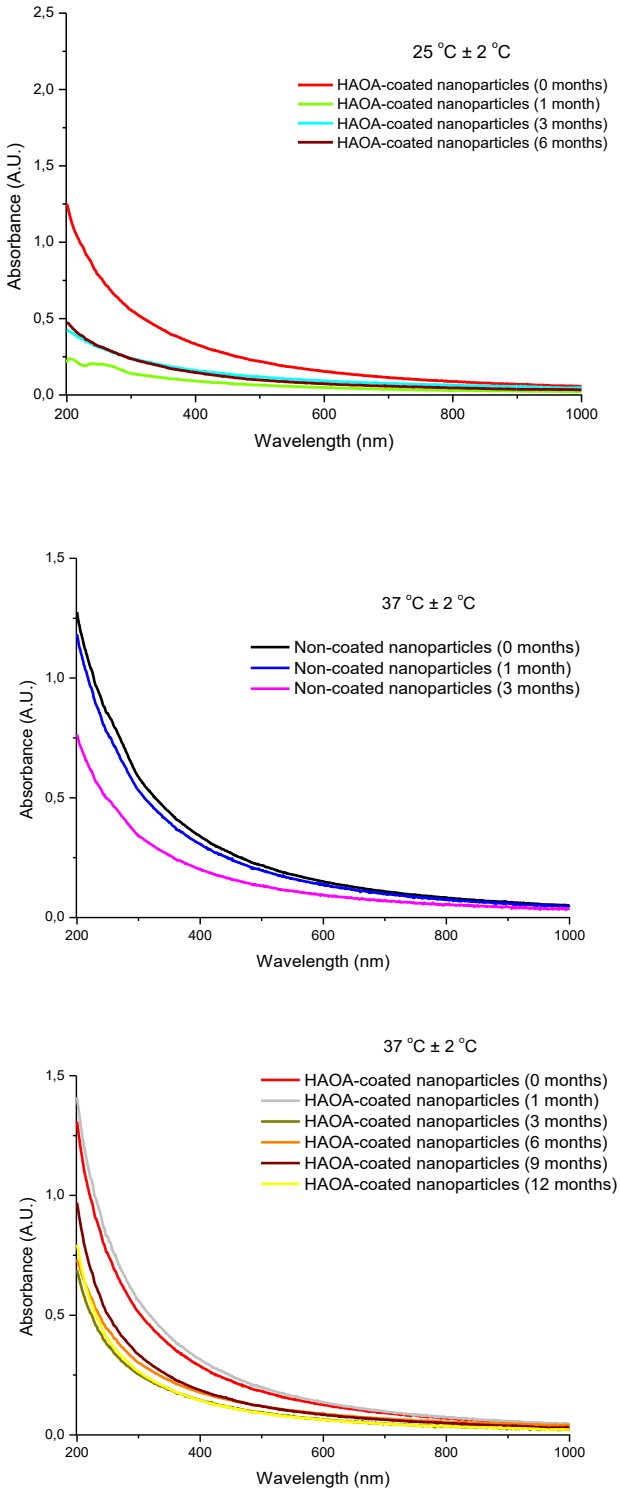

Figure S1. UV-Visible spectra (from 200 nm until 1000 nm) of non-coated nanoparticles and HAOA-coated nanoparticles, as an aqueous suspension, exposed to 4ºC (total time: 12 months), 25ºC (total time: 6 months) and 37ºC (total time: 6-12 months), for over 12 months.

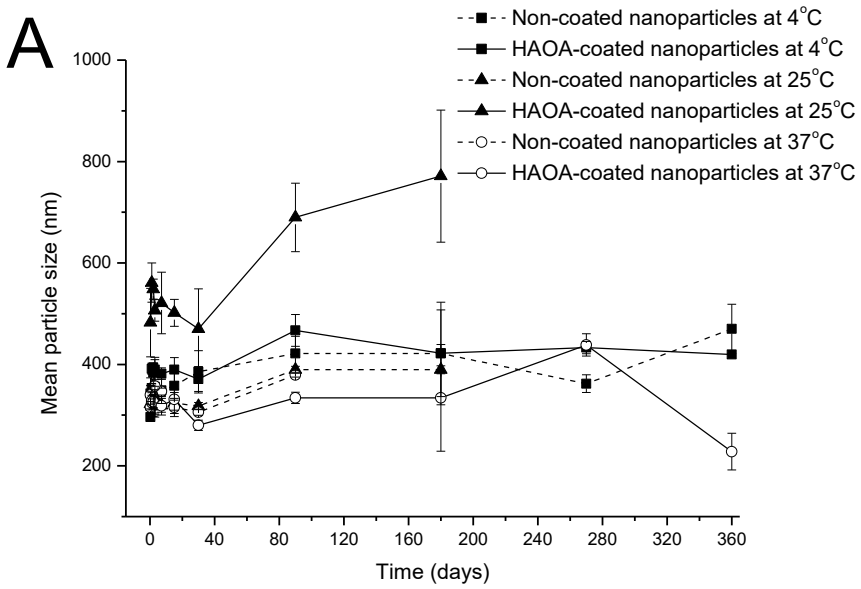
A
Non-coated nanoparticles at 4°C
HAOA-coated nanoparticles at 4°C
Non-coated nanoparticles at 25°C
HAOA-coated nanoparticles at 25°C
Non-coated nanoparticles at 37°C
HAOA-coated nanoparticles at 37°C
Mean particle size (nm)
1000
800
600
400
200
0
40
80
120
160
200
240
280
320
360
Time (days)

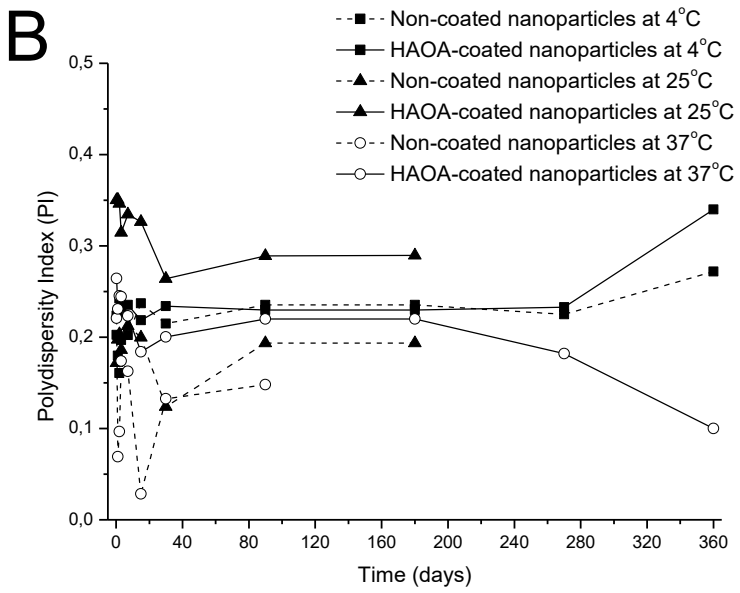
B
Non-coated nanoparticles at 4°C
HAOA-coated nanoparticles at 4°C
Non-coated nanoparticles at 25°C
HAOA-coated nanoparticles at 25°C
Non-coated nanoparticles at 37°C
HAOA-coated nanoparticles at 37°C
Polydispersity Index (PI)
0,5
0,4
0,3
0,2
0,1
0,0
0
40
80
120
160
200
240
280
320
360
Time (days)

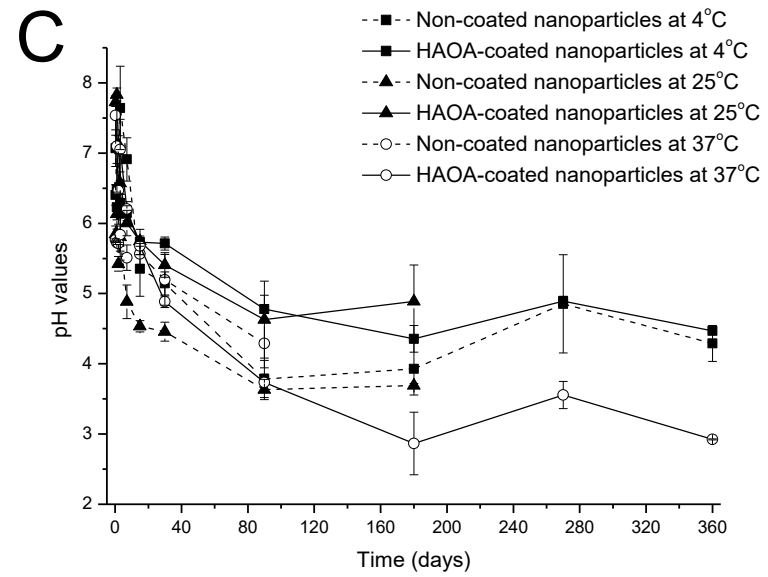

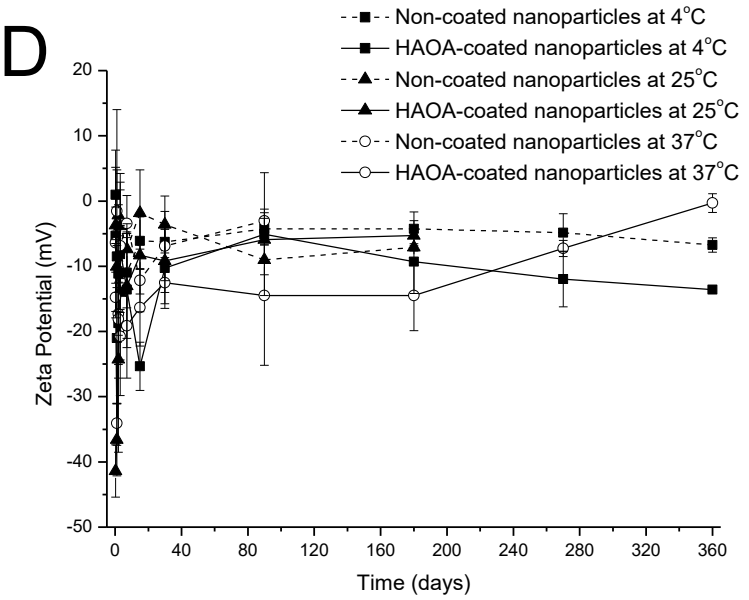

Figure S2. Nanoparticle physicochemical parameters, as aqueous suspensions: (A) size, (B) polydispersity index, PI, (C) pH and (D) zeta potential, ZP, of empty non-coated nanoparticles (i.e., bare core nanoparticles), as dashed line, and HAOA-coated nanoparticles, as continuous line, over 12 months (360 days) for nanoparticles stored at 4 ± 2ºC (■), 6 months (180 days) for nanoparticles stored at 25 ± 1ºC (▲) and 3-12 months (90-360 days) for nanoparticles stored at 37 ± 1ºC (○).Results are expressed as mean of measurements of three independent nanoparticles batches ± SD (n=3).

Table S2. FT-IR spectra main peaks and correspondent functional groups identified for all tested samples as raw components. For physical mixtures and nanoparticles, the peaks are identified based on the functional groups of the raw components (wavenumbers: 4000-400 cm^{-1}).

Samples	Peaks and correspondent functional groups
Raw Materials	
Poly-ε-caprolactone	IR (KBr) v 1730 cm^{-1} (C=O stret.), 1296 cm^{-1} (C-O, C-C stret. in crystalline phase), 1106 cm^{-1} (C-O stret.), 1046 cm^{-1} (C-C stret.) and 732 cm^{-1} (CH_2 rock.).
Pluronic® F-127	IR (KBr) v 2887 cm^{-1} (C-H stret.), 1467 cm^{-1} (O-H in-plane), 1343 cm^{-1} (O-H bend.), 1281 cm^{-1} (C-O stretch.), 1113 cm^{-1} (C-O-C stret.), 964 cm^{-1} and 842 cm^{-1}.
Stearic Acid	IR (KBr) v 2915 cm^{-1}, 2849 cm^{-1}, 2655 cm^{-1}, 1702 cm^{-1},1464 cm^{-1} (O-H in-plane),1298 cm^{-1} (C=C),~ 900 cm^{-1} (O-H out-plane) and 719 cm^{-1} (C=C rock.).
Oleic Acid	IR (KBr) v 2926 cm^{-1} (CH_2 strech.),2856 cm^{-1} (CH_2 strech.), 1711 cm^{-1} (C=O stretch.), 1467 cm^{-1} (O-H in-plane), 1287 cm^{-1} (C-O stretch.),1245 cm^{-1},~ 900 cm^{-1} (O-H out-plane) and 617 cm^{-1}
Hyaluronic Acid	IR (KBr) v 3412 cm^{-1} (NH stretch.), 2908 cm^{-1}, 1652 cm^{-1} (NH_2 bend.), 1618 cm^{-1} (amine I), 1558 cm^{-1} (amine II), 1418 cm^{1}, 1370 cm^{-1}, 1322 cm^{-1} (amine III), 1314 cm^{-1}, 1233 cm^{-1} and 1035 cm^{-1}.
PvD	IR (KBr) v 3328 cm^{-1}, 2959 cm^{-1}, 2923 cm^{-1}, 2347 cm^{-1}, 1668 cm^{-1}, 1609 cm^{-1}, 1591 cm^{-1}, 1520 cm^{-1}, 1443 cm^{-1}, 1351 cm^{-1}, 1314 cm^{-1}, 1292 cm^{-1} (C-O, C-C

	stret.), 1163 cm^{-1}, 1119 cm^{-1}, 1049 cm^{-1}, 846 cm^{-1} and 772 cm^{-1}.
Physical mixtures (1:1 w/w)	
All components (except drug and peptide)	IR (KBr) v 2917 cm^{-1} (CH_2 strech.), 2856 cm^{-1}(CH_2 strech.), 1705 cm^{-1} (C=O stretch.), 1465 cm^{-1} (O-H in-plane), 1406 cm^{-1}, 1359 cm^{-1}, 1340 cm^{-1}, 1292 cm^{-1} (C-O stretch.), 1056 cm^{-1}, 957 cm^{-1} (O-H out-plane) and 717 cm^{-1}.
Hyaluronic and oleic acids (1:1, w/w)	IR (KBr) v 3008 cm^{-1}, 2924 cm^{-1} (CH_2 strech.), 2853 cm^{-1} (CH_2 strech.), 1709 cm^{-1} (C=O stretch.), 1650 cm^{-1} (NH_2 bend.), 1408 cm^{-1}, 1336 cm^{-1} (Amine III), 1075 cm^{-1}, 912 cm^{-1} (O-H out-plane) and 717 cm^{-1}.
HAOA polymer	IR (KBr) v 3432 cm^{-1} (NH stretch.), 2924 cm^{-1}, 2849 cm^{-1} (CH_2 strech.), 2362 cm^{-1}, 2325 cm^{-1}, 1738 cm^{-1} (C=O stret.), 1701 cm^{-1} (C=O stret.), 1561 cm^{-1}, 1462 cm^{-1}, 1403 cm^{-1}, 1384 cm^{-1} (amine III), 1288 cm^{-1}, 1252 cm^{-1}, 1089 cm^{-1}, 1034 cm^{-1}, 931 cm^{-1} (O-H out-plane), 853 cm^{-1} and 721 cm^{-1}
Empty HAOA-coated nanoparticles + free PvD (1:1, w/w)	IR (KBr) v 2946 cm^{-1}, 2863 cm^{-1}, 2360 cm^{-1}, 1727 cm^{-1} (C=O stret.), 1668 cm^{-1} (NH_2 bend.), 1606 cm^{-1}, 1591 cm^{-1}, 1521 cm^{-1}, 1365 cm^{-1} (O-H bend.), 1241 cm^{-1}, 1049 cm^{-1}, 960 cm^{-1}, 842 cm^{-1} and 769 cm^{-1}.
Nanoparticles	
Empty non-coated nanoparticles	IR (KBr) v 2947 cm^{-1}, 2869 cm^{-1}, 1727 cm^{-1} (C=O stret.), 1559 cm^{-1}, 1472 cm^{-1}, 1419 cm^{-1}, 1294 cm^{-1}, 1241 cm^{-1}, 1177 cm^{-1}, 1110 cm^{-1}, 1049 cm^{-1}, 962 cm^{-1} and 734 cm^{-1}.

Empty HAOA-coated nanoparticles	IR (KBr) v 2912 cm^{-1}, 2860 cm^{-1}, 1749 cm^{-1} (C=O stret.), 1715 cm^{-1}, 1652 cm^{-1} (NH_2 bend.), 1558 cm^{-1}, 1418 cm^{-1}, 1368 cm^{-1}, 1234 cm^{-1}, 1048 cm^{-1}, 961 cm^{-1} and 933 cm^{-1}.
PvD-loaded HAOA-coated nanoparticles	IR (KBr) v 2945 cm^{-1}, 2868 cm^{-1}, 2360 cm^{-1}, 2342 cm^{-1}, 1728 cm^{-1} (C=O stret.), ~ 1652 cm^{-1} (NH_2 bend.), 1631 cm^{-1}, 1554 cm^{-1}, 1419 cm^{-1}, 1367 cm^{-1} (O-H bend.), 1242 cm^{-1}, 1049 cm^{-1}, 841 cm^{-1} and 733 cm^{-1}.
α-MSH-conjugated HAOA-coated nanoparticles	IR (KBr) v 3400 cm^{-1}, 2929 cm^{-1}, 2862 cm^{-1}, 1730 cm^{-1} (C=O stret.), 1645 cm^{-1}, 1364 cm^{-1} (O-H bend.), 1241 cm^{-1}, 1050 cm^{-1}, 961 cm^{-1} and 933 cm^{-1}.

Table S3. Description of the main NMR signals for ^{1}H-NMR and ^{13}C-NMR (300 MHz, D_2O, DMSO-d*6* and $CDCl_3$*)* of the following samples: empty non-coated nanoparticles (i.e., bare core), empty HAOA-coated nanoparticles and PvD-loaded HAOA-coated nanoparticles.

Sample	**Empty non-coated nanoparticles**	**δ ^{13}C (ppm)**	**δ ^{1}H (ppm)**
$CDCl_3$	Stearic acid, (CH_3; CH_2)	28.33	0.064 (*m*); 1.61(*m*)
	Poly-ε-caprolactone ($COCH_2$; CH_2COO; CH_2O)	24.55; 25.50; 34.10; 64.14; 173.52	1.64 (*m*); 2.28 (*t*); 4.03 (*t*)
	Pluronic® F-127 (C_2H_4)	70.54	3.64 (*s*)
DMSO-*d6*	SA (CH_3)	-	0.059 (*t*); 1.21(*s*)
	Poly- ε -caprolactone ($COCH_2$, CH_2COO, CH_2O)	-	1.50 (*m*); 2.25 (*t*); 3.96 (*t*)
	Pluronic® F-127 (C_2H_4)	-	1.01 (*d*); 3.49 (*m*)
D_2O	Pluronic® F-127 (OCH_2CHCH_3O)	69.47; 105.0	1.01(*d*); 3.54 (*s*)
Sample	**Empty HAOA-coated nanoparticles**	**δ ^{13}C (ppm)**	**δ ^{1}H (ppm)**
$CDCl_3$	Stearic and oleic acids, CH_3	30.96	0.87 (*m*); 1.24 (*s*); 3.38 (*m*); 5.34 (*t*)
	Poly- ε -caprolactone, $(CH_2)_3$, $COCH_2$, CH_2COO, CH_2O	24.55; 25.51; 28.31; 29.27; 34.08; 64.12; 173.52	1.39 (*m*); 1.64 (*m*); 2.30 (*t*); 4.05 (*t*)
	Hyaluronic acid	-	1.99 (*t*); 3.54 (*m*); 4.22 (*t*)
	Pluronic F-127®	70.52	3.67 (*m*)
DMSO-*d6*	Stearic and oleic acids, CH_3	28.57; 54.68; 69.28	0.83 (*d*); 1.22 (*d*); 1.28 (*s*); 2.25 (*t*); 5.30 (*t*)
	Poly- ε-caprolactone $(CH_2)_3$, $COCH_2$, CH_2COO, CH_2O)	23.58; 26.05; 33.69	1.53 (*m*); 2.26 (*s*); 3.96 (*t*)

	Hyaluronic acid	-	1.95 (*d*); 2.11 (*t*); 3.54 (*s*)
	Pluronic® F-127	-	1.02 (*d*); 2.71 (*s*); 3.48 (*s*);
D_2O	Pluronic® F-127 (OCH_2CHCH_3O)	70.21	1.13 (*m*); 3.54 (*s*)
	Hyaluronic acid (anomeric H)	-	4.60 (*s*); 4.70 (*s*)
Sample	**PvD-loaded HAOA-coated nanoparticles**	**δ ^{13}C (ppm)**	**δ ^{1}H (ppm)**
$CDCl_3$	Stearic and Oleic acid (CH_3; CH_2)	29.68	0.87 (*m*); 1.25 (*s*); 5.34 (*t*)
	Poly- ε-caprolactone ($COCH_2$; CH_2COO; CH_2O)	24.55; 25.51; 28.33; 34.14; 64.14; 173.50	1.38 (*m*); 1.70 (*m*); 2.30 (*t*); 4.07 (*t*)
	Pluronic® F-127 (C_2H_4)	63.26; 70.51	3.64 (*s*)
	Hyaluronic acid	-	2.02 (*d*); 3.65 (*m*); 4.21 (*t*)
	PvD	22.66; 69.06; 129.70	1.12 (*m*); 1.35 (*d*); 3.71 (*d*)
DMSO-*d6*	Stearic and Oleic acid (CH_3; CH_2)		0.83 (*d*); 2.25 (*t*); 5.31 (*t*)
	Poly- ε-caprolactone ($COCH_2$; CH_2COO; CH_2O)	22.50; 24.89; 63.87	1.48 (*m*); 3.94 (*t*)
	Pluronic® F-127 (C_2H_4)	70.872	1.01 (*d*); 3.48 (*s*)
	Hyaluronic acid	-	1.95 (*d*)
	PvD	130.05	1.22 (*m*); 3.28 (*t*)
D_2O	Pluronic® F-127 (OCH_2CHCH_3O)	29.26; 69.47; 75.04; 129.62; 173.15	0.96 (*m*); 1.13 (*m*)
	Hyaluronic acid (anomeric H)	-	3.41 (*m*); 4.59 (*s*); 4.70 (*s*)

Table S4. Elemental Composition of C 1s and O 1s, for non-coated nanoparticles and HAOA-coated nanoparticles, regarding position (binding energy, counts eV), full width at half-maximum intensity (FWHM) (counts, eV) and area (%) of the X-PS spectra.

Sample	Element	Binding energy (counts eV)	FWHM Intensity (counts eV)	Area (%)
Non-coated nanoparticles	C 1s	287.6	3.41	71.75
	O 1s	534.6	2.53	28.25
HAOA-coated nanoparticles	C 1s	286.6	2.50	86.39
	O 1s	534.6	2.85	13.61

Annex I

EGF functionalized polymer-coated gold nanoparticles promote EGF photostability and EGFR internalization for photothermal therapy.

Catarina Oliveira Silva[1, 2], Steffen B. Petersen[3], Catarina Pinto Reis[1, 4*], Patrícia Rijo[1, 5], Jesús Molpeceres[2], Ana Sofia Fernandes[1, 5], Odete Gonçalves[3, 6, 7], Andreia C. Gomes[6], Isabel Correia[8], Henrik Vorum[9] and Maria Teresa Neves-Petersen[10*]

[1]CBiOS, Research Center for Biosciences & Health Technologies, Universidade Lusófona, Campo Grande 376, 1749-024, Lisboa, Portugal.

[2]Department of Biomedical Sciences, Faculty of Pharmacy, University of Alcalá, Ctra. A2, Km 33.600 – Campus Universitario, 28871 Alcalá de Henares, Spain.

[3]Medical Photonics Lab, Department of Health Science and Technology, Faculty of Medicine, Aalborg University, Fredrik Bajers vej 7, DK-9220, Aalborg, Denmark.

[4]IBEB, Biophysics and Biomedical Engineering, Faculty of Sciences, University of Lisbon, 1749-016, Lisbon, Portugal.

[5]iMed.ULisboa, Instituto de Investigação do Medicamento, Faculdade de Farmácia, Universidade de Lisboa, Av. Prof. Gama Pinto, 1649-003 Lisboa, Portugal.

[6]CBMA (Centre of Molecular and Environmental Biology), University of Minho, Campus de Gualtar, 4710-057 Braga, Portugal.

[7]CFUM (Centre of Physics of University of Minho), Department of Physics, University of Minho, Campus de Gualtar, 4710-057 Braga, Portugal.

[8]Centro de Química Estrutural, Instituto Superior Técnico, Universidade de Lisboa, Av. Rovisco Pais 1, 1049-001 Lisbon, Portugal.

[9]Department of Ophthalmology, Aalborg University Hospital, Hobrovej 18-22, 9000 Aalborg, Denmark.

[10]Department of Clinical Medicine, Aalborg University Hospital, Hobrovej 18-22, 9000 Aalborg, Denmark.

***Corresponding Authors:** Prof. Dr. Catarina Pinto Reis and Prof. Dr. Teresa Neves-Petersen

(Publication Pending – submitted to PLOsOne)

Abstract

Background: UVB induced photochemistry of tryptophan and tyrosine residues in proteins leads to the formation of photoproducts, such as kynurenine, N–formylkynurenine and dityrosine and to the disruption of disulphide bridges. Epidermal Growth Factor (EGF) is a small peptide with key medical relevance and a good model protein for photochemical studies. **Methods:** This study reports the behaviour of EGF when exposed to UVB light (295 nm), temperature and quenchers, such as polymer-coated gold nanoparticles. **Results:** Gold nanoparticles (100 – 200 nm) were produced by reduction with an aqueous plant extract and coated with oleic acid and hyaluronic acid, showing a plasmon absorption band located within the near-infrared range (650-900 nm), optimal for photothermal therapy applications. Conjugation of EGF onto the nanoparticles was verified by fluorescence spectroscopy, confocal fluorescence microscopy and circular dichroism. Cytotoxicity studies of EGF-conjugated nanoparticles carried out in normal-like human keratinocytes (HaCaT) showed small decreases in cell viability (0-25%), concentration dependent. EGF-conjugated nanoparticles were able to activate and induce the internalization of EGFR in human lung carcinoma cells (A549 cells) overexpressing EGFR tagged with GFP. **Conclusions:** EGF photochemistry is observed to be both temperature and light power dependent and conjugation of EGF with polymeric-coated gold nanoparticles reduced or even avoided the formation of photoproducts, such as, kynurenine and N–formylkynurenine.

Keywords: Epidermal Growth Factor; Epidermal Growth Factor Receptor; UVB light; Photochemistry; Gold nanoparticles; Receptor activation and internalization.

1. Introduction

UV induced photo-oxidation causes protein conformational changes upon excitation of the aromatic residues, i.e., tryptophan (Trp), tyrosine (Tyr) and phenylalanine (Phe). Three main photoproducts are kynurenine (Kyn, a photoproduct of Trp), N–formylkynurenine (NFK, a photoproduct of Trp) and dityrosine (DT, a photoproduct of Tyr) [1–5]. Since fluorescence excitation and emission spectra of NFK, Kyn and DT differ from the fluorescence spectra of Trp and Tyr, formation of photoproducts can be monitored by fluorescence spectroscopy [1]. Furthermore, UV excitation of the side chains of aromatic residues induces the disruption of disulphide (SS) bonds mediated by an electron transfer process, leading to the formation of a transient disulphide electron adduct [4]. SS bonds are known to be excellent quenchers of protein fluorescence and their reduction leads to changes in the fluorescence quantum yield of proteins [3].

The effect of UV light on the structure and function of key medically relevant proteins, such as Epidermal Growth Factor Receptor (EGFR) [6], insulin [1] and plasminogen [2] has been reported. Correia *et al.* (2014) have shown that 280 nm excitation of EGFR hinders EGF binding to this specific receptor, which most likely explains why such wavelengths can halt signalling pathways (e.g., AKT and ERK1/2 pathways) responsible for cancer cells' proliferation and differentiation [6]. EGFR is involved in cell proliferation, migration, in cancer growth and invasion [6,7]. EGFR is a cell surface receptor that belongs to the ErbB family of receptors and to the subfamily of receptor tyrosine kinases [8]. EGFR is upregulated in several cancers, such as melanoma [8], and its overexpression is correlated with the appearance of melanoma metastases [9]. EGF shows high affinity to EGFR, promoting its dimerization and internalization by endocytosis, which then activates the intracellular tyrosine kinase domain and a downstream signaling pathway necessary for cell growth.

Bio-functionalization of nanoparticles with EGF has been applied to specific targeting cancer cells, which overexpress EGFR and, therefore, with ample interest for cancer treatment. EGF offers many advantages for this type of pharmaceutical application: 1) EGF is smaller (53 amino acids; MW 6 kDa) than antibodies or other EGFR specific ligands used for the same purpose; 2) unlike EGF, antibodies can trigger severe immune response leading to cytotoxicity [10,11]; 3) EGF has three SS bonds, three Trp and five Tyr and hydrophobic residues, all suitable for interactions with nanocarriers [12,13]; and 4) EGF is stable at physiological conditions and neutral pH since its pI value is around

4.55, conferring the peptide a negative charge at pH > 7 [14]. The use of oleic acid (OA) and polymers like hyaluronic acid (HA) can further promote the interaction and entrapment of EGF onto gold nanoparticles, independently of the pI and pH of the solution, as previously reported [15]. Fourier Transform Infrared (FT-IR) studies also showed that EGF presents a thermal unfolding at pH 7.2 that starts at 40ºC, with the transition midpoint at 55.5 ºC and complete denaturation is observed above 76ºC [16]. Another study evaluated the application of EGF for skin patches, showing the resistance of this peptide to temperature (T_m ~ 79 ºC) [17].

It is our aim to use EGF-conjugated HAOA-coated gold nanoparticles with plasmon absorption band located in the near-infrared (NIR) range (i.e., 650-900 nm), for photothermal therapy and local hyperthermia, without damage to the surrounding tissues [18]. This study describes the behaviour of EGF when exposed to temperature, UVB light (295 nm) and quenchers, such as gold nanoparticles coated by hyaluronic and oleic acids (HAOA). The presence of quenchers shortens the fluorescence lifetimes and may confer protection against photochemistry. HA is described to be an excellent fluorescence quencher [19] and to give structural stability to small proteins [20]. OA is also described as a good protein fluorescence quencher [21]. The present study reports the time dependent effect of continuous 295 nm excitation of free EGF on the peptide's fluorescence emission intensity, as a function of irradiance level (power/unit area) and temperature. Trp was selected as an intrinsic molecular probe and SYPRO® Orange was used as an extrinsic molecular probe in order to monitor protein conformational changes [22]. The formation of photoproducts, NKF, Kyn and DT, has been monitored. Moreover, the expected protective effect provided by HAOA-coated gold nanoparticles against 295 nm-induced photochemistry on EGF was investigated by fluorescence spectroscopy. Kinetics of the observed photochemical processes were analyzed and compared for free EGF and EGF conjugated to HAOA-coated gold nanoparticles. Structures of free EGF and EGF-conjugated HAOA-coated gold nanoparticles were monitored using circular dichroism spectroscopy. Binding of EGF and EGF-conjugated HAOA-coated gold nanoparticles to EGFR, present on the cell membrane of A549 human lung carcinoma cells, was monitored using confocal fluorescence microscopy. Cytotoxicity assays (MTT) were carried out in human immortalized keratinocytes, HaCaT cell line, in order to assess the toxicity of the nanoparticles on non-cancerous cells.

2. Materials and methods

2.1 Materials

Gold (III) chloride trihydrate ($HAuCl_4$) (PubChem ID: 24895143; Product number: G4022), L-ascorbic acid (L-AA) (PubChem ID: 24891246; Product number: A7506), silver nitrate ($AgNO_3$) (PubChem ID: 24852543; Product number: S0139), hyaluronic acid (HA) sodium salt from *Streptococcus equi* (MW 7,000-250,000 $g.mol^{-1}$) (PubChem ID: 24878223; Product number: 53747), oleic acid (OA) (MW 282.46 $g.mol^{-1}$) (PubChem ID: 24886786; Product number: 75090) were all supplied by Sigma-Aldrich (Steinheim, Germany). Recombinant Human Epidermal Growth Factor (EGF) (PubChem ID: 62253638), Alexa Fluor® 647 and SYPRO® Orange Protein Gel Stain (5,000X Concentrate in DMSO) were purchased from Life Technologies as molecular probes for confocal microscopy and protein conformational studies. Primary mouse monoclonal antibody anti-EGFR neutralizer antibody LA1 was obtained from Millipore (05-101). The water used for buffer preparation was purified through a Millipore system. Thiazolyl Blue Tetrazolium Bromide (MTT), Fetal Bovine Serum (FBS), puromycin and penicillin/streptomycin were supplied by Sigma-Aldrich (Steinheim, Germany), as of cell culture grade. Dulbecco's Modified Eagle's medium (DMEM) was supplied by Biowest (Nuaillé, France) and DMSO was supplied by Merck (Darmstadt, Germany).

2.2 Preparation of EGF stock solution and EGF-conjugated gold nanoparticles

A 2.5 µM (16.5 µg/mL) stock solution of EGF was prepared in 2 mM Phosphate Buffer Saline (PBS) at pH 7.4. In order to prepare EGF-conjugated HAOA-coated gold nanoparticles, the EGF stock solution at 2.5 µM was mixed with the gold nanoparticles solution (0.22 mM) and hyaluronic acid-oleic acid (HAOA) solution (1 mg/mL), at a 1:1 (v/v) ratio. The reaction mixture was kept for 30 min at room temperature and, then, left overnight at 4ºC protected from the light. Gold nanoparticles were produced based on the addition of an aqueous extract of *Plectranthus saccatus* (10 mg/ mL) as the main reducing and capping agent. The aqueous plant extract was used in alternative to cetyl trimethylammonium bromide (CTAB), and prepared according to the procedure described by Rijo *et al.* (2014), using a microwave method [23]. The nanoparticles suspension was centrifuged twice at 500 x g for 20 min in a FV2400 Microspin (BioSan, Riga, Latvia) to remove unbound peptides. The pellet was re-suspended in PBS buffer (pH 7.4). EGF stock solution was stored at -20 ºC until further use.

2.3 EGF structure analysis and gold nanoparticles structure design

Crystallographic data used for the display of the 3D protein structure was extracted from 1JL9.pdb (3D structure of EGF, chain B), using Discovery Studio 4.1 (Accelrys Software, San Diego, CA, USA). Distances between protein residues were obtained by using the monitor tool in the program. Adobe Illustrator CS5 (Adobe Systems Software Ireland Ltd.) was used in order to graphically display the EGF-conjugated HAOA-coated gold nanoparticles.

2.4 Steady-state fluorescence spectroscopy studies

Steady-state fluorescence emission spectra were collected upon excitation of the Trp pool of the protein at 295 nm. Excitation spectra were acquired with emission wavelength at 330 nm. All measurements were conducted on a fluorescence RTC 2000 spectrometer (Photon Technology International, Canada, Inc.347 Consortium Court London, Ontario N6E 2S8) with a T-configuration, using a 75-W Xenon arc lamp coupled to a monochromator. Samples were analyzed in quartz high precision cell with 10 cm x 2 cm of light path (Hellma Analytics) and gently shaken before each measurement. All slits were set to 5 mm.

2.4.1 Continuous 295 nm illumination of EGF

2.4.1.1 Temperature effect on EGF photochemistry

Continuous 295 nm illumination of EGF (fresh sample, 2.5 µM) was carried out for 2 hours and the protein's fluorescence emission intensity at 330 nm was monitored at five different temperatures: 10 ºC, 15 ºC, 20 ºC, 25 ºC and 30 ºC. Excitation slit was set at 0.8 mm, with an equivalent lamp power of 1.67 µW. Fresh samples were used for each experiment. Emission and excitation intensity spectra were corrected in real-time for oscillations in the emission intensity of the excitation lamp. The Arrhenius plot for free EGF was also represented and all parameters calculated, as explained further in the "Data analysis" section.

2.4.1.2 Light power effect on EGF photochemistry

Continuous 295 nm illumination of EGF (fresh sample, 2.5 µM) was carried out for 2 hours and the peptide's fluorescence emission intensity at 330 nm was monitored using different excitation slit openings: 0.1 mm, 0.5 mm, 0.8 mm, 1.2 mm and 2.0 mm corresponding to 0.12 µW, 0.30 µW, 1.67 µW, 2.34 µW and 4.40 µW, respectively. Fluorescence excitation (em. fixed at 330 nm) and emission (exc. fixed at 295 nm) spectra of EGF were acquired before and after each EGF illumination using different excitation slit openings. The

excitation slit size *versus* excitation power was determined by measuring the power level at the cuvette location with a power meter (Ophir Photonics StarLite Meter ASSY ROHS, P/N7Z01565, Jerusalem, Israel) and a power head (Ophir Photonics, 30A-BB-18 ROHS, P/N7Z02692, Jerusalem, Israel) upon varying the excitation slit size, as previously reported for lysozyme [24]. The temperature of the solution was kept at 20 °C using a Peltier element at the cuvette holder location. A fresh sample was used for each illumination session.

2.4.1.3 SYPRO® Orange: probing EGF conformation changes induced by 295 nm and temperature

SYPRO® Orange is used as a molecular probe in order to monitor protein conformational changes since its fluorescence is greatly enhanced upon contact with hydrophobic environments [25]. A 2 µL aliquot (dilution 1:1000) of SYPRO® Orange stock solution (5,000X Concentrate in DMSO) was added to a cuvette containing a fresh sample of EGF (2.5 µM, 0.2 mL) prior to the 295 nm continuous illumination experiment. The sample was gently shaken to mix both solutions. Fluorescence emission of SYPRO® Orange at 580 nm was monitored upon continuous illumination at 470 nm for 2 hours, at each of the above mentioned temperatures, i.e., 10 ºC, 15 ºC, 20 ºC, 25 ºC and 30 ºC. Fluorescence intensity changes were quantified. In addition, the fluorescence emission of SYPRO® Orange at 580 nm was monitored upon continuous illumination at 470 nm for 2 hours, at each of the above mentioned power levels, i.e., 0.12 µW, 0.30 µW, 1.67 µW, 2.34 µW and 4.40 µW (corresponding to 0.1 mm, 0.5 mm, 0.8 mm, 1.2 mm and 2.0 mm slits, respectively). Fluorescence spectral changes were quantified.

2.4.1.4 Photoproducts of tryptophan and tyrosine

Fluorescence excitation and emission spectra of the Trp and Tyr photoproducts (e.g., NFK, Kyn and DT) were monitored. Excitation and emission fluorescence spectra of the photoproducts differ from the ones of Trp and Tyr: NFK and Kyn are excited at 320 nm and 360 nm and show a maximum emission between 400-440 nm and between 434-480 nm, respectively [26–28]. Therefore, EGF fluorescence intensity changes and spectral shifts were quantified, before and after the illumination of EGF at 295 nm, at different temperatures and different light power slit openings.

2.4.2 Photochemistry of EGF conjugated with HAOA-coated gold nanoparticles

The effect of continuous 295 nm excitation of EGF has been investigated for EGF conjugated to gold nanoparticles covered by natural polymers, such as hyaluronic acid

(HA) and oleic acid (OA). Results were compared with data obtained with free EGF. Four samples were continuously illuminated with 295 nm light for 2 hours at 20 ºC and their fluorescence emission intensity at 330 nm has been monitored: a) free EGF, b) EGF-conjugated HAOA-coated nanoparticles, c) plain non-coated gold nanoparticles and d) HAOA-coated gold nanoparticles. Based on previous studies [24], excitation slit was set to 2.0 mm, with an equivalent power of 4.40 μW at the entrance of the excitation chamber. Conjugation of EGF onto the HAOA-coated gold nanoparticles has been confirmed using steady state fluorescence spectroscopy. Fluorescence excitation (em. fixed at 330 nm) and emission (exc. fixed at 295 nm) spectra of non-conjugated EGF, of the supernatant after centrifugation of the solution containing conjugated and non-conjugated EGF, and of conjugated EGF onto HAOA-coated gold nanoparticles, have been acquired in order to detect the presence of protein. In order to detect likely light-induced conformational changes in EGF, SYPRO® Orange was used as a molecular probe. Fluorescence emission spectra of SYPRO® Orange (excitation fixed at 470 nm) and fluorescence excitation spectra of SYPRO® Orange (emission fixed at 580 nm) were also acquired prior and after continuous illumination of EGF and EGF-conjugated HAOA-coated gold nanoparticles at 295 nm for 2 hours. Formation of Trp photoproducts (Kyn and NFK) upon 295 nm excitation of free EGF and EGF-conjugated HAOA-coated gold nanoparticles has been confirmed using steady state fluorescence spectroscopy. In order to detect Kyn and NFK, fluorescence emission spectra were acquired upon 320 nm excitation of the solution before and after 2 hours of continuous illumination at 295 nm. In order to detect the presence of Kyn, emission spectra were obtained upon 360 nm excitation before and after 295 nm continuous excitation. Fluorescence spectral changes have been quantified and compared for free and conjugated EGF. A fresh sample was used for each illumination run.

2.5 Physical characterization of EGF-conjugated HAOA-coated gold nanoparticles

Mean particle size, polydispersity index (PI) and zeta potential (ZP) for EGF-conjugated HAOA-coated gold nanoparticles were determined with a Coulter Nano-sizer Delsa Nano™C (Fullerton, CA). A low value of PI factor (< 0.25) will indicate a less dispersed nanoparticles distribution in size. “D-value” was determined as the size distribution in 10%, 50% and 90% of the nanoparticles population [29]. EGF-conjugated HAOA-coated gold nanoparticles were characterized by UV-visible spectroscopy (Evolution 600, UK) and the respective maximum absorbance wavelength (λ_{max}) was determined.

2.6 TEM analysis of EGF-conjugated HAOA-coated gold nanoparticles

Structure and surface morphology of EGF-conjugated HAOA-coated gold nanoparticles were analyzed by Transmission Electron Microscopy (TEM, Zeiss M10, Germany). Samples were prepared through "sequential two-droplet" method by re-suspending the nanoparticles in distilled water and placing a drop (5-10 µL) of the suspension on to a formvar grid for 30-60 sec. When the nanoparticles suspension had partly dried, the surface of the grid was washed three times with distilled water and the excess of water was removed with a filter paper. Then, sodium phosphotungstate (PTA, 2%, w/v) was applied to the grid for 10 sec, the excess of stain removed with a filter paper and the grid was left to dry at room temperature for 24 hours. Samples were analyzed at voltage setting of 60 kV. Different fields of the images were recorded digitally.

2.7 Confocal fluorescence microscopy studies with EGF-conjugated HAOA-coated gold nanoparticles

EGF-conjugated HAOA-coated gold nanoparticles were marked with two different fluorescent probes, Coumarin-6 and Alexa Fluor 647, as described below, for confocal microscope visualization and colocalization. Firstly, an aliquot (20 µL) of a saturated solution of Coumarin-6 (λ_{max_ex} = 460 nm, λ_{max_em} = 500 nm) in ethanol was added to an aqueous suspension, containing the polymer HAOA and the gold nanoparticles at 1:1 (v/v). Then, EGF marked with Alexa Fluor 647 (λ_{max_ex} = 650 nm, λ_{max_em} = 665 nm) was added to the HAOA-coated gold nanoparticles suspension. Coumarin-6 labeled nanoparticles were allowed to conjugate with the EGF-Alexa Fluor 647 for 30 min at room temperature, and were left 24 hours at 4 ºC, protected from the light. The suspension was centrifuged twice at 500 x g for 20 min in a FV2400 Microspin (BioSan, Riga, Latvia) to remove unbound EGF. The pellet was re-suspended in PBS buffer (pH 7.4). Confocal Laser Scanning Microscopy (CLSM, Leica, SP5, Mannheim, Germany) was used to verify the colocalization of both dyes on the EGF-conjugated HAOA-coated gold nanoparticles. The chosen excitation laser line He-Ne was 561 nm and the fluorescence emission selected range was set to 569-666 nm. Each sample was analyzed at room temperature and upon letting it dry on a glass slide. Different fields of the images were recorded digitally.

2.8 Circular dichroism spectroscopy

Far UV circular dichroism (CD) spectroscopy was carried out to detect any changes in EGF secondary structure after conjugation with HAOA-coated gold nanoparticles using a Jasco J-720 spectropolarimeter (Jasco Corporation, Easton, MD, USA), with a

photomultiplier suitable for the 200-700 nm range. After calibration to remove the noise of the device, the PBS buffer used to prepare the native EGF solution and Milli-Q water used for nanoparticles formulations were used as references to obtain the respective baselines. Far UV spectra were acquired using a quartz cell containing solutions of free EGF (0.3 mg/mL), EGF-conjugated HAOA-coated gold nanoparticles (16.5 µg/mL) and HAOA-coated gold nanoparticles (without peptide). Furthermore, spectra of EGF extracted from HAOA-coated gold nanoparticles by two different methods were recorded: 1) EGF non-conjugated present in the supernatant after centrifugation of EGF-conjugated HAOA-coated gold nanoparticles at 7200 x g for 10 min and 2) after incubation of EGF-conjugated HAOA-coated gold nanoparticles in PBS pH 5.5, at 37ºC, for 72 hours, followed by centrifugation at 9000 x g for 3 min. Scanning of each sample was conducted from 200 nm to 260 nm with a resolution of 1 nm band width, 3 accumulations, scan speed 100 nm/min and 2 seconds response time. Data was processed using 10 point smoothing in Origin 8.1 (OriginLab Corporation, Northampton, MA, USA).

2.9 Cytotoxicity assays in HaCaT cell line model

Cell viability studies were conducted in human immortalized keratinocytes (HaCaT) using the MTT assay [30,31] in order to assess the cytotoxicity of EGF-conjugated HAOA-coated gold nanoparticles. Cells were cultured in Dulbecco's Modified Eagle Medium (DMEM) medium supplemented with 10% fetal bovine serum (FBS) and 1% penicillin/streptomycin solution. HaCaT cells were seeded onto 96-well plate at a density of 5,000 cells/ well to reach the desired confluence. EGF-conjugated HAOA-coated gold nanoparticles were tested at different concentrations: 0-80 µM (based on the concentration of gold). DMSO 5% (v/v) was used as the positive control. Cells were exposed to nanoparticle suspension for 24 hours. After this period, cells were washed twice with PBS and incubated with MTT solution (0.5 mg/mL in culture medium) for 2.5 hours at 37 ºC. Culture medium was then removed and cells were washed again with PBS. DMSO (200 µL per well) was added to dissolve the formazan crystals and absorbance was read at 595 nm (Thermo Scientific Multiskan FC, Shanghai, China). Three to four independent experiments were carried out, each comprising four replicate cultures.

2.10 EGFR binding assay on A549 cells GFP-EGFR

In vitro studies were carried out in A549 cells, in which the genomic EGFR gene has been endogenously tagged with a Green Fluorescent Protein gene (GFP) (Sigma-Aldrich

ref. CLL1141), since this is a specific and well-studied cell model for EGFR binding assay [32]. A549 cells were cultured in DMEM medium with FBS 10% and 1 µg/mL puromycin and maintained at a 37 ºC in a 5% CO_2 atmosphere, in order to analyze the effects of adding free EGF (4 µg/mL), EGF-conjugated HAOA-coated gold nanoparticles (4 µg/mL EGF; 60 µM gold nanoparticles) and HAOA-coated gold nanoparticles (non-conjugated; 60 µM). EGF-conjugated HAOA-coated gold nanoparticles were marked with two different fluorescent probes, Coumarin-6 (λ_{max_ex} = 460 nm, λ_{max_em} = 500 nm) and Alexa Fluor 647 (λ_{max_ex} = 650 nm, λ_{max_em} = 665 nm), as previously described, for confocal microscope visualization and colocalization experiments**.** Free EGF was marked with Alexa Fluor 647, while nanoparticles were labeled with Coumarin-6. Prior to the image acquisition in the confocal fluorescence microscope, the cells were incubated 1.5 hours with the free EGF and with the EGF-conjugated HAOA-coated gold nanoparticles. In specific wells, a primary mouse monoclonal antibody anti-EGFR (1 µg/mL of neutralizer antibody LA1, Millipore (05-101)) was used to block EGFR. After 1 hour of incubation with the antibody, free EGF or EGF-conjugated HAOA-coated gold nanoparticles were added to the A549 cells' incubation medium, for incubation during 1.5 hours, to see if they compete for the receptor binding and consequent receptor internalization. As controls, non-treated cells and HAOA-coated gold nanoparticles loaded with Coumarin-6 (without EGF) were used. EGFR binding and activation was analyzed by confocal fluorescence microscopy (CLSM, Leica, SP5, Mannheim, Germany). Ligand binding to EGFR activates the receptor and the GFP tagged receptor initially localized on the cell membranes, is then internalized. This leads to the appearance of fluorescence granules in the cell cytoplasm, as described previously for Human EGFR Live Cell Fluorescent Biosensor Assay (Sigma-Aldrich, Germany).

2.11 Data Analysis

All data analysis, plotting and fitting procedures were done using Origin 8.1 (OriginLab Corporation, Northampton, MA, USA).

2.11.1 Emission Spectra and Excitation Spectra

Emission and excitation spectra were first smoothed using a 10 points adjacent averaging. All fluorescence spectra obtained were first Raman corrected by subtracting the spectra recorded for the buffer in solution. Normalized emission and excitation spectra were obtained by dividing each data point by the maximum intensity value in each spectrum.

2.11.2 Fitting Procedures

2.11.2.1 EGF fluorescence emission kinetic traces (em. at 330 nm) upon 295 nm continuous excitation as a function of light power and temperature

Each decay curve acquired upon 2 hours of continuous 295 nm illumination of EGF exposed at different temperatures (10 ºC, 15 ºC, 20 ºC, 25 ºC and 30 ºC) and different excitation slit openings (0.5 mm, 0.8 mm, 1.2 mm and 2.0 mm), was fitted using a single exponential decay model given by the function $F(t) = C_1*exp(-x*k_1) + y_0$ or a double exponential decay model, according to $F(t)=y_0+C_1*exp(-k_1*x)+C_2*exp(-k_2*x)$. $F(t)$ is the fluorescence emission intensity at 330 nm (a.u.) upon 295 nm at excitation time t (min), y_0, C_1 and C_2 are constants and k_1, k_2 are the rate constant of fluorescence emission intensity decrease (min^{-1}); y_0 value was fixed to 0. Root mean square error R^2 was > 0.99 for all fitted traces. A double exponential decay model was selected if the single decay model did not provide a good fit. Data obtained with 0.1 mm slit size, was fitted using a linear model ($F(t)=y_0+C_1*x$). A good fit was based on the errors associated to the different parameters and the root mean square error. Fitted parameter values and corresponding errors, and root mean square error values obtained after fitting the 330 nm emission kinetic traces are displayed in Tables 2 and 3.

2.11.2.2 EGF photochemistry: Arrhenius plot and activation energy

Temperature dependence of the decay constant of the EGF kinetic traces (Fig. 2A) (where the fluorescence emission intensity at 330 nm is displayed upon 295 nm excitation), was analyzed using four different temperatures: 15 ºC, 20 ºC, 25 ºC and 30 ºC. Data was fitted according to the logarithmic form of the Arrhenius equation: $ln\ k = ln\ A_0 + (E_a/RT)$, where A_0 is the pre-exponential factor, E_a is the activation energy, R is the universal constant for perfect gases (R = 8.314 J/ mol.K) and T is the temperature (in Kelvin). The Arrhenius plot and extracted parameters are displayed in Fig. 3.

2.11.2.3 Free EGF and EGF conjugated HAOA–coated gold nanoparticles fluorescence kinetics (em. at 330 nm) upon 295 nm excitation

Fluorescence emission intensity kinetic traces at 330 nm for free EGF, plain non-coated gold nanoparticles, HAOA-coated gold nanoparticles and EGF-conjugated HAOA-coated gold nanoparticles samples are displayed in Fig. 5. Traces were acquired upon continuous 295 nm illumination for 2 hours, at 20 ºC, except for plain gold nanoparticles and HAOA-coated gold nanoparticles without EGF, which were illuminated for 1 hour. All traces were fitted using a double exponential decay model according to the formula

$F(t)=y_0+C_1*exp(-k_1*x)+C_2*exp(-k_2*x)$. $F(t)$ is the fluorescence emission intensity at 330 nm (a.u.) upon 295 nm excitation at time t (min), y_0, C_1 and C_2 are constants and k_1 *and* k_2 is the rate constant of fluorescence emission intensity decrease (min^{-1}); y_0 value was fixed to 0. The root mean square error R^2 was > 0.99 for all kinetics. The fitted parameter values and corresponding errors, and root mean square error values obtained after fitting the 330 nm emission kinetic traces are displayed in Table 4.

3. Results

Fig. 1 displays the 3D molecular structure of Epidermal Growth Factor, EGF (1JL9.pdb). Although EGF is formed by two amino acid chains (A and B), only chain B is represented. Tryptophan (Trp), Tyrosine (Tyr) residues and disulphide bridges (SS) are highlighted in red, blue and green, respectively. In total, EGF has 2 Trp residues, 5 Tyr residues and 3 SS bridges. Table 1 lists the shortest distances between each Trp and Tyr residues and the nearest SS bonds. The shortest distance between Tyr13 (atom CD1) and the SS bridge C14-C31 is 4.4 Å. All considered distances were < 12 Å. In addition, EGF has no Phenylalanine (Phe) residues but has a considerable number of Arginine (Arg) residues in its structure, close to Trp residues. Arg residues are of considerable importance since they quench the aromatic residues fluorescence emission, when the NH_2 groups become protonated. The closest distances between these two amino acids occur between Arg45 (NE) and Trp50 (CH2) and Trp49 (CE3) at 4.5 Å and 7.5 Å, respectively.

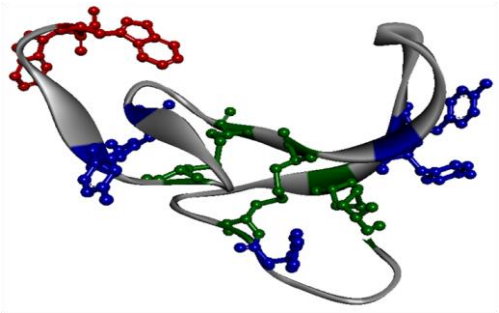

Figure 1.Molecular structure of EGF (chain B) according to (1JL9.pdb). Aromatic residues are represented by different colors: Trp (red), Tyr (blue) and Cys (green).

Table 1. Shortest spatial distances between disulphide (SS) bonds and aromatic residues (tryptophan and tyrosine) in EGF chain B (1JL9.pdb). The shortest distances (< 12 Å) between atoms of each pair of elements (Trp, Tyr and disulphide bonds) were considered. For Trp and Tyr residues, only atoms belonging to the indole and benzene rings were considered, and for SS bonds one of the SG atoms. (W = Trp; Y = Tyr; PDB atomtype descriptor used is given in parentheses).

Disulphide Bond	Aromatic Residue	Distance (Å)
C6-C20	Y13 (CD1)	5.5
	Y22 (CG)	9.2
	Y29 (CD1)	4.8
C14-C31	Y13 (CD1)	4.4
	Y29 (CD1)	9.5
	Y37 (CD2)	9.7
	Y44 (CD2)	11.8
C33-C42	Y13 (CD1)	7.9
	Y37 (CG)	5.7
	Y44 (CD2)	9.5
	W49 (CZ3)	7.3

Figs. 2A and 2B display the fluorescence kinetic traces for EGF upon 2 hours excitation at 295 nm (emission fixed at 330 nm) and for SYPRO® Orange an analogous experiment (excitation of 470 nm and emission fixed at 580 nm), respectively. Traces were acquired at five different temperatures: 10 ºC, 15 ºC, 20 ºC, 25 ºC and 30 ºC. At all temperatures, fluorescence emission intensity of Trp is observed to decay as a function of illumination time. On the other hand, fluorescence emission intensity of SYPRO® Orange increases with illumination time. The parameters and corresponding errors, as well as root mean square error values, obtained after fitting each kinetic trace are displayed in Table 2. At 10 ºC and 15 ºC, EGF showed similar fluorescence emission decays with a decrease in

Trp fluorescence emission intensity at 330 nm of 56.2%, 52.8%, respectively. The corresponding increase in the fluorescence emission of SYPRO® Orange after 2 hours excitation of EGF at 295 nm at 10 ºC and 15 ºC was 15.6% and 22.7%, respectively. At 20 ºC and 30 ºC, the fluorescence emission intensity of Trp decreased 59.6% and 59.1%, respectively, after 2 hours excitation of EGF at 295 nm, while the fluorescence emission intensity of SYPRO® Orange increased 2.3% and 17.3%, respectively. At last, continuous 295 nm excitation of EGF at 25 ºC led to a 59.7% decrease in the fluorescence emission intensity of the protein and to a 6.7% increase in the fluorescence emission intensity of SYPRO® Orange.

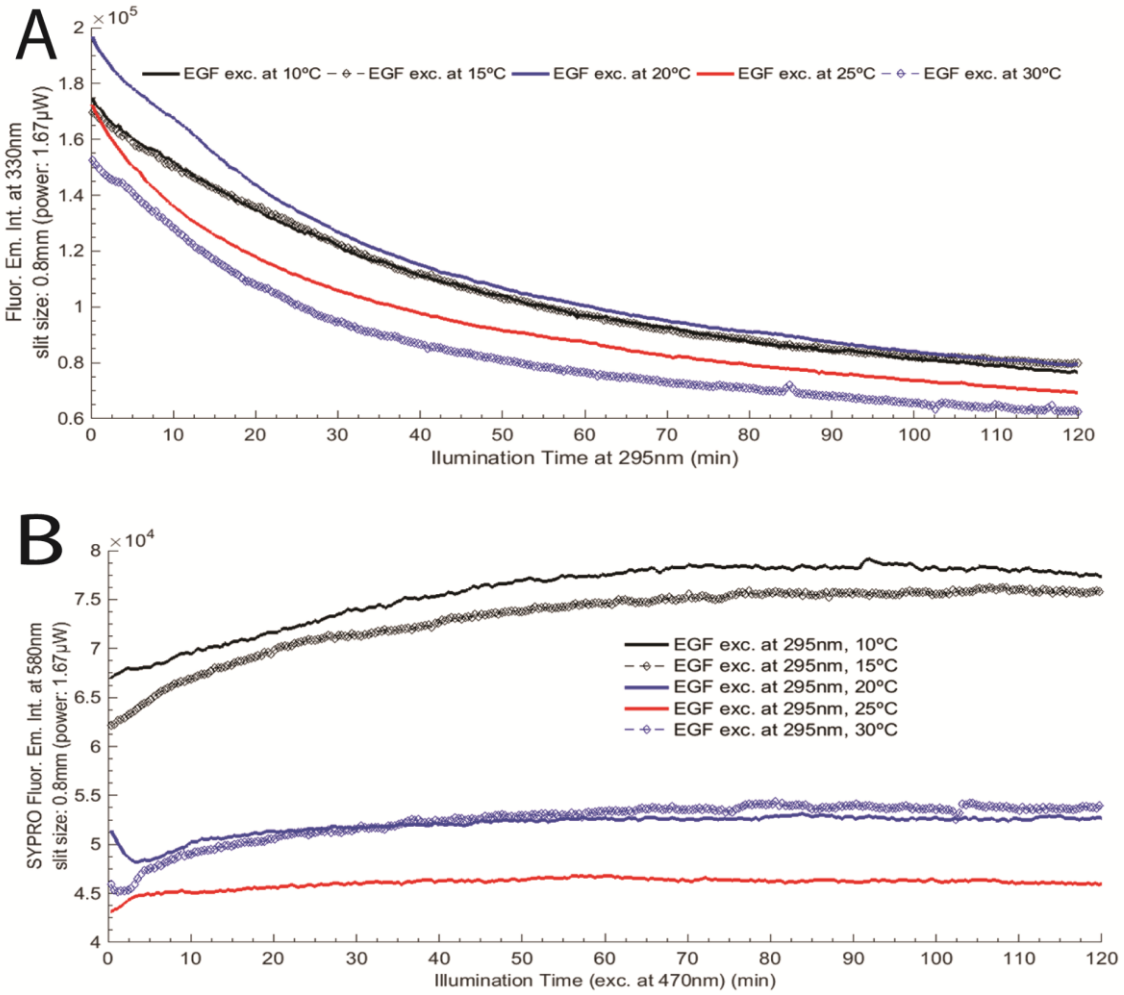

Figure 2. Temperature effect on EGF photochemistry: A) EGF fluorescence excitation and emission wavelengths were fixed at 295 nm and 330 nm, respectively, at 10 ºC, 15 ºC, 20 ºC, 25 ºC and 30 ºC; B) SYPRO® Orange fluorescence excitation and emission wavelengths were fixed at 470 nm and 580 nm, at the same temperatures. Continuous

illumination was conducted during 2 hours and the excitation slit size was set at 0.8 mm (1.67 µW) for all experiments.

Table 2.Single exponential fit using model $F(t) = C_1*exp(-x*k_1) + y_0$ for each decay curve of EGF at 10 ºC, 15 ºC, 20 ºC and 30 ºC. For the decay curve of EGF at 25 ºC, a double exponential fit using model $F(t)=y_0+C_1*exp(-k_1*x)+C_2*exp(-k_2*x)$ was selected (see Fig.2A). Fit parameters are displayed in this table. Adj. R^2 stands for Adjusted R- Square.

Decay	Parameters					Statistic
	y_0	C_1	C_2	k_1	k_2	Adj. R^2
10 ºC	7.1E+4±1.5E+2	1.0E+6±1.4E+2	-	1.1E+3±4.7	-	0.999
15 ºC	7.2E+4±1.5E+2	9.8E+4±1.4E+2	-	1.1E+3±6.2	-	0.999
20 ºC	7.7E+4±2.0E+2	1.2E+5±2.4E+2	-	2.2E+3±1.3E+1	-	0.999
25 ºC	5.6E+4±3.9E+2	4.3E+4±5.9E+2	7.1E+4±3.1E+2	2.8E+2±4.1	1.7E+3±3.0E+1	0.999
30 ºC	6.3E+4±1.7E+2	9.0E+4±2.8E+2	-	7.5E+2±5.9	-	0.997

In Fig. 3 is displayed the Arrhenius plot. Due to the temperature dependence of the EGF rate constant (k), recovered from the fluorescence emission decays at 330 nm (excitation at 295 nm), at the five different temperatures studied, we obtained an activation energy (E_a) and a pre-exponential factor (A_0) of 19.9±0.9 kJ.mol^{-1} and 0.44±0.37 s^{-1}, respectively. The equation obtained was y = -1.1x – 1933.4 (R^2= 0.994).

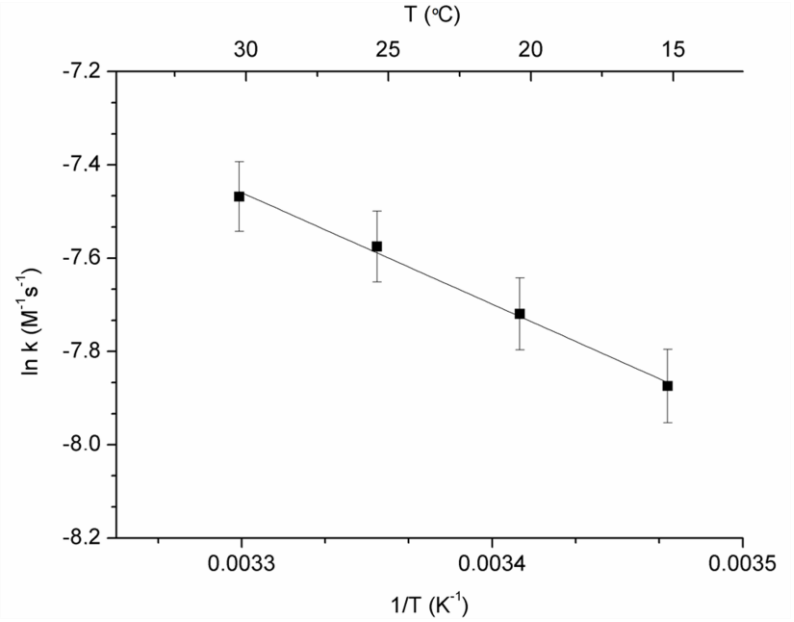

Figure 3. Arrhenius plot showing the linear correlation between the logarithm of the kinetic rate constant (*ln k*) and the inverse of temperature *1/T* (*ln k = ln A_0 - E_a/RT)*, R^2 = 0.994). The activation energy (E_a) and the pre-exponential factor (A_0) were 19.9±0.9 kJ.mol^{-1} and 0.44±0.37 $M^{-1}.s^{-1}$, respectively. Uncertainty errors for *ln k* values are represented as error bars (percent of data: 1%).

In Figs. 4A and 4B are displayed, respectively, the kinetic traces for free EGF during 2 hours excitation at 295 nm (emission at 330 nm) at 20 ºC and the kinetic traces for SYPRO® Orange (excitation of 470 nm and emission at 580 nm) using different excitation powers. Excitation of free EGF at 295 nm for 2 hours with different excitation slit sizes of 0.1 mm, 0.5 mm, 0.8 mm, 1.2 mm and 2.0 mm led to a 8.0%, 48.6%, 59.6%, 65.6% and 70.8% decrease in Trp fluorescence emission intensity, respectively. After 295 nm excitation of EGF for 2 hours, the fluorescence emission intensity of SYPRO® Orange increases 9.1%, 2.3%, 21.5% and 6.1% for slit sizes of 0.5 mm, 0.8 mm, 1.2 mm and 2.0 mm, respectively. In the same experiments, the fluoresce emission intensity of SYPRO® Orange has maximally increased by 9.1%, 3.2%, 26.8% and 19.3% for 0.5 mm, 0.8 mm, 1.2 mm and 2.0 mm, respectively. No change was observed in the fluorescence emission intensity of SYPRO® Orange at a slit size of 0.1 mm (decrease: 0.2% = ~0%). A single exponential model ($F(t) = y_0 + C_1 * exp(-x * k_1)$) was selected to fit the 330 nm decay curves obtained with 0.5 mm and 0.8 mm slit openings. The traces obtained with larger slit openings (1.2 mm and 2.0 mm) were fitted with a double exponential model ($F(t)=y_0+C_1 * exp(-k_1 * x)+C_2 * exp(-k_2 * x)$). The corresponding fitted parameter values (C_1, C_2

k_1, k_2, y_0) and corresponding errors, as well as root mean square error values, are displayed in Table 3. The 330 nm fluorescence decay obtained when a slit 0.1 mm was chosen was best fitted by a linear model.

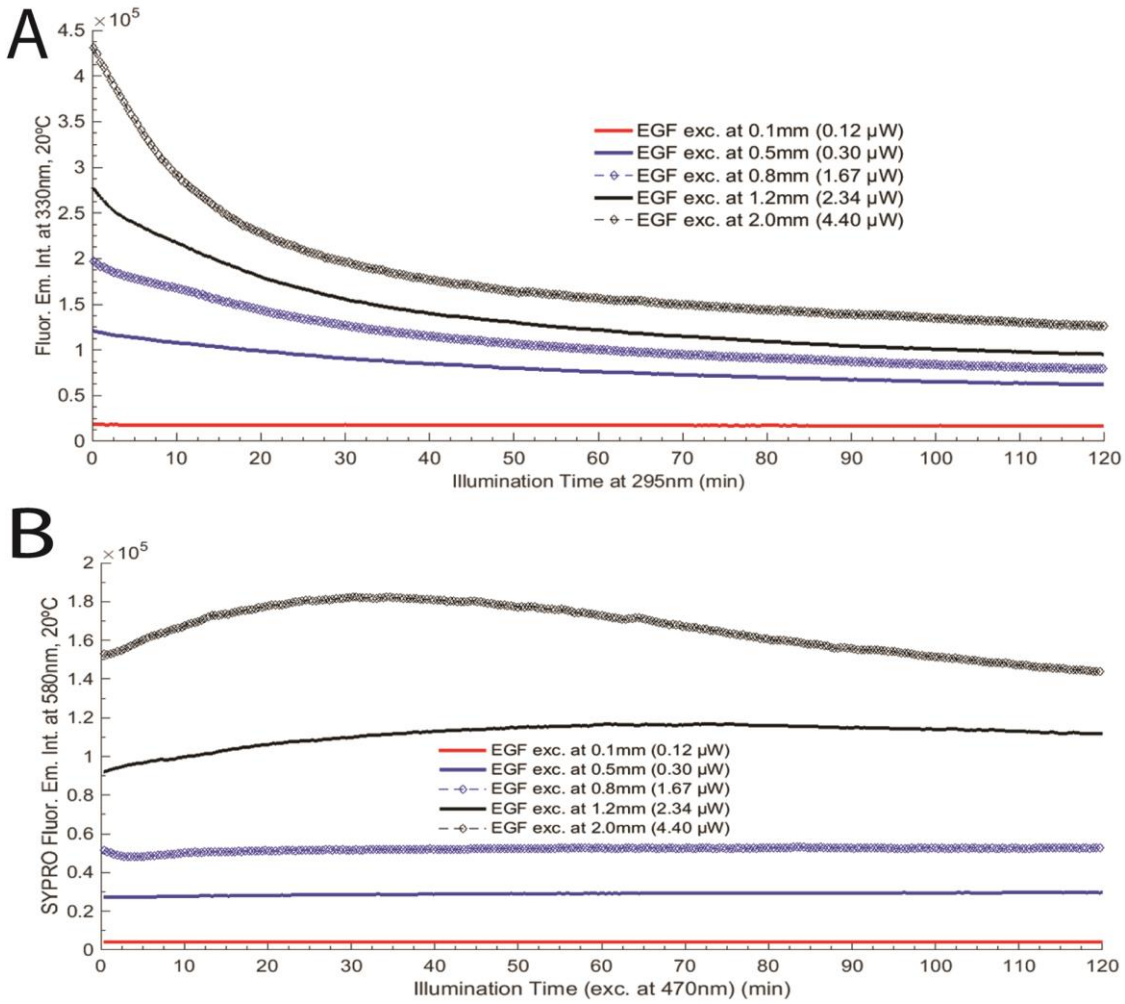

Figure 4. UV-light power effect (different excitation slit openings) on EGF photochemistry: A) EGF fluorescence excitation and emission wavelengths were fixed at 295 nm and 330 nm, respectively, for 0.1 mm (0.12 µW), 0.5 mm (0.30 µW), 0.8 mm (1.67 µW), 1.2 mm (2.34 µW) and 2.0 mm (4.40 µW); B) SYPRO® Orange fluorescence excitation and emission wavelengths were fixed at 470 nm and 580 nm, for the same power levels. Continuous illumination was conducted during 2 hours and the temperature of each solution was kept at 20 °C for all experiments.

Table 3. Single exponential fit using model $F(t) = C_1*exp(-x*k_1) + y_0$ for each decay curve of EGF at a power slit size of 0.5 mm and 0.8 mm (corresponding to 0.30 µW and 1.67 µW, respectively) and double exponential fit using model $F(t)=y_0+C_1*exp(-k_1*x)+C_2*exp(-k_2*x)$ for each decay curve of EGF at a power slit size of 1.2 mm and 2.0 mm (corresponding to 2.34 µW and 4.40 µW, respectively) (see Fig.4A). For slit 0.1 mm (0.12 µW), a linear model was selected. Fit parameters are displayed in this table. R^2 stands for Adjusted R- Square.

Slit (mm)	Decay Parameters					Statistic
	y_0	C_1	C_2	k_1	k_2	R^2
0.1	1.8E+4±1.1E+1	-0.16±2.7E-3	-	-	-	0.921
0.5	5.7E+4±1.2E+2	6.2E+4±1.0E+2	-	3.0E+4±1.5E+1	-	0.999
0.8	7.7E+4±2.0E+2	1.2E+5±2.4E+2	-	2.2E+3±1.3E+1	-	0.999
1.2	5.8E+4±1.1E+4	9.0E+4±5.6E+3	1.2E+5±5.5E+3	7.9E+3±2.1E+3	1.2E+3±3.7E+1	0.999
2.0	9.8E+4±1.8E+3	2.2E+5±1.3E+3	1.2E+5±6.4E+2	6.8E+2±4.9	5.1E+3±2.1E+2	0.999

After studying the temperature and power dependence of the kinetic traces for free EGF, the behavior of this peptide has been monitored after conjugation with a nanosystem made of a gold core and a biodegradable polymeric coating of HAOA. HAOA-coated gold nanoparticles (i.e., non-conjugated with EGF) showed a mean particle size of 300 nm (PI: 0.2) and a negatively charged surface (-19 mV) [24]. After conjugation with EGF, the volume distribution for 90% of HAOA-coated gold nanoparticles (D 90%) was 220 nm, as confirmed by TEM analysis, where EGF-conjugated HAOA-coated gold nanoparticles showed a size around 100-200 nm and a spherical morphology (see Fig. 5). EGF-conjugated HAOA-coated gold nanoparticles are displayed, both as an illustration (upper left corner) and when imaged by TEM. EGF-conjugated HAOA-coated gold nanoparticles are composed by a dense gold core observed in the TEM image as a dark core, and by a soft polymeric coating of HAOA on the surface, visible in the TEM image as a grey area around the core. EGF may be associated to the HAOA coating of the gold nanoparticles as illustrated. Zeta potential of EGF-conjugated HAOA-coated gold nanoparticles was around -5 mV when compared to the lower value of -19 mV for the

HAOA-coated gold nanoparticles alone. EGF-conjugated HAOA–coated gold nanoparticles showed a spherical morphology with the polymeric coating envelope. In addition, a maximum absorbance peak at 655 nm compared to 800 nm observed for the plain non-coated gold nanoparticles, indicating that a 145 nm blue shift has occurred after conjugation.

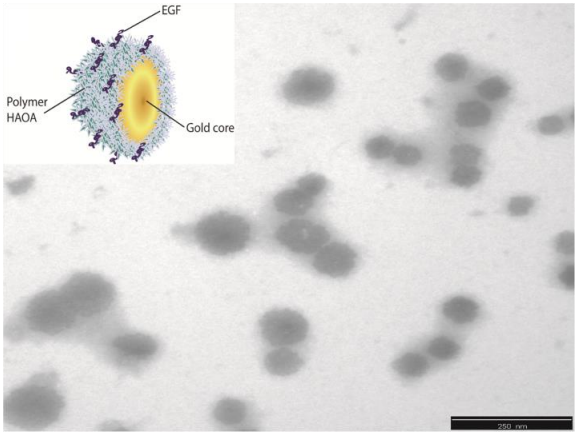

Figure 5. EGF conjugated HAOA-coated gold nanoparticles represented as an illustration (upper corner) and as the TEM image at scale bar of 250 nm.

In Fig. 6, the EGF fluorescence emission intensity at 330 nm during 2 hours of continuous 295 nm excitation is displayed and compared for free EGF, EGF-conjugated HAOA-coated gold nanoparticles, empty HAOA–coated gold nanoparticles and non-coated plain gold nanoparticles, exposed to a 1 hour excitation at 295 nm (emission fixed at 330 nm). Plain gold nanoparticles (i.e., without HAOA coating) and HAOA-coated gold nanoparticles were used as controls. The double exponential fit model ($F(t)=yo+C_1*exp(-k_1*x)+C_2*exp(-k_2*x)$) used to fit the kinetic traces for free EGF and EGF-conjugated HAOA-coated gold nanoparticles showed that the fluorescence emission intensity of free EGF decayed faster than the one for conjugated EGF with HAOA-coated gold nanoparticles. For free EGF, k_1 and k_2 were, respectively, k_1 = 6.8E+2 ± 4.9 $min^{-1}$and k_2 = 5.1E+3 ± 2.1E+2 min^{-1}, while for EGF-conjugated HAOA-coated gold nanoparticles, k_1 and k_2 were, respectively, k_1= 4.3E+2 ± 1.8E+1 min^{-1} and k_2= 3.9E+3 ± 2.3E+2 min^{-1}. Decay constants for conjugated EGF were 1.5-fold (k_1) and 1.3-fold (k_2) lower compared to the ones for free EGF. Also, the initial Trp 330 nm fluorescence emission intensity (excitation at 295 nm) for EGF-conjugated HAOA-coated gold nanoparticles is almost three times lower than the initial fluorescence emission intensity of free EGF. Fitting results are represented in Table 4.

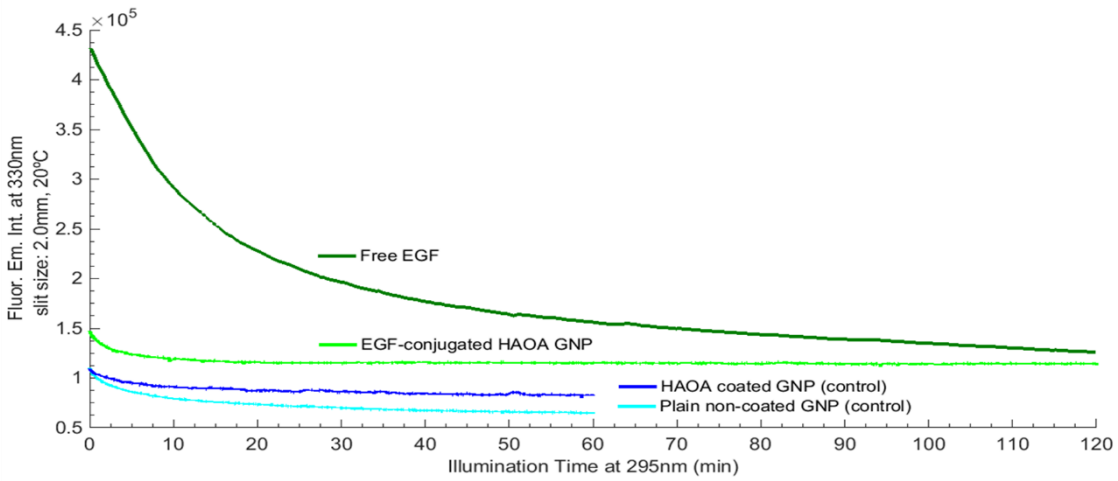

Figure 6. EGF fluorescence emission intensity at 330 nm for free EGF (2 hours 295 nm excitation), EGF-conjugated HAOA-coated gold nanoparticles (2 hours 295 nm excitation), and empty HAOA-coated gold nanoparticles and non-coated plain gold nanoparticles (1 hour 295 nm excitation). All samples were analyzed at 20 ºC and excitation slit size fixed at 2.0 mm (4.40 µW).

Table 4. Double exponential fit using model $F(t)=yo+C_1*exp(-k_1*x)+C_2*exp(-k_2*x)$ for free EGF, EGF-conjugated HAOA-coated GNP (gold nanoparticles), plain non-coated GNP (control) and HAOA-coated GNP (control) (see Fig. 5). Fit parameters are displayed in this table. Adj. R^2 stands for Adjusted R- Square.

Samples	Constants (y_0, k_1, k_2)	Adj. R^2	Pre-exponential factors (C_1, C_2)
Free EGF	y_0 = 9.8E+4 ± 1.8E+3 k_1 = 6.8E+2 ± 4.9 k_2 = 5.1E+3 ± 2.1E+2	0.999	C_1 =2.2E+5 ± 1.3E+3 C_2 =1.2E+5 ± 6.4E+2
EGF – conjugated HAOA GNP	y_0 = 1.2E+5 ± 4.4E+2 k_1= 4.3E+2 ± 1.8E+1 k_2= 3.9E+3 ± 2.3E+2	0.996	C_1=1.8E+4 ± 4.4E+2 C_2=2.2E+4 ± 2.2E+2

Plain non-coated GNP (control)	y_0 = 7.7E+4 ± 1.0E+3 k_1= 5.7E+2 ± 5.2E+1 k_2=6.5E+3 ± 5.2E+2	0.997	C_1=6.2E+3 ± 3.7E+2 C_2=2.6E+4 ± 6.6E+2
HAOA-coated GNP (control)	y_0= 8.9E+4 ± 1.0E+3 k_1= 3.5E+2 ± 8.7E+1 k_2= 7.6E+3 ± 7.1E+2	0.989	C_1=2.1E+3 ± 2.6E+2 C_2=1.8E+4 ± 8.1E+2

Fig. 7 displays the effect of conjugation on the fluorescence spectra of EGF. Fluorescence excitation spectra (emission fixed at 330 nm) and fluorescence emission spectra (excitation fixed at 295 nm) were compared for free EGF in supernatant, EGF-conjugated HAOA–coated gold nanoparticles (before centrifugation) and EGF-conjugated HAOA–coated gold nanoparticles (after centrifugation) (see Fig. 7A). Experiments were carried out at 20 ºC, with a fixed excitation slit of 2.0 mm (power: 4.40 µW) and EGF was only illuminated with the light necessary for obtaining the represented spectra. Centrifugation at 500 x g for 20 min was essential for the elimination of the non-conjugated EGF. Isolated EGF-conjugated HAOA–coated gold nanoparticles (after centrifugation) showed a clear emission peak at 326 nm, which confirms the presence of Trp residues at the HAOA–coated gold nanoparticles' surface (see Fig. 7B).

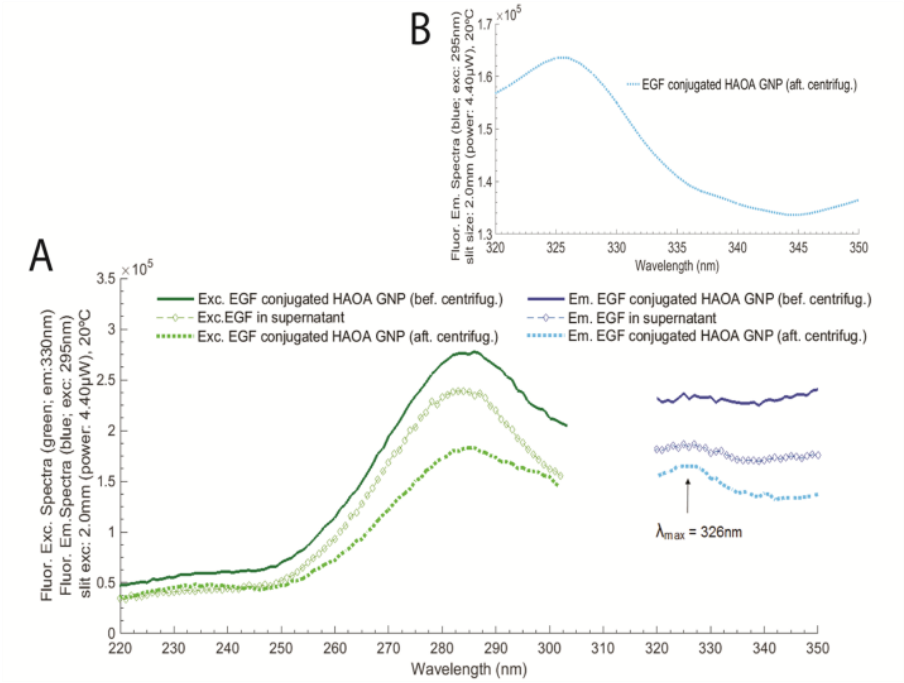

Figure 7. A) Conjugation effect: EGF in supernatant (after conjugation) compared with free EGF and EGF-conjugated HAOA-coated gold nanoparticles; B) EGF-conjugated HAOA-coated gold nanoparticles, at different scale bar. Fluorescence excitation spectra was fixed at 330 nm and fluorescence emission spectra was fixed at 295 nm. Experiments were conducted at 20 ºC and excitation slit size fixed at 2.0 mm (4.40 μW). No continuous excitation of EGF was conducted, beside the necessary for obtaining the represented spectra.

Figs. 8 and 9 display the fluorescence excitation and emission spectra of EGF, as free peptide and as conjugated with HAOA-coated gold nanoparticles, and of SYPRO® Orange, acquired before and after 2 hours of 295 nm illumination. The fluorescence emission and excitation intensity of SYPRO® Orange is 10 and 18.6 higher, respectively, when added to EGF-conjugated HAOA-coated gold nanoparticles than when added to free EGF. After 2 hours of illumination, free EGF excitation intensity at 284 nm decreased 81.2%, while EGF-conjugated HAOA-coated gold nanoparticles excitation intensity, at 474 nm, decreased 41.0%. Fluorescence emission intensity of free EGF at 328 nm decreased 74.8%, after illumination, and a blue shift occurred from 344 nm to 328 nm, while the fluorescence emission intensity of EGF-conjugated HAOA-coated gold nanoparticles at 347 nm decreased 25.7%. After 295 nm illumination of free EGF for 2 hours, fluorescence excitation intensity of SYPRO® Orange increased 10.7%. On the other hand, fluorescence excitation intensity of SYPRO® Orange after 2 hours of 295 nm

illumination of EGF-conjugated HAOA-coated gold nanoparticles decreased 40.9%. Fluorescence emission intensity of SYPRO® Orange decreased 21.4% and 23.8% after illumination of both free EGF and EGF-conjugated HAOA-coated gold nanoparticles, respectively. Interestingly, the fluorescence emission spectra of SYPRO® Orange showed a blue shift (from 610 nm to 594 nm) when added to free EGF, while when added to EGF-conjugated HAOA-coated gold nanoparticles, the peak of SYPRO® Orange emission spectra showed a red shift from 584 nm to 628 nm (see Fig. 9).

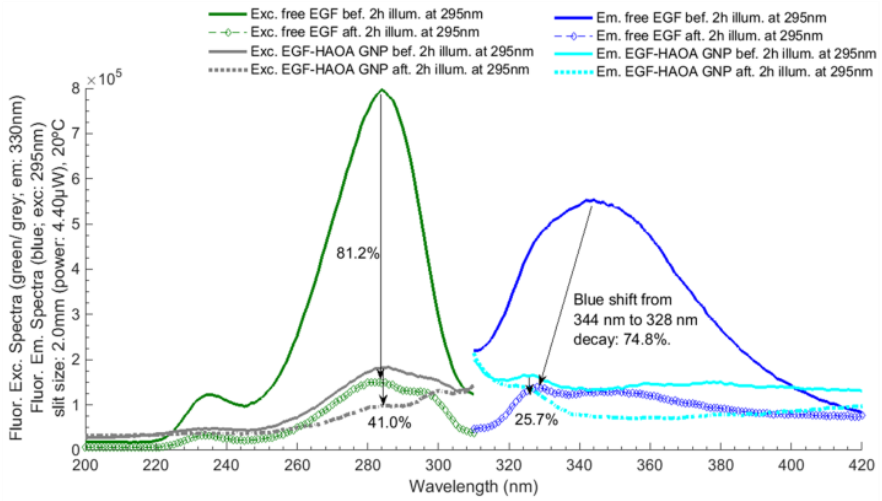

Figure 8. EGF fluorescence excitation and emission spectra acquired before and after 295 nm illumination for 2 hours. Trp fluorescence excitation and emission wavelengths were fixed at 295 m and 330 nm, respectively. Excitation slit size was set at 2.0 mm (4.40 μW) and the temperature of each solution was kept at 20 °C for all experiments.

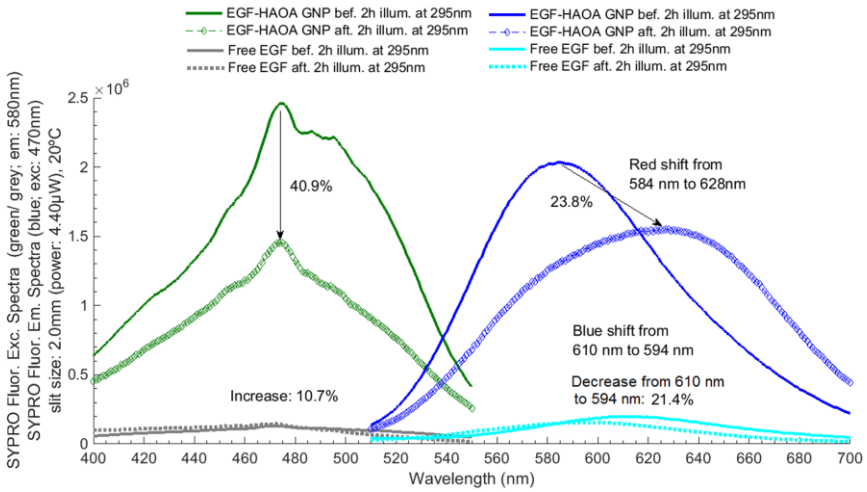

Figure 9. SYPRO® fluorescence excitation and emission spectra acquired before and after EGF 295 nm illumination for 2 hours. SYPRO® Orange fluorescence excitation and emission wavelengths were fixed at 470 nm and 580 nm, respectively. Excitation slit size was set at 2.0 mm (4.40 µW) and the temperature of each solution was kept at 20 °C for all experiments.

In order to detect the putative presence of photochemical species such as NFK and Kyn, fluorescence emission spectra upon 320 nm excitation were acquired for free EGF and for EGF-conjugated HAOA-coated gold nanoparticles, before and after 295 nm continuous illumination of the samples (see Fig. 10A). HAOA-coated gold nanoparticles spectra, before and after 2 hours illumination at 295 nm, were used as controls. For free EGF, a peak centered at 418 nm was observed upon 320 nm excitation. The fluorescence emission intensity of the peak increases 51.0% after continuous excitation with 295 nm for 2 hours. For EGF-conjugated HAOA-coated gold nanoparticles, two peaks were observed: a peak centered at 392 nm and a larger peak at 598 nm. The second peak at 596-598 nm is also visible for the controls HAOA-coated gold nanoparticles, without EGF, before and after continuous illumination, though 3 to 4 times less intense. After continuous excitation with 295 nm for 2 hours, the fluorescence emission intensity decreased by 14.8% and 5.8%, for the peak centered at 392 nm and 598 nm, respectively. In Fig. 10B are displayed the fluorescence emission intensity spectra upon 360 nm excitation in order to detect the putative presence of the photochemical species Kyn and NFK. HAOA-coated gold nanoparticles spectra, before and after 2 hours illumination at 295 nm, were used as controls. For free EGF, a peak centered at 460 nm is observed upon 360 nm excitation. The fluorescence emission

intensity of the peak increases 127% after continuous excitation with 295 nm for 2 hours. Two emission peaks were observed for EGF-conjugated HAOA-coated gold nanoparticles: a peak centered at 461 nm and a larger peak at 580 nm. The second peak at 580 nm is also visible for the control HAOA-coated gold nanoparticles, without EGF, before and after continuous illumination, but with less intensity, like observed upon 320 nm excitation. After continuous excitation with 295 nm for 2 hours, the fluorescence emission intensity decreased by 5.7% and 40.8%, for the peak centered at 461 nm and 580 nm, respectively.

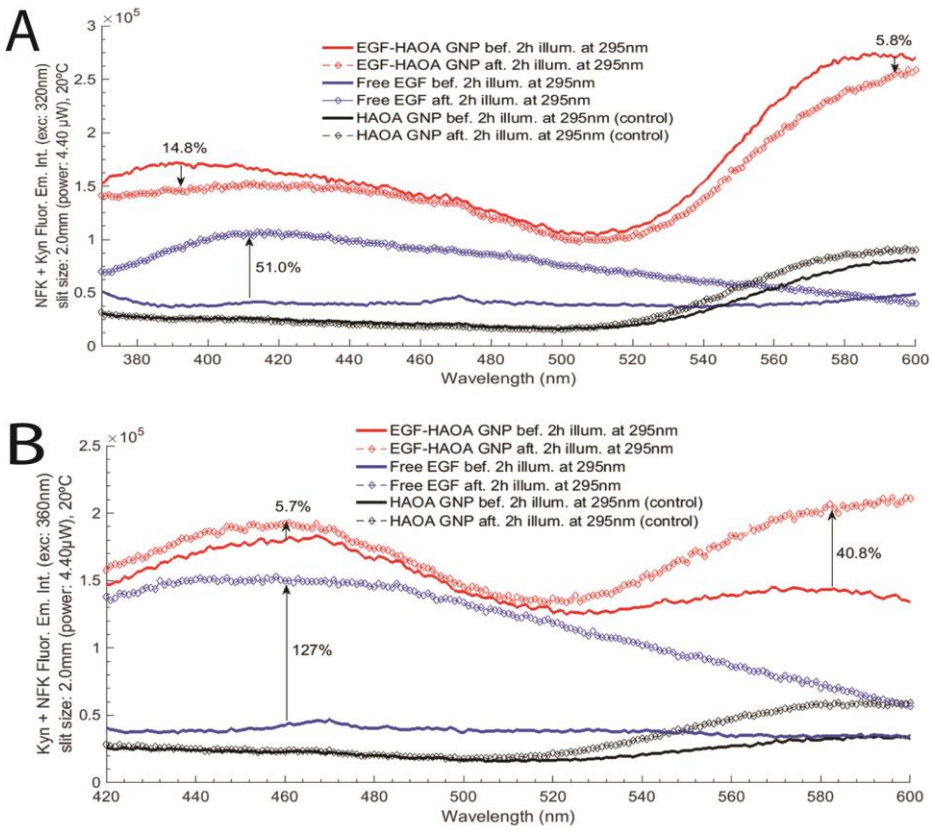

Figure 10. A) Fluorescence emission spectra for NFK + Kyn, before and after excitation of free EGF and EGF-conjugated HAOA-coated gold nanoparticles, at a fixed wavelength of 320 nm. Experiments were conducted at 20 ºC and excitation slit size fixed at 2.0 mm (4.40 µW); B) Fluorescence emission spectra for Kyn + NFK, before and after excitation of free EGF and EGF-conjugated HAOA-coated gold nanoparticles, at a fixed wavelength of 360 nm. Experiments were conducted at 20 ºC and excitation slit size fixed at 2.0 mm (4.40 µW).

In Fig.11 is displayed the fluorescence emission of EGF-conjugated HAOA-coated gold nanoparticles. EGF labeled with Alexa Fluor 647 appears in red and HAOA-coated gold nanoparticles labeled with Coumarin-6 appear in green. Colocalization of both dyes, and therefore of EGF and HAOA-coated gold nanoparticles, is displayed in yellow. The sample was imaged in a confocal microscope (scale bar at 5 µm). Some aggregation is observed.

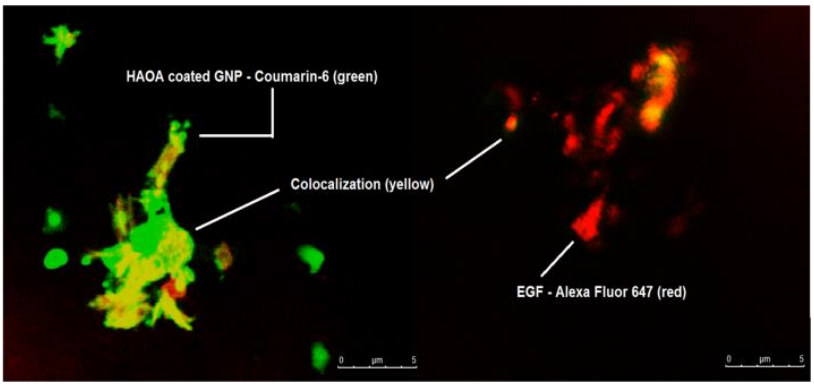

Figure 11. Colocalization of HAOA-coated gold nanoparticles conjugated with EGF. EGF was dyed with Alexa Fluor 647 (red color) and HAOA-coated gold nanoparticles were dyed with Coumarin-6 (green color). The parts were the HAOA-coated gold nanoparticles are associated with EGF, in the same localization, are visible in yellow (scale bar at 5 µm).

Circular dichroism (CD) is a good method to evaluate changes in the secondary structure of proteins. Fig. 12 shows far UV CD spectra collected for different samples. The spectra show that after conjugation with HAOA-coated gold nanoparticles EGF maintains its secondary structure. Although free EGF (non conjugated) has a signal of higher intensity than the rest of the studied samples (i.e., EGF-conjugated HAOA-coated gold nanoparticles, EGF in supernatant and extracted EGF with acidic pH solution), its concentration was also 18 times higher. The CD spectra indicate that EGF probably has a secondary structure, with contributions from different secondary elements. This is suggested by the presence of a negative peak around 208 - 210 nm, characteristic of α-helix structure. However, the negative band at 220 nm, also characteristic of α-helix structure was not detected. The absence of CD bands above 215 – 220 nm range suggests the presence of EGF's β-sheets.

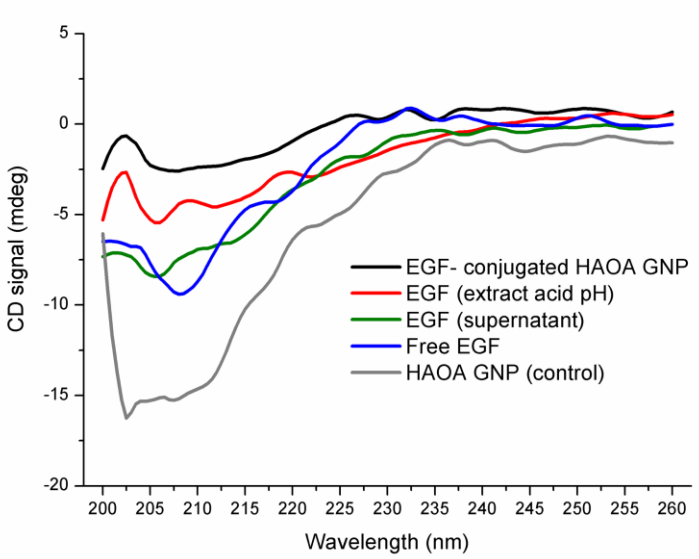

Figure 12. The CD spectra of: free EGF (0.3 mg/mL), HAOA coated gold nanoparticles (without EGF), EGF-conjugated HAOA-coated gold nanoparticles (16.5 µg/mL), non-conjugated EGF in supernatant, extracted by centrifugation, and EGF extracted after incubation of EGF-conjugated HAOA-coated gold nanoparticles in phosphate buffer pH 5.5, at 37 ºC, for 72 hours.

In Fig. 13 is represented the cell viability of human keratinocytes (HaCaT) exposed to EGF-conjugated HAOA-coated nanoparticles for 24 hours. No aggregates were visible after addition of the nanoparticles to the plaque wells. EGF has slightly promoted HaCaT growth at lowest concentrations (1-35 µM). EGF-conjugated HAOA-coated gold nanoparticles at 80 µM the highest concentration tested, showed a cell viability of around 75% of that of non-treated control cultures.

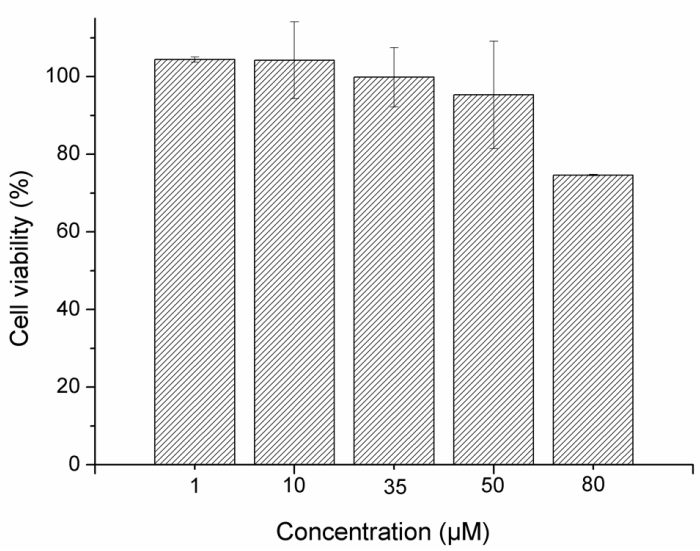

Figure 13. Viability (%) of HaCaT cells exposed to EGF-conjugated HAOA-coated gold nanoparticles for 24 hours, assessed by MTT assay (n=3-4; mean ± SD).

Fig.14 displays the results from the EGFR binding assay carried out with human lung carcinoma A549 cells. Images were taken 1.5 hours after the cells being in contact with EGF and for the negative control. Three different samples were tested: free EGF labeled with Alexa Fluor 647 (A1); EGF-conjugated HAOA-coated gold nanoparticles, being EGF labeled with Alexa Fluor 647 (B1); and EGF-conjugated HAOA-coated gold nanoparticles, with EGF labeled with Alexa Fluor 647 and the HAOA-coated gold nanoparticles labeled with Coumarin-6 (C1). In addition, the same samples were tested after the cells were incubated for 1 hour with anti-EGFR antibody, in order to block the EGF receptors. Finally, two control groups were studied: CN1, corresponding to cells from the non-treated group (i.e., cells without the addition of EGF or nanoparticles and of the anti-EGFR antibody) and CN2, corresponding cells in presence of HAOA-coated gold nanoparticles (without dye or EGF conjugation). In panels A1, B1 and C1 it can be observed that EGF has induced EGFR internalization, alone and when conjugated with the HAOA-coated gold nanoparticles. Both free EGF and EGF-conjugated HAOA-coated gold nanoparticles (panels B1 and C1) entered the cells' cytoplasm but not its nucleus. The anti-EGFR antibody blocked the binding of EGF to EGFR, preventing receptor internalization (panel A2); however, the EGF-conjugated HAOA-coated gold nanoparticles could still enter the cells (panels B2 and C2) despite the presence of the antibody. The controls (panels CN1 and CN2) confirm that in the absence of EGF and in the absence of nanoparticles there is no EGFR activation.

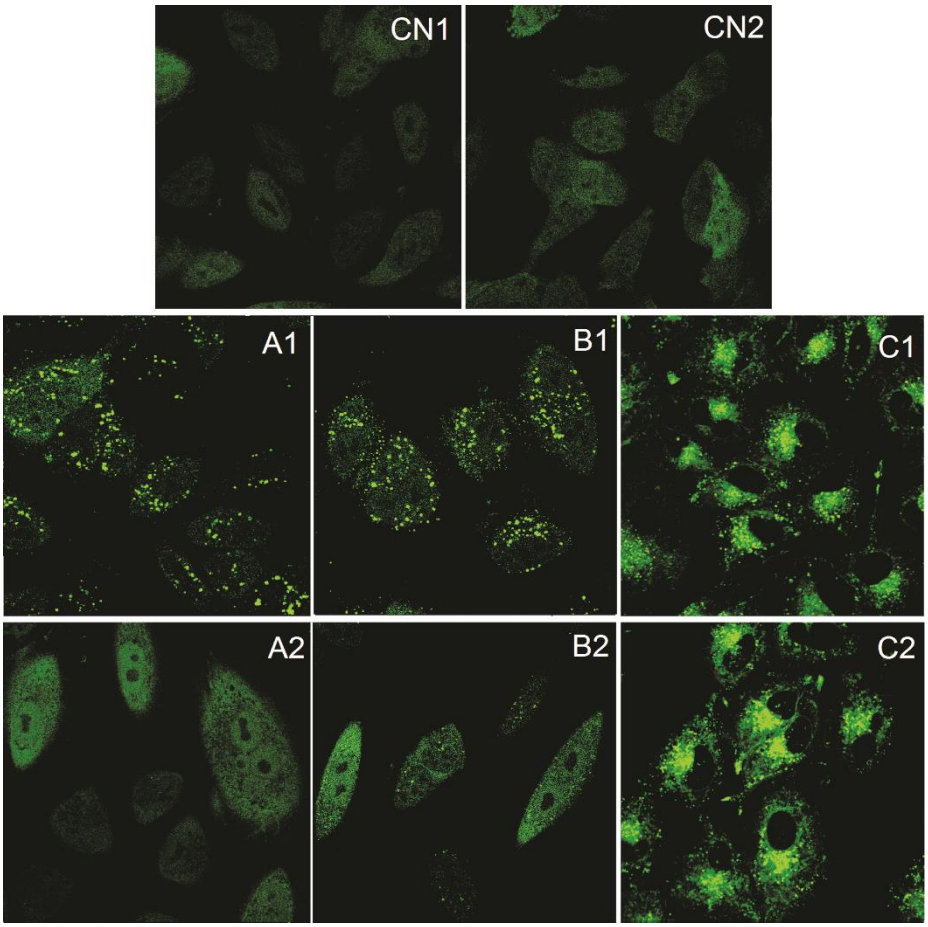

Figure 14. EGFR binding assay in A549 cell model, for 1.5 hours in contact with treatment (100X). CN1 corresponds to the non-treated cells, while CN2 shows the exposure to HAOA-coated gold nanoparticles (without any dye). As for the treatment groups: A1) free EGF with Alexa Fluor 647, B1) EGF-conjugated HAOA-coated gold nanoparticles (only EGF is marked with Alexa Fluor 647), and C1) EGF-conjugated HAOA-coated gold nanoparticles (both EGF and HAOA-coated gold nanoparticles are marked with Alexa Fluor 647 and Coumarin-6, respectively). For A2, B2 and C2, anti-EGFR antibodies were added 1 hour before the addition of the tested samples.

4. Discussion

The presented data has shown that the structure of EGF (Fig. 1) can be modulated by UV-light (295 nm) and that the photochemical changes are reduced when EGF is bound to HAOA-coated gold nanoparticles (Fig. 6). Like other small proteins and peptides (e.g., cutinase, insulin, α-lactoalbumin) [1,4,33], EGF is an interesting model protein for

photostability studies due to the close spatial proximity between its aromatic residues and its disulphide (SS) bridges. SS bridges are key structural elements in small proteins [34], responsible for maintaining the proteins´ structure and therefore their function. Disruption of SS bonds induced by UV excitation of aromatic residues in those peptides will most likely destroy its structure and impair its function [1,4,33]. Table 1 lists the three SS bonds of EGF located in close spatial proximity to aromatic residues (Trp and Tyr). The observed close distances will allow for electron transfer between the aromatic residues and the SS bridges [4], leading to the disruption of such bridges. EGF is a peptide where these reactions will occur in the presence of UVB light leading to conformational changes and to loss of functionality.

EGF is a natural ligand for EGFR with significant biomedical importance in cancer treatment and diagnostic [6]. Changes in the fluorescence spectra of the extrinsic fluorescence probe SYPRO® Orange confirmed structural changes of EGF induced by temperature (Fig. 2), prolonged illumination at 295 nm (Fig. 4) and pH, as its fluorescent emission is enhanced upon binding to hydrophobic regions of the protein [22]. Temperature-dependent time based photochemical studies (see Fig. 2A) show that EGF photochemistry and protein conformational space is temperature dependent, being similar at 10 ºC and 15 ºC, at 20 ºC and 30 ºC but distinct at 25 ºC. At 25 ºC, SYPRO® Orange appears to bind less to the peptide than at other temperatures, indicating that EGF has fewer hydrophobic surfaces exposed to the solvent. The Arrhenius plot (see Fig. 3) showed that the activation energy (E_a) associated with the photochemical reactions induced by 295 nm on EGF was 19.9±0.9 kJ.mol^{-1} (i.e., 4.76 kcal/mol). This value was similar to the one found for α-lactalbumin (E_a = 21.8±2.3 kJ.mol^{-1}) [33]. Power-dependent irradiation studies of EGF (see Fig. 4A) reveal that the larger the power used, the faster the kinetics associated with the fluorescence decays. A single exponential model was used to fit the Trp decay curves acquired with 0.30 µW and 1.67 µW (see Table 3) but for larger powers (2.34 µW and 4.40 µW) a double exponential model was needed. This shows that different photochemical processes are initiated at higher powers when compared to lower powers. Experiments carried out with SYPRO® Orange (see Fig. 4B) show the same trend. Conformational changes induced in EGF are larger when illumination was carried out with higher powers: when using a 2.0 mm slit size opening, the fluorescence emission intensity of SYPRO® Orange was higher than when working with a 0.1 mm slit, indicating that the extrinsic probe is in contact with a larger hydrophobic surface rendered accessible due to light induced conformational changes.

Conjugation of EGF to HAOA-coated gold nanoparticles protected EGF from photochemistry (Fig. 6, Table 4): the presence of the particles decreased the rate of the light induced fluorescence changes and induced quenching. Both HA, OA and gold are known to be fluorescence quenchers. EGF has a promising therapeutic value as a targeting ligand for tumors overexpressing EGFR, such as melanoma [8,9]. Therefore, it has been coupled to nano-sized delivery systems, made of either and both metallic and polymeric materials [35–39]. The photochemical protection conferred by nanoparticulate carriers is advantageous.

Gold nanoparticles were prepared according to a seed-growth method [40]. An aqueous extract of *Plectranthus saccatus* (Benth.), rich in anti-oxidative compounds (e.g., rosmarinic acid, caffeic acid and chlorogenic acid [41]), was used as the main reducing and capping agent. Furthermore, a coating made of hyaluronic and oleic acids (HAOA) was added to the gold nanoparticles. Natural polymers can work as reducing and capping agents, activating “green” reduction of gold and being less toxic for healthy tissues, which make them advantageous in the reduction and morphology of gold nanoparticles [42]. Furthermore, the use of polymeric coatings is also interesting as a way to control drug release and to increase the adsorption of ligands. Recently, Su *et al.* (2014) showed that HA scaffolds can increase the adsorption and sustained release of EGF, attached to the polymeric surface through self-assembly and electrostatic interactions [43]. In addition, HA is reported to confer structural stability to proteins [20]. Herein, we studied the effect of mounting EGF to HAOA-coated gold nanoparticles. In Fig. 5, it can be observed that EGF-conjugated HAOA-coated gold nanoparticles show the gold core (dark core) surrounded by HAOA polymer. On the upper left corner of Fig. 5 is displayed a model of the EGF-conjugated HAOA-coated gold nanoparticles. Kinetic data displayed in Table 4 and Fig. 6 confirms that the polymers and the gold core promoted protein quenching and induced slower decay kinetics when compared with the data obtained with free EGF, protecting EGF from photochemistry. The same has been reported by Oliveira Silva *et al.* (2015) when studying the photochemistry of free lysozyme and comparing it to the photochemistry of lysozyme mounted onto HAOA-coated gold nanoparticles [24]. It is likely that the structure of EGF, after conjugation to HAOA-coated nanoparticles, sustains excitation at 295 nm for longer time periods, prior to possible loss of structure and function. The presence of EGF conjugated to the HAOA-coated gold nanoparticles was confirmed by fluorescence spectroscopy, after centrifugation and re-suspension with PBS, demonstrating a clear emission peak at 326 nm for Trp residues (Fig. 7). The conjugation of EGF onto HAOA-coated gold

nanoparticles conferred enhanced photostability to EGF. This is observed in Fig. 8, where a smaller intensity reduction occurs in both fluorescence excitation spectra (41.0% *versus* 81.2%) and fluorescence emission spectra (25.7% *versus* 74.8%), after 295 nm continuous illumination. Furthermore, the observed blue shift in the fluorescence emission spectra of free EGF, after 295 nm continuous illumination, is no longer visible for EGF-conjugated HAOA-coated gold nanoparticles (Fig. 8). This is probably due to the fact that conjugation of EGF has prevented conformational changes that rendered the Trp moieties more apolar, responsible for the blue shift. SYPRO® Orange was used as an extrinsic probe for monitoring UV-light (295 nm) induced conformational changes in EGF (Fig. 9). Firstly, it was observed that SYPRO® Orange showed affinity towards hydrophobic moieties in HAOA-coated gold nanoparticles, leading to an increase of its fluorescence emission intensity signal compared to its fluorescence emission intensity in free EGF solution (Fig. 9). Secondly, the fluorescence emission spectra of EGF-conjugated HAOA-coated nanoparticles suffered a red shift (from 584 nm to 638 nm) after 2 hours of continuous 295 nm illumination. On the other hand, the fluorescence emission spectra of free EGF suffered a blue shift (from 610 nm to 594 nm) after 2 hours of continuous 295 nm illumination. The observed red shift for SYPRO® Orange reveals that the probe is in a more polar environment after illumination.

Finally, the antioxidant compounds of *Plectranthus saccatus,* present in the HAOA-coated nanoparticles formulation, can also have an important role in protecting EGF from light induced reactions. Phenolic compounds are highly present in natural plant extracts and are described to show anti-oxidant effects on Trp oxidation and to be fluorescence quenchers [44–46]. It has been shown that the oxidation of the indole ring of Trp can be inhibited and, consequently, the formation of NFK and Kyn, by associating proteins with phenolic compounds from natural plant extracts [47]. This is positively correlated with our data. Conjugation of EGF to HAOA-coated gold nanoparticles reduced or even avoided the formation of photoproducts, such as NFK and Kyn (see Figs.10A and B).

The presence of oxidative conditions induced by light can lead to the oxidation of the aromatic residues in proteins [1,2,6,33,48]. UVB excitation of aromatic residues in proteins leads to the disruption of SS bridges [1–4,6] and to the formation of photoproducts, such as N-formylkynurenine (NFK), kynurenine (Kyn) [26,49] and dityrosine (DT) [27]. Since 295 nm excites specifically Trp residues, it is very likely that the photoproducts formed are Trp derivatives such as NFK and Kyn and not Tyr derivatives like DT. Furthermore, the emission spectrum of EGF upon 295 nm leads to

a fluorescence emission spectrum that peaks around 330 nm, which makes it unlikely that Tyr residues will be excited by EGF emission. Two excitation wavelengths were used in order to detect the presence of photochemical products: 320 nm (Fig. 10A) and 360 nm (Fig. 10B). Light at 320 nm excites both NFK ($\varepsilon_{NFK(321nm)}$=3750 $M^{-1}cm^{-1}$) [50–53] and Kyn ($\varepsilon_{Kyn(321nm)}$= 1812 $M^{-1}cm^{-1}$) [54]. At 315 nm, DT has an extinction coefficient equal to 5200 $M^{-1}cm^{-1}$ but, as explained above, it is unlikely that it has been formed [55,56]. Light at 360 nm excites NFK ($\varepsilon_{NFK(360nm)}$=1607 $M^{-1}cm^{-1}$ [54] and Kyn ($\varepsilon_{Kyn(365nm)}$=4530 $M^{-1}cm^{-1}$ [57,58]) but does not excite DT. In Fig. 10A, the peak with maximum fluorescence emission intensity (320 nm excitation) for free EGF occurs at 418 nm and for EGF-conjugated HAOA-coated occurs at 392 nm. In Fig. 10B, the peak with maximum fluorescence emission intensity (360 nm excitation) for free EGF occurs at 460 nm and for EGF-conjugated HAOA-coated nanoparticles it is seen at 461 nm. This peak cannot belong to DT, since DT is not excited at 360 nm. Therefore, it can be Kyn since the wavelength of maximum fluorescence emission of Kyn lies within 434-480 nm.

Colocalization experiments carried out with confocal fluorescence microscopy (Fig. 11) confirmed that EGF (red colour) appears to be associated and colocalized with HAOA-coated gold nanoparticles (green colour), which can be visualized as yellow coloured spots. Since EGF shows a pI around 4.55 and HAOA-coated gold nanoparticles have a superficial negative charge (-19 mV), attractive electrostatic interaction between the protein and the nanocarrier are not likely to occur at pH 7.4. In spite of this, a slight increase of the nanoparticles' surface charge after EGF conjugation (-5 mV) is observed and, as already mentioned, the peptide conjugation onto the particles has also been confirmed by fluorescence spectroscopy. Moreover, literature described that EGF is likely to be associated to HA scaffolds through the polymer's carboxylic groups and since HA is a hydrogel with high hygroscopic character, interactions between EGF and the polymer can occur by hydrophilic interactions [20,43,59]. Another possible mechanism for EGF conjugation onto HAOA-coated gold nanoparticles is by means of binding between an amino acid residue of the peptide and the HAOA coating or gold core. Histidine has been described as a very strong metal binding amino acid [60]. EGF has two histidine residues (His10 and His16). Lysine residues (Lys28 and Lys48) of EGF were also pointed out as a potential binding site for EGF conjugation with HA polymer [61], especially Lys48, which is located at the end of lateral chain of EGF.

Far UV spectra for CD showed that EGF maintained its non-helical, random coil structure, before and after conjugation and after extraction from the HAOA-coated gold

nanoparticles, when incubated at 37 ºC in pH 5.5 phosphate buffer (Fig. 12). The native structure of EGF is described to be mainly composed of random coil elements (72%) and β-helical elements (25%) and only a trace of α-helical content [12,62]. The random coil secondary structure contributes to the presence of a negative peak at 200 – 210 nm [63]. Although a typical shoulder formation at 220 nm is described for EGF [63], as indicative of the presence of random non-helical forms and β-sheets, spectra with a flat curve around 215 – 225 nm is also expected for EGF, suggesting a low content on β forms [64]. It has been observed this flat curvature for all spectra of EGF samples above 215 – 220 nm (Fig. 12). EGF-conjugated HAOA-coated gold nanoparticles showed a negative peak at 208 nm, as free EGF in its native form, in PBS pH 7.4. However, a spectral blue shift was detected for both EGF in supernatant, as for the unbound peptide, recovered after centrifugation of the EGF-conjugated HAOA-coated nanoparticles and EGF extracted after incubation of EGF-conjugated HAOA-coated gold nanoparticles in phosphate buffer pH 5.5, at 37 ºC, for 72 hours. Both EGF in the supernatant and extracted EGF's peaks shifted to 206 nm. Furthermore, HAOA-coated gold nanoparticles, without EGF, showed an intense signal for the main negative peak at 200-210 nm, with a minimum at 201 nm, which can be due to the fact that HAOA coating of gold nanoparticles, especially HA, also absorb in the far UV range [65].

After characterizing the EGF-conjugated HAOA-coated gold nanoparticles in terms of pharmaceutical technology and protein stability, its potential biological application was evaluated. Firstly, the cell viability in normal-like human keratinocytes (HaCaT cell line) was tested in order to verify if our nanoparticles were safe when in contact with a healthy non-cancer tissue (see Fig.13). Statistical analysis was based on Student's t-test for comparisons between cell viability values with non-conjugated HAOA-coated gold nanoparticles [66] and EGF-conjugated HAOA-coated nanoparticles (present work). No significant differences ($p > 0.05$) were found between the viability of HaCat cells treated with HAOA-coated gold nanoparticles and EGF-conjugated HAOA-coated gold nanoparticles at equal concentrations. Finally, when testing the biologic activity of EGF-conjugated HAOA-coated nanoparticles, compared to free EGF, for EGFR binding, we have used a well-studied cell model for described previously for Human EGFR Live Cell Fluorescent Biosensor Assay [32]. Therefore, it was observed that both peptides, in those different conditions, were able to bind to the receptor and activate its internalization (visible green fluorescence as shown in Fig.14), making possible the downstream signal transduction. It has been observed in our study that the antibody anti-EGFR competitively inhibits the binding of free EGF to EGFR, but not for EGF-conjugated to

HAOA-coated gold nanoparticles. Therefore, nanoparticles can also enter the A549 cells by a putative different internalization mechanism than EGFR-modulated internalization. EGF-conjugated HAOA-coated gold nanoparticles may modulate the endocytic pathways for entering the cells. One example is the use of other cell receptors, such as CD44, for which hyaluronic acid is a specific ligand, which are also described to be also overexpressed in many solid tumor cells including breast, melanoma and lung cancer, like the A549 cell model used in this study [67,68]. Quattal *et al.* (2011) confirmed this possibility when they demonstrated by fluorescence microscopy that HA-coated liposomes, made of high-molecular weight HA, led to increased uptake of liposomes by A549 cells, with high and irreversible binding affinity [69]. As observed in Fig.14, EGF-conjugated HAOA-coated gold nanoparticles accumulate around the peri-nuclear area, but do not penetrate into the cell nucleus, after 1.5 hours-incubation. Wang *et al.* (2013) showed that lipid-coated gold nanoparticles promoted the formation of acidic compartments, which appear to be lamellar bodies, in A549 cells [70]. These vesicles appear to internalize the nanoparticles, allowing them to enter the cell. Wang *et al.* (2013) also state that internalization occurs as a result of the negative charge of gold nanoparticles penetrating the lung surfactant, which primarily contains a mixture of phosphatidyl choline and phosphatidyl glycerol lipids [70]. Other polymeric coated gold nanoparticles, also highly negatively charged (-40 mV) were retained in the endolysosomal compartments, also predominant presence at the perinuclear region, after 1 and 2 hours-incubation with A549 cells [71]. This internalization was reported to occur very quickly, around 1 hour to 2 hours, probably due to EGF small size and high affinity to EGFR. Maybe, as a consequence, the clearance is also faster in lysosomes and in cells with high expression of EGFR [72]. Finally, another study using A549 lung cancer cells, sulfhydryl-activated EGF conjugation with lipidic nanoparticles were colocalized with the labeled EGF receptors and the internalization of EGF-conjugated nanoparticles was visible [37]. Therefore, the EGF-conjugated HAOA-coated gold nanoparticles developed in this work show a potential application for near infrared (NIR, 650-800 nm) photothermal therapy, which may efficiently destroy cancer cells. NIR photothermal therapy reduces the damage of the healthy tissue compared to visible photothermal therapy [73].

5. Conclusions

The photochemistry of free EGF, EGF-conjugated HAOA-coated nanoparticles and non-conjugated nanoparticles (both coated and uncoated) has been compared as a function of 295 nm excitation power and temperature. EGF attachment to HAOA-coated nanoparticles was confirmed by fluorescence spectroscopy, confocal microscopy and circular dichroism. HAOA-coated gold nanoparticles protected EGF from 295 nm induced photochemistry and did not induce EGF denaturation, reducing the formation of photoproducts such as NFK and Kyn. EGF-conjugated HAOA-coated nanoparticles did not markedly decrease HaCaT cell viability and were able to enter the EGFR-overexpressing tumor cell line A549, by different internalization mechanisms.

Abbreviations

CD, Circular Dichroism; CTAB, Hexadecyltrimethylammonium bromide; DMEM, Dulbecco's Modified Eagle's medium; DMSO, Dimethyl sulfoxide; DT, Dityrosine; EGF; Epidermal Growth Factor; EGFR, Epidemal Growth Factor Receptor; FBS, Fetal Bovine Serum; GFP, Green Fluorescent Protein; GI, Growth Inhibition; HaCaT, human adult low-calcium high-temperature keratinocytes; HA, hyaluronic acid; HAOA, hyaluronic and oleic acids; Kyn, Kynurenine; MTT, Thiazolyl Blue Tetrazolium Bromide; MW; Molecular Weight; NIR, Near Infrared; NFK, N′-Formylkynurenine; PBS, Phosphate Buffer Saline; PI, Polydispersity Index; Phe, Phenylalanine; SD, Standard Deviation; SS; Disulphide; Tyr: Tyrosine; Trp: Tryptophane; UV; Ultraviolet; ZP, Zeta Potential.

Acknowledgments

The authors would like to thank to Fundação para a Ciência e Tecnologia (FCT) for the financial support under the project reference PTDC/BBB-BMC/0611/2012. The work at CBMA was supported by the strategic programme UID/BIA/04050/2013 (POCI-01-0145-FEDER-007569) funded by national funds through the FCT I.P. and by the ERDF through the COMPETE2020 - Programa Operacional Competitividade e Internacionalização (POCI). The authors acknowledge the funding from the European Commission through the project H2020-644242 –SAPHELY and the project H2020-634013-2-PHOCNOSIS. Finally, the authors would also like to thank the master student João Lopes from Universidade Lusófona (Portugal) for the help with *in vitro* cytotoxic assays. Isabel Correia acknowledges FCT for Investigator FCT contract.

Conflicts of interest

The authors declare no conflicts of interest.

References

1. Correia M, Neves-Petersen MT, Jeppesen PB, Gregersen S, Petersen SB. UV-light exposure of insulin: Pharmaceutical implications upon covalent insulin dityrosine dimerization and disulphide bond photolysis. *PLoS One*. 7(12), e50733 (2012).
2. Correia M, Snabe T, Thiagarajan V, *et al.* Photonic activation of plasminogen induced by low dose UVB. *PLoS One*. 10(1), e0116737 (2015).
3. Neves-Petersen MT, Gryczynski Z, Lakowicz J, *et al.* High probability of disrupting a disulphide bridge mediated by an endogenous excited tryptophan residue. *Protein Sci.* 11(3), 588–600 (2002).
4. Neves-Petersen MT, Klitgaard S, Pascher T, *et al.* Flash photolysis of cutinase: Identification and decay kinetics of transient intermediates formed upon UV excitation of aromatic residues. *Biophys. J.* 97(1), 211–226 (2009).
5. Neves-Petersen MT, Snabe T, Klitgaard S, Duroux M, Petersen SB. Photonic activation of disulfide bridges achieves oriented protein immobilization on biosensor surfaces. *Protein Sci.* 15(2), 343–351 (2006).
6. Correia M, Thiagarajan V, Coutinho I, Gajula GP, Petersen SB, Neves-Petersen MT. Modulating the structure of EGFR with UV light: New possibilities in cancer therapy. *PLoS One*. 9(11), e111617 (2014).
7. Master AM, Sen Gupta A. EGF receptor-targeted nanocarriers for enhanced cancer treatment. *Nanomedicine*. 7(12), 1895–1906 (2012).
8. Boone B, Jacobs K, Ferdinande L, *et al.* EGFR in melanoma: Clinical significance and potential therapeutic target. *J. Cutan. Pathol.* 38(6), 492–502 (2011).
9. Bracher A, Cardona AS, Tauber S, *et al.* Epidermal growth factor facilitates melanoma lymph node metastasis by influencing tumor lymphangiogenesis. *J Invest Dermatol*. 133(1), 230–238 (2013).
10. Jung K-H, Choe YS, Paik J-Y, Lee K-H. 99mTc-Hydrazinonicotinamide epidermal growth factor–polyethylene glycol–quantum dot imaging allows quantification of breast cancer epidermal growth factor receptor expression and monitors receptor

downregulation in response to cetuximab therapy. *J. Nucl. Med.* . 52 (9), 1457–1464 (2011).

11. Delehanty JB, Boeneman K, Bradburne CE, Robertson K, Bongard JE, Medintz IL. Peptides for specific intracellular delivery and targeting of nanoparticles: implications for developing nanoparticle-mediated drug delivery. *Ther. Deliv.* 1(3), 411–433 (2010).

12. Holladay LA, Savage CR, Cohen S, Puett D. Conformation and unfolding thermodynamics of epidermal growth factor and derivatives. *Biochemistry*. 15(12), 2624–2633 (1976).

13. Master A, Livingston M, Sen Gupta A. Photodynamic nanomedicine in the treatment of solid tumors: Perspectives and challenges. *J. Control. Release*. 168(1), 88–102 (2013).

14. Matrisian LM, Planck SR, Magun BE. Intracellular processing of epidermal growth factor. I. Acidification of ^{125}I-epidermal growth factor in intracellular organelles. *J. Biol. Chem.* 259(5), 3047–3052 (1984).

15. Zhang S, Moustafa Y, Huo Q. Different interaction modes of biomolecules with citrate-capped gold nanoparticles. *ACS Appl. Mater. Interfaces*. 6(23), 21184–21192 (2014).

16. Yang C-H, Wu P-C, Huang Y-B, Tsai Y-H. A new approach for determining the stability of recombinant human epidermal growth factor by thermal fourier transform infrared (FTIR) microspectroscopy. *J. Biomol. Struct. Dyn.* 22(1), 101–110 (2004).

17. Lim J, Kim N, Lim D, Kim K, Jeong S. Effects of thermal and mechanical stress on the physical stability of human growth hormone and epidermal growth factor. *Arch. Pharm. Res.* 38(8), 1–11 (2014).

18. Lu W, Xiong C, Zhang G, *et al.* Targeted photothermal ablation of murine melanomas with melanocyte-stimulating hormone analog-conjugated hollow gold nanospheres. *Clin. Cancer Res.* 15(3), 876–886 (2010).

19. Neves-Petersen MT, Klitgaard S, Skovsen E, Petersen SB, Tømmeraas K, Schwach-Abdellaoui K. Biophysical properties of phenyl succinic acid derivatised hyaluronic acid. *J. Fluoresc.* 20(2), 483–492 (2010).

20. Water JJ, Schack MM, Velazquez-Campoy A, Maltesen MJ, van de Weert M, Jorgensen L. Complex coacervates of hyaluronic acid and lysozyme: Effect on

protein structure and physical stability. *Eur. J. Pharm. Biopharm.* 88(2), 325–331 (2014).

21. Yang Jr F, Zhang M, Chen J, Liang Y. Structural changes of α-lactalbumin induced by low pH and oleic acid. *Biochim. Biophys. Acta - Proteins Proteomics*. 1764(8), 1389–1396 (2006).

22. Avanti C, Saluja V, van Streun ELP, Frijlink HW, Hinrichs WLJ. Stability of lysozyme in aqueous extremolyte solutions during heat shock and accelerated thermal conditions. *PLoS One*. 9(1), e86244 (2014).

23. Rijo P, Falé PL, Serralheiro ML, Simões MF, Gomes A, Reis C. Optimization of medicinal plant extraction methods and their encapsulation through extrusion technology. *Measurement*. 58(0), 249–255 (2014).

24. Oliveira Silva C, Petersen SB, Pinto Reis C, *et al.* Lysozyme photochemistry as a function of temperature. the protective effect of nanoparticles on lysozyme photostability. *PLoS One*. 10(12), e0144454 (2015).

25. Geerlof A, Brown J, Coutard B, *et al.* The impact of protein characterization in structural proteomics. *Acta Crystallogr. Sect. D*. 62(10), 1125–1136 (2006).

26. Fukunaga Y, Katsuragi Y, Izumi T, Sakiyama F. Fluorescence characteristics of kynurenine and n′-formylkynurenine, their use as reporters of the environment of tryptophan 62 in hen egg-white lysozyme. *J. Biochem.* 92(1), 129–141 (1982).

27. Malencik DA, Anderson SR. Dityrosine as a product of oxidative stress and fluorescent probe. *Amino Acids*. 25(3-4), 233–247 (2003).

28. Jacob JS, Cistola DP, Hsu FF, *et al.* Human phagocytes employ the myeloperoxidase-hydrogen peroxide system to synthesize dityrosine, trityrosine, pulcherosine, and isodityrosine by a tyrosyl radical-dependent pathway. *J. Biol. Chem.* 271(33), 19950–19956 (1996).

29. Merkus HG. Particle size measurements: Fundamentals, practice, quality. Springer Science & Business Media, 17(1), 534 (2009).

30. Rijo P, Matias D, Fernandes A, Simões M, Nicolai M, Reis C. Antimicrobial plant extracts encapsulated into polymeric beads for potential application on the skin. *Polymers (Basel).* 6(2), 479–490 (2014).

31. Oliveira CA de, Peres DD, Graziola F, *et al.* Cutaneous biocompatible rutin-loaded gelatin-based nanoparticles increase the SPF of the association of UVA and UVB filters. *Eur. J. Pharm. Sci.* 81(0), 1–9 (2015).

32. Antczak C, Bermingham A, Calder P, *et al.* Domain-based biosensor assay to screen for epidermal growth factor receptor modulators in live cells. *Assay Drug Dev. Technol.* 10(1), 24–36 (2012).

33. Correia M, Neves-Petersen M, Parracino A, di Gennaro A, Petersen S. Photophysics, photochemistry and energetics of uv light induced disulphide bridge disruption in apo-α-lactalbumin. *J. Fluoresc.* 22(1), 323–337 (2012).

34. Petersen MTN, Jonson PH, Petersen SB. Amino acid neighbours and detailed conformational analysis of cysteines in proteins. *Protein Eng.* 12 (7), 535–548 (1999).

35. Creixell M, Herrera AP, Ayala V, *et al.* Preparation of epidermal growth factor (EGF) conjugated iron oxide nanoparticles and their internalization into colon cancer cells. *J. Magn. Magn. Mater.* 322(15), 2244–2250 (2010).

36. Fonge H, Lee H, Reilly RM, Allen C. Multifunctional block copolymer micelles for the delivery of 111in to EGFR-positive breast cancer cells for targeted auger electron radiotherapy. *Mol. Pharm.* 7(1), 177–186 (2009).

37. Zhang Z, Chen J, Ding L, *et al.* HDL-mimicking peptide–lipid nanoparticles with improved tumor targeting. *Small*. 6(3), 430–437 (2010).

38. Shimada T, Ueda M, Jinno H, *et al.* Development of targeted therapy with paclitaxel incorporated into egf-conjugated nanoparticles. *Anticancer Res.* 29(4), 1009–1014 (2009).

39. Jin H, Lovell J, Chen J, *et al.* Investigating the specific uptake of EGF-conjugated nanoparticles in lung cancer cells using fluorescence imaging. *Cancer Nanotechnol.* 1(1-6), 71–78 (2010).

40. Murphy CJ, Sau TK, Gole AM, *et al.* Anisotropic metal nanoparticles: Synthesis, assembly, and optical applications. *J Phys Chem B.* 109(29), 13857–13870 (2005).

41. Rijo P, Batista M, Matos M, Rocha H, Jesus S, Simões MF. Screening of antioxidant and antimicrobial activities on *Plectranthus* spp. extracts. *Biomed. Biopharm. Res.* 9(2), 225–235 (2013).

42. Shen L, Rapenne L, Chaudouet P, Ji J, Picart C. *In situ* synthesis of gold nanoparticles in exponentially-growing layer-by-layer films. *J. Colloid Interface Sci.* 388(1), 56–66 (2012).

43. Su Z, Ma H, Wu Z, *et al.* Enhancement of skin wound healing with decellularized

scaffolds loaded with hyaluronic acid and epidermal growth factor. *Mater. Sci. Eng. C. Mater. Biol. Appl.* 44(0), 440–8 (2014).

44. Soares S, Mateus N, de Freitas V. Interaction of different polyphenols with bovine serum albumin (BSA) and human salivary α-amylase (HSA) by fluorescence quenching. *J. Agric. Food Chem.* 55(16), 6726–6735 (2007).

45. Salminen H, Heinonen M. Plant phenolics affect oxidation of tryptophan. *J. Agric. Food Chem.* 56(16), 7472–7481 (2008).

46. Salminen H, Jaakkola H, Heinonen M. Modifications of tryptophan oxidation by phenolic-rich plant materials. *J. Agric. Food Chem.* 56(23), 11178–11186 (2008).

47. Salminen H. Effect of phenolic-rich plant materials on protein and lipid oxidation reactions. Dissertation. University of Helsinki (2009).

48. Neves-Petersen MT, Gajula GP, Petersen S. UV light effects on proteins: From photochemistry to nanomedicine. Dr. Satyen Saha (Ed.), InTech (2012).

49. Kerwin BA, Remmele RL. Protect from light: Photodegradation and protein biologics. *J. Pharm. Sci.* 96(6), 1468–1479 (2007).

50. Dooley MM, Mudd JB. Reaction of ozone with lysozyme under different exposure conditions. *Arch. Biochem. Biophys.* 218(2), 459–471 (1982).

51. Dreaden TM, Chen J, Rexroth S, Barry BA. N-formylkynurenine as a marker of high light stress in photosynthesis. *J. Biol. Chem.* 286(25), 22632–22641 (2011).

52. Pryor WA, Uppu RM. A kinetic model for the competitive reactions of ozone with amino acid residues in proteins in reverse micelles. *J. Biol. Chem.* 268(5), 3120–3126 (1993).

53. Mehler AH, Knox WE. The conversion of tryptophan to kynurenine in liver: The enzymatic hydrolysis of formylkynurenine. *J. Biol. Chem*. 187(1), 431–438 (1950).

54. Pirie A. Fluorescence of N'-formylkynurenine and of protein exposed to sunlight. *Biochem. J.* 128(5), 1365 (1972).

55. Marquez LA, Dunford HB. Kinetics of oxidation of tyrosine and dityrosine by myeloperoxidase compounds I and II implications for lipoprotein peroxidation studies. *J. Biol. Chem.* 270(51), 30434–30440 (1995).

56. Bayse GS, Michaels AW, Morrison M. The peroxidase-catalyzed oxidation of tyrosine. *Biochim. Biophys. Acta (BBA)-Enzymology*. 284(1), 34–42 (1972).

57. Qian H, Howard R, Jianyong L. Biochemical identification and crystal structure of

kynurenine formamidase from Drosophila melanogaster. *Biochem. J.* 446(2), 253–260 (2012).

58. Kurnasov O, Goral V, Colabroy K, *et al.* NAD biosynthesis: Identification of the tryptophan to quinolinate pathway in bacteria. *Chem. Biol.* 10(12), 1195–1204 (2003).

59. Liu Y, Duan L, Kim M, Kim J-H, Chung D. *In situ* sodium alginate-hyaluronic acid hydrogel coating method for clinical applications. *Macromol. Res.* 22(3), 240–247 (2014).

60. Chevrier DM, Chatt A, Zhang P. Properties and applications of protein-stabilized fluorescent gold nanoclusters: Short review. *J. Nanophotonics*. 6(1), 64504–64516 (2012).

61. Ferguson EL, Alshame AMJ, Thomas DW. Evaluation of hyaluronic acid-protein conjugates for polymer masked-unmasked protein therapy. *Int. J. Pharm.* 402(1-2), 95–102 (2010).

62. Taylor JM, Mitchell WM, Cohen S. Epidermal Growth Factor: Physical and chemical properties. *J. Biol. Chem.* 247 (18), 5928–5934 (1972).

63. Santana H, González Y, Campana PT, *et al.* Screening for stability and compatibility conditions of recombinant human epidermal growth factor for parenteral formulation: Effect of pH, buffers, and excipients. *Int. J. Pharm.* 452(1-2), 52–62 (2013).

64. Taylor JM, Mitchell WM, Cohen S. Characterization of the binding protein for Epidermal Growth Factor. *J. Biol. Chem.* 249 (7), 2188–2194 (1974).

65. Chakrabarti B, Balazs EA. Optical properties of hyaluronic acid. *J. Mol. Biol.* 78(1), 135–141 (1973).

66. Oliveira Silva C, Rijo P, Molpeceres J, *et al.* Bio-production of gold nanoparticles for photothermal therapy. *Ther. Deliv.* 7(5), 287-304 (2016).

67. Naor D, Sionov RV, Ish-Shalom D. CD44: Structure, function and association with the malignant process. *Adv. Cancer Res.* 71(0), 241–319 (1997).

68. Teder P, Bergh J, Heldin P. Functional hyaluronan receptors are expressed on a squamous cell lung carcinoma cell line but not on other lung carcinoma cell lines. *Cancer Res.* 55 (17), 3908–3914 (1995).

69. Qhattal HSS, Liu X. Characterization of CD44-mediated cancer cell uptake and intracellular distribution of hyaluronan-grafted liposomes. *Mol. Pharm.* 8(4), 1233–

1246 (2011).

70. Wang M, Petersen NO. Lipid-coated gold nanoparticles promote lamellar body formation in A549 cells. *Biochim. Biophys. Acta*. 1831(6), 1089–97 (2013).

71. Minati L, Antonini V, Torrengo S, *et al.* Sustained *in vitro* release and cell uptake of doxorubicin adsorbed onto gold nanoparticles and covered by a polyelectrolyte complex layer. *Int. J. Pharm.* 438(1-2), 45–52 (2012).

72. Ryu JH, Shin M, Kim SA, *et al. In vivo* fluorescence imaging for cancer diagnosis using receptor-targeted epidermal growth factor-based nanoprobe. *Biomaterials*. 34(36), 9149–9159 (2013).

73. Kennedy LC, Bickford LR, Lewinski NA, *et al.* A new era for cancer treatment: Gold-nanoparticle-mediated thermal therapies. *Small*. 7(2), 169–183 (2011).

Annex II

In vivo efficiency and safety studies of photothermal therapy for human cutaneous melanoma

Catarina Oliveira Silva[1, 2], Isabel V. Figueiredo[3, 4], Jesús Molpeceres[2], Ricardo Gomes[5], João M. P. Coelho[5, 6], Ana Gabriel[7], Pedro Vieira[7], Pedro Faísca[1, 8], Patrícia Rijo[1, 9] and Catarina Pinto Reis[1, 6, #]

[1]CBiOS, Research Center for Biosciences & Health Technologies, Universidade Lusófona, Campo Grande 376, 1749-024 Lisboa, Portugal.
[2]Department of Biomedical Sciences, Faculty of Pharmacy, University of Alcalá, Ctra. A2, km 33.600. Campus Universitario, 28871 Alcalá de Henares, Spain.
[3]Pharmacology and Pharmaceutical Care, Faculty of Pharmacy, Universidade de Coimbra, Azinhaga de Santa Comba, 3000-354 Coimbra, Portugal.
[4]IBILI, Institute for Biomedical Imaging and Life Sciences, Universidade de Coimbra, Azinhaga de Santa Comba, 3000-548 Coimbra, Portugal
[5]Laboratório de Óptica, Lasers e Sistemas, Faculty of Sciences, Universidade de Lisboa, Lumiar, 1649-038 Lisboa, Portugal.
[6]Instituto de Biofísica e Engenharia Biomédica, Faculdade de Ciências, Universidade de Lisboa, Campo Grande, 1749-016, Lisboa, Portugal.
[7]Universidade Nova de Lisboa, Faculty of Sciences and Technology, CFA - Center of Atomic Physics, 2829-516 Caparica, Portugal.
[8]Faculty of Veterinary Medicine – Universidade Lusófona Grande 376, 1749-024 Lisboa, Portugal.
[9]iMed.ULisboa, Instituto de Investigação do Medicamento, Faculdade de Farmácia, Universidade de Lisboa, 1649-003, Lisboa, Portugal.

***Corresponding Author:** Prof. Dr. Catarina Pinto Reis

(Publication Pending)

Abstract

In this work *in vivo* efficiency and safety of multifunctional hybrid nanoparticulate systems for cutaneous melanoma treatment were assessed for a targeted photothermal therapy. Hairless severely immunocompromised mice were selected for xenograft models of inoculated A375 human melanoma cells. Tumor-bearing mice were monitored twice a week for weight, body conditions and tumor growth. For photothermal therapy studies, a near-infrared laser at 811 nm was used in combination with hyaluronic and oleic acids-coated gold nanoparticles conjugated with Epidermal Growth Factor. This treatment allowed a tumor reduction of around 80% in volume and led to the formation of several necrotic foci, observed after histological analysis. No significant skin erythema at the irradiation zone was verified, as well as for other excised organs. In conclusion, conducted preliminary *in vivo* assays show the potential of this local anti-tumor therapies, based on multiple and specific targeted moieties conjugated with nanosystems.

Keywords: Human melanoma; Xenograft model; Photothermal therapy; Multifunctional nanoparticles; Targeted delivery; Epidermal Growth Factor.

1. Introduction

Pre-clinical studies for predicting efficiency and toxicity of anti-cancer therapies still depend mostly on animal models [1,2]. Several cancer models have been developed for pre-clinical animal studies, but xenograft models are still widely preferred, as they allow the transplant of human cancer cells into mice [3]. Immunocompromised animals are selected to avoid the rejection of the human cells by the mice immune system. In general, human melanoma xenograft models show many advantages, such as the possibility of human cells to interact directly with the murine stroma environment (i.e., lymphatic and blood vessels) and the possibility of controlling the tumor growth and experimental points, through a standardized technique of the injected cells [4]. Moreover, these orthotopic tumor models also allow the evaluation of anti-tumor efficacy with reproducibility, cost and time-effectiveness and are applicable to many cell lines [2].

Human melanoma is characterized to have a hypervascular tissue and metastasis formation is associated with blood vessel density [5,6]. In addition, human melanoma shows a natural tumorogenic potential, promoting the cancer proliferative and invasive properties [4]. Xenografts of melanoma metastatic cells, such as A375 cells are used both for local orthotopic tumor development through intra-dermal (i.d.) administration [7], and for metastases appearance (e.g., lungs and brain), when administered intravenously (i.v.) via tail vein [8]. Local administration (i.d.) can hinder this effect as compared to subcutaneous (s.c.) or i.v. injected cells by the tail vein [4,7]. Thus, A375 human melanoma cell line has been used successfully in many pre-clinical studies [9–12].

As a result of the evolution of cancer study, nanotechnology has been applied, with a significant outcome, in cancer treatment and diagnosis, by helping in molecular characterization and detection of cancerous or even precancerous tissues, with high accuracy and specificity [13]. Several and complex drug delivery systems that have been developed in research environment are now reaching the pharmaceutical pipelines and clinical trials [14]. Aiming a specific ligand-target receptor mechanism for internalization by cancer cells, conjugation of drug delivery systems with polymers (e.g., polyethylene glycol (PEG)) and targeting moieties (e.g., hormones, growth factors and antibodies), by chemical coupling reaction or electrostatic interactions, can improve their specific accumulation in the tumor site [15,16].

In terms of targeted therapies for melanoma, there is an enormous increase in the number of new medicines that enter clinical trials and are already available for patients [17]. Furthermore, novel approaches aiming a targeted and more efficient melanoma treatment are being studied, with promising outcomes, by the use of nanoparticles, such as in gene and cell therapies, light-based therapies (i.e., photothermal and photodynamic therapies) and chemotherapy [18]. In photothermal therapy, gold nanoparticles show a great flexibility for obtaining multifunctional systems, as a result of their plasmonic tunable properties and surface functionalization [19,20]. Recently, near infrared (NIR) light-based therapies are being intensively studied to promote activation of metallic-based nanoparticles [21]. NIR light is slightly absorbed by the chromophores present in our healthy tissue (also called as the “optical window” or “therapeutic window”) and allows a greater penetration depth (approximately 10-20 mm) [19,22]. Moreover, research studies have shown that gold nanoparticles have greater accumulation and tumor residence, when administered directly into the tumor (i.e., via intra-tumor injection), rather than by systemic routes (e.g., tail vein i.v. injection) [23]. The addition of targeting moieties and ligands, by physical adsorption of a coating polymer or by the use of linkers, are also helpful in accomplishing a localized and selective therapy [21,24]. Additionally, nanoparticles are extensively applied as carriers for anti-cancer drugs. These systems are generally used to reduce systemic adverse effects of conventional chemotherapy, improving the therapeutic efficacy of drug and its biodistribution specifically at the tumor site, as a result of a higher drug accumulation in targeted tissue [25]. The uptake of nanoparticles by tumor cells can also occur by passive uptake, via the enhanced permeability and retention (EPR) effect, due to leaky tumor vasculature, as well as by active uptake, where targeting receptor-mediated internalization takes place [18,25,26].

Herein, we aim to study the efficiency and safety of multifunctional nanoparticulate systems, conjugated with multiple targeting moieties specific for melanoma cells, applied to local and targeted phototherapy. Previously, we have developed and characterized the nanosystems: firstly, Epidermal Growth Factor (EGF) conjugated gold nanoparticles, coated with a biopolymer (Hyaluronic acid, HA) and oleic acid (OA), were developed for NIR photothermal therapy [27]. Thus, aiming the separated study of both strategies as cutaneous melanoma therapies, orthotropic models made from A375 cells were selected, since this cell line is described to overexpress multiple receptors with medical relevance, on the cells’ surface, such as: 1) CD44 receptors, which natural ligand is the hyaluronic acid, also present in the HAOA coating material of both developed nanoparticles [28] and 3) EGFR, for which EGF is also the natural peptide ligand [29].

2. Materials and methods

2.1 Materials

Gold (III) chloride trihydrate ($HAuCl_4$) (PubChem ID: 24895143; Product number: G4022), L-ascorbic acid (L-AA) (PubChem ID: 24891246; Product number: A7506), silver nitrate ($AgNO_3$) (PubChem ID: 24852543; Product number: S0139), hyaluronic acid (HA) sodium salt from *Streptococcus equi* (MW 7,000-250,000 $g.mol^{-1}$) (PubChem ID: 24878223; Product number: 53747), oleic acid (OA) (MW 282.46 $g.mol^{-1}$) (PubChem ID: 24886786; Product number: 75090) were all supplied from Sigma-Aldrich (Steinheim, Germany). Recombinant Human Epidermal Growth Factor (EGF) (PubChem ID: 62253638) was purchased from Life Technologies. The water used for buffer preparation was purified through a Millipore system. Fetal Bovine Serum (FBS) and penicillin/streptomycin were supplied by Sigma-Aldrich (Steinheim, Germany), as of cell culture grade. Dulbecco's Modified Eagle's medium (DMEM) was supplied by Biowest (Nuaillé, France).

2.2 Cell culture

To conduct the *in vivo* preliminary assays for evaluation of both targeted photothermal and chemotherapies, human melanoma A375 cell line (ATCC® CRL-1619™) was selected for the implementation of cancer xenografts in immunodeficient mice. The human melanoma A375 cell line is commonly used for human xenograft models and has overexpressed receptors for all the two targeting moieties that are conjugated with the nanosystems we assessed the *in vivo* efficiency profile: Epidermal Growth Factor (EGF)/ Epidermal Growth Factor Receptors (EGFR) [29], Hyaluronic acid (HA)/ CD44 receptor [28]. Firstly, A375 cells were cultured in an incubator at 37 ºC and 5% CO_2 for one week in DMEM with 10% FBS and 1% penicillin/streptomycin, to obtain a confluence around 80%, before the day of the injection [3,12]. At the day of the injection, cells were treated with versene and $NaCO_3$ for alkalinization and harvested with trypsin and EDTA. Then, cells were centrifuged at 800 x g for 5 min (Eppendorf AG, Hamburg, Germany) and re-suspended in a 50 mL- falcon tube with Phosphate Buffer Saline pH 7.4 (USP XXX) for injection in mice.

2.3 Human melanoma xenograft

Hairless 42 days-old male SHO-SCID mice (code: 474, Charles River, Barcelona), immunosuppressed for T and B cells were selected for the formation of melanoma xenografts models. The compatibility in implementing models of melanoma xenografts

with A375 cells has been described in literature [30,31]. This study was conducted in accordance to the internationally accepted principles for laboratory animal use and care as found in Directive 2010/63/EU and the project was approved by the Portuguese Veterinary General Division (DGAV). Animals were allowed to adapt to the laboratory for 7 days before testing and then they were maintained with food and water *ad libitum* and kept at 22.0 ± 1.0ºC with controlled 12 h light/dark cycle at Faculty of Pharmacy, University of Coimbra. After this period, cells from section 2.2 were inoculated in the fold-back of the neck, using a 1 mL syringe (needle size: 25 G x 5/8 in.) at a concentration of $1x10^6$ A375 cells/ mouse in 200 µL of PBS pH 7.4 as described in the literature [9]. Animals were monitored twice a week for weight control, body conditions (body condition score, BCS), behavior and signs of tumor progression. The size of the tumor and rate of growth were measured until they reached the desired size (around 1,000 mm^3) for inclusion in the study. Tumor volume was calculated by the following equation (1):

(1) length $(width)^2$ /2

where length is the largest diameter and width is the smallest diameter perpendicular to the length.

Follow-up was carried out in total over 60-90 days. After this period of evaluation, it was concluded that there was a small change in total weight, over time, and physical and behavioral conditions of the animals were kept stable.

2.3.1 Photothermal therapy

2.3.1.1 Preparation of the EGF-conjugated HAOA-coated gold nanoparticles

Firstly, EGF-conjugated gold nanoparticles, coated with hyaluronic and oleic acids (HAOA-coated gold nanoparticles) were prepared as previously described [27]. Gold nanoparticles were produced based on the addition of an aqueous extract of *Plectranthus saccatus* (10 mg/mL) as the main reducing and capping agent. Then, the gold nanoparticles were allowed to react with the coating material HAOA for 15 min at 800 rpm, with a final concentration 0.5 mg/mL. Next, the EGF peptide (10 µg/mL) was added to the formulation and allowed to interact with the HAOA-coated gold nanoparticles for 30 min at 800 rpm. EGF-conjugated HAOA-coated gold nanoparticles were stored for 24h at 4ºC, protected from light, and afterwards centrifuged at 10,900 x g for 10 min (Hermle Labortechnik Gmbh, type Z36HK, Wehingen, Germany) to remove unbound peptide. Finally, EGF-conjugated HAOA-coated gold nanoparticles were frozen

and lyophilized for 24 h at -50.0 ± 2.0ºC, in FreeZone 2.5 L Benchtop Freeze Dry System (Labconco, Kansas City, Missouri, USA) and stored at -20 ºC until the day of the *in vivo* experiment.

2.3.1.2 Irradiation laser procedure

In this preliminary test, the following parameters were evaluated, such as variations in tumor growth rate and weight of the mice over time, safety of laser application at 811 nm (power: 2.5 W/cm^2) and the effectiveness of treatment with nanoparticles and laser at 811 nm, at different exposure times (5 min and 10 min). The size and volume of the tumors were determined before and 24 h after treatment application. After the appearance of tumors (size ~1,000 mm^3), mice were randomly chosen to integrate the different treatment groups: 1) only laser exposure during 5 min (n = 4); 2) Intra-tumoral injection of EGF-conjugated HAOA-coated gold nanoparticles and exposure to the laser for 5 min (n = 4); 4) Intra-tumoral injection of EGF-conjugated HAOA-coated gold nanoparticles and laser exposure for 10 min (n = 4); 5) Control group (i.e., no treatment) (n = 3). In the case of treatment with laser and nanoparticles, EGF-conjugated HAOA-coated gold nanoparticles were reconstituted in Milli-Q water at the time of administration. EGF-conjugated HAOA-coated gold nanoparticles were injected at the tumor site (i.t.) at a concentration *per* mouse of 20 mg/kg in 100 µL. After 4 h of the injection EGF-conjugated HAOA gold nanoparticles, the animals were anesthetized with a mixture of Ketamine + Chlorpromazine 10 mg/kg (intramuscular, i.m. injection), and subjected to laser irradiation of 811 nm (JDSU L4-2495-003 coupled to a source Laserpak ARO-485 -08-05) with a diameter of 2 mm and power at the target of 2.5 W/cm^2. The significance of differences was assessed using a Student's t-test conducted for independent (unpaired) samples for weight and size measurements of the organs and tumors, for each group ($p < 0.01$ vs. control, as the significance level).

2.3.1.3. Evaluation of phototherapy-induced *in vivo* safety and efficacy

Before and after laser exposure, mice were also evaluated for possible formation of erythema, at the irradiation zone, by colorimetry (a *, AU) (Minolta Chroma meter CR-300, Konica Minolta Sensing Americas, Inc. NJ, USA) (Figure 1). The significance of differences was assessed using a Student's t-test that was conducted for independent (unpaired) samples for weight and size measurements of the organs and tumors, for each group ($p < 0.01$ vs. control (before irradiation), as the significance level).

2.3.1.4. Evaluation of phototherapy-induced *in vivo* efficacy

For histological evaluation, 24 h after each treatment previously described, animals were sacrificed according animal welfare principles. Tumor and organs (i.e., lungs, heart, liver, spleen and kidneys) were excised, weighed and measured. Then, organs were fixed in 10% formalin, paraffin embedded, and cut into five-micrometer sections for hematoxylin-eosin staining. Slices were examined under an Olympus BX51 microscope (Olympus Corporation, Tokio, Japan) and images were taken using an Olympus U-TV1X-2 color camera and the extent of tumor necrosis was analyzed with Olympus analySIS software (Olympus Corporation, Tokio, Japan).

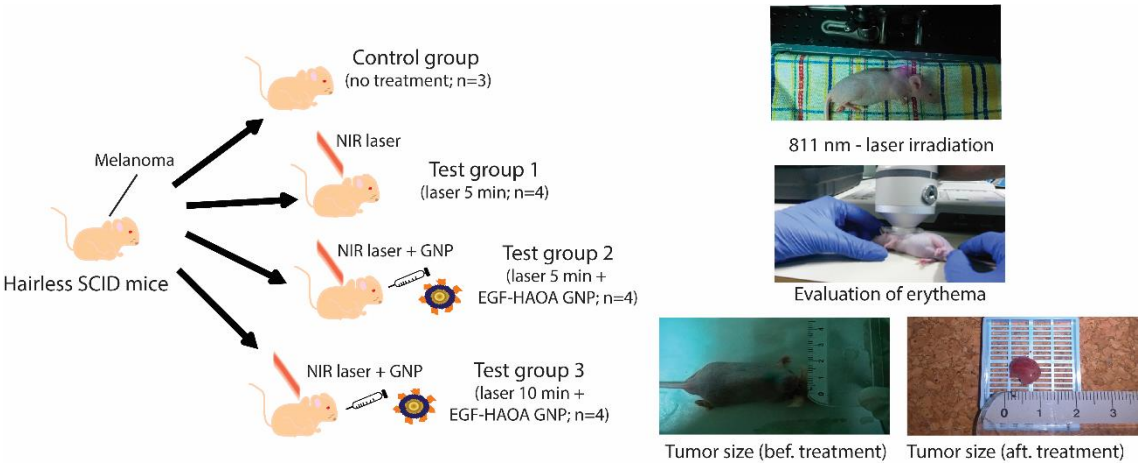

Figure 1. Illustrated scheme of melanoma xenograft models assessed for *in vivo* anti-cancer efficiency with photothermal therapy.

3. Results

3.1 Induction and follow-up of human xenograft models of melanoma in hairless SCID mice

The variation of tumors growth in SHO-SCID mice was high, ranging from 2 weeks to 2 months. In spite of this fact, SCID mice showed stable body conditions with a BCS > 3. All mice were monitored for 60-90 days, showing an average weight of 28.5 ± 1.5 g (mean ± SD, n = 15). The weight was kept within these values throughout the study. In addition, all rodents showed a normal water and food intake, normal respiratory activity, posture (independently from the size of the tumor) and mobility. After necropsies, control and treated groups showed similar histological morphology and size of internal organs

(i.e., except the tumor), namely lungs (right and left), spleen, heart, kidneys (right and left) and liver. The average weight and measures (for heart and spleen), for each group included in the photothermal therapy, are represented in Table 1, showing that there was no important variation in size of the organs. No micro or macrometastases for melanoma were found in the lungs and there were no size variations of these organs between control and test groups. As for the tumors, the average weight and volume was 0.46 ± 0.03 g and 773.3 ± 51.5 mm^3 (mean ± SEM; n = 15). Statistical analysis as Student's t-test (*p<0.01) showed that there were no significant differences for the treatment groups compared to the control, in terms of weight and size of the organs.

Table 1. Average weight of excised organs after treatment or as control groups, for photothermal therapy. Size measures were taken for the heart and spleen of the mice. Results are presented as mean ± SEM. Legend: (R) - Right; (L) – Left.

Group	Organ		Weight (g)	Size (mm^3)
Control (n = 3)	Lungs	R	0.163 ± 0.011	-
		L	0.060 ± 0.004	-
	Heart		0.183 ± 0.012	180.0 ± 12.0
	Kidneys	R	0.260 ± 0.017	-
		L	0.247 ± 0.016	-
	Liver		1.723 ± 0.115	-
	Spleen		0.063 ± 0.004	141.5 ± 9.4
Laser (5 min) (n = 4)	Lungs	R	0.141 ± 0.009	-
		L	0.055 ± 0.004	-
	Heart		0.174 ± 0.012	165.0 ± 11.0
	Kidneys	R	0.248 ± 0.017	-
		L	0.248 ± 0.017	-
	Liver		1.477 ± 0.098	-
	Spleen		0.045 ± 0.003	81.0 ± 5.4
Laser (5 min) + EGF-HAOA GNP (n = 4)	Lungs	R	0.118 ± 0.008	-
		L	0.055 ± 0.004	-
	Heart		0.151 ± 0.010	191.5 ± 12.8
	Kidneys	R	0.242 ± 0.016	-
		L	0.233 ± 0.016	-
	Liver		1.856 ± 0.124	-

	Spleen		0.048 ± 0.003	65.6 ± 4.4
Laser (10 min) + EGF-HAOA GNP (n = 4)	Lungs	R	0.429 ± 0.029	-
		L	0.046 ± 0.003	-
	Heart		0.143 ± 0.010	146.1 ± 9.7
	Kidneys	R	0.236 ± 0.016	-
		L	0.229 ± 0.015	-
	Liver		1.543 ± 0.103	-
	Spleen		0.060 ± 0.004	102.7 ± 6.8

3.2 Photothermal therapy

Mice with melanoma treated with photothermal therapy showed that laser at 811 nm applied with EGF-conjugated HAOA-coated nanoparticles promoted tumor local necrosis (Figure 2). Mice treated with EGF-conjugated HAOA-coated nanoparticles and 5 min-exposure 811 nm laser beam showed a reduction to 81.1 ± 20.3% (mean ± SEM, n = 4). However, when we increased the laser exposure to 10 min, this value decreased to 32.3 ± 8.1% (mean ± SEM, n = 4). In addition, we have evaluated the degree of erythema (a *, AU) by colorimetry, before and after laser irradiation (mean ± SEM, n = 4 for each group). Results showed that there was a small change on the skin redness after laser irradiation alone for 5 min (Δa*= 0.44 ± 0.34 AU) and also for laser irradiation for 5 min after injection of the nanoparticles (Δa*= 1.44 ± 0.01 AU) and for 10 min laser irradiation after injection of nanoparticles (Δa*= 1.00 ± 0.25 AU). Statistical analysis as Student's t-test (*p <0.01) showed that there were no significant differences between the skin colorimetry, before and after irradiation, of each treatment group.

In terms of histological analysis, it was observed the presence of several necrotic foci in tumor samples exposed to the laser at 811 nm for 5 min, combined with EGF-conjugated HAOA-coated gold nanoparticles, as mostly as coagulative necrosis (Figure 2). Regarding the laser irradiation alone (without local injection of nanoparticles), few morphological changes (< 30% extended necrosis) were also observed in the tumor tissue of the mice. As for the control groups, no histological or morphological changes were observed (Figure 2).

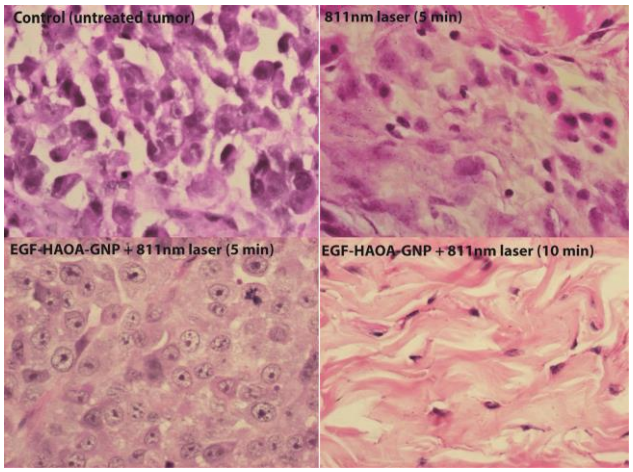

Figure 2. Histological images (400X microscopic approach) of the tumor tissue from the control group (i.e., without treatment), from the group treated with 811 nm-laser irradiation for 5 min and from the groups treated with i.t. administration of EGF-conjugated HAOA-coated gold nanoparticles and 811 nm-laser irradiation for 5 and 10 min. All tissues were marked with Hematoxylin-Eosin staining (H & E staining).

Then, we compared the histology of the different organ's tissues (i.e., heart, kidney, liver, spleen, lung and normal skin without tumor) in mice after exposure to laser irradiation at 811 nm for 5 min combined with EGF-conjugated HAOA-coated gold nanoparticles and the control group since a high tumor volume reduction was observed. Similarly, the histology of the mice's organs (i.e., heart, kidney, liver, spleen and lung), exposed to the laser and nanoparticles confirm that there were no morphological changes and were comparable to the control (Figure 3), suggesting a very localized inoculation of tumor cells and treatment. Dermis tissue from normal skin sample was, as expected, a stratified epithelium, fibrous with sweat glands, present in the fatty tissue (hypodermis).

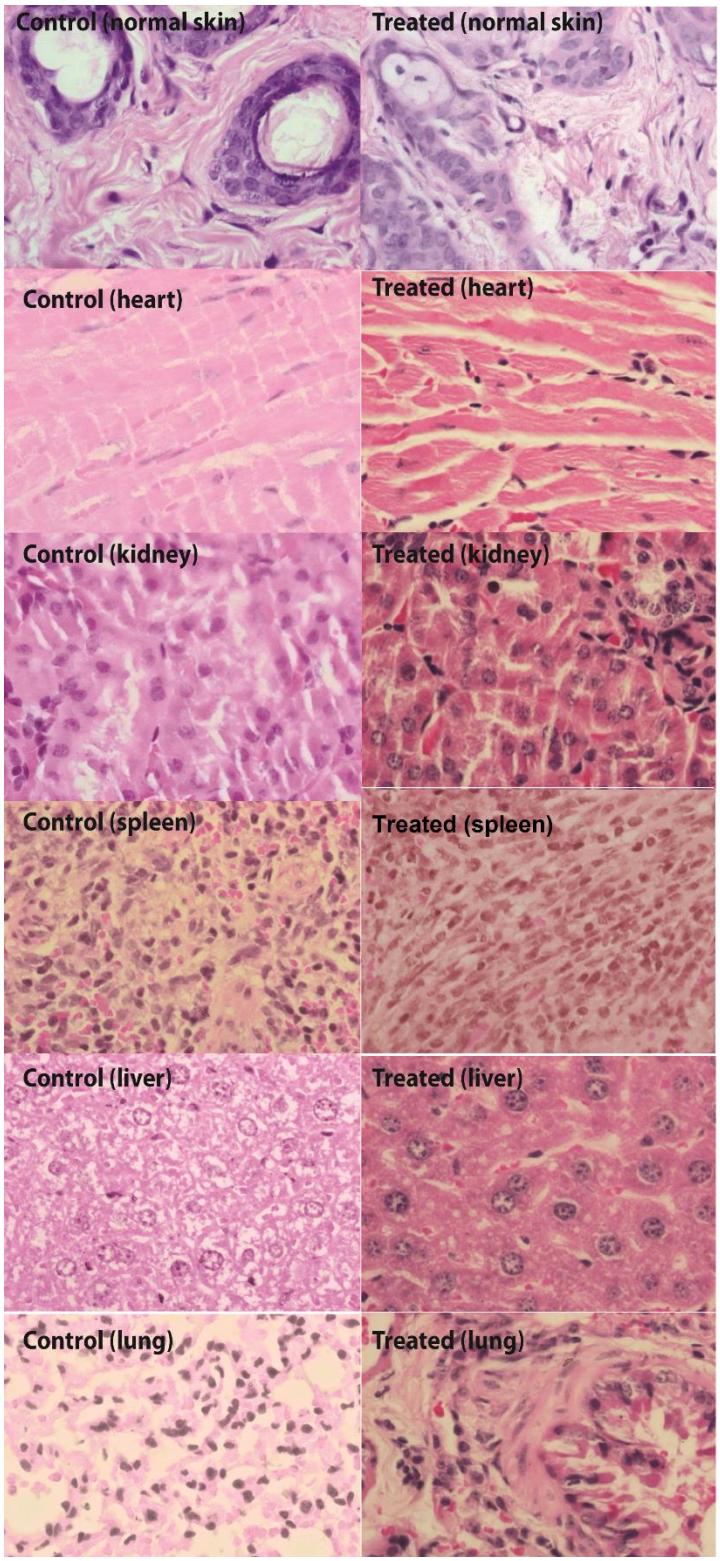

Figure 3. Histological images (400X microscopic approach) of the tumor tissue from the control group (i.e., without treatment) and from the group treated with 811 nm-laser irradiation for 5 min and i.t. administration of EGF-conjugated HAOA-coated gold nanoparticles. Each image is representative of the organs removed for analysis after

necropsy (i.e., heart, kidney, liver, spleen, lung and skin). All tissues were marked with Hematoxylin-Eosin staining (H & E staining).

4. Discussion

Preliminary results obtained in the present *in vivo* studies indicated that both therapeutic strategies induce cancer cells death and may avoid melanoma progression to more aggressive stages. Hairless SCID mice used in this study have been bread by crossing an outbred SCID with an immunocompetent outbred hairless mouse (SKH1), resulting in hairless immunocompromised SCID mice with higher tumor engraftment efficiency than athymic nude mice. Although the animals have defects in T and B cell development, which results in absent murine T and B lymphocytes, they have high natural killer (NK) cell levels [31]. Xenograft models are normally successfully recreated but some variation can occur. In this study, we wanted to develop a localized cutaneous melanoma and not to recreate a model for metastatic and angiogenic melanoma. Therefore, SCID animals were selected, since they tend to reduce formation of metastases and delay cell growth, as demonstrated for transformed A375 cell line with lung tropism due to the presence of NK cells [32]. As a consequence, an increased variation in tumor growth was verified. Another research group have studied the variability of implantation of human melanoma cells from patients into NOD/SCID mice, showing that there was a high variability and that it could take more than 32 weeks for tumors to develop [33]. It was determined that less than 10^5 cells *per* injection would fail greatly to form tumors in mice. Between 10^5 and 10^7 cell per injection, a palpable tumor appeared after 8 weeks. When using Matrigel (25%), melanoma cells become highly tumorigenic and, therefore, tumors were formed faster (around 7 weeks). Matrigel can stimulate a faster tumor growth, but also influence the cancer cells metastatic behavior and expression, since the addition of angiogenic factors, present in Matrigel composition, modify the conditions of the tumor extracellular matrix [34, 35]. On the other hand, it is known that melanoma shows natural tumorigenic potential, which is related with the malignant behavior of cancer cells [4,36].

EGF-conjugated HAOA-coated gold nanoparticles were tested in association with a 811 nm-laser for 5 min at 2.5 W/cm^2, as the photothermal therapy for cutaneous melanoma. By photothermal therapy, tumors exposed to NIR laser and nanoparticles showed a characteristic coagulative necrosis, resulting from denaturation of the tissue structural proteins [37–39]. Therefore, histological images appear pale in staining since there is a

loss of cytoplasmatic and nuclear matter. In presence of tumor and without local injection of the nanoparticles, some necrosis foci were observed (< 30%) after laser irradiation (5 and 10 min). In spite of this, after laser irradiation also, the mice's skin integrity was maintained, as the dermis kept its stratified epithelium and fibrous with sweat glands, present in the fatty tissue (hypodermis), which can be associated to the low temperature reached at the site of the irradiation (< 40ºC). The latter was also observed in other studies [40,41]. NIR laser irradiation has been reported to not cause any type of morphological tissue damage or cause less than 10% of necrosis after irradiation [39]. Different laser parameters were selected in those studies: in the first study, where the laser caused no damage, irradiation was conducted at a wavelength of 785 nm, for 10 min with a power of 9.5 W/cm^2; in the second study, laser irradiation occurred at a wavelength of 808 nm, for 1 min at a power of 0.5 W/cm^2 [39]. NIR lasers are considered as safe for skin irradiation and to penetrate deeper (up to 10 mm) than UV-visible laser [19,22]. However, it has been reported the presence of thermal side effects and coagulative necrosis in skin tissues, where NIR-laser was applied alone, mainly for the first biological window (650–900 nm) region [42–44]. This can be avoided if the epidermal skin area is efficiently cooled (< 20 ºC) before laser irradiation [42,43]. Therefore, it is critical to always verify the safety of the laser irradiation, at specific experimental conditions, in every study. As an alternative, the actual use of low fluency lasers, such as nanosecond and femtosecond lasers, allow a localized energy transfer, which induces a temporary increase of cell permeability without affecting cell viability [45].

Regarding the treatment with EGF-conjugated HAOA-coated gold nanoparticles, the nanoparticles were administered 4 h before laser irradiation, via single i.t. injection. Further, after 24 h -post laser irradiation for 5 min, several necrotic foci were detected. In this case, a high tumor volume reduction was observed after laser irradiation. Several factors may contribute to this reduction. Firstly, it is known that gold nanoparticles reach their maximum absorption after the laser irradiation, promoting local hyperthermia of the tissues (temperature in the range 41–47°C) and, consequently, irreversible cell damage caused by the disruption of cell's membrane permeability and protein denaturation [21,46]. Hyperthermia is known to induce apoptotic cell death in many tissues and has been shown to increase local control and overall survival in combination with radiotherapy and chemotherapy in randomised clinical trials. Normal tumor vasculature dilates to aid heat dissipation, tumor vasculature constricts, providing some tumor selectivity [46]. Secondly, the combination of polymeric coatings and bio-conjugation avoid interactions with the immune cells and capture of the nanoparticles by the

mononuclear phagocyte system (i.e., spleen, liver and lung) [47]. In our case, EGF-conjugated HAOA-coated nanoparticles showed a size around 100-200 nm, a negative surface change (- 5 mV) and a spherical morphology. Tumor tissue has leaky vasculature and, thus, it may be possible an accumulation of the nanoparticles in this tissue occurred by both EPR effect and active binding of the EGF ligand to overexpressed EGFR [48,49]. As in another study, clusters of iron oxide magnetic nanoparticles for NIR-laser PTT were developed by Shen *et al.* (2015) for testing on A549 human lung adenocarcinoma epithelial cell line [50]. The clusters were prepared by a modified solvothermal reaction, in autoclave, and administered i.t. in mice. After 2 h of cell-nanoparticle interaction, tumors were irradiated with a 808 nm continuous-wave NIR laser at 5 W/cm^2. Clustered nanoparticles were more efficient than individual nanoparticles inducing tumor local hyperthermia, reaching a temperature around 50 ºC and killing 72.8% of cancerous cells; in spite of this, the clusters were slowly cleared from the tumor after therapy, being detected several days after the treatment in the mice's organism [50]. In our study, we have accomplished a high tumor reduction (> 80%), demonstrating an effective hyperthermia and tumor destruction, at lower temperature values.

Finally, orthotopic xenografts models are widely used in pre-clinical studies, as they easily allow the establishment of primary tumor or human transplanted cells to *in vivo* conditions. However, these models do not reproduce exactly the tumor microenvironment and cannot always represent the vast heterogeneity and complexity of cancer tissues [4,51]. Immunodeficient environment, as a consequence for xenograft human cells acceptance, can also compromise the tumor architecture and microenvironment [4,51]. Cutaneous melanoma is a very heterogeneous cancer associated with many signaling pathways and mutations that divide this cancer in several subtypes. Thus, this cancer is one of the most challenging and clinically complex in terms of anti-cancer drug efficacy studies.

5. Conclusions

Hybrid nanosystems were developed, comprising multiple targeting moieties for an active uptake by melanoma cells by photothermal therapy. Palpable tumors were assessed for volume growth after 15 days. Internal organs, such as, heart, lungs, liver, spleen and kidneys did not show any structural change, suggesting a very localized tumor cell inoculation. We also observed that the laser did not affect or slightly affected

the skin integrity. In presence of the tumor, photothermal therapy showed that the light-absorbing nanoparticles improved coagulative necrosis and strongly reduced the volume of the tumors. The study of molecular mechanisms behind this anti-cancer effects on human melanoma is still ongoing. Further, we will concentrate on the association of laser-activated drug delivery systems, comprising an anti-cancer drug, as a promising approach for an effective melanoma therapy.

Abbreviations

DMEM, Dulbecco's Modified Eagle's medium; EDTA, ethylenediamine tetraacetic acid; EGF, Epidermal Growth Factor; EGFR, Epidermal Growth Factor Receptor; EPR; Enhanced Permeability and Retention Effect; HA, Hyaluronic Acid; HAOA, Hyaluronic and oleic acids; FBS, Fetal Bovine Serum; NIR Near Infrared; MTT, Thiazolyl Blue Tetrazolium Bromide; NK, Natural Killer; PBS, Phosphate Buffer Saline; P/S, Penicillin/ Streptomycin; OA, Oleic acid; SCID, Sever Combined Immunodeficiency Model.

Acknowledgments

The authors thank to Fundação para a Ciência e Tecnologia (FCT) for the financial support under the project reference PTDC/BBB-BMC/0611/2012 and to Professor Ana Sofia Fernandes from CBIOS/ULHT for the help with cell cultures.

Conflicts of interest

No potential conflict of interest was reported by the authors.

References

1. Morton CL, Houghton PJ. Establishment of human tumor xenografts in immunodeficient mice. *Nat. Protoc.* 2(2), 247–250 (2007).
2. Ruggeri BA, Camp F, Miknyoczki S. Animal models of disease: pre-clinical animal models of cancer and their applications and utility in drug discovery. *Biochem. Pharmacol.* 87(1), 150–161 (2014).
3. Combest AJ, Roberts PJ, Dillon PM, *et al.* Genetically engineered cancer models, but not xenografts, faithfully predict anticancer drug exposure in melanoma tumors. *Oncologist*. 17(10), 1303–1316 (2012).
4. Beaumont KA, Mohana-Kumaran N, Haass NK. Modeling melanoma *in vitro* and *in vivo*. In: *Healthcare*. Multidisciplinary Digital Publishing Institute, 27–46 (2013).
5. Yamaura H, Sato H. Quantitative studies on the developing vascular system of rat

hepatoma. *J. Natl. Cancer Inst.* 53(5), 1229–1240 (1974).

6. Lee C-H, Lai P-S, Lu Y-P, *et al.* Real-time vascular imaging and photodynamic therapy efficacy with micelle-nanocarrier delivery of chlorin e6 to the microenvironment of melanoma. *J. Dermatol. Sci.* 80(2), 124–132 (2015).
7. Rozenberg GI, Monahan KB, Torrice C, Bear JE, Sharpless NE. Metastasis in an orthotopic murine model of melanoma is independent of RAS/RAF mutation. *Melanoma Res.* 20(5), 361–371 (2010).
8. Craft N, Bruhn KW, Nguyen BD, *et al.* Bioluminescent imaging of melanoma in live mice. *J. Invest. Dermatol.* 125(1), 159–165 (2005).
9. Paine-Murrieta GD, Taylor CW, Curtis RA, *et al.* Human tumor models in the severe combined immune deficient (SCID) mouse. *Cancer Chemother. Pharmacol.* 40(3), 209–214 (1997).
10. Yang H, Higgins B, Kolinsky K, *et al.* RG7204 (PLX4032), A selective BRAFV600E inhibitor, displays potent antitumor activity in preclinical melanoma models. *Cancer Res.* 70(13), 5518–5527 (2010).
11. Zamboni WC, Strychor S, Joseph E, *et al.* Plasma, tumor, and tissue disposition of stealth liposomal CKD-602 (S-CKD602) and nonliposomal CKD-602 in mice bearing A375 human melanoma xenografts. *Clin. Cancer Res.* 13(23), 7217–7223 (2007).
12. Kamran MZ, Gude RP. Preclinical evaluation of the antimetastatic efficacy of Pentoxifylline on A375 human melanoma cell line. *Biomed. Pharmacother.* 66(8), 617–26 (2012).
13. Baptista PV. Gold nanobeacons: A potential nanotheranostics platform. *Nanomedicine*. 9(15), 2247–2250 (2014).
14. Rink JS, Plebanek MP, Tripathy S, Thaxton CS. Update on current and potential nanoparticle cancer therapies. *Curr. Opin. Oncol*. 25(6), 646–651 (2013).
15. Fernandes A, Viana Baptista P. Nanotechnology for cancer diagnostics and therapy–An update on novel molecular players. *Ther. Rev.* 9(3), 163–172 (2013).
16. Figueiredo S, Cabral R, Luís D, Fernandes AR, Baptista P V. Conjugation of gold nanoparticles and liposomes for combined vehicles of drug delivery in cancer. In: *Nanomedicine*. 48-82 (2013).
17. Niezgoda A, Niezgoda P, Czajkowski R. Novel approaches to treatment of advanced melanoma: A review on targeted therapy and immunotherapy. *Biomed Res. Int.* 2015 (2015).
18. Lloyd-Hughes H, Shiatis AE, Pabari A, Mosahebi A, Seifalian A. Current and future nanotechnology applications in the management of melanoma: A review. *J.*

Nanomed. Nanotechnol. 2015 (2015).

19. Alkilany AM, Murphy CJ. Toxicity and cellular uptake of gold nanoparticles: what we have learned so far? *J. Nanoparticle Res.* 12(7), 2313–2333 (2010).
20. Sajanlal PR, Sreeprasad TS, Samal AK, Pradeep T. Anisotropic nanomaterials: Structure, growth, assembly, and functions. *Nano Rev.* 2 (2011).
21. Dykman LA, Khlebtsov NG. Gold nanoparticles in biology and medicine: recent advances and prospects. *Acta Naturae*. 3(2), 34 (2011).
22. Miwa M, Shikayama T. ICG fluorescence imaging and its medical applications. In: *International Conference of Optical Instrument and Technology*. International Society for Optics and Photonics, 71600K–71600K–9 (2008).
23. Kennedy LC, Bickford LR, Lewinski NA, *et al.* A new era for cancer treatment: Gold nanoparticle mediated thermal therapies. *Small*. 7(2), 169–183 (2011).
24. Huang X, Jain PK, El-Sayed IH, El-Sayed MA. Plasmonic photothermal therapy (PPTT) using gold nanoparticles. *Lasers Med. Sci.* 23(3), 217–228 (2008).
25. van der Meel R, Vehmeijer LJC, Kok RJ, Storm G, van Gaal EVB. Ligand-targeted particulate nanomedicines undergoing clinical evaluation: Current status. *Adv. Drug Deliv. Rev.* 65(10), 1284–1298 (2013).
26. Lu W, Xiong C, Zhang R, *et al.* Receptor-mediated transcytosis: A mechanism for active extravascular transport of nanoparticles in solid tumors. *J. Control. Release*. 161(3), 959–966 (2012).
27. Oliveira Silva C, Rijo P, Molpeceres J, et al. Bioproduction of gold nanoparticles for photothermal therapy. *Ther Deliv.* 7(5):287-304 (2016).
28. Scodeller P, Catalano PN, Salguero N, Duran H, Wolosiuk A, Soler-Illia GJAA. Hyaluronan degrading silica nanoparticles for skin cancer therapy. *Nanoscale*. 5(20), 9690–9698 (2013).
29. Liu D, Liu X, Xing M. Activities of multiple cancer-related pathways are associated with BRAF mutation and predict the resistance to BRAF/MEK inhibitors in melanoma cells. *Cell Cycle*. 13(2), 208–219 (2014).
30. Charles River Laboratoires International I. Charles River Immunodeficient Models Xenograft Data Catalog.
31. Cassard L, Cohen-Solal JFG, Galinha A, *et al.* Modulation of tumor growth by inhibitory Fcγ receptor expressed by human melanoma cells. *J. Clin. Invest.* 110(10), 1549–1557 (2002).
32. Carreno BM, Garbow JR, Kolar GR, *et al.* Immunodeficient mouse strains display marked variability in growth of human melanoma lung metastases. *Clin. Cancer Res.* 15(10), 3277–3286 (2009).

33. Quintana E, Shackleton M, Sabel MS, Fullen DR, Johnson TM, Morrison SJ. Efficient tumor formation by single human melanoma cells. *Nature*. 456(7222), 593–598 (2008).
34. Benton G, Arnaoutova I, George J, Kleinman HK, Koblinski J. Matrigel: From discovery and ECM mimicry to assays and models for cancer research. *Adv. Drug Deliv. Rev.* 79, 3–18 (2014).
35. Barkan D, Green JE, Chambers AF. Extracellular matrix: A gatekeeper in the transition from dormancy to metastatic growth. *Eur. J. Cancer*. 46(7), 1181–1188 (2010).
36. Shackleton M, Quintana E. Progress in understanding melanoma propagation. *Mol. Oncol.* 4(5), 451–457 (2010).
37. Li Z, Huang P, Zhang X, *et al.* RGD-conjugated dendrimer-modified gold nanorods for *in vivo* tumor targeting and photothermal therapy. *Mol. Pharm.* 7(1), 94–104 (2009).
38. Jr Fleury LFF, Jr Sanches Jr JA. Primary cutaneous sarcomas. Sarcomas cutâneos primários. *An Bras Dermatol*. 81(3), 207–221 (2006).
39. Lu W, Xiong C, Zhang G, *et al.* Targeted photothermal ablation of murine melanomas with melanocyte-stimulating hormone analog-conjugated hollow gold nanospheres. *Clin. Cancer Res.* 15(3), 876–886 (2010).
40. Green HN, Crockett SD, Martyshkin D V, *et al.* A histological evaluation and *in vivo* assessment of intratumoral near infrared photothermal nanotherapy-induced tumor regression. *Int. J. Nanomedicine*. 9, 5093 (2014).
41. Tsai M-F, Chang S-HG, Cheng F-Y, *et al.* Au nanorod design as light-absorber in the first and second biological near-infrared windows for *in vivo* photothermal therapy. *ACS Nano*. 7(6), 5330–5342 (2013).
42. Sugiura T, Matsuki D, Okajima J, *et al.* Photothermal therapy of tumors in lymph nodes using gold nanorods and near-infrared laser light with controlled surface cooling. *Nano. Res.* 8(12), 3842–3852 (2015).
43. Shafirstein G, Bäumler W, Hennings LJ, *et al.* Indocyanine green enhanced near-infrared laser treatment of murine mammary carcinoma. *Int. J. Cancer*. 130(5), 1208–1215 (2012).
44. Tabakoğlu HÖ, Gülsoy M. *In vivo* comparison of near infrared lasers for skin welding. *Lasers Med. Sci.* 25(3), 411–421 (2010).
45. Jumelle C, Mauclair C, Houzet J, *et al.* Delivery of molecules into human corneal endothelial cells by carbon nanoparticles activated by femtosecond laser. *PLoS One*. 10(7), e0132023 (2015).

46. Huang X, El-Sayed MA. Plasmonic photo-thermal therapy (PPTT). *Alexandria J. Med.* 47(1), 1–9 (2011).
47. Banu H, Sethi DK, Edgar A, *et al.* Doxorubicin loaded polymeric gold nanoparticles targeted to human folate receptor upon laser photothermal therapy potentiates chemotherapy in breast cancer cell lines. *J. Photochem. Photobiol. B.* 149, 116–128 (2015).
48. Melancon MP, Lu W, Yang Z, *et al. In vitro* and *in vivo* targeting of hollow gold nanoshells directed at epidermal growth factor receptor for photothermal ablation therapy. *Mol. Cancer Ther.* 7(6), 1730–1739 (2008).
49. Girotti MR, Pedersen M, Sanchez-Laorden B, *et al.* Inhibiting EGF receptor or SRC family kinase signaling overcomes BRAF inhibitor resistance in melanoma. *Cancer Discov.* 3(2), 158–167 (2013).
50. Shen S, Wang S, Zheng R, *et al.* Magnetic nanoparticle clusters for photothermal therapy with near-infrared irradiation. *Biomaterials*. 39, 67–74 (2015).
51. Choi SYC, Lin D, Gout PW, Collins CC, Xu Y, Wang Y. Lessons from patient-derived xenografts for better *in vitro* modeling of human cancer. *Adv. Drug Deliv. Rev.* 79, 222–237 (2014).

CONCLUSIONS

CONCLUSIONS

The experimental work included in this thesis aimed the design and characterization of novel formulations based on hybrid nanoparticles for two different strategies in cutaneous melanoma targeted therapy. Briefly, hybrid gold nanoparticles were designed for a photothermal therapy approach (physical approach) and hybrid polymeric-lipidic nanoparticles were developed for chemotherapy (chemical approach). The results obtained allowed us to conclude the following points:

1. Polymeric-lipidic nanoparticles, made of poly-ε-caprolactone and stearic acid, showed high encapsulation efficiency, improved drug stability and sustained drug release of the topical glucocorticosteroid, betamethasone-21-acetate. In addition, coating with the permeation enhancer, oleic acid, increased drug permeation *in vitro* and *in vivo* animal models, without causing skin irritation or other side effects.

2. Gold nanoparticles were successfully produced by reduction with an aqueous extract of *Plectranthus saccatus* Benth., rich in rosmarinic, caffeic and chlorogenic acids, allowed us to obtain clusters of 100 nm-sized nanoparticles, with a spherical morphology and a surface plasmon band at near infrared region (830 nm). These nanoparticles were successfully coated with hyaluronic and oleic acids (HAOA), maintaining their physico-chemical characteristics, a safe *in vitro* toxicity profile and responding to thermal activation (up to 50ºC).

3. Conjugation of HAOA-coated gold nanoparticles with lysozyme (herein used as a model protein) showed that these hybrid nanoparticles were able to positively incorporate this model protein, by electrostatic interactions. In addition, HAOA-coated gold nanoparticles enhanced the protection of this protein against UV photodegradation, reducing the fluorescence decay of the aromatic residues, mainly tryptophan, and the formation of photo-oxidative products.

4. Conjugation of HAOA-coated gold nanoparticles with Epidermal Growth Factor (EGF) showed that these hybrid nanoparticles were also able to successfully incorporate such a key relevant medical peptide, by electrostatic interactions. HAOA-coated gold nanoparticles also increased EGF UV photostability and reduced the formation of photo-degradation products. In addition, EGF-

conjugated HAOA-coated gold nanoparticles were actively internalized by tumor cells through EGFR-mediated endocytosis and showed safe *in vitro* cytotoxic profile over normal-like cells.

5. Coating of hybrid polymeric-lipid nanoparticles, made from poly-ε-caprolactone and stearic acid, with hyaluronic and oleic acids (HAOA) was also successful and increased the sustained release of a novel anti-tumor compound, Parvifloron D, extracted from *Plectranthus eckloni*, with remarkable cytotoxic action but low selectivity. Parvifloron D showed a fast onset and high potency *in vitro* anti-tumor action. HAOA-coated hybrid nanoparticles showed a size of 300 nm and a spherical shell-core structure, confirmed by several physico-chemical techniques. In addition, α-Melanocyte Stimulating Hormone (α-MSH) was positively conjugated onto HAOA-coated hybrid nanoparticles, by electrostatic interactions. *In vitro* cytotoxicity and internalization studies showed that those nanoparticles were uptaken by tumor cells (B16V5 and A375), according to different mechanisms.

6. *In vivo* efficiency studies showed that both therapeutic approaches promoted necrosis of human cutaneous melanoma cells in xenograft models of immunodeficient mices. Near infrared-based photothermal therapy in association with EGF-conjugated HAOA-coated gold nanoparticles reduced tumor volume in 80% and caused several coagulative necrotic foci on tumor tissue, but no significant damage of the surrounding tissue or other side effects. Meanwhile, local chemotherapy with Parvifloron D and α-MSH-conjugated HAOA-coated polymeric-lipidic nanoparticles promoted an extensive necrosis of the tumors (up to 90%).

7. Finally, we can conclude that it is possible to modify different nanosystems, starting from different core structures, and modulating the surface through a successful and broad functionalization with multiple and distinct targeting moieties. Thus, different therapeutic strategies can be applied in heterogeneous cancers, such as cutaneous melanoma, destroying the tumor by diverse approaches. Physico-chemical characterization and both *in vitro* and *in vivo* biologic models are, therefore, crucial to obtain a robust, reproducible and efficient hybrid nanosystem.

8. As future prospect, we aim to conjugate synergistically both therapies studied in this thesis. Therefore, we will continue to study the functionalization of hybrid nanoparticles with different anti-tumor targeting moieties, comprising a light-absorbing core, for photothermal therapy, and a polymeric structure, capable of sustaining the release of novel anti-tumor drugs, for a local chemotherapy.

SUPPLEMENTARY INFORMATION

inpi instituto nacional da propriedade industrial

SGCR
- 2 MAIO 2016

Exmo. Sr.
JOÃO LUÍS PEREIRA GARCIA
RUA CASTILHO, 167 2º
1070 - 050 LISBOA

Direção de Marcas e Patentes
Departamento de Patentes e Modelos de Utilidade

Ref. DP/01/2016/37319	PATENTE DE INVENÇÃO NACIONAL n.º 108994	Data: 2016.04.26

OFÍCIO

Informa-se, que o pedido de Patente de Invenção em epígrafe irá ser objeto de publicação no Boletim da Propriedade Industrial n.º 104/2017 que será editado em 2017.05.30, nos termos do artigo 66.º do Código da Propriedade Industrial.

Mais se informa que, após essa publicação, qualquer pessoa que se sinta prejudicada poderá apresentar reclamação no prazo de dois meses a contar da data de publicação do referido Boletim.

Com os melhores cumprimentos,

Susana Armário
Técnico(a) Superior

inpi instituto nacional da propriedade industrial

Campo das Cebolas - 1149-035 Lisboa - Portugal
Tel: +351 218818100 / Linha Azul: 808 200689 / Fax: +351 218875308 / Fax: +351 218860066 / E-mail: atm@inpi.pt / www.inpi.pt

Nº	CÓDIGO	DATA E HORA DE RECEÇÃO	MODALIDADE	PROCESSO RELACIONADO
20151000093093	0199	2015/11/30-16:06:25	PAT	108994 T

PAGAMENTO CONFIRMADO

PEDIDO DE PATENTE, MODELO DE UTILIDADE OU DE TOPOGRAFIA DE PRODUTOS SEMICONDUTORES

1 REQUERENTES

Código **Nacionalidade** PORTUGUESA
Nome COFAC - COOPERATIVA DE FORMAÇÃO E ANIMAÇÃO CULTURAL
Endereço UNIVERSIDADE LUSÓFONA DE HUMANIDADES E TECNOLOGIAS, AVENIDA DO CAMPO GRANDE, Nº 376
Localidade LISBOA **Código Postal**
Telefone **Telemóvel** **Fax** 501679529
E-mail SGCR@SGCR.PT
Atividade (CAE)
NIF 501679529

Código **Nacionalidade** PORTUGUESA
Nome FACULDADE DE CIÊNCIAS DA UNIVERSIDADE DE LISBOA
Endereço FACULDADE DE CIÊNCIAS DA UNIVERSIDADE DE LISBOA - EDIFÍCIO C5, CAMPO GRANDE
Localidade LISBOA **Código Postal** 1749-016
Telefone **Telemóvel** **Fax**
E-mail SGCR@SGCR.PT
Atividade (CAE)
NIF 502618418

Código **Nacionalidade** PORTUGUESA
Nome FACULDADE DE CIÊNCIAS E TECNOLOGIA - UNIVERSIDADE NOVA DE LISBOA
Endereço CAMPUS DA CAPARICA
Localidade CAPARICA **Código Postal** 2829-516
Telefone **Telemóvel** **Fax**
E-mail SGCR@SGCR.PT
Atividade (CAE)
NIF 505954702

Tipo de Representação Agente Oficial da Propriedade Industrial ou Procurador Autorizado
Nome JOÃO LUÍS PEREIRA GARCIA **Código** 64
Exclusivo para este ato? NÃO

2 MODALIDADE / TIPO DE PEDIDO

Modalidade: PATENTE DE INVENÇÃO NACIONAL
Nº de reivindicações apresentadas: 12

3 EPÍGRAFE OU TÍTULO

NANOSSISTEMA DE OURO COM REVESTIMENTO BIOPOLIMÉRICO E GAMA DE ABSORÇÃO NO INFRAVERMELHO PRÓXIMO E MÉTODO PARA A SUA PREPARAÇÃO

4 RESUMO

NANOSSISTEMA COMPOSTO POR NANOPARTÍCULAS DE OURO PRODUZIDAS ATRAVÉS DE UM EXTRATO DE PLANTA (4) COMO AGENTE REDUTOR ADSORVIDO À SUPERFÍCIE DE UM NÚCLEO METÁLICO DE OURO (1) E UM REVESTIMENTO POLIMÉRICO (2) E PEPTÍDICO (3), DE FORMA ESSENCIALMENTE ESFÉRICA E COM GAMA DE ABSORÇÃO NO INFRAVERMELHO PRÓXIMO, E MÉTODO PARA A SUA PREPARAÇÃO A PARTIR DE ÁCIDO HIALURÓNICO (5) E ÁCIDO OLEICO (6). O NANOSSISTEMA APRESENTA ATIVIDADE TERAPÊUTICA EM TUMORES SUPERFICIAIS, NOMEADAMENTE LOCALIZADOS A PROFUNDIDADE INFERIOR A 5 CENTÍMETROS, E PROFUNDOS, NOMEADAMENTE LOCALIZADOS A PROFUNDIDADE SUPERIOR A 5 CENTÍMETROS, E EM PATOLOGIAS DERMATOLÓGICAS QUANDO ATIVADO POR HIPERTERMIA ATRAVÉS DA INCIDÊNCIA DE UM LASER OU DE UMA FONTE DE LUZ DE APLICAÇÃO SIMILAR.

5 FIGURAS

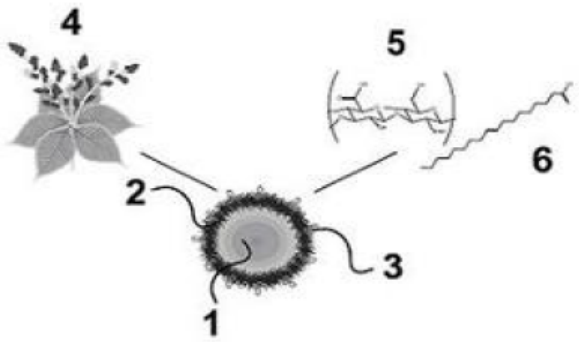

6 INVENTORES

Nacionalidade PORTUGUESA

Nome CATARINA MENDES ALVES DE OLIVEIRA SILVA
Endereço RUA DA EIRA, Nº54, 5ºESQ
Localidade ALGÉS **Código Postal** 1495-233
Telefone
E-mail SGCR@SGCR.PT
NIF 255360002

Nacionalidade PORTUGUESA

Nome ANA CATARINA BECO PINTO REIS
Endereço RUA JOSÉ MARIA NICOLAU, N.º 5 RD/C-B
Localidade LISBOA **Código Postal** 1500-374
Telefone
E-mail SGCR@SGCR.PT
NIF 210126442

Nacionalidade PORTUGUESA

Nome PATRÍCIA DIAS DE MENDONÇA RIJO
Endereço RUA VISCONDE DE SANTARÉM, N.º36, R/C
Localidade LISBOA **Código Postal** 1000-287
Telefone
E-mail SGCR@SGCR.PT
NIF 210014571

Nacionalidade PORTUGUESA

Nome JOÃO MIGUEL PINTO COELHO
Endereço R. MARIA ALDA BARBOSA NOGUEIRA, Nº 14, 7ºA, FALAGUEIRA
Localidade AMADORA **Código Postal** 2700-393
Telefone
E-mail SGCR@SGCR.PT
NIF 194466523

Nacionalidade PORTUGUESA
Nome RICARDO FILIPE DOS SANTOS GOMES
Endereço RUA DE FRANÇA, Nº 6, 2º DTO
Localidade BELAS **Código Postal** 2605-222
Telefone
E-mail SGCR@SGCR.PT
NIF 214213730

Nacionalidade PORTUGUESA
Nome PEDRO MANUEL CARDOSO VIEIRA
Endereço RUA FERNANDO PESSOA Nº65
Localidade QT DO ANJO **Código Postal** 2950-783
Telefone
E-mail SGCR@SGCR.PT
NIF 128859636

Nacionalidade PORTUGUESA
Nome ANA TERESA MARTINS VIDEIRA GABRIEL
Endereço AV. D. JOÃO II, Nº44. 2ºB
Localidade SETÚBAL **Código Postal** 2910-549
Telefone
E-mail SGCR@SGCR.PT
NIF 254290264

7 REIVINDICAÇÃO DE PRIORIDADE

8 DOCUMENTOS ANEXOS

DESCRIÇÃO (Descrição 30-11-2015.pdf)
REIVINDICAÇÕES (Reivindicações 30-11-2015.pdf)
RESUMO (Resumo 30-11-2015.pdf)
DESENHOS (Figuras 30-11-2015.pdf)

9 OBSERVAÇÕES

10 TAXAS

Taxa	Importância
PEDIDO DE PATENTE NAC.	104,08 €
Total:	104,08 €
Por Extenso:	CENTO E QUATRO EUROS E OITO CÊNTIMOS

11	**PAGAMENTO**
Tipo de Pagamento	Débito em Conta
Banco	BANCO SANTANDER TOTTA
NIB	0018.0003.18751974020.11
Montante	104,08 €
Débito a partir de	16-12-2015

12 ASSINATURA DO REQUERENTE OU MANDATÁRIO/REPRESENTANTE LEGAL

Assinatura/Nome João Luís Pereira Garcia
Nº B.I. 6943638 **Data** 2015/11/30

Atenção: Os dados relativos ao nome e morada serão publicados no Boletim da Propriedade Industrial, de acordo com o previsto no Código da Propriedade Industrial, aprovado pelo Decreto-Lei n.º 36/2003, de 5 de Março, ficando também incluídos nas bases de dados de marcas e patentes disponibilizadas neste portal.
Se desejar que a morada não seja conhecida pode optar por indicar um Apartado Postal.
Caso o requeira, poderá também aceder e retificar os seus dados. Para mais informações consulte a política de privacidade deste portal.

DESCRIÇÃO

NANOSSISTEMA DE OURO COM REVESTIMENTO BIOPOLIMÉRICO E GAMA DE ABSORÇÃO NO INFRAVERMELHO PRÓXIMO E MÉTODO PARA A SUA PREPARAÇÃO

DOMÍNIO TÉCNICO DA INVENÇÃO

A presente invenção pertence ao domínio das nanopartículas com atividade farmacêutica para uso terapêutico.

A presente invenção diz respeito a um nanossistema desenvolvido para aplicação em fototerapia, que consiste em nanopartículas de ouro produzidas através de um agente redutor à base de extrato de planta que poderá encontrar-se adsorvido à superfície, com revestimento polimérico e peptídico e com gama de absorção no infravermelho próximo. As nanopartículas da invenção possuem um extrato de planta como agente redutor do ouro, adsorvido à superfície do núcleo de ouro, bem como um revestimento polimérico e peptídico que confere ao nanossistema estabilidade e o direciona para o local do ação. O nanossistema da invenção apresenta um comprimento de onda na gama ótima de terapia, designadamente no infravermelho próximo, e adquire atividade terapêutica quando exposto à incidência de um laser ou de uma fonte de luz de aplicação similar.

A invenção compreende também um método de preparação do nanossistema de ouro, que consiste nos passos de redução de ácido cloroáurico ($HAuCl_4$) com o extrato aquoso de uma planta, com elevada concentração de compostos antioxidantes, adição de nitrato de prata e L-ácido ascórbico e revestimento das nanopartículas assim obtidas com uma solução polimérica e peptídica, que confere um aumento da estabilidade e

vectorização das nanopartículas de ouro para o local do tumor, ou de forma generalizada, para o local de ação.

Quando aplicável, este nanossistema poderá ser associado a fármacos citostáticos e aplicado como sistema de veiculação para administração direcionada no local do tumor, sendo igualmente, ativado por hipertermia através da incidência de um laser ou de uma fonte de luz de aplicação similar.

ANTECEDENTES DA INVENÇÃO

A versatilidade de aplicações farmacológicas, a facilidade de produção, as propriedades ópticas e a escala compatível com a difusão celular fazem com que as nanopartículas sejam uma das áreas de maior interesse na biologia molecular e na medicina. Em particular, as nanopartículas têm merecido atenção como sistemas dispensadores de fármacos.

O pedido de patente internacional WO 2011/116963 A2, por exemplo, apresenta um sistema nanoparticulado baseado numa camada de encapsulamento lipídica. O composto activo é encapsulado num revestimento polimérico de natureza lipídica.

Já o pedido de patente internacional WO 2012/038061 A2 divulga nanocápsulas poliméricas contendo microemulsões de óleo em água, sem recorrer a reagentes orgânicos, que podem ser aplicadas como sistemas de veiculação de compostos farmacêuticos, alimentares e/ou cosméticos.

Apesar da facilidade de difusão, estes sistemas de camada de revestimento polimérica apresentam o inconveniente de não serem muito específicos quanto ao local de administração. Frequentemente, a camada lipídica dissolve-se antes de atingir o alvo o que reduz o tratamento da terapia.

Procuraram-se assim outras nanopartículas que oferecessem maior estabilidade, biocompatibilidade e especificidade.

Neste domínio, um dos tipos de nanopartículas que tem merecido mais atenção são as nanopartículas com núcleo metálico e em particular as de ouro. Uma vez que o ouro é um metal nobre, reagindo com um número limitado de espécies químicas, e tem a capacidade de formar complexos coordenados estáveis com uma diversidade de compostos, as nanopartículas de ouro apresentam-se actualmente como particularmente promissoras no desenvolvimento de métodos de diagnóstico e terapias antitumorais. Em particular, a atividade ótica das nanopartículas de ouro tornam-nas especialmente adequadas para a fototerapia.
Os nanossistemas formados pela associação de nanopartículas a outros compostos, designadamente ligandos, adquirem uma função no diagnóstico de tumores, quando os ligandos são biomarcadores para as células tumorais, ou terapêutica, quando os ligandos são compostos activos que o nanossistema veicula até à célula ou células alvo.

A conjugação das nanopartículas de ouro com ligandos específicos representa neste momento o maior desafio científico. Por um lado os nanossistemas constituídos pelas nanopartículas e pelos ligandos têm de ser estáveis e específicos para a função a desempenhar, seja ela a marcação das células tumorais ou a administração de fármacos, por outro têm de ser biocompatíveis ou seja, a difusão do nanossistema pelas membranas celulares até à célula tumoral tem de ser possível.
Acontece que frequentemente a natureza do ligando deforma a estrutura do nanossistema. Assim, em vez de uma forma esférica que promove e facilita a difusão celular, os

nanossistemas apresentam-se frequentemente com formas cilíndricas, alongadas ou triangulares. Desta forma, continua a procurar-se um nanossistema com núcleo de ouro que seja simultaneamente estável, biocompatível e eficaz.

O pedido de patente internacional WO 2012/039685 A1 descreve um sistema coloidal contendo nanopartículas de ouro revestidas por polietilenoglicol que se liga ao composto farmacologicamente ativo para a sua veiculação ao local de administração. Verifica-se no entanto que frequentemente as partículas adquirem uma forma oblonga ou trilobada, o que dificulta a difusão celular. Além disso, a gama de absorção do sistema situa-se nos 530 nanómetros, uma gama de absorção que não é a mais adequada em fototerapia já que tem uma maior absorção e um maior potencial para danificar os tecidos saudáveis.

A patente americana US 8057682 B2 diz respeito a nanopartículas metálicas, entre elas de ouro, e a um método para a sua preparação, envolvendo um extrato natural de uma planta. A partícula envolve ainda o uso de um agente redutor sintético, de elevada reatividade e toxicidade. A nanopartícula é assim usada para captação e remoção de contaminantes presentes em água para abastecimento, água residual e solos contaminados, demonstrando ser inadequada para aplicações farmacêuticas.

O pedido de patente americano US 2009/0117045 A1 divulga também nanopartículas com base num extrato natural de uma planta e respetivo método de produção. O composto natural é proveniente de uma planta da família Fabaceae, em particular soja ou lentilha dando origem a um nanossistema com gama de absorção na ordem dos 535 nanómetros.

A presente invenção vem dar resposta às dificuldades enumeradas, com um nanossistema de ouro constituído por nanopartículas (maior área de superfície de contacto) de ouro com um revestimento à base de extrato de planta natural, revestida por um polímero e vetorizada com um péptido. O extrato de planta natural é da família Lamiaceae o que confere ao nanossistema propriedades químicas antioxidantes, contrariamente aos nanossistemas do estado da técnica que recorrem a agentes redutores com efeitos tóxicos.

As nanopartículas de ouro da invenção são preparadas a partir da redução do ácido cloroáurico como fonte de ouro. O nanossistema é formando por adição às nanopartículas de polímeros e péptidos com afinidade para recetores específicos em células tumorais.
O nanossistema assim preparado apresenta uma forma essencialmente esférica, o que favorece a difusão celular e o torna particularmente adequado para a veiculação de fármacos.

Com vista à administração farmacêutica, as nanopartículas de ouro são formuladas em nanossistemas à base de polímeros, vetorizados com péptidos, adquirindo desta forma a capacidade de veicular fármacos.

Verifica-se ainda que o nanossistema da invenção apresenta um comprimento de onda de absorção das nanopartículas de ouro na gama do infravermelho próximo, entre os 650 e os 900 nanómetros, a gama considerada óptima para fototerapia uma vez que a pele tolera a radiação sem sofrer alterações morfológicas. Em particular, verifica-se que na gama do infravermelho próximo, entre os 650 e os 900 nanómetros, os

tecidos apresentam uma menor absorção da radiação, minimizando a possibilidade de alterações morfológicas.

As nanopartículas de ouro aqui divulgadas, quando expostas a radiação no infravermelho próximo (650 – 900 nanómetros), absorvem essa radiação sob a forma de energia, sobreaquecendo e promovendo a destruição dos tecidos (necrose), por hipertermia. A ativação e ação hipertérmicas das nanopartículas ocorrem após a sua ligação por via dos vetores específicos (péptidos) conjugados à superfície das nanopartículas de ouro.

A presente invenção fornece assim um nanossistema de elevada estabilidade, seguro, biocompatível e com elevada especificidade para os recetores alvo.

SUMÁRIO DA INVENÇÃO

A presente invenção diz respeito a um nanossistema para fototerapia de tumores e patologias dermatológicas, administrado localmente e ativado por hipertermia através da incidência de um laser ou de uma fonte de luz de aplicação similar.

A invenção aqui divulgada compreende nanopartículas de ouro, com um extrato de planta como agente redutor adsorvido à sua superfície, com um revestimento polimérico e peptídico e apresenta um comprimento de onda na ordem dos 650 a 900 nanómetros, na gama de infravermelho próximo. O nanossistema apresentando atividade terapêutica, quando exposto à incidência de um laser ou de uma fonte de luz de aplicação similar, por hipertermia. Trata-se de um produto, com

atividade multifuncional, na medida em que é adaptável a diversos tumores, e vetorizado, na medida em que possui especificidade para se ligar a diferentes recetores, sobreexpressos nas células tumorais.

A invenção diz ainda respeito ao um método de preparação do nanossistema com três fases distintas:

1. Redução de ácido cloroáurico ($HAuCl_4$) com o extrato aquoso de uma planta com elevada concentração de compostos antioxidantes;
2. Adição de nitrato de prata e L-ácido ascórbico;
3. Revestimento das nanopartículas com uma solução polimérica e peptídica, que confere um aumento da estabilidade e vectorização do nanossistema de ouro para o local do tumor.

As nanopartículas de ouro aqui descritas apresentam uma morfologia essencialmente esférica, com uma população monodispersa, com um tamanho médio de 100 nanómetros, índice de polidispersão de 0,2 e carga superficial média negativa (-19 mV). O facto do nanossistema apresentar uma morfologia maioritariamente esférica é crucial para executar o objeto da invenção, uma vez que o nanossistema de ouro ocupa um pequeno volume e, consequentemente, apresenta uma maior área de superfície de contacto com as células alvo.

Contrariamente aos métodos de preparação de nanopartículas de ouro convencionais, em que habitualmente se recorre a agentes redutores sintéticos, o método da presente invenção recorre à utilização de um extrato aquoso de uma planta da família Lamiaceae, com elevada concentração de compostos antioxidantes, que são responsáveis pela redução do composto de ouro existente nas nanopartículas de ouro. Ou seja, o

extrato da planta funciona como agente redutor maioritário das nanopartículas de ouro aqui descritas.

Os compostos com atividade antioxidante usados na invenção são por exemplo os polifenóis, mais precisamente o ácido rosmarínico, ácido cafeico e ácido clorogénico. Estes compostos estão naturalmente presentes nas plantas da família Lamiaceae e permitem evitar a utilização de compostos sintéticos, como é o caso do brometo de hexadeciltrimetilamónio, que é um agente redutor e/ou estabilizador com efeitos tóxicos.

As nanopartículas de ouro compreendem também a sua funcionalização com um péptido, o fator de crescimento epidérmico (EGF), à superfície das próprias nanopartículas que conduz à vetorização da formulação para as células alvo. Por exemplo, no caso de um tratamento para o cancro, considerando que as células tumorais sobreexpressam um recetor específico para o péptido, o fator de crescimento epidérmico, o nanossistema de ouro liga-se às células tumorais. Deste modo o nanossistema é direcionado para as células tumorais. Este tipo de direcionamento do nanossistema de ouro permite que os tecidos não-alvo (isto é, as células saudáveis nas regiões circundantes da zona do tumor) não sejam expostos ao tratamento antitumoral, diminuindo possíveis efeitos secundários adversos.

A presente invenção referente a um nanossistema de ouro apresenta vantagens sobre outros nanossistemas do estado da técnica com o mesmo objetivo, nomeadamente:

a) Aumento da viabilidade de células não tumorais (devido à utilização de compostos naturais para redução do ouro, ao revestimento com polímeros biocompatíveis e

biodegradáveis e à vetorização eficaz do nanossistema de ouro multifuncional, especificamente para as células tumorais);

b) Eficácia na vetorização do nanossistema de ouro para as células tumorais, devido à presença de um péptido, designadamente o fator de crescimento epidérmico (EGF), na superfície da própria nanopartícula, que se liga aos recetores do fator de crescimento epidérmico (EGFR) sobreexpressos em células tumorais, que se torna específico e dirigido para o local do tumor;
c) Especificidade do nanossistema de ouro para as células tumorais, não afetando as células não tumorais localizadas na região do tumor, o que permite um tratamento com menores efeitos secundários;
d) Ativação do nanossistema de ouro por um processo exógeno e não invasivo ao organismo, através da hipertermia tecidual por um laser ou por uma fonte de luz de aplicação similar, na gama de absorção da proximidade aos infravermelhos, na ordem de 650 a 900 nanómetros;
e) Permite a utilização de diversas técnicas de fototerapia que apenas eliminam células tumorais, após concentração do nanossistema de ouro nessa região, por mecanismos de ativação fotónica;
f) Adaptabilidade do nanossistema de ouro modificado para diferentes tumores e outras patologias dermatológicas, bem como para associação com fármacos citostáticos.

Na presente invenção é utilizada uma planta da família Lamiaceae para preparação do extrato natural e obtenção de compostos com atividade antioxidante que são adsorvidos à superfície das nanopartículas de ouro. O extrato das plantas da família Lamiaceae apresenta uma elevada concentração de antioxidantes, sendo eficaz na redução do ouro, sem

comprometer a biocompatibilidade das nanopartículas de ouro quando administradas no local de ação.

A presente invenção é útil no tratamento de tumores, sejam estes superficiais ou profundos, e de outras patologias dermatológicas, como por exemplo a psoríase, a rosácea, a queratose, ou outras patologias. Alguns exemplos dos tumores para os quais esta invenção é aplicável e apresenta efeitos positivos na redução de células tumorais, são os carcinomas da pele, carcinoma do pulmão, tumor da mama, entre outros tumores, quer estes sejam tumores superficiais, até 5 centímetros de profundidade, quer sejam tumores profundos, com mais de 5 centímetros de profundidade. Sobre os tumores é utilizado um laser ou uma fonte de luz de aplicação similar, que ativa o nanossistema de ouro por hipertermia tecidual. O nanossistema de ouro liga-se às células tumorais, ao ser ativada por hipertermia pela incidência de um laser ou de uma fonte de luz de aplicação similar, promove o aquecimento local do tumor e, consequente, provoca a morte celular (efeito antitumoral hipertérmico).

DESCRIÇÃO DAS FIGURAS

A **Figura 1** consiste numa representação esquemática da disposição dos componentes do nanossistema e do seu processo de produção por intermédio dos agentes redutores naturais. Na figura pode observar-se o núcleo de nanopartícula de ouro (1), o revestimento polimérico (2), os vetores péptidicos (3), o extrato de planta da família Lamiaceae (4), o ácido hialurónico (5) e o ácido oleico (6).

A **Figura 2** representa o espetro de absorção ótica com o comprimento de onda em nanómetros no eixo das abscissas e a absorvância no eixo das ordenadas de: A) nanopartículas esféricas comerciais (pico de absorvância máxima: 530 nm)(linha interrompida); B) nanopartículas de ouro produzidas com o extrato aquoso de planta da família Lamiaceae, com um comprimento de onda de absorção máxima na gama ótima de terapia, isto é, no infravermelho próximo (650 - 900 nanómetro) (linha contínua).

A **Figura 3** é uma imagem microscópica de transmissão electrónica onde se observa a forma essencialmente esférica do nanossistema da invenção.

DESCRIÇÃO DETALHADA DA INVENÇÃO

A presente invenção diz respeito a um nanossistema desenvolvido para a fototerapia que contém nanopartículas de ouro com atividade multifuncional, funcionalizadas com polímeros e péptidos.
As nanopartículas de ouro produzida através de um extrato de uma planta da família Lamiaceae como agente redutor do ouro, bem como um revestimento polimérico (2) e peptídico (3) que, por sua vez, confere estabilidade ao nanossistema e o direciona para o local do ação. O nanossistema de ouro da invenção tem como particularidade apresentar um comprimento de onda na gama ótima de terapia, isto é, em infravermelho próximo, e apresentar atividade antitumoral quando exposta à incidência de um laser ou de uma fonte de luz de aplicação similar.

Os seguintes termos usados até aqui têm o seguinte significado:

"Água purificada" refere-se a água deonizada e bi-destilada, seguida por um processo de esterilização por raios ultravioleta.

"Biopolímero" entende-se como um material polimérico, de origem natural e fonte de carbono, estruturalmente classificado como polissacárido, poliéster ou poliamida.

"Compostos antioxidantes" compreendem moléculas capazes de inibir a oxidação de outras moléculas e, consequentemente, são moléculas com um potencial ação como agentes de redução.

"Diterpenóide" ou "diterpeno" consistem em metabolitos secundários da classe dos terpenos constituídos por 20 átomos de carbono, correspondendo a quatro unidades de isopreno.

"Gama ótima de terapia" compreende o intervalo de comprimentos de onda no infravermelho próximo (650 - 900 nanómetros), para o qual está descrito que os tecidos têm uma absorção muito reduzida da energia.

"Laser" refere-se a um dispositivo que produz radiação eletromagnética resultante da ampliação de luz por emissão estimulada de radiação.

Por "fonte de luz de aplicação similar" a laser entende-se qualquer dispositivo de amplificação de luz por emissão estimulada de radiação como por exemplo led superluminescente.

"Polifenol" consiste num composto antioxidante que possui uma ou mais grupos hidroxilos ligados a um anel aromático, podendo apresentar um ou mais grupos hidroxilo e mais de um anel aromático. São substâncias naturais encontradas em plantas, tais como flavonóides, taninos, lignanas, derivados do ácido cafeico, entre outras.

A designação genérica "nano" refere-se a uma estrutura cujo diâmetro está compreendido entre 1 e 1000 nanómetros.

"Nanopartícula de ouro" refere-se ao núcleo metálico de ouro (1).
"Nanossistema" refere-se à estrutura formada por nanopartículas e por um ou mais componentes depositados na sua superfície.
"Nanossistema de ouro" refere-se à estrutura formada pelo núcleo metálico de ouro (1), pelo extrato natural de planta (4) e pelo revestimento polimérico (2) e peptídico (3).
"Revestimento polimérico" (2) refere-se ao polímero que está adsorvido à superfície do núcleo metálico de ouro (1), formado por redução do extrato de planta (4), cobrindo-o uniformemente.
"Revestimento peptídico" refere-se aos vectores peptídicos (3) que se ligam em lugares específicos ao revestimento polimérico (2).
"Vetorização" entende-se como o direcionamento de uma nanopartícula (ou outro sistema de veiculação de fármaco) para um local de ação específico, onde atua por ligação a recetores específicos, para os quais possui alta afinidade.

A presente invenção diz respeito a um nanossistema de ouro composto por nanopartículas de ouro com extrato de planta (4) da família Lamiaceae adsorvido à superfície como agente redutor, com revestimento polimérico (2) e peptídico (3) e que apresenta um comprimento de onda gama de infravermelho próximo, na ordem dos 650 a 900 nanómetros. O nanossistema da invenção apresenta atividade antitumoral quando exposto à incidência de um laser ou de uma fonte de luz de aplicação similar. Trata-se de um produto, baseado em nanopartículas de ouro com atividade multifuncional, na medida em que é adaptável a diversos tumores, e vetorizada, na medida em que possui especificidade para ligar-se aos recetores sobreexpressos nas células tumorais.

A invenção diz ainda respeito a um método de preparação do nanossistema, em três fases:

1. Redução de ácido cloroáurico ($HAuCl_4$) com o extrato aquoso de uma planta com elevada concentração de compostos antioxidantes (como por exemplo, ácido rosmarínico, ácido cafeico e ácido clorogénico);
2. Adição de nitrato de prata e L-ácido ascórbico;
3. Revestimento das nanopartículas com uma solução polimérica e peptídica, que confere vectorização das nanopartículas de ouro para o local do tumor.

A presente invenção recorre à utilização do extrato aquoso de uma planta da família Lamiaceae que funciona como agente redutor por ação dos compostos antioxidantes presentes na planta, nomeadamente os polifenóis e os diterpenóides. Em particular, as plantas desta família são ricas em compostos antioxidantes polifenólicos, mais precisamente, ácido rosmarínico, ácido cafeico e ácido clorogénico. As plantas da família Lamiaceae são endémicas das regiões mediterrânicas, embora possam também encontrar-se noutras regiões. São habitualmente plantas de flor aromática devido aos óleos essenciais, com caules quadrangulares e folhas simples, opostas, pecioladas ou sésseis. Exemplos de plantas da família Lamiceae são as plantas da subfamília Salvia, espécie Acanthomintha, Achyrospermum, Acinos, Acrocephalus, Acrotome, Acrymia, Adelosa, Aegiphila , Aeollanthus , Agastache, Ajuga, Ajugoides, Alajja, Alvesia, Amasonia, Amethystea, Anisochilus, Anisomeles, Antonina , Aphanochilus, Archboldia, Ascocarydion, Asterohyptis, Atelandra, Audibertia, Ballota, Basilicum, Becium, Benguellia, Betonica, Blephilia, Bostrychanthera, Bovonia, Brachystemum, Brazoria, Brittonastrum Bystropogon, Calamintha, Calapodium,

Callicarpa, Capitanopsis, Capitanya, Caryopteris, Catoferia, Cedronella, Ceratanthus, Ceratominthe, Chaiturus, Chamaesphacos, Chaunostoma, Chelonopsis, Chloanthes, Cleonia, Clerodendranthus, Clerodendrum, Clinopodium, Colebrookea, Collinsonia, Colobandra, Colquhounia, Comanthosphace, Congea, Conradina, Coridothymus, Cornutia, Craniotome, Cruzia, Cuminia, Cunila, Cyanostegia, Cyclonema, Cyclotrichium, Cymaria, Dauphinea, Dentidia, Dicerandra, Dicrastylis, Dorystaechas, Dracocephalum, Drepanocaryum, Dysophylla, Eichlerago, Elsholtzia, Endostemon, Englerastrum, Epimeredi, Eremostachys, Eriope, Eriophyton, Eriopidion, Eriothymus, Erythrochlamys, Euhesperida, Eurysolen, Eusteralis, Faradaya, Fuerstia, Galeobdolon, Galeopsis, Gardoquia, Garrettia, Geniosporum, Germanea, Geunsia, Glecoma, Glechon, Glossocarya, Gmelina, Gomphostemma, Gontscharovia, Hanceola, Haplostachys, Harlanlewisia: Haumaniastrum, Hedeoma, Hemiandra, Hemigenia, Hemiphora, Hemizygia, Hesperozygis, Heterolamium, Hoehnea, Holmskioldia, Holocheila, Holostylon, Horminum, Hosea, Hoslundia, Hosta (botânica), Huxleya, Hymenocrater, Hymenopyramis, Hypenia, Hypogomphia, Hyptidendron, Hyptis, Hyssopus, Iboza, Isanthus, Isodictyophorus, Isodon , Isoleucas, Karomia, Keiskea, Kinostemon, Koellia, Kudrjaschevia, Kurzamra, Lachnostachys, Lagochilus, Lagopsis, Lallemantia, Lamiastrum, Lamiophlomis, Lamium, Lavandula, Leocus, Leonotis, Leonurus, Lepechinia, Leucas, Leucosceptrum, Leucophae, Limniboza, Lophanthus, Loxocalyx, Lycopus, Macbridea, Majorana, Mahya, Mallophora, Marmoritis, Marrubium, Marsypianthes, Meehania, Melissa, Melittis, Mentha, Meriandra, Mesona, Metastachydium, Microcorys, Micromeria, Microtoena, Minthostachys, Moldavica, Moluccella, Monarda, Monardella, Monochilus, Moschosma, Mosla, Neoeplingia, Neohyptis, Neomuellera, Neorapinia, Nepeta , Newcastelia, Nosema, Notochaete, Ocimum , Octomeron,

Ombrocharis, Oncinocalyx, Oreosphacus, Origanum , Orthodon, Orthosiphon, Otostegia, Oxera, Panzerina, Paraeremostachys, Paralamium, Paraphlomis, Paravitex, Peltodon, Pentapleura, Perilla, Perillula, Perilomia, Peronema, Perovskia, Perrierastrum, Petitia, Petraeovitex, Phlomidoschema, Phlomis, Phlomoides, Phyllostegia, Physoleucas, Physopsis, Physostegia, Piloblephis, Pitardia, Pityrodia, Platostoma, Plectranthastrum, Plectranthus, Pogogyne, Pogostemon, Poliomintha, Porphyra, Prasium, Premna, Prostanthera, Prunella, Pseuderemostachys, Pseudocarpidium, Pseudochamaesphacos, Pseudomarrubium, Pulegium, Puntia, Pycnanthemum, Pycnostachys, Rabdosiella, Renschia, Rhabdocaulon, Rabdosia, Rhaphiodon, Rhododon, Rosmarinus, Rostrinucula, Rotheca, Roylea, Rubiteucris, Sabaudia, Saccocalyx, Salazaria, Salvia, Salviastrum, Satureja, Schizonepeta, Schnabelia, Scutellaria, Sideritis, Siphonanthus, Siphocranion, Skapanthus, Solenostemon, Spartothamnella, Sphacele, Sphenodesme, Stachydeoma, Stachyopsis, Stachys, Stenogyne, Stiptanthus, Sulaimania, Suzukia, Symphorema, Symphostemon, Synandra, Syncolostemon, Taligalea, Tectona, Teijsmanniodendron, Tetraclea, Tetradenia, Teucridium, Teucrium, Thorncroftia, Thuspeinanta, Thymbra, Thymus, Tinnea, Trichostema, Tsoongia, Tullia, Vitex, Viticipremna, Volkameria, Wenchengia, Westringia, Wiedemannia, Wrixonia, Xenopoma, Zappania, Zataria, Zhumeria, Ziziphora. Em particular, as plantas preferidas da família Lamiaceae são as plantas da espécie Plectranthus ornatus, Plectranthus ecklonii, Plectranthus barbatus, Plectranthus saccatus, Lavandula stoechas ssp. luisieri, Lavandula pedunculata, Salvia officinalis e Rosmarinus officinalis.

Exemplo 1

Preparação do extrato aquoso a partir de uma planta da espécie Plectranthus saccatus

A planta é seca e cortada em pequenos fragmentos. A extração é obtida quando os fragmentos são expostos ao microondas, com uma frequência a 2,45 Ghz., e liofilizados. Um miligrama de planta seca origina 5,9% ácido rosmarínico, 0,026% ácido cafeico e 0,042% ácido clorogénico.

A fase da preparação do nanossistema de ouro consiste na preparação das nanopartículas de ouro e mistura do extrato de planta (4) da família Lamiaceae para adsorção do composto redutor à superfície do núcleo de ouro (1).

Exemplo 2

Redução do ácido cloroáurico ($HAuCl_4$) através do extrato aquoso de planta e formação das nanopartículas de ouro

As nanopartículas de ouro são preparadas por redução do ácido cloroáurico ($HAuCl_4$) com o extrato aquoso de planta preparado no Exemplo 1. São adicionados 9 mL de uma solução de ácido cloroáurico ($HAuCl_4$) com a concentração de 1 mM. Em seguida adicionam-se sequencialmente os compostos seguintes:

a) solução aquosa de nitrato de prata (10 mM; 5 µL);
b) solução aquosa de L-ácido ascórbico (20 mM; 500 µL);
c) solução aquosa de extrato de planta (10 mg/mL; 100 – 1000 µL) preparado no Exemplo 1

Consoante a espécie de planta usada também o conteúdo em compostos antioxidantes varia e deste modo, a razão molar do extrato aquoso da planta para as nanopartículas de ouro altera-se. Regra geral, a razão molar do extrato aquoso da planta para as nanopartículas de ouro varia entre 2:1 a 1:20, conforme a massa molar do composto antioxidante maioritário

presente na planta e a concentração do ouro nas nanopartículas de ouro. Habitualmente, as plantas da família Lamiaceae contêm ácido rosmarínico como composto antioxidante maioritário.

A concentração da solução de ácido cloroáurico usada na redução pode variar entre os 0,2 e 1 mM e o tempo de reação pode variar entre 15 minutos a 24 horas, com uma agitação entre as 200 e as 1000 rotações por minuto, para um pH compreendido entre os 7 e os 10 e uma temperatura entre os 25°C e os 35°C.

A adição de agentes moduladores e co-adjuvantes no processo de redução do ouro, nomeadamente nitrato de prata, em concentrações entre o 1 e os 10 mM, e L-ácido ascórbico, em concentrações entre os 2 e os 20 mM é vantajosa para o rendimento da reação.

Após obtenção das nanopartículas de ouro com o agente redutor adsorvido à superfície, aplica-se o revestimento polimérico (2) e peptídico (3) sobre as nanopartículas para obtenção do nanossistema de ouro.

Exemplo 3

Revestimento das nanopartículas de ouro com uma solução polimérica e peptídica

A preparação do nanossistema de ouro compreende os passos seguintes:

a) Adição de ácido hialurónico (5) e ácido oleico (HAOA) (6) (1:1, v/v), à concentração de 1 mg/mL para cada composto, que são incubados numa solução aquosa, com pH = 10 (NaOH 1M, 0,3%, v/v), durante 24 horas a 60°C, à

solução contendo as nanopartículas de ouro preparada no Exemplo 2;

b) Adição do péptido fator de crescimento epidérmico (EGF), à concentração de 2,5 µM (em tampão fosfato salino pH 7.4), à solução de nanopartículas de ouro, ácido hialurónico (5) e ácido oleico (6) (1:1:1, v/v/v), sob agitação a 800 rotações por minuto, durante 30 minutos, à temperatura ambiente e, posteriormente, em repouso a 4°C;

c) Centrifugação de 1,820g a 7,200g da mistura obtida nos passos a) e b), durante 15 minutos e conservação das nanopartículas de ouro, em água purificada ou tampão fosfato salino.

O nanossistema de ouro da invenção e produzido de acordo com o método descrito, foi caracterizado em termos de:

a) Tamanho médio das partículas e índice de polidispersão (PI)

As nanopartículas de ouro aqui descritas apresentam uma morfologia essencialmente esférica, com uma população monodispersa, com um tamanho médio de 100 nanómetros, índice de polidispersão de 0,2 e carga superficial média negativa (-19 mV).

b) Comprimento de onda para a absorvância máxima da amostra ($\lambda_{máx}$)

Foi obtido o espetro de absorção ótica da **Figura 2** onde se pode observar um pico de absorção na gama ótima de terapia, ou seja, no infravermelho próximo (650 - 900 nanómetro).

c) Morfologia e superfície das nanopartículas, por microscopia eletrónica de transmissão e analisados com uma tensão de aceleração de 10-20kV.
Foi obtida a imagem microscópica de transmissão electrónica da **Figura 3**, onde se observa a forma essencialmente esférica do nanossistema da invenção.

As nanopartículas de ouro que apresentam estruturas anisotrópicas não são favoráveis em termos de termodinâmica; contudo, quando associadas a agentes estabilizantes como, por exemplo, as biomoléculas presentes nos extratos de plantas, apresentam uma banda de absorção na região do infravermelho próximo na ordem dos 650 a 900 nanómetros.

As partículas preparadas segundo a invenção apresentam morfologia essencialmente esférica. Esta característica é relevante para cumprir o objetivo terapêutico da invenção. Se por um lado a morfologia esférica facilita a difusão celular do nanossistema, por outro, o facto de ocupar um pequeno volume faz com que o nanossistema tenha uma maior área de superfície de contacto com as células alvo.

A atividade terapêutica do nanossistema de ouro da invenção é confirmada através de diversos ensaios, nomeadamente:

- Ensaio de vectorização para a célula alvo, após a conjugação das nanopartículas de ouro com diferentes péptidos (Exemplo 4);
- Teste de inocuidade das células não alvo através de ensaios de viabilidade celular sobre linhas celulares "normais"/ células não tumorais (Exemplo 5);
- Ensaio de eficácia do nanossistema por análise da internalização celular em linhas celulares tumorais (Exemplo 6).

Exemplo 4

Comprovação da vectorização para a célula alvo

Para comprovar a vectorização do nanossistema para uma célula ou células alvo, são aqui apresentados dois ensaios das nanopartículas de ouro conjugada com dois modelos de proteína/péptido, de cargas distintas. São feitos ensaios, um com fator de crescimento epidérmico (EGF – "epidermal growth factor") e outro com lisozima.

A fim de preparar as nanopartículas de ouro conjugadas com os dois péptidos de diferentes cargas superficiais e massas moleculares, tanto o fator de crescimento epidérmico EGF como a lisozima, foram reconstituídos em tampão fosfato 20 mM (pH 7,4) a 10 µM e 2,5 µM, respetivamente. Em seguida, as três soluções (proteína/péptido, nanopartículas de ouro e solução polimérica) foram misturadas numa proporção de 1:1:1 (v/v/v) e deixou-se interagir durante 30 minutos à temperatura ambiente e 24 horas a 4°C, sem agitação. A solução foi centrifugada para remover péptidos não ligados e o nanossistema de ouro foram resuspensas em tampão fosfato pH 7,4.

As partículas do nanossistema de ouro apresentam um tamanho de cerca de 100–150 nanómetros (PI = 0,2), após análise de caracterização de partículas. O comprimento de onda de absorção das partículas foi de aproximadamente 800 – 830 nanómetros.

Após conjugação com o fator de crescimento epidérmico estas apresentaram uma banda de absorção aproximada aos 650 – 900 nanómetros. Após conjugação com fator de crescimento epidérmico, o potencial zeta das nanopartículas manteve-se

negativo. A conjugação do fator de crescimento epidérmico às nanopartículas também foi verificada através da visualização das mesmas através de microscópio confocal. Foi aplicada a técnica de "co-localização" com dois marcadores fluorescentes, cujos espectros de emissão apresentam comprimentos de onda distintos. As partículas do nanossistema de ouro foram marcadas com Coumarina-6, enquanto o fator de crescimento epidérmico utilizado para conjugação nestes estudos foi o fator de crescimento epidérmico marcado com Alexa Fluor 647. A presença de regiões em que há sobreposição de cores permitiu confirmar que o fator de crescimento epidérmico está conjugado ao nanossistema de ouro.

Estudaram-se também as possíveis modificações associadas à proteína lisozima e ao péptido fator de crescimento epidérmico, após exposição à radiação ultravioleta-B (foto-iluminação), temperatura e após conjugação com as nanopartículas de ouro. Os resultados obtidos através de ensaios com espectroscopia de fluorescência mostraram a iluminação contínua a 295 nanómetros (radiação utravioleta-B) da proteína lisozima e do péptido fator de crescimento epidérmico, no seu estado livre (ou seja, não conjugadas às nanopartículas biopoliméricas) conduziu à diminuição da fluorescência dos resíduos aromáticos (espectros de excitação e emissão) e à formação de produtos fotoquímicos oxidativos (por exemplo, di-tirusina, quinurenina, N'-formil-quinurenina), provocando alterações na sua estrutura nativa. Por sua vez, a conjugação com nanopartículas de ouro não induziu a desnaturação das proteínas. Além disso, as nanopartículas de ouro promoveram a proteção tanto para a lisozima como para o fator de crescimento epidérmico, reduzindo a cinética de decaimento da fluorescência e,

comparativamente, os efeitos de foto-oxidação e alteração de conformação/estrutura proteicas foram inferiores.

Exemplo 5

Comprovação da inocuidade das células não alvo

A inocuidade das células não alvo é aqui comprovada através de ensaios de viabilidade celular sobre linhas celulares "normais"/ células não tumorais. Para tal, foram estudadas em linhas celulares de queratinócitos humanos (modelo HaCaT), através do método colorimétrico de brometo de tetrazolina. Inicialmente, avaliou-se a citotoxicidade do extrato isolado da planta da família Lamiaceae a diferentes concentrações e, posteriormente, das nanopartículas de ouro, com e sem conjugação com fator de crescimento epidérmico. As células foram cultivadas em meio de Eagle modificado por Dulbelcco (DMEM – "Dulbelcco's modified Eagle médium") suplementado com 10% soro fetal bovino e solução de antibióticos (penicilina/estreptomicina, 1%). As células HaCaT foram semeadas em placa de 96 poços a uma densidade de 5000 células/poço. A solução aquosa de extrato da planta da família Lamiaceae foi preparada por diluição em dimetilsufóxido, com as seguintes concentrações finais: 0-500 µg/mL. O nanossistema de ouro foi também testado a diferentes concentrações: 0-80 µM (a partir da concentração de ouro). As células foram expostas aos diferentes tratamentos durante 24 horas. Após este período, as células foram lavadas com tampão fosfato salino pH 7.4 e incubadas com uma solução de brometo de tetrazolina (0,5 mg/mL em meio de cultura) durante 2,5 horas e a 37°C. Por último, o meio foi removido e as células foram lavadas com tampão fosfato salino pH 7.4. Uma alíquota de 200 µL de dimetilsufóxido por poço foi adicionada para dissolver os cristais de formazan e a absorvância foi lida a

595 nanómetros. Foram realizados, para cada tratamento, três ensaios independentes, cada um composto por quatro réplicas.
O extrato da planta usado apresentou valores elevados de viabilidade celular (> 80%, para concentração mais elevada, usada para a produção das nanopartículas de ouro). Tanto as nanopartículas de ouro conjugadas com fator de crescimento epidérmico, como as nanopartículas de ouro não conjugadas, demonstraram um valor elevado (> 70%) de viabilidade celular em modelo HaCaT.

Exemplo 6

Comprovação da eficácia do nanossistema de ouro

Para comprovar a eficácia das nanopartículas de ouro, foram realizados ensaios para verificar a internalização celular e ligação do nanossistema de ouro em linhas celulares tumorais. O ensaio foi realizado numa linha de células de carcinoma do pulmão (células A549).
Foram usadas nanopartículas de ouro conjugadas com fator de crescimento epidérmico em linhas de células A549, *in vitro*. O ensaio baseia-se na expressão da proteína fluorescente GFP ("green fluorescence protein"), que está acoplada aos recetores membranares da linha celular A549. Quando ocorre internalização, o recetor muda para a cor verde, sendo possível monitorizar *in loco* este processo.

As células foram cultivadas em poços e após 24 horas foram adicionados, para além do controlo (sem tratamento), as amostras em análise, nomeadamente:
- Fator de crescimento epidérmico livre;
- Fator de crescimento epidérmico-nanopartículas de ouro (fator de crescimento epidérmico marcado com Alexa Fluor 647);

- Fator de crescimento epidérmico-nanopartículas de ouro (duplamente marcadas: Alexa Fluor 647 para o péptido; Coumarina-6 para as nanopartículas de ouro).

Em alguns poços foi também previamente adicionado anticorpo neutralizante anti-EGFR ("primary mouse monoclonal antibody anti-EGFR neutralizer antibody LA1), de modo a avaliar o possível efeito competidor do fator de crescimento epidérmico livre, e o fator de crescimento epidérmico conjugado às nanopartículas de ouro. As células foram expostas aos vários tratamentos durante dois tempos diferentes, a 1,5 horas e a 3 horas, à temperatura de 37°C. Após este período, as células foram lavadas com tampão fosfato salino pH 7.4, para remover resíduos de péptido e partículas não internalizadas e foram analisadas.

Os resultados foram idênticos para ambos os ensaios. Observou-se que tanto o fator de crescimento epidérmico livre, como as nanopartículas de ouro conjugadas com fator de crescimento epidérmico internalizam ao final de 1,5h em contacto com a linha celular de carcinoma do pulmão. Nestes ensaios foi igualmente possível verificar que as nanopartículas de ouro conjugadas com fator de crescimento epidérmico são internalizadas pelas células de forma eficiente, uma vez que acrescem nos mecanismos de ativação comparativamente ao fator de crescimento epidérmico isolado e também competem diretamente com o anticorpo anti-EGFR.

Os exemplos de aplicação anteriores visam confirmar a atividade do nanossistema da invenção e o seu importante potencial em terapia antitumoral.

Ao demonstrar através de ensaios a vectorização do nanossistema de ouro da invenção para o local de ação comprova-se que a invenção vem dar resposta à necessidade de nanopartículas especificas e direcionadas para o desenvolvimento de uma terapêutica contra o cancro ou patologia dermatológica.

Por outro lado, ao confirmar através de ensaios a inocuidade do nanossistema de ouro da invenção para as células não alvo demonstra-se a segurança do nanossistema.

Finalmente, ao confirmar a internalização celular do nanossistema de ouro quando aplicado a uma linha celular de carcinoma humano de pulmão (linha A549), demonstra-se a biocompatibilidade do nanossistema da invenção e a sua adaptabilidade a condições patológicas diversas.

No entanto, os exemplos de aplicação anterior não devem ser interpretados como limitadores da vocação dos nanossistemas de ouro da invenção, podendo surgir aplicações futuras com o aprofundamento da investigação associada a estes compostos.

Lisboa, 30 Novembro de 2015

REIVINDICAÇÕES

1. Nanossistema de ouro **caracterizado pelo facto** de ser constituído por um núcleo metálico de ouro (1) com um extrato de planta (4) adsorvido à superfície como agente redutor e por um revestimento de um polímero (2) e de um péptido (3) e por apresentar uma morfologia essencialmente esférica.

2. Nanossistema de ouro de acordo com a reivindicação 1 **caracterizado pelo facto** de a planta usada no extrato de planta (4) usado como agente redutor pertencer à família Lamiaceae.

3. Nanossistema de ouro de acordo com a reivindicação 1 e 2 **caracterizado pelo facto** de o polímero ser seleccionado entre o grupo constituído por polissacáridos, poliésteres ou poliamidas.

4. Nanossistema de ouro de acordo com a reivindicação 1 a 3 **caracterizado pelo facto** de o péptido ser seleccionado entre o grupo constituído pelo fator de crescimento epidérmico (EGF) e pela lisozima.

5. Nanossistema de ouro de acordo com a reivindicação 1 a 4 **caracterizado pelo facto** da gama de absorção no infravermelho próximo apresentar um máximo na ordem dos 650 a 900 nm.

6. Nanossistema de ouro de acordo com as reivindicações 1 a 5 **caracterizado pelo facto** de apresentar atividade terapêutica quando exposto à incidência de um laser ou de uma fonte de luz de aplicação similar por hipertermia.

7. Nanossistema de ouro de acordo com as reivindicações 1 a 6 **caracterizado pelo facto** de ser administrado localmente e

ativado por hipertermia através da incidência de um laser ou de uma fonte de luz de aplicação similar.

8. Processo de preparação das nanopartículas de ouro constituintes do nanossistema de ouro das reivindicações 1 a 7, **caracterizado** por:
a) Se dissolver o ácido cloroáurico numa concentração compreendida entre 0,2 e 1 mM durante 15 minutos a 24 horas;
b) Se adicionar o extracto aquoso de planta da família Lamiaceae numa razão molar seleccionada entre o grupo 2:1, 1:2, 1:4, 1:8, 1:10 e 1:20;
c) Se adicionarem agentes moduladores e co-adjuvantes no processo de redução do ouro.

9. Nanopartículas de ouro preparadas de acordo com a reivindicação 8 **caracterizadas por** conterem um núcleo metálico de ouro (1) e um extrato de planta (4) adsorvido à superfície do metal com função redutora.

10. Processo de preparação do nanossistema de ouro das reivindicações 1 e 7 **caracterizado pelo** fato de a solução de revestimento das nanopartículas de ouro ser preparada segundo os passos seguintes:
a) Adição de uma solução de ácido hialurónico (5) e de ácido oleico (6) numa proporção de 1:1;
b) Adição de um péptido seleccionado entre o grupo constituído por Fator de Crescimento Epidérmico (EGF) e Lisozima;
c) Obtenção das partículas do nanossistema de ouro por centrifugação.

11. Uso do nanossistema de ouro das reivindicações 1 a 7, na fototerapia de tumores seleccionados entre o grupo

constituído por carcinomas da pele, carcinoma do pulmão e tumor da mama.

12. Uso do nanossistema de ouro das reivindicações 1 a 7, na fototerapia de tumores localizados a mais de 5 centímetros de profundidade.

Lisboa, 30 Novembro de 2015

RESUMO

NANOSSISTEMA DE OURO COM REVESTIMENTO BIOPOLIMÉRICO E GAMA DE ABSORÇÃO NO INFRAVERMELHO PRÓXIMO E MÉTODO PARA A SUA PREPARAÇÃO

Nanossistema composto por nanopartículas de ouro produzidas através de um extrato de planta (4) como agente redutor adsorvido à superfície de um núcleo metálico de ouro (1) e um revestimento polimérico (2) e peptídico (3), de forma essencialmente esférica e com gama de absorção no infravermelho próximo, e método para a sua preparação a partir de ácido hialurónico (5) e ácido oleico (6). O nanossistema apresenta atividade terapêutica em tumores superficiais, nomeadamente localizados a profundidade inferior a 5 centímetros, e profundos, nomeadamente localizados a profundidade superior a 5 centímetros, e em patologias dermatológicas quando ativado por hipertermia através da incidência de um laser ou de uma fonte de luz de aplicação similar.

1/3

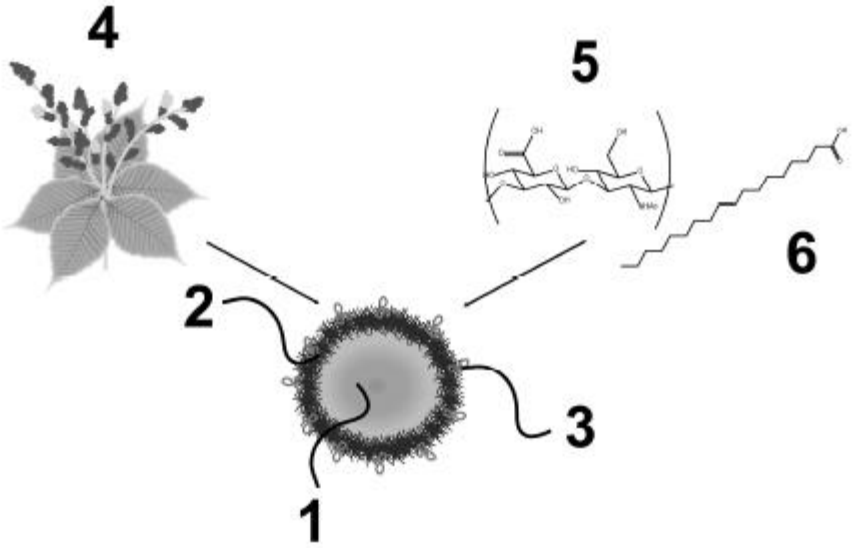

Figura 1

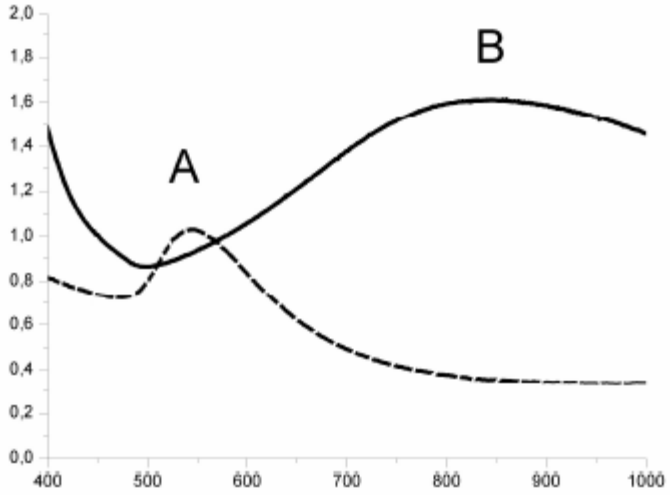

Figura 2

3/3

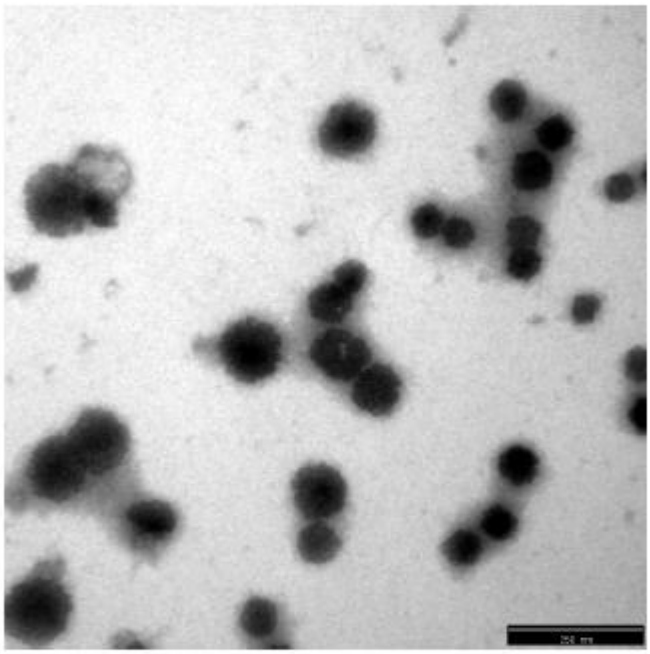

Figura 3